New-Measurement Techniques to Diagnose Charged Dust and Plasma Layers in the Near-Earth Space Environment Using Ground-Based Ionospheric Heating Facilities

Alireza Mahmoudian

Dissertation submitted to the Faculty of the
Virginia Polytechnic Institute and State University
in partial fulfillment of the requirements for the degree of

Doctor of Philosophy
in
Electrical Engineering

Wayne A Scales, Chair
Scott M Bailey
Gregory D Earle
Christopher J Roy
Timothy Pratt

November 30th, 2012
Blacksburg, Virginia

Keywords: Ionospheric Modification, Plasma, Numerical Simulations, Analytical model

New-Measurement Techniques to Diagnose Charged Dust and Plasma Layers in the Near-Earth Space Environment Using Ground-Based Ionospheric Heating Facilities

Alireza Mahmoudian

(ABSTRACT)

Recently, experimental observations have shown that radar echoes from the irregularity source region associated with mesospheric dusty space plasmas may be modulated by radio wave heating with ground-based ionospheric heating facilities. These experiments show great promise as a diagnostic for the associated dusty plasma in the Near-Earth Space Environment which is believed to have links to global change. Such experiments may provide an alternative to more complicated and costly space-based observational approaches to investigating these layers. This dissertation seeks to develop new analytical and computational models to investigate fundamental physics of the associated dusty plasmas as well as utilize experimental observations during High Frequency HF ground-based heating experiments to develop practical techniques for diagnosing these dusty plasma layers.

The dependency of the backscattered signal strength (i.e. Polar Mesospheric Summer Echoes PMSEs) after the turn-on and turn-off of the radio wave heating on the radar frequency is an unique phenomenon that can shed light on the unresolved issues associated with the basic physics of the natural charged mesospheric dust layer.

The physical process after turn-on and turn-off of radio wave heating is explained by competing ambipolar diffusion and dust charging processes. The threshold radar frequency and dust parameters for the enhancement or suppression of radar echoes after radio wave heating turn-on are investigated for measured mesospheric plasma parameters. The effect of parameters such as the electron temperature enhancement during radiowave heating, dust density, dust charge polarity, ion-neutral collision frequency, electron density and dust radius on the temporal evolution of electron irregularities associated with PMSE is investigated. The possibility of observing the turn-on overshoot (enhancement of radar echoes after the radiowave turn-on) in the high frequency HF radar band is discussed based on typical mesospheric parameters. It is shown that predicted enhancement of electron irregularity amplitude after heater turn-on at HF band is the direct manifestation of the dust charging process. Therefore further PMSE heating experiment should be pursued at HF band to illuminate the fundamental charging physics of dusty plasmas in the mesosphere. Preliminary observation results of HF PMSE heating experiments with the new 7.9 MHz radar at the European Incoherent Scatter EISCAT facility appear promising for the existence of PMSE turn-on overshoot. Therefore, future experimental campaigns are planned to validate these predictions.

Computational model results are used to make predictions for PMSE active modification experiments at 7.9, 56, 139, 224 and 930MHz corresponding to existing ionospheric heating facilities. Data from a 2009 very high frequency VHF (224 MHz) experiment at EISCAT is compared with the computational model to obtain dust parameters in the local mesospheric

dust layer at 85 km. The estimated dust parameters as a result of these comparisons show very reasonable agreement to dust radius and density at PMSE altitudes measured during a recent sounding rocket experiment providing validation to the computational model.

The first comprehensive analytical model for the temporal evolution of PMSE after heater turn-on is developed and compared to the more accurate computational model as a reference. It is shown that active PMSE heating experiments involving multiple observing frequencies at 7.9 (HF), 56, and 224 MHz (VHF) may contribute further diagnostic capabilities since the temporal evolution of radar echoes is substantially different for these frequency ranges. It is shown that conducting PMSE active experiments at HF and VHF band simultaneously may allow estimation of the dust density altitude profile, dust charge state variation during the heating cycle, and ratio of electron temperature enhancement in the irregularity source region.

These theoretical and computational models are extended to study basic physics of the evolution of relevant dusty plasma instabilities thought to play an important role in irregularity production in mesospheric dust layers. A key focus is the boundary layer of these charged dust clouds. Several aspects of the cloud's structure (thickness of boundary layer, average particle size and density, collisional processes, and cloud expansion speed) and the ambient plasma are varied to determine the effect of these quantities on the resulting irregularities. It was shown that for high collision frequencies, the waves may be very weakly excited (or even quenched) and confined to the boundary layer. The excited dust acoustic waves inside the dust cloud with frequency range of 7-15Hz and in the presence of electron bite-outs is consistent with measured low frequency waves near 10 Hz by sounding rocket experiments over the past decade. The observed radar echoes associated with the artificially created dust clouds at higher altitudes in the ionosphere including space shuttle exhaust and upcoming active space experiments in which localized dust layers will be created by sounding rockets could be related to the excited acoustic waves predicted.

Finally, variation of spatial structures of plasma and dust (ice) irregularities in the PMSE source region in the presence of positively charged dust particles is investigated. The correlation and anti-correlation of fluctuations in the electron and ion densities in the background plasma are studied considering the presence of positive dust particle formation. Recent rocket payloads have studied the properties of aerosol particles within the ambient plasma environment in the polar mesopause region and measured the signature of the positively charged particles with number densities of (2000 cm^{-3}) for particles of 0.5-1 nm in radius. The measurement of significant numbers of positively charged aerosol particles is unexpected from the standard theory of aerosol charging in plasma. Nucleation on the cluster ions is one of the most probable hypotheses for the positive charge on the smallest particles. The utility being that it may provide a test for determining the presence of positive dust particles. The results of the computational model described show good agreement with observed rocket data. As an application, the model is also applied to investigate the electron irregularity behavior during radiowave heating assuming the presence of positive dust particles. It is shown that the positive dust produces important changes in the behavior during Polar Meso-

spheric Summer Echo PMSE heating experiments that can be described by the fluctuation correlation and anti-correlation properties.

The second part of this dissertation is dedicated to Stimulated Electromagnetic Emissions SEEs produced by interaction of high power electromagnetic waves in the ionosphere. Near-earth ionospheric plasma presets a natural laboratory for investigation of nonlinear wave phenomena in plasma which can not be studied in the laboratory environment due to the effect of physical boundary conditions. This process has been of great interest due to the important diagnostic possibilities involving ability to determine mass of constitutive ions in the interaction region through measurements of various gyro-frequencies. Objectives include the consideration of the variation of the spectral behavior under pump power, proximity to the electron gyro-harmonic frequency, and beam angle. Also, the relationship between such spectral features and electron acceleration and creation of plasma irregularities was an important focus.

Secondary electromagnetic waves excited by incident high power electromagnetic waves transmitted into the ionosphere, commonly know as Stimulated Electromagnetic Emissions SEEs, produced through Magnetized Stimulated Brillouin Scatter MSBS are first investigated. Data from two recent research campaigns at the High Frequency Active Auroral Research Program facility HAARP in Gakona, Alaska is presented in this work. These experiments have provided additional quantitative interpretation of the SEE spectrum produced by MSBS to yield diagnostic measurements of the electron temperature in the heated ionosphere. SEE spectral emission lines corresponding to ion acoustic IA and electrostatic ion cyclotron EIC modes were observed with a shift in frequency up to a few tens of Hz from radio waves transmitted near the third harmonic of the electron gyro-frequency $3f_{ce}$. The threshold of each emission line has been measured by changing the pump wave amplitude. The experimental results aimed to show the threshold for transmitter power to excite IA waves propagating along the magnetic field lines as well as for EIC waves excited at oblique angles relative to the background magnetic field. A full wave solution has been used to estimate the amplitude of the electric field at the interaction altitude. The estimated growth rate using the theoretical model is compared with the threshold of MSBS lines in the experiment and possible diagnostic information for the background ionospheric plasmas is discussed. Simultaneous formation of artificial field aligned irregularities FAIs and suppression of the MSBS process is investigated.

Recently, there has been significant interest in ion gyro-harmonic structuring the Stimulated Electromagnetic Emission SEE spectrum due to the potential for new diagnostic information available about the heated volume and ancillary processes such as creation of artificial ionization layers. These relatively recently discovered emission lines have almost exclusively been studied for second electron gyro-harmonic heating. The first extensive systematic investigations of the possibility of these spectral features for third electron gyro-harmonic heating are provided here. Discrete spectral features shifted from the transmit frequency ordered by harmonics of the ion gyro-frequency were observed for third electron gyro-harmonic heating for the first time at a recent campaign at a High Frequency Active Auroral Research Program

Facility HAARP. These features were also closely correlated with a broader band feature at a larger frequency shift from the transmit frequency known as the Downshifted Peak DP. The power threshold of these spectral features was measured, as well as their behavior with heater beam angle, and proximity of the transmit frequency to the third electron gyro-harmonic frequency. Comparisons were also made with similar spectral features observed during 2^{nd} electron gyro-harmonic heating during the same campaign. A theoretical model is provided that interprets these spectral features as resulting from parametric decay instabilities in which the pump field ultimately decays into high frequency upper hybrid/electron Bernstein and low frequency neutralized ion Bernstein IB and/or obliquely propagating ion acoustic waves at the upper hybrid interaction altitude. Coordinated optical and SEE observations were carried out in order to provide a better understanding of electron acceleration and precipitation processes. Optical emissions were observed associated with SEE gyro-harmonic features for pump heating near the second electron gyro-harmonic during the campaign. The observations affirm strong correlation between the gyro-structures and the airglow.

Acknowledgments

First and foremost I would like to express my deepest and sincere gratitude to my advisor, Dr. Wayne A. Scales, for his valuable advice, guidance and encouragement during the course of this work. I sincerely appreciate his enthusiasm and patience in guiding me during this research work. His insight, kindness, and genuine concern for his students made working with him a truly memorable experience.

I am also grateful to Professors Christopher Roy, Scott Bailey, Greg Earle, Tim Pratt for their time spent serving on my advisory committee.

No words can express my gratitude to my parents and brother for endless encouragement, support, and kind words throughout my life.

This work was supported by the National Science Foundation.

Contents

List of Figures

List of Tables

Chapter 1

Introduction

Over 40 metric tons of meteoric dust enters the Earths atmosphere every day. This dust settles and creates natural dust layers in the altitude range between 80 and 100 km which spans the Earths upper mesosphere to lower thermosphere. Since these dust layers are immersed in the Earths upper atmosphere, they become electrically charged due to a collection of electrons and ions from Earths ionospheric plasma. Noctilucent clouds (NLCs) are a fascinating visual manifestation of these dust layers. The so-called polar mesospheric summer echoes (PMSEs) are radar echoes that are a direct consequence of the subvisible charged dust that exists at altitudes above the NLC regions (Cho, J.Y.N., and Kelley, M.C., 1993; Cho, J.Y.N., and J. Rottger, 1997). The radar echoes are produced by electron irregularities that result from electron charging onto the irregular dust density (Lie-Svenson et al., 2003). Because of the intimate relationship between these phenomenological signatures and the global environment, the study of such dust layers is a forefront issue in upper atmospheric space science.

Although this is a vigorous area of research, there are many unresolved issues regarding the basic physics of natural dust layers in the upper atmosphere. An alternate approach to understanding natural dust layers is to perform active space experiments in which a dust cloud is created in a controlled manner in the upper atmosphere. Its evolution can then be more carefully observed and studied and then compared with the characteristics of natural dust clouds. Such experiments are currently under development and are planned for the near future.

A comparison of natural and artificially created dust clouds is expected to be quite enlightening and could lead to more insight into the physical processes associated with natural dust clouds. Several important issues to be investigated include dust charging processes, plasma flows, electrodynamic structure, plasma irregularities, and coupling between the neutral components of the upper atmosphere and the dust clouds. In addition, possibilities of remote sensing plasma processes in these clouds through radar measurements will be investigated. The physical processes expected to be important during the early time phase after creation

of an artificial dust cloud in the Earths ionosphere will be considered here. Of principal importance will be the production of plasma irregularities which may lead to radar echoes and the possibility of their relationship to PMSEs observed from natural dusty space plasmas.

1.1 Polar Mesospheric Clouds PMCs

Noctilucent clouds from ground observations, or polar mesospheric clouds in the case of space observations, have first been recorded in 1885 (Backhouse et al., 1885; Balsley et al., 1983) and are the highest clouds in the Earth's atmosphere. PMCs are most frequently observed above 70°-75° in latitude (mostly near the polar regions) and have a season of 60 to 80 days duration centered about a peak which occurs about 20 days after the summer solstice when the mesosphere is coldest ($\sim$ 150k). A Typical profiles of neutral atmospheric temperature is shown in Figure 1.1. They are made of crystals of water ice and located in the mesosphere at altitudes of around 76 to 85 kilometres. Particles responsible for NLCs usually grow sufficiently that they can be observed by lidars (Baumgarten et al., 2008), space born cameras (Russell et al., 2009), and rocket born photometers (Gumbel et al., 2001). Analysis has shown that visible NLC particles typically have the characteristic sizes in the range 20-100 nm (Baumgarten et al., 2008) and are visible when illuminated by sunlight from below the horizon. On April 25, 2007, the AIM satellite (Aeronomy of Ice in the Mesosphere) was launched as the first satellite dedicated to studying noctilucent clouds.

Polar mesospheric summer echoes (PMSEs) are strong radar echoes produced by particle clouds which are formed at mesopause altitudes 83 -88km (Rapp and Lubken, 2004). The electron irregularities are produced as a result of charging onto the irregularity structures in the subvisible particle density (Inhester et al., 1994). These subvisible particles are located a few kilometers above the NLCs and smaller in size in comparison with those creating NLCs (Robertson et al., 2009). The Polar Mesosphere Summer Echoes (PMSE), were first observed using the 50 MHz VHF radar at Poker Flat, Alaska (Ecklund and Balsley, 1981) but have subsequently been detected using a number of different radio sounding frequencies including 1.29 GHz, 933, 224, 53.5, 8, 7.6, 4.9, 3.3, 2.43 MHz (Cho and Kelley, 1993; Rottger, 1994; Cho and Rottger, 1997; Ramos et al., 2009; Rapp and Lubken, 2004). PMSE particles are dusty ice particles and are a combination of dust and ice (Brattli et al., (2009), and special issue devoted to the measurements of ice particles) and for remainder of this work will be referred to as simply dust particles.

Polar Mesospheric Clouds PMCs have been investigated by radar, lidar, satellite and rocket. Remote sensing techniques such as lidar as well as in-situ sounding rocket measurements have been implemented to measure the size and possibly charge of dust (ice) particles associated with PMCs. A main objective of the past works was to measure the density of positively and negatively charged dust particles as well as plasma densities. First detection of charged dust particles was reported by Havnes et al. (1996). Both positive and negative particles were observed in this experiment. Another sounding rocket experiment was carried out in 2002

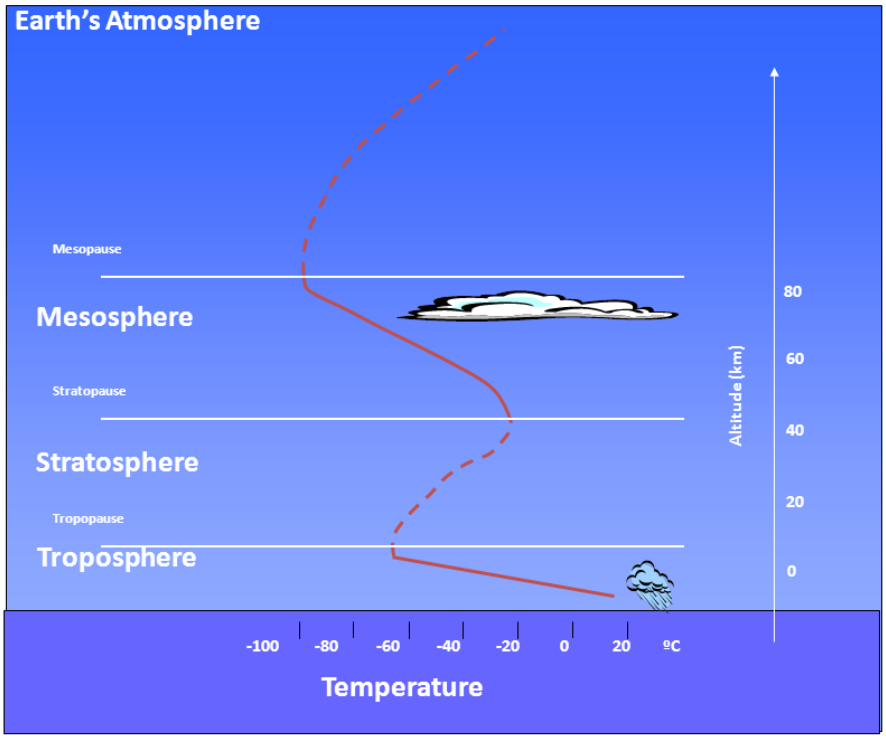

Figure 1.1: Typical profiles of neutral atmospheric temperature.

when both Noctilucent cloud NLC and PMSE were present (Blix et al., 2003; Smiley et al., 2003). Positive and negative particles were detected in the PMSE source region which proves the relationship of positive particles and electron fluctuations (Blix et al., 2003; Smiley et al., 2003). This had been also observed in another experiment and in the absence of NLC conditions (Gelinas et al., 1998). Observations made during the DROPPS program also indicate the presence of positively charged aerosols/dust at PMSE/NLC altitudes (Croskey et al., 2001).

1.2 Polar Mesospheric Summer Echoes and Active Modulation Experiment

Polar Mesospheric Summer Echoes (PMSEs) are very strong radar echoes produced by structures in the electron density at half the radar wavelength. Those structures in electron density are formed due to the charging onto the subvisible irregularity structures in the dust density. These echoes have been observed typically in the 50 MHz to 1.3 GHz frequency range in the summer polar mesosphere (Eklund and Balsley, 1981; Rapp and Lubken, 2004; Cho and Kelley, 1993; Cho and Rottger, 1997, and references therein). The electron bite-outs observed by in-situ rocket measurements are direct evidence for the presence of charged ice aerosol particles at PMSE altitudes (Pfaff et al., 2001; Ulwick et al., 1988; Havnes et al., 1996). The cause of these dust density structures and their persistence over relatively long intervals (10s to 100s of milliseconds) has been an open scientific question (Rapp and Lubken, 2004).

There has been an extensive effort to measure the dust particles in the mesosphere through space-based and ground-based measurements (Robertson et al., 2009; Chandran et al., 2009; Hervig et al., 2008; Baumgarten et al., 2008). In recent years, ground based observation techniques have drawn considerable interest in the space science community although it may be lacking in spatial and time resolution. More direct investigations which resolve these issues are possible by sounding rocket. However, with these in-situ methods, the short time frame of the experiments becomes a problem as many of the most interesting mesospheric phenomenon occur over a longer time interval. PMSE heating experiments have possibilities as an alternative approach that can be implemented to diagnose the PMSE source region at much lower cost. PMSE heating experiments have opened a new experimental window for the study of PMSE by modifying the electron temperature at altitudes where PMSE to temperatures of 3000 K.

The EISCAT heating transmitter including a phased array antenna is designed to transmit a narrow beam of high power radio signals in the 2.8 to 10 MHz frequency range. During the PMSE heating experiment HF transmitter is on to perturb the PMSE source region for 40s and off for 140s, while 3 radars are measuring the temporal of evolution of radar echoes in three different frequency bands (7.9, 56 and 224 MHz). The schematic of PMSE heating experiment using three diagnostic radars at 7.9 MHz, 56 MHz, and 224 MHz is shown in Fig

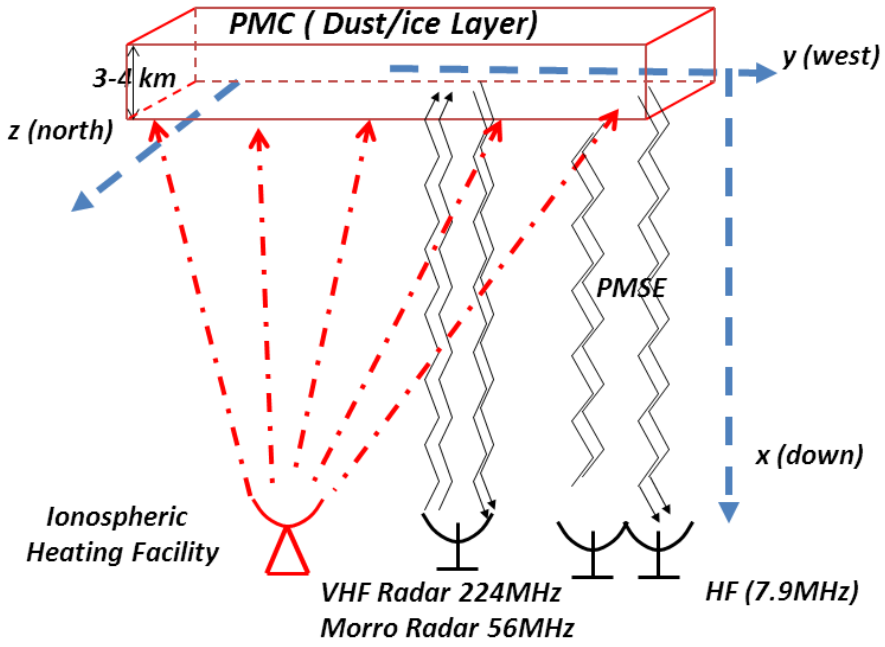

Figure 1.2: Schematic of PMSE heating experiment using three diagnostic radars at 7.9 MHz, 56 MHz, and 224 MHz.

1.2.

It has been observed in experiments that artificial perturbation of the PMSE by radio waves from a ground based ionospheric heating facility can lead to a useful diagnostic for parameters of the dust clouds (Chilson et al., 2000; Belova et al., 2001, 2003). The first modulation of PMSE with radiowave heating was reported by Chilson et al (2000), where it was shown that backscatter could be reduced in intensity as the heater is switched on, and thereafter return to its original strength when the heater was switched off . The temporary enhancement of PMSE, described as the PMSE overshoot, was observed in experiments by Havnes et al. (2003) and Havnes (2004) and occurs when the artificial electron heating is turned off (shown in Figure 1.3). This behavior was also observed in other PMSE heating experiments and lead to a powerful tool to investigate the physical processes at mesopause altitudes (Belova 2001, 2003; Havnes 2004; Havnes et al., 2004).

The first theoretical model was developed by Havnes to explain the overshoot effect after heater turn-off for VHF radar data (Havnes et al., 2003; Havnes, 2004). The original theoretical model was successfully utilized to predict this behavior and was the first major step in utilizing PMSE modification as a diagnostic tool. However, it should be noted that due to the incorporation of a Boltzmann model for electrons and ions and therefore neglecting finite diffusion time effects, the original model is not able to accurately predict the temporal evolution of modified PMSE for a range of radar frequencies and dust parameters.

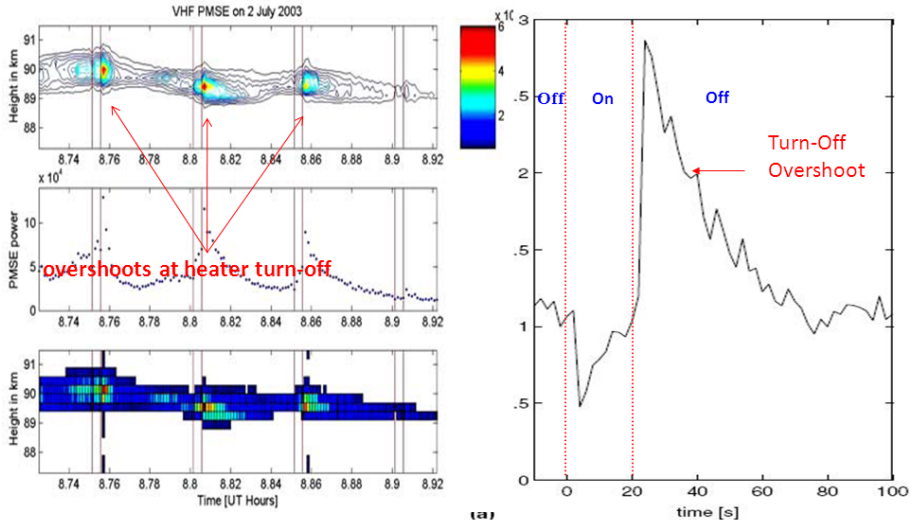

Figure 1.3: The time evolution of electron irregularities during radio wave heating for varying irregularity scale size (radar frequency) utilizing the computational model. The heating is turned on at 25 seconds. Figure reproduced from Havnes et al., 2003. Used under fair use, 2012.

Enhancement of the radar echoes after turn-off of the artificial electron heating was observed in several experiments in the UHF and VHF band (Havnes et al., 2003; Havnes, 2004; Biebricher et al., 2006; Naesheim et al., 2008). Similar behavior was observed in VHF and UHF PMSE with the same amount of reduction of backscattered power after heater turn-on. The same turn-off overshoot was measured which was argued as the same generating source for both VHF and UHF PMSE. Therefore, both VHF and UHF PMSE are produced by electron irregularity structures shaped by dust density irregularities (Naesheim et al., 2008).

La Hoz also recently reported the first joint measurements of PMSE, during heating using the EISCAT facility, with the EISCAT VHF radar at 224MHz (Bragg scale of 0.67 m) and the MORRO radar at 56MHz (Bragg scale of 2.7m)(La Hoz et al., 2010). Weakening of the PMSE after heater turn-on was observed for both radar frequencies. Although an intensification of PMSE was measured by MORRO radar over some intervals after heater turn-off, the enhancement of radar echoes measured by the MORRO radar was modest (La Hoz et al., 2010).

In this work, ice particle measurements described in Robertson et al. (2009) are used for our model calculations. Negative particles with radii 1.2nm and positive particles with radii 0.5-1nm, each with a number density near 2×10^9 m^{-3} were measured in the altitude range 86-88km (Robertson et al., 2009). The signature of the larger ice particles with radii >3nm and number density 0.5×10^9 m^{-3} were observed at 84-88km. Negative particles with a number density of 4.5×10^9 m^{-3} and radii 1-2nm were also detected from 85-87.5km during the second rocket flight (Robertson et al., 2009).

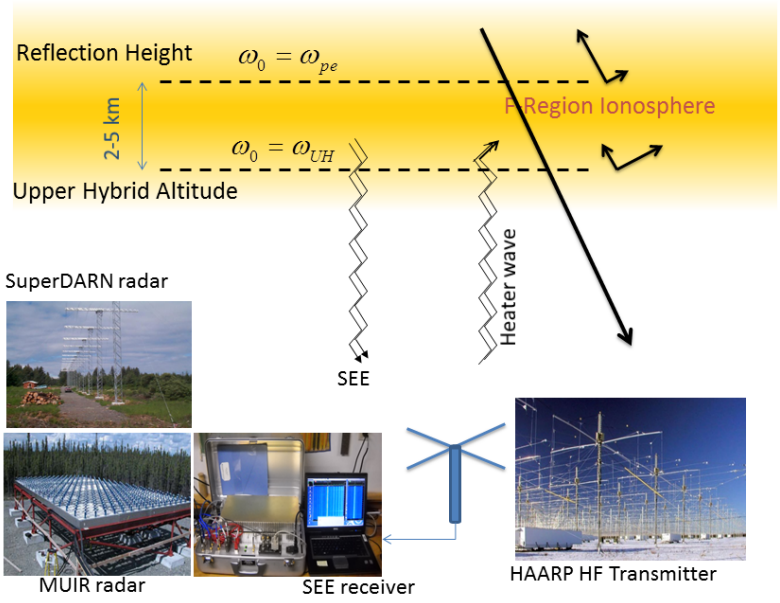

Figure 1.4: A schematic diagram showing the experimental geometry for the generation of SEE and diagnostic tools for observation of secondary waves.

1.3 Stimulated Electromagnetic Emission

Stimulated Electromagnetic Emission (SEE), secondary electromagnetic waves detected on the ground, was discovered during heating experiments near Tromso, Norway, when a powerful O-mode electromagnetic pump wave with a frequency near the harmonics of electron cyclotron frequency nf_{ce} was injected into the ionosphere from a ground station, (Thide, 1982). Generated emission lines in the spectra are the great manifestation of the excited irregularities and plasma waves in the modified ionosphere that can be employed to diagnose the ionospheric parameters. We participated in three campions at HAARP during the summer in 2010, 2011, and 2012. As can be seen in Fig 1.4, scattered electromagnetic wave was measured by SEE receiver. Simultaneous probing of the heated region was also conducted using incoherent scatter radar (MUIR) to measure the ion lines, SuperDARN radar to investigate the artificial field aligned irregularities, and telescope to observe artificial optical emissions.

Use of high frequency heating experiments has been extended in recent years as a useful methodology for plasma physicists wishing to remotely study the properties and behavior of the ionosphere as well as nonlinear plasma processes (Hysell and Nossa, 2009; Kosch et al., 2007; Pedersen and Gerken, 2005; Pedersen et al., 2010). This technique also has been used extensively to investigate the charged dust layer in the mesosphere (Chilson et al.,

2001; Havnes et al., 2003; Mahmoudian et al., 2011; Mahmoudian and Scales, 2012). High power electromagnetic waves transmitted from the ground interact with the local plasma in the ionosphere and can produce Stimulated Electromagnetic Emissions (SEEs) through the parametric decay instability (Thide et al., 1982). The interaction of the injected radio beam with local plasma may generate different types of waves, instabilities, and turbulence and as a result a variety of spectral features in the scattered wave are expected. The EM pump wave may undergo a direct conversion in which EM pump decays into a scattered EM and electrostatic (ES) wave. The direct parametric decay instability can be distinguished by strong SEE spectral sidebands. Magnetized stimulated Brillouin scatter (MSBS) which involves decay of the EM pump wave into ion acoustic IA or electrostatic ion cyclotron (EIC) and a scattered EM wave is an example of the direct conversion (Norin et al., 2009; Bernhardt et al., 2009; 2010). The other possible scenario is the conversion of the EM wave first to a high frequency ES wave and irregularities through the oscillating two stream instability (OTSI) (Dysthe et al, 1983, Huang and Kuo, 1995). The ES wave then decays into another high frequency ES wave and low frequency ES wave. Finally the high frequency ES wave scatters from irregularities back into the EM wave measured on the ground. The downshifted maximum (DM), a distinct peak at a frequency approximately 10 kHz below the pump (Leyser, 2001) involving electrostatic lower hybrid waves is believed to be produced through this mechanism (Bernhardt et al. 1994; Huang and Kuo, 1995; Leyser et al., 1989, 1990). Broad Upshifted Maximum BUM, a broadband peak upshifted from the pump about 14 kHz-200 kHz generated by interaction of UH waves and striations (Mityakov et al., 1975; Wong et al., 1981), and usually seen with the pump frequency slightly below to 100 kHz above the harmonics of electron gyro-frequency, are two of the prominent spectral features that have been observed in many experiments (Leyser et al., 1992; Thide et al., 2005; Lyser, 2001).

The strength and frequency shift of the SEE emission lines is a powerful diagnostic tool to estimate ionospheric parameters and get a sense of the possible physical processes/plasma waves involved in the decay process as well as possible conditions for acceleration of electrons (Leyser, 2001). IA and EIC mode excitation through the MSBS instability can be used to estimate the electron temperature and as ion mass spectrometers to determine the composition of the E and F layers, respectively (Bernhardt et al., 2009; 2010). It also has been shown that the spatial scale of striations involved in the formation of the DM and broad upshifted maximum BUM can be estimated by measuring the decay rate of the peak intensity of the DM and BUM (Norin et al., 2008).

MSBS has been studied extensively in the laboratory experiments, but recently by high power HF wave-ionospheric experiments where IA emission lines with offset up to 30 Hz from pump frequency. The MSBS instability in a magnetized ionospheric plasma was studied for the first time by Bernhardt (2009; 2010). The experimental data showed both Ion Acoustic IA and electrostatic ion cyclotron EIC waves which were predicted by theory for MSBS process (as shown in Fig 1.5). It has been shown that SEE can been employed to measure electron temperatures with ion acoustic waves (Bernhardt et al., 2009), ion composition with

electrostatic ion cyclotron waves (Bernhardt et al., 2010).

There has been an extensive recent interest in associated ionospheric processes when tuning the transmitter to harmonics of the electron gyro-frequency f_{ce} in the ionosphere (e.g Pedersen et al., 2010; 2011). Recent studies at the High Frequency Active Auroral Research Program (HAARP) facility, showed new SEE spectral features within 1 kHz of the pump frequency due to so-called Stimulated Ion Bernstein Scatter (SIBS) during pump heating near the second electron gyro-harmonic $2f_{ce}$ (Bernhart et al. 2011, Scales et al., 2011, Samimi et al. 2012a,b). SEE spectral structures ordered by harmonics of the ion gyro-frequency f_{ci} (near 50 Hz) were observed. A theory based on the interaction at the reflection altitude was originally proposed by Bernhardt et al. (2011) which suggests the parametric decay of O-mode EM pump wave into electron Bernstein EB and ion Bernstein IB modes. Other observations have shown a new spectral feature associated with SIBS process. A broadband spectral feature, within 1 kHz of pump frequency was observed during heating near $2f_{ci}$ on occasion as well (Samimi et al., 2012a, b). A new theory based on the interaction at the UH altitude, where the pump frequency equals the local UH frequency, was developed by Samimi et al. (2012a and b) which not only was able to explain the ion gyro-structures as a result of SIBS decay process but also predicted the oblique IA decay process as a possible source responsible for broadband spectral features observed in the experiment. The capability of SEE features in predicting irregularities generated during heating experiments can be employed to investigate the generation mechanism and plasma waves involved for other associated processes such as artificial airglow.

Artificial airglow is another phenomenon associated with ionospheric heating experiments and creation of visible artificial optical emissions has been reported by Bernhardt et al. (1988) and Pedersen et al. (2010). High frequency plasma waves parametrically excited during pump heating near $2f_{ce}$ may cause acceleration of electrons. Superthermal electrons may enhance airglow emissions through the collisional excitation of neutral species (Bernhardt et al., 1988) or even create new plasma when their energy exceeds the ionization potential of gasses (Gustavsson et al., 2006).

Objectives of this investigation include the consideration of the SEE spectral behavior under pump power, proximity to the gyro-harmonic frequency nf_{ce}, and beam angle variation. Also, the relationship between such spectral features and electron acceleration and creation of plasma irregularities is an important focus.

During experimental campaigns at the High Frequency Active Auroral Program HAARP facility in 2011 and 2012 excitation of SIBS has been observed for the first time for the pump heating of the ionosphere near the third electron cyclotron frequency $3f_{ce}$. It is observed that the previously observed SEE downshifted peak DP feature and the newly discovered ion gyro-structures appear simultaneously in the SEE spectra which may show that these two features are produced with the same physical process but at different altitudes. Further relationship between these features and the well known DP feature in SEE will be discussed in light of these recent observations.

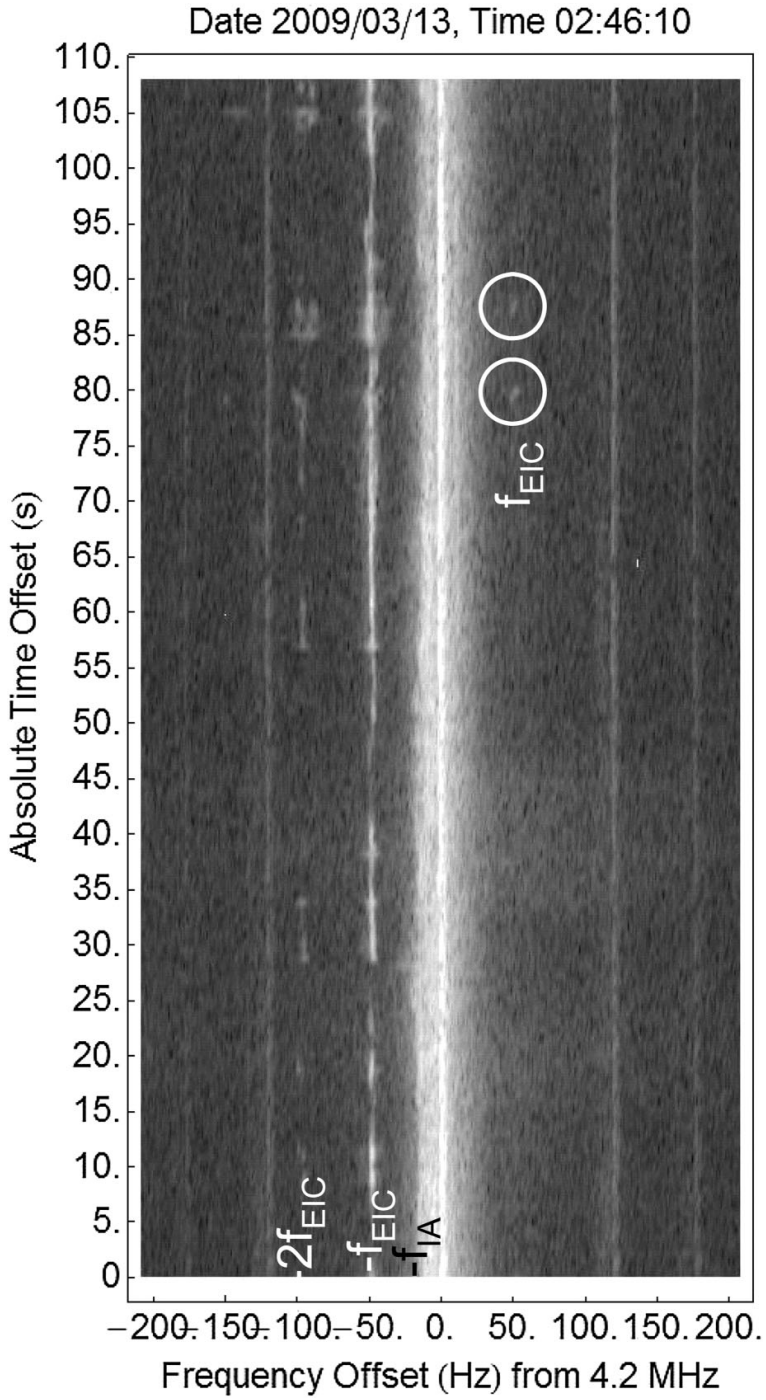

Figure 1.5: First observation of EIC lines in the spectrogram of the stimulated Brillouin scatter lines for a pump wave beam offset 21.4 degrees from the magnetic field direction. Figure reproduced from Bernhardt et al., 2010. Used under fair use, 2012.

Chapter 2

Mesospheric Dusty Plasmas

Importance of studying Polar Mesospheric Clouds PMCs

1. This phenomenon is believed to be closely linked to global change. We investigate noctilucent clouds as a rare cloud type that scientists think could be a climate-change indicator. It is widely believed that there is direct link between the global warming (increase of carbon dioxide and methane) and an increasing trend in the number and extent of Noctilucent cloud observations over the last 100 years. In other words, although the sources of both presence of the cold temperature and water vapor in the upper atmosphere are not known with certainty, some studies have shown that increase of carbon dioxide and methane may cool the mesopause region and increase the water vapor, respectively, which are necessary for the formation of Polar Mesospheric Clouds. Therefore, developing a new measurement technique to monitor the variation of dust (ice) density altitude profile with time and comparing that against the variation of carbon dioxide and methane may lead to an insight on the relationship between the global change and PMCs.

2. It has been shown that waves, irregularities and turbulence generated by dust clouds in space may cause disturbance in telecommunication systems such as GPS and satellite signals. Therefore, PMSE source region provides a natural dusty plasma laboratory to study the irregularities associated with dusty plasmas as well as dust charging process in space.

3. The chemical and physical properties of aerosols are measured to assess their effects on weather, human health, visibility, and climate. As a result, aerosol and dust particles in the PMSE source region may have a great impact on human life on the ground which makes the study of PMCs so important.

2.1 Sources of Water Vapor in the Mesosphere

Volcanism, transport of tropospheric H_2O, methane conversion, and solar ultraviolet (UV) are considered as the major sources of middle atmospheric H_2O (Thomas and Olivero, 2001). Observations have shown that methane and solar forcing are the strongest factors in PMC variations and H_2O concentration. It has been shown that increase of water vapor at the mesopause by $\sim 50\%$ over the past century may be as the result of increased atmospheric CH_4 which has been doubled in the last 100 years (Khalil and Rasmussen, 1994). Oxidized CH_4 in the middle atmosphere ultimately results in H_2O so that each molecule of CH_4 is converted to two H_2O in the lower mesosphere (Hurst et al., 1999). Water molecule produced by the photo dissociation of methane have an average lifetime of 3-10 days.

2.2 Cooling mechanism of mesosphere

The first Cooling mechanism of mesosphere could be as a result of carbon dioxide increase in recent years due to human activities on the earth. Greenhouse gases (CO_2, O_3) absorb infrared radiation from the surface of the Earth and trap the heat in the troposphere. If this absorption is really strong, the greenhouse gas blocks most of the outgoing infra-red radiation close to the Earth's surface. This means that only a small amount of outgoing infrared radiation reaches carbon dioxide in the upper troposphere and the lower stratosphere. On the other hand, carbon dioxide emits heat radiation, which is lost from the stratosphere into space. In the stratosphere, this emission of heat becomes larger than the energy received from below by absorption and, as a result, there is a net energy loss from the stratosphere and a resulting cooling. Other greenhouse gases, such as ozone and chloro fluorocarbons, have a weaker impact because their concentrations in the troposphere are smaller.

Another parameter that may effect the temperature profile of mesosphere is gravity waves. Atmospheric gravity waves play important role in atmospheric circulations, and the thermal and constituent structures of the middle atmosphere. The answer to this question is surprising - the attenuation of vertically propagating gravity waves (or buoyancy waves; these are not the waves of gravity field the astronomers are trying to discover). As the gravity waves propagate upward, they transfer momentum and air parcels from lower altitude to the higher altitude. The pressure at higher altitude is less than pressure at lower altitude therefore, the rising air parcel will expand out at higher altitude. The molecules of air do work as they expand. This will reduce the parcel's temperature and is called Adiabatic cooling. This drop in temperature causes any water vapor present in the rising air mass to form ice particles.

These waves are mainly caused by jet streams, thunder clouds, and mountains. Vertically propagating waves transfer a lot of momentum from the lower atmosphere upwards. The transfer of momentum takes place when waves attenuate; this can happen by radiative cooling or convective overturning (if waves are unstable). It turns out that gravity waves are the

only waves that can propagate upwards to the summer mesosphere, and not even all kinds of gravity waves but only those that have strong east-moving phase velocity. As they propagate higher, their amplitude increases, until they eventually become statically unstable and break up, transferring their eastward momentum to the mean flow. In the atmosphere, winds and temperature gradients are interconnected; thus the introduction of momentum also changes the local temperature field. This mechanism cools the summer polar mesopause so strongly that the region is actually the coldest place in the Earth's atmosphere, with temperatures typically around 130 K; about 60 K lower than in the winter polar mesopause where the solar heating is absent.

There can also be cooling during special events like Stratospheric warming by gravity waves. It has been shown numerically that doubling CO_2 results in the cooling of mesosphere by about 10k. As a result of increase of trace gas concentrations into 21 century, troposphere is expected to warm and stratosphere to cool. This cooling process may also have a significant impact on the compositional distributions of species throughout the mesosphere. For example, doubling of trace gases may decrease O_2 and N_2 by about 40% and increase atomic oxygen by about 20% in the mesosphere because of change in chemistry and downward diffusion from thermosphere.

The most dominant sources of gravity waves are topography, convection and wind shear. Flow over orography is proposed as a major source for large amplitude gravity wave (Fritts and Alexander, 2003). These kind of gravity waves usually have horizontal wavelength of the order of ≈10-100 km (Bacmeister et al., 1990; Lilly and Kennedy, 1973; Nastrom and Fritts, 1992; Leutbecher and Volkert, 2000). Theoretical predictions have shown that mountain waves are most likely responsible for a very large fraction of gravity wave induced forcing in the mesosphere. Mountain waves have been studied using two dimensional numerical simulations (Durran and Klemp, 1987; Farmer and Armi, 1999; Nance and Durran, 1998), three dimensional numerical simulations (Dornbrack et al., 1999) as well as observations by different means (Fritts et al., 1990; Shutts et al., 1988; Smith, 1978; Kennedy and Shapiro, 1979; Lilly and Kennedy, 1973).

2.3 Origin of dust particles in the mesosphere

Existence of polar mesospheric summer echoes PMSE and Noctilucent clouds NLC provides unambiguous evidence for presence of water ice/dust particles in the mesosphere (Thomas, 1991; Rapp and Lubken, 2004). As was discussed in the previous section and is shown in Fig. , the temperature is extremely low in the altitude range 80-90km, with mean values as low as 130k (Witt et al., 1964; Lubken, 1999). This temperature may also vary up to ±15 k due to gravity waves (Rapp et al., 2002). Hence, infrared cooling by carbon dioxide and mesospheric water provided by methane, make mesospheric region a suitable environment for ice particle formation with atmospheric temperature below the frost point of water vapor. Saturation ratio, ratio of water vapor partial pressure to equilibrium vapor pressure of water vapor

over ice ($S = P_{H_20}/P_{Sat}$), get very large near the mesopause altitude. Considering typical value of saturation ratio $S \sim 100$ between ∼86 km and 90 km, homogenous nucleation, spontaneous formation of new particles from a pure gas phase (Rapp and Thomas, 2006), should be negligible and condensation nuclei is required for the formation of ice particles (Gadsden and Schroder, 1989). Meteoric dust, water vapor, and sulfate aerosol are the possible condensation nuclei for ice particles in the mesosphere. Therefore dust/ice particles are assumed to be composed of ice and nucleation cores. Dust particles are settled down due to gravity and as a result larger and heavier particles are located at the lower altitude. It turns out that particles fall below this altitude will evaporate because of the increase of temperature at them bottom of ice layer. NLC is formed by largest particles at the bottom of ice particle layer and visible even with naked eye.

2.4 Radar echoes and density fluctuations

Radar waves are scattered at irregularities in the radar refractive index which at mesopause altitudes is solely determined by the electron number density. For efficient scatter, the electron number density must reveal structures at the radar half wavelength (Bragg condition; 3 m for typical VHF radars). Different hypothesis have been proposed as a generation source for fluctuations in the plasma density responsible for radar echoes in the PMSE source region. The main idea is that mesospheric neutral air turbulence in combination with a significantly reduced electron diffusivity due to the presence of heavy charged ice aerosol particles (radii 550 nm) leads to the creation of structures at spatial scales significantly smaller than the inner scale of the turbulent velocity field itself. At altitudes above 86 km the turbulence occurrence rate is even larger than the PMSE occurrence rate and on the other hand at lower altitudes, the PMSE occurrence rate is significantly larger than the turbulence occurrence rate. Experimental observations have also shown the presence of PMSE in the absence of neutral air turbulence. Therefore, there is clearly no one to one correlation between the occurrence of turbulence and the occurrence of PMSE (Lubken et al., 2002). The so-called fossil turbulence described by Cho (1993, and references therein) was also proposed to produce plasma fluctuation when the turbulence of the main constituent (neutral particles) is no longer present which is due to the fact that diffusion rate of the electron and/or charged dust density is smaller than the viscosity of the neutral air. Therefore, it has been suggested that fossil turbulence may be used to justify the cases in which PMSE is observed while no measurable neutral air turbulence exists, either because neutral turbulence has died off there or because the passive scalar could have been transported from a turbulent region to a non-turbulent one where it is measured (Cho, 1993).

During the motion, the particles are further subject to transport by mean winds (vertical and horizontal), and small-scale motions, i.e., waves and turbulence. Once the particles have reached sizes (equivalent spherical radii) in excess of ∼30 nm, they scatter light efficiently such that they may eventually be observed optically from ground-based or spaceborne optical

Figure 2.1: Gravity wave and instability structure pbserved in Noctilucent Clouds at Turku, Finland on 21-22 July, 1999. The copyright to the photograph lies with Pekka Pravianen.

instruments. Besides this optical effect, the ice particles further interact with the ambient plasma of the lower D-region, leading to signatures from small-scale structures observable by suitable radars as strong backscattering (the so-called polar mesosphere summer echoes, or PMSE) (e.g., La Hoz et al., 2006; Rapp and Lubken, 2004).

Dusty plasma scattering, scattering from the coherent clouds of polarization electrons surrounding multiple charged ice particles, was also introduced as another scattering mechanism that may cause PMSE (Cho et al., 1992a), which is (Havnes et al., 1990; La Hoz, 1992; Hagfors, 1992). Recently, it has been shown that irregularity generated at the boundary layer of charge dust layer may also be another source for fluctuations in the electron density at mesopause altitudes (Scales and Ganguli, 2004ab; Mahmoudian and Scales, 2012).

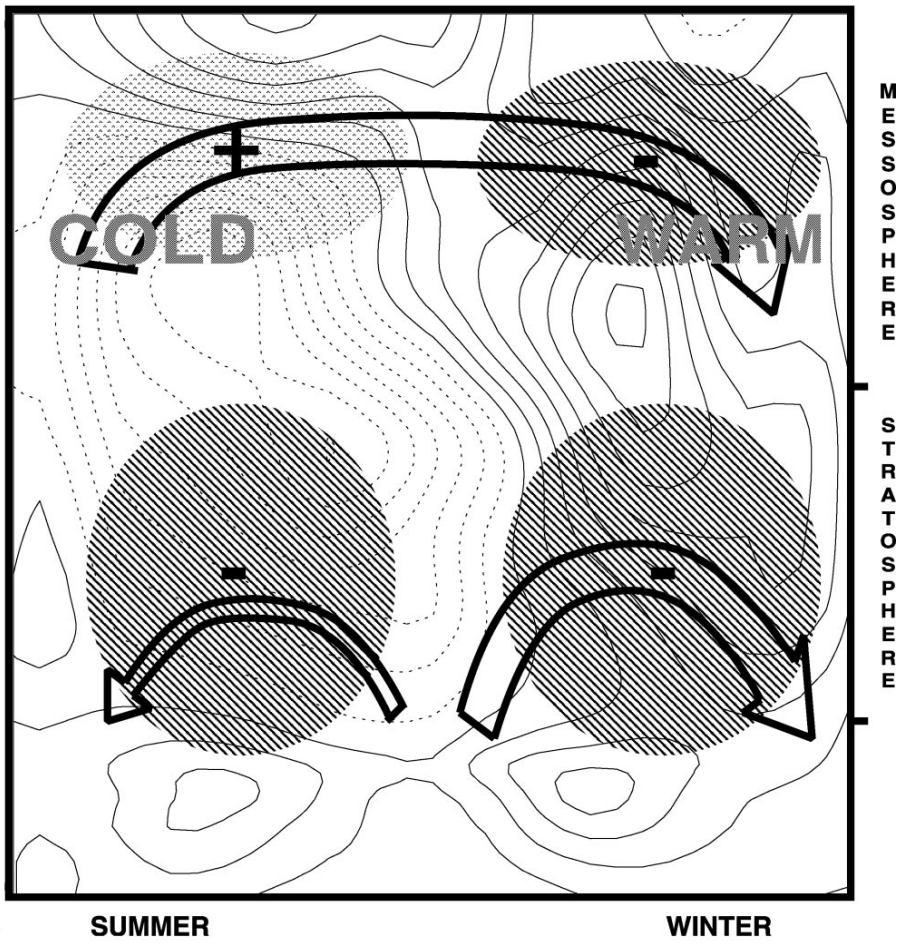

Figure 2.2: Schematic diagram illustrating gravity wave driving of the middle atmosphere transport circulation and effects on the zonal-mean extratropical winds and temperatures. The circulation is indicated by the arrows and + and - denote eastward and westward forcing respectively. Figure reproduced from Fritts and Alexander, 2003. Used under fair use, 2012.

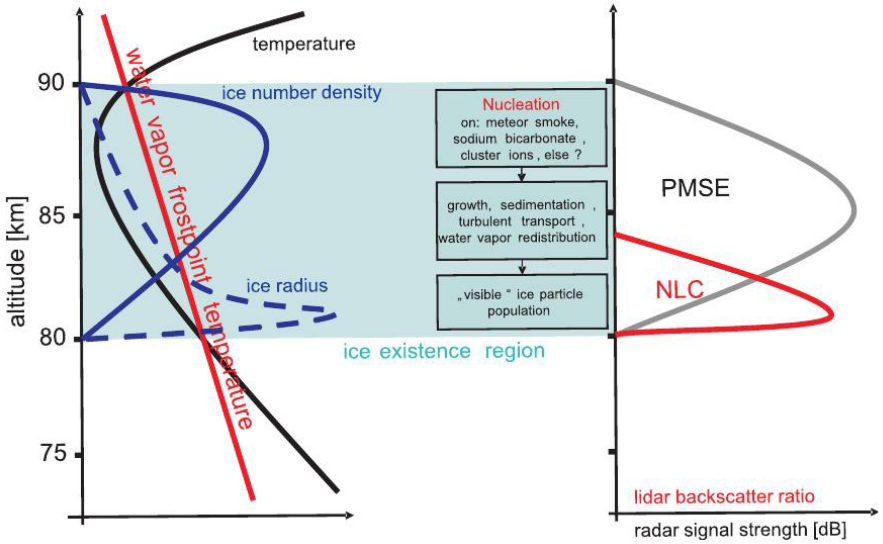

Figure 2.3: Schematic of the altitude profile of the temperature and the frost point of water vapor (Left panel). Schematic of the altitude distribution of PMSE and NLC and the relevant physical mechanisms at different altitudes (Right panel). Figure reproduced from Rapp and Lubken, 2004. Used under fair use, 2012.

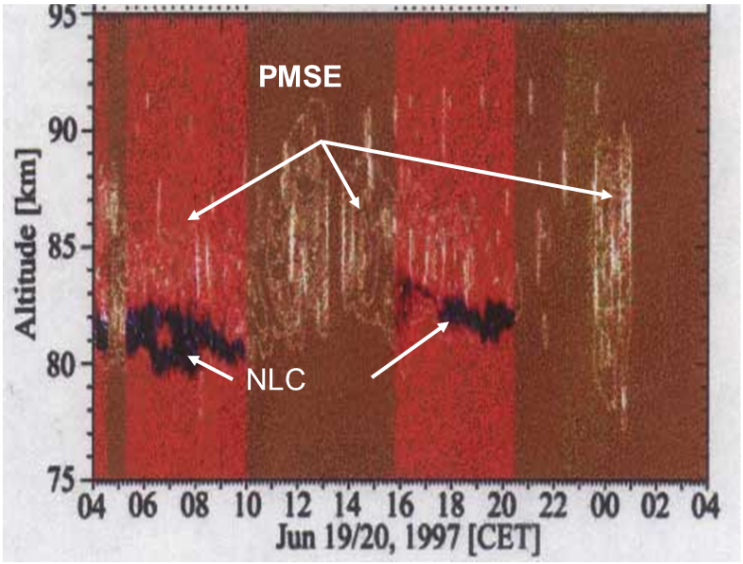

Figure 2.4: Simultaneous observation of PMSE with radar and NLC using Lidar. As can be seen NLC is located about couple of km below the PMSE source region.

Chapter 3

Computational Model for Dusty Space Plasmas

A hybrid computational model is used to study the temporal behavior of irregularities during active modification of PMSE (Scales and Chen, 2008; Chen and Scales, 2005). In the hybrid computational model, the electrons and ions are described with fluid equations and the dust is modeled with simulation particles using the Particle-In-Cell (PIC) method. Variation of the ion density is described by the continuity equation:

$$\frac{\partial n_{\mathrm{i}}}{\partial t} + \frac{\partial}{\partial x}(n_{\mathrm{i}} v_{\mathrm{i}}) = P_{\mathrm{i}} + L_{\mathrm{i}} + \frac{\mathrm{d}n_{\mathrm{i}}}{\mathrm{dt}}|_{\mathrm{charging}} \tag{3.1}$$

Here, L_{i} denotes the loss due to dissociative recombination and P_{i} denotes the ion production due to photoionization and energetic particle precipitation. The recombination rate is modeled using $L_{\mathrm{i}} = \alpha n_e n_i$ and a recombination rate coefficient $\alpha = 10^{-12}\mathrm{m}^3/\mathrm{s}$ for mesopause altitudes. The term $\frac{\mathrm{d}n_{\mathrm{i}}}{\mathrm{dt}}|_{\mathrm{charging}}$ represents the ion density reduction due to ion flux onto the dust. An electron density of $10^9 m^{-3}$ is used for the PMSE altitude near 85km which is reasonable (Friedrich and Rapp, 2009). The electron density is determined from quasi-neutrality $n_e(x) = n_i(x) - \rho_d(x)/e$ where $\rho_d(x)$ is the dust charge density and e the unit charge. The continuity equation is solved using the Crank Nicolson method (average of explicit and implicit method):

$$\frac{n_i^{t+\triangle t} - n_i^t}{\triangle t} + \frac{dn_i^{t+\triangle t} v_i^{t+\triangle t/2}}{2dx} + \frac{dn_i^t v_i^{t-\triangle t/2}}{2dx} = \frac{Q_i^{t+\triangle t} + Q_i^t}{2} \tag{3.2}$$

where Q denoted the production and loss term. Equation (3.2) was solved directly by Thomas algorithm. Neglecting inertial effects, the momentum equation can be written in this form:

$$\mathrm{v_e} = \frac{1}{\nu_{\mathrm{en}}}\left(\frac{\mathrm{q_e}}{\mathrm{m_e}}\mathrm{E} - \frac{\mathrm{KT_e}}{\mathrm{m_e}}\frac{\partial}{\partial \mathrm{x}}(\log(\mathrm{n_e}))\right) \tag{3.3}$$

where q_e, m_e, and T_e are the electron charge, mass, and temperature, and ν_{en} is the electron-neutral collision frequency. Also, K is Boltzmanns constant. The electrostatic field is denoted by E. The simulation is designed to include more ion species. The full ion momentum equation is given by:

$$m_i\frac{\partial v_i}{\partial t} + m_i v_i\frac{\partial v_i}{\partial z} = Eq_i - m_i\nu_{in}(v_i - v_n) - m_i\sum_{i\neq j}^{I} v_{ij}(v_i - v_j) + g_z m_i - \frac{kT_i}{n_i}\frac{\partial n_i}{\partial z} \tag{3.4}$$

where $g_z m_i$ represents the gravity effect on the ion species and I denotes the number of ion species. Here q_i, m_i,T_i and ν_{in} are the ion species charge, mass, temperature and collision frequency with neutral, respectively. Considering that the region of study is very collisional $m_i\frac{\partial v_i}{\partial t} \ll \nu_{in}$ or ν_{ij} and subsonic flow $v_i \ll C_i$, the left hand side of the equation can be neglected. Ion neutral collision frequency is given by (Banks and Kockarts, 1973):

$$\nu_{in} = \frac{n_n A_{in}}{m_\alpha} \tag{3.5}$$

where m_n and n_n are the mass (in kilogram) and density of neutral species, respectively. A_{in} for ion can be written in this form (Banks and Kockarts, 1973):

$$A_{in} = 1.06 \times 10^{-28}(\mu_{in}\alpha_n) \tag{3.6}$$

where α_n is the polarizability in 10^{-23} m^3. For ion-ion collision frequency

$$\nu_{ij} = \frac{n_j B_{ij}}{m_j} \tag{3.7}$$

where B_{ij} is given by:

$$B_{ij} = 5.19 \times 10^{-20}\mu_{ij}\left(\frac{T_i}{m_i} + \frac{T_j}{m_j}\right) \tag{3.8}$$

and $\mu_{ij} = m_i m_j/(m_i + m_j)$ in which m_i and m_j are the masses of the colliding species. It turns out that momentum equation can be simplified and written in the matrix form:

$$F_i \left(n_n A_{in} + \sum_{(j \neq i)}^{I} n_j B_{ij} \right) - \sum_{(j \neq i)}^{I} n_i B_{ij} F_j = n_i q_i E_z + F_n n_i A_{in} - K T_i \frac{\partial n_i}{\partial x} + g_z n_i m_i \quad (3.9)$$

The governing fluid equations are written in the formulation described by Bernhardt et al. (1991). The new algorithms not only reduce the computational time substantially but also provide greater accuracy.

The mesopause temperature for both ions and electrons is taken to be $T_e = T_i = 150K$. Proton hydrates with mass between 59 and 109 proton masses are the dominant ion compositions at the PMSE height range. O_2^+ ions are more numerous than NO^+. NO^+ and O_2^+ together can be slightly more dense than the proton hydrates at 88km and above (Kopp et al., 1985). It should be noted that the variation of ion mass from 50 to 100 proton masses does not have a significant impact on the irregularity amplitude evolution during heating. The ion-neutral collision frequency is of order $10^5 s^{-1}$ (Lie-Svenson et al., 2003). The variation of ion-neutral collision frequency is predicted to be between $3 \times 10^4 s^{-1}$ and $3 \times 10^5 s^{-1}$ in the altitude range 80-90km (Turunen et al., 1988) and its effect on the irregularity amplitude during active modification is studied in this work. We investigate the temporal behavior of charged dust associated with electron irregularities during electron temperature enhancements caused by radio wave heating. Therefore, the variation of electron-neutral collision frequency and recombination rate coefficient with temperature is included in the model. The electron-neutral collision frequency temperature dependence is assumed to be $\nu_{en} \sim T_e$ and recombination rate dependence on temperature is taken to be $\alpha \sim T_e^{-1/2}$.

The dust charge is modeled using a standard continuous charging model. It has been shown that a discrete charging model has reasonably close behavior with a continuous charging model for relatively small size of the dust grains at PMSE altitudes (Chen and Scales, 2007). The time varying charge for each dust particle according to the Orbital-Motion-Limited (OML) approach (Shukla and Mamun, 2002) is given by:

$$\frac{dQ_{\mathrm{d}}}{dt} = I_{\mathrm{e}} + I_{\mathrm{i}}, \quad (3.10)$$

where I_{e} and I_{i} are the electron and ion current on each dust particle, respectively. These currents for the negative dust particles are given by:

$$I_{\mathrm{e}} = \sqrt{8\pi} r_{\mathrm{d}}^2 q_{\mathrm{e}} n_{\mathrm{e}} v_{\mathrm{te}} \exp(-q_{\mathrm{e}} \phi_{\mathrm{d}} / K T_{\mathrm{e}}), \quad (3.11)$$

$$I_{\mathrm{i}} = \sqrt{8\pi} r_{\mathrm{d}}^2 q_{\mathrm{i}} n_{\mathrm{i}} v_{\mathrm{ti}} (1 - q_{\mathrm{i}} \phi_{\mathrm{d}} / K T_{\mathrm{i}}), \quad (3.12)$$

For positive dust particles, the ion and electron currents are given by:

$$I_{\mathrm{e}} = \sqrt{8\pi} r_{\mathrm{d}}^2 q_{\mathrm{e}} n_{\mathrm{e}} v_{\mathrm{te}} (1 - q_{\mathrm{e}}\phi_{\mathrm{d}}/KT_{\mathrm{i}}), \tag{3.13}$$

$$I_{\mathrm{i}} = \sqrt{8\pi} r_{\mathrm{d}}^2 q_{\mathrm{i}} n_{\mathrm{i}} v_{\mathrm{ti}} \exp(-q_{\mathrm{i}}\phi_{\mathrm{d}}/KT_{\mathrm{e}}), \tag{3.14}$$

Here, r_d is the dust radius, $v_{te}(i)$ electron (ion) thermal velocity and ϕ_{d} dust floating potential. The effect of a Gaussian dust radius distribution with an RMS dust radius of 10nm, uniform distribution and constant dust radius on the temporal evolution of the electron irregularities during radio wave heating was investigated by Chen and Scales (2005). They showed that there is only a minor difference in the temporal behavior for these different dust distributions. The relation of the dust floating potential and the dust radius to the number of charges on the dust particle can be written in the form:

$$Z_d = \frac{4\pi\epsilon_0 r_d \phi_d}{q_e} \tag{3.15}$$

The initial uncharged dust is taken to have an irregular density of the form:

$$n_{\mathrm{d}}(x) = n_{\mathrm{d0}} \left(1 + \frac{\delta n_{\mathrm{d0}}}{n_{\mathrm{d0}}} \sin(2\pi m x/\ell)\right) \tag{3.16}$$

where n_{d0} is the undisturbed dust density, δn_{d0} is the dust density irregularity amplitude which is set to 0.2 in the simulation, m is the irregularities mode number and l is the system length in this model. A zero current condition often used in ionospheric plasma studies is implemented to calculate the electrostatic field (E):

$$\nabla . J = 0 \longrightarrow \frac{\partial J}{\partial x} = 0 \tag{3.17}$$

therefore the total current can be written as follow

$$J_T = q_e n_e v_e + q_i n_i v_i + J_d = 0 \tag{3.18}$$

where J_T is the total current density of ions, electrons and dust and J_d is the dust current density calculated from the simulation dust particles. Substituting the previous expressions for the electron and ion velocities into equation (4.11), the electrostatic field can be calculated as

$$E_x(i_x) = \frac{\frac{n_e q_e}{\nu_{en}} \frac{q_e K T_e}{m_e} \frac{\partial n_e}{\partial x} - J_d + \sum_{j=1}^{I} G_{i_x} \left(-n_j(i_x)(F_n(i_x) A_{jn} + g_z m_j) + K T_j \frac{\partial n_j(i_x)}{\partial x}\right)}{\sum_{j=1}^{I} G_{i_x} n_j(i_x) q_j + \frac{n_e q_e}{\nu_{en}} \frac{q_e}{m_e}} \tag{3.19}$$

where J_d is the dust current density calculated from the simulated dust particles, ν_{en} electron-neutral collision frequency and ν_{in} ion-neutral collision frequency. Considering energy conservation, variation of the electron temperature in the D region due to interaction with the radio wave is described by:

$$\frac{dT_e}{dt} = -\frac{2}{3} e\nu_e E/k_B - \delta v_e(T_e - T) \tag{3.20}$$

The first term on the right-hand side denotes the electron energy increase by an external electric field and the second term is the electron energy loss from collisions with neutral particles. The effective fractional energy loss during a collision is δ, v_e is the Gurevich's electron velocity and the effective electron-neutral collision frequency is ν_e. T denotes the effective temperature of the background species, E is the electric field of the radio wave and k_B is the Boltzmann's constant. The timescale for this heating is milliseconds and therefore in the simulation model, this is essentially considered as an instantaneous electron temperature change when the radio wave pump is turned 'on' or 'off'.

In this model, initially, electron and ion densities are taken to be uniform and equal $n_{e0} = n_{i0}$. The uncharged aerosols (dust) are taken to have two forms of density. The first profile of dust density is regarded as the Gaussian distribution:

$$n_d(x) = n_{d0} e^{-(x-x_0)^2/2\sigma^2} \tag{3.21}$$

where n_{d0} is maximum density of uncharged aerosols , x_0 is the location of the center of dust cloud and σ is the parameter which determines the width of dust cloud. Another dust cloud model that has been considered in this paper is in this form:

$$n_d(x) = n_{d0}[\tanh(\frac{x - x_1}{w}) - \tanh(\frac{x - x_2}{w})] \tag{3.22}$$

where n_{d0} is maximum density of uncharged aerosols and x_1 and x_2 are the location of the right and left boundary of dust cloud, respectively, and w is the scale length of the boundary. The collision of charged dust with neutrals is implemented by using a Langevin method and the dust-neutral collision frequency is denoted by ν_{dn}. The dust grain collision with neutral is implemented by randomly scattering the velocity vectors every time step. The magnitude of the particle velocity vectors is conserved. The velocity vector after collision with neutral particles can be written in this form for each dust particle (Winske and Rosenberg, 1998:

$$\nu_d(t + \Delta t) = \nu_d(t) e^{-\nu_{dn}\Delta t} + v_{thd} \left(1 - e^{-2-\nu_{dn}\Delta t}\right)^{1/2} N_i \tag{3.23}$$

where v_{thd} is dust thermal velocity and N_i is a random number [01]. This model is used to consider time scales much longer than the dust plasma period unlike previous work (Scales and Ganguli, 2004a, 2004b).

Table 3.1: Parameter regimes used in the simulation.

Parameter	Range
Electron Density	$10^8 - 10^{10}\mathrm{m}^{-3}$
Negative dust radius	1-20nm
Negative dust number density	$1 - 4.5 \times 10^9\mathrm{m}^{-3}$
Positive dust radius	0.5-1nm
Positive dust number density	$1 - 2 \times 10^9\mathrm{m}^{-3}$
Ion-neutral collision frequency	$10^4 - 3 \times 10^5\mathrm{Hz}$
The ratio of electron to ion temperature increase	2-4
recombination rate	$10^{-12}\mathrm{m}^3/\mathrm{s}$
electron-ion production rate	$3.6 \times 10^7\mathrm{m}^{-3}/\mathrm{s}$
Ion compositions	Proton hydrates with the mass $59 - 109 \times \mathrm{m_p}$

The parameter regimes that have been considered in the simulation study are summarized in Table 3.1.

Chapter 4

Computational Modeling of PMSE Heating experiments

The objective of this chapter is to consider the temporal behavior of electron irregularity amplitudes after turn-on and turn-off of radio wave heating based on the radar facilities and frequencies which are available at EISCAT and HAARP for actual experimental predictions. The more general work of Scales and Chen (2008) and Chen and Scales (2007) were not based on the radar facilities and frequencies available at EISCAT and HAARP nor real mesospheric parameters. The variation of plasma parameters and their effect on electron irregularity amplitude is also studied in the current work. Our investigation also utilizes more realistic dust and background plasma parameters than past work. The influence of electron density variation, as well as the size and number densities of ice particles on the turn-off overshoot characteristic curve has been considered by Havnes et al.(2004) within the context of the Boltzmann electron and ion model. In this section, the effect of these parameters on the temporal evolution of the irregularity amplitude at different radar frequencies may be investigated since finite diffusion effects are incorporated unlike in previous work. We show that for 56MHz the turn-off overshoot may be suppressed in comparison with 224MHz, which is consistent with the recent experimental data (La Hoz et al., 2010). The effect of positive ice particles observed in the in-situ experiments, electron density and ion-neutral collision frequency variation and realistic parameters of mesospheric altitudes are considered in this work which were overlooked in previous works (e.g. Scales and Chen, 2008; Chen and Scales, 2005).

4.1 Temporal behavior after pump turn-on

Two physical processes have important effects on the initial behavior of the irregularities after turn-on of the radio wave pump: 1) charging of the electrons onto the dust and, 2) the

ambipolar diffusion process. Another physical process that may have a secondary effect on the electron irregularity amplitude before heater turn-off is the recombination of electrons and ions. The recombination time $\tau_{recombination} \approx \frac{1}{\alpha n_{i0}} \frac{1}{\sqrt{r_h}}$ where α is the recombination rate and r_h is the ratio of electron temperature increase during heating. In the simulation $\alpha = 10^{-12}$ m^3/s is assumed and the recombination time is of the order of $1000s$. The diffusion process tends to smooth out irregularities and can be approximated by (Chen and Scales, 2005):

$$\tau_{\text{diff}} \approx \nu_{in} (\frac{\lambda}{2\pi v_{\text{thi}}})^2 \frac{1}{(1 + \frac{T_e}{T_i}(1 + \frac{z_{d0} n_{d0}}{n_{e0}}))} \tag{4.1}$$

where ν_{in}, λ and v_{thi} are the ion-neutral collision frequency, irregularity wavelength and ion thermal velocity, respectively. Eq.(4.1) shows that the diffusion timescale depends on T_e/T_i; therefore, after the radio wave heating turn-on, the time decreases. For irregularities observed in the 50 MHz range, $\tau_{diff} \sim 1s$. The timescale for electron attachment onto the dust immediately after heater turn-on is approximated by

$$\tau_{chg} \approx \frac{1}{k n_{d0}} \tag{4.2}$$

where k can be written as $k \approx \frac{I_e}{e n_e} = \sqrt{8\pi} r_d^2 v_{te0} \sqrt{r_h} e^{\frac{-4.1}{r_h}}$ using the electron charging current in Eq.(3.11). The constant -4.1 provides a description of the equilibrium normalized floating potential of the dust prior to the radio wave heating. As can be seen in Figure 4.1, the simulation runs for 25s before heater turn-on such that the plasma reaches equilibrium, which can be considered as the time interval after the previous heater 'on' period when plasma relates back to its equilibrium. Prior to radio wave heating, the charging time onto uncharged dust is $\tau_{chg} \sim 1s$ for the parameters given in Table 1. Therefore after turn-on of the radio wave heating, there is competition between the dust charging process and plasma diffusion process. Depending upon which process dominates, irregularities may be suppressed or enhanced. According to the diffusion and charging timescales, the temporal behavior of the irregularities depends on the irregularity scale size, ratio of electron temperature increase after turn-on of radio wave heating, dust radius and dust density. Therefore the turn-on overshoot is sensitive to several parameters. The PMSE enhancement after the pump turn-on for a set of parameters may change to a suppression in the electron irregularity amplitude because of small variations of these parameters.

According to Eq.(4.1), the diffusion timescale is less than the charging timescale for the smaller irregularity wavelengths. After turn-on of the radio wave pump, the electron temperature starts to increase. Irregularities will diffuse out by the ambipolar diffusion process. This process suppresses the electron irregularity amplitude. For larger irregularity scale sizes, according to the Eq.(4.1), the diffusion time increases by a factor of λ^2 and the charging timescale can be less than the diffusion timescale after pump turn-on. Therefore, electron irregularity amplitudes start to grow until the point at which the diffusion timescale becomes

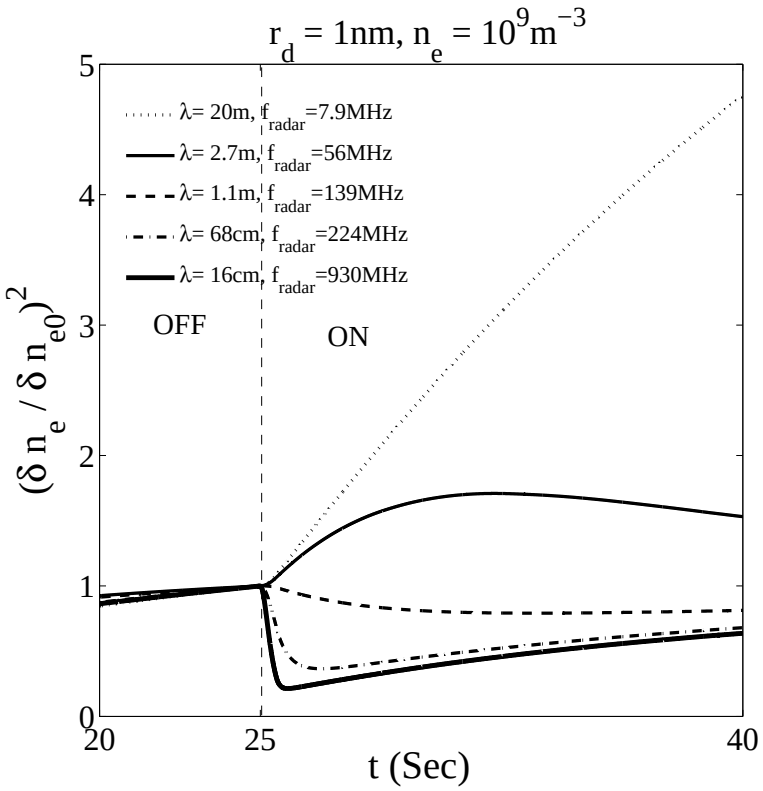

Figure 4.1: The time evolution of electron irregularities during radio wave heating for varying irregularity scale size (radar frequency) utilizing the computational model. The heating is turned on at 25 seconds.

comparable to the charging timescale. After this point, the electron irregularity amplitude will be diminished to a steady state value before turn-off of the radio wave pump where the dust charge will reach a final charge state by satisfying the equilibrium condition $I_e + I_i = 0$.

Figure 4.1 shows the effect of irregularity scale size on the electron irregularity amplitude. Considering the altitude region around 85km for the generation of PMSE irregularities, plasma densities are assumed to be $n_e = n_i \equiv n_0 = 10^9$ m^{-3} and the dust particles are charged up negatively and have density near 2×10^9 m^{-3}. The dust radius is assumed to be 1nm. The electron temperature is assumed to increase by a factor of 4 during heating by radio waves which is a reasonable value according to Kassa et al. (2005). It should be noted that the ratio of electron temperature increase during heating of the ionosphere by radio waves is critically dependent on altitude, and the peak heated electron temperature normally occurs below the PMSE layer, but not always (Routledge et al., 2011). As can be seen in Figure 4.1, the electron irregularity amplitude increases after the pump turn-on for irregularity scale sizes of $\lambda \approx 20$m and 2.7m, approximately corresponding to radar frequencies of 7.9 and 56MHz, respectively. The charging timescale for these two wavelengths are less than the diffusion timescale, therefore irregularities start to grow until the diffusion timescale becomes less than the charging timescale, then diffusion will be the dominant physical process and the electron irregularity amplitude starts to decrease. The irregularities peak approximately when τ_{diff}/τ_{chg} becomes less than 1. It should be noted that the predicted turn-on overshoot at 7.9MHz is very strong. For the chosen mesospheric parameters, 56MHz is near the threshold frequency to observe the turn-on overshoot. Using a radar frequency greater than 56MHz, PMSE suppression after pump turn-on can be observed due to the dominant diffusion process. For shorter wavelengths of $\lambda = 1.1$m, 68cm, and 16cm, corresponding to radar frequencies of approximately 139, 224 and 930MHz, respectively, the diffusion timescale is expected to reduce by a factor of λ^2 according to Eq.(4.1). In this case, the diffusion timescale initially is less than the charging timescale and the electron irregularity amplitude starts to reduce, i.e. suppression in electron irregularity can be observed after turn-on. This behavior has been observed in PMSE pumping experiments at VHF such as Belova et al., (2001, 2003). As can be seen in Figure 4.1, the amount of suppression of the irregularity amplitude after heater turn-on is approximately the same for 224 and 930MHz. There is good agreement when comparing the computational results with the UHF(930MHz) and VHF(224MHz) PMSE of Fig.12 in Naesheim et al. (2008) observed during an active experiment at EISCAT. Considering the EISCAT radar facilities for 224MHz and 930MHz, MORRO radar operating at 56MHz,and 139MHz radar at HAARP, these results may be applicable to estimate the PMSE parameters.

The irregularity amplitude right before the pump turn-off is related to the new charge state of the dust. This new charge state depends on different parameter values, such as dust density, electron temperature increase, dust density irregularity amplitude, dust radius and plasma irregularity scale size. Measuring some of these parameters during an active experiment can be useful to find the new charge state for the dust after artificial perturbation.

Figure 4.2 shows the effect of electron density and ion-neutral collision frequency on the

irregularity amplitude. The results are for an irregularity scale size of $\lambda = 2.7$m which roughly corresponds to a radar frequency of 56MHz. The dust radius is assumed to be 2nm and dust density 2×10^9 m^{-3} (Robertson et al., 2009). Typical values of electron density at mesospheric altitudes are $10^8 - 10^9$ m^{-3} (Friedrich and Rapp, 2009) but electron density as high as 6×10^9 m^{-3} have also been observed (Blix et al., 1999). The effect of electron density variation from $10^8 - 10^{10}$ m^{-3} on the turn-on overshoot at 56MHz is shown in Figure 4.2a. There is a turn-on overshoot for electron densities of 5×10^9 m^{-3}-10^{10} m^{-3} that may be high for this region and seen in extreme cases such as solar proton events and hard electron precipitation. For an electron density larger than 5×10^9 m^{-3}, the charging time is less than the diffusion time after pump turn-on, therefore the irregularity amplitude starts to increase until the diffusion timescale reaches a value less than the charging timescale. At this point, the irregularity amplitude will decrease due to the diffusion process which appears as a peak in the electron irregularity curve. Due to the low diffusion timescale in comparison with the dust charging timescale after the turn-on for $n_e = 10^8, 5 \times 10^8$ m^{-3} and 10^9 m^{-3}, the electron irregularity amplitude reduces after the pump turn-on before the charging process can act to increase the electron density gradients. Therefore, electron density has a significant effect on the time at which irregularity amplitude peaks after pump turn-on.

Another parameter that can affect the temporal evolution of electron irregularity amplitude after pump turn-on is the ion-neutral collision frequency. According to Eq.(4.1), the diffusion timescale reduces as ν_{in} decreases and this may cause the diffusion process to dominate and therefore cause suppression of the irregularity amplitude after heater turn-on. It has been shown that the ion-neutral collision frequency varies by an order of magnitude between 80km (3×10^4Hz) and 90km (3×10^5Hz)(Turunen et al., 1988). As can be seen in Figure 4.2b, by reducing collision frequency to 10^4Hz no turn-on overshoot is expected due to the dominant diffusion process. In a recent experiment by La Hoz et al., (2010), a weakening of PMSE was observed with the EISCAT VHF radar at 224MHz and the MORRO radar at 56MHz during active modification. Comparing the results presented in Figure 4.2 with this observation shows that the computational model also predicts the suppression of radar echoes for electron densities less than $10^9 m^{-3}$ or collision frequencies less than 3×10^4Hz.

Another parameter which affects the evolution of irregularities after turn-on of radio wave heating is the ratio of electron temperature increase with respect to the background ion temperature. The effect of this heating ratio on the time of the irregularity peak is negligible since τ_{diff}/τ_{chg} reaches unity approximately at the same time for all T_e/T_i values. Another characteristic of the ratio of electron temperature increase after pump turn-on on the behavior of the irregularities is that the rate of variation of the electron irregularity amplitude in time (not shown) is larger for higher electron temperature ratios (Kassa et al., 2005). This effect can be a significant diagnostic to estimate the plasma temperate of PMSE heating by radio waves.

Figure 4.3 compares the effect of dust radius on the evolution of irregularities during radio wave heating in more detail. The dust density and electron density are 10^9 m^{-3}. According to the Bragg scattering condition, the scale size of irregularities corresponding to 7.9 MHz

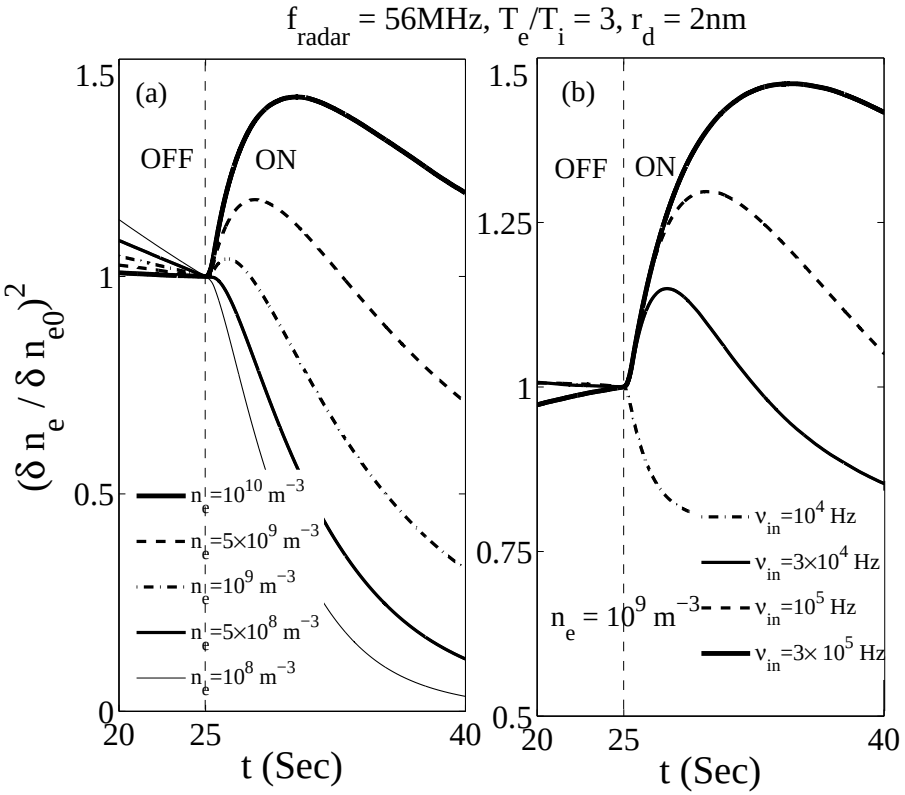

Figure 4.2: The time evolution of electron irregularities during radio wave heating with varying (a) electron density and (b) ion-neutral collision frequency utilizing the computational model for a radar frequency of 56MHz. The heating is turned on at 25 seconds.

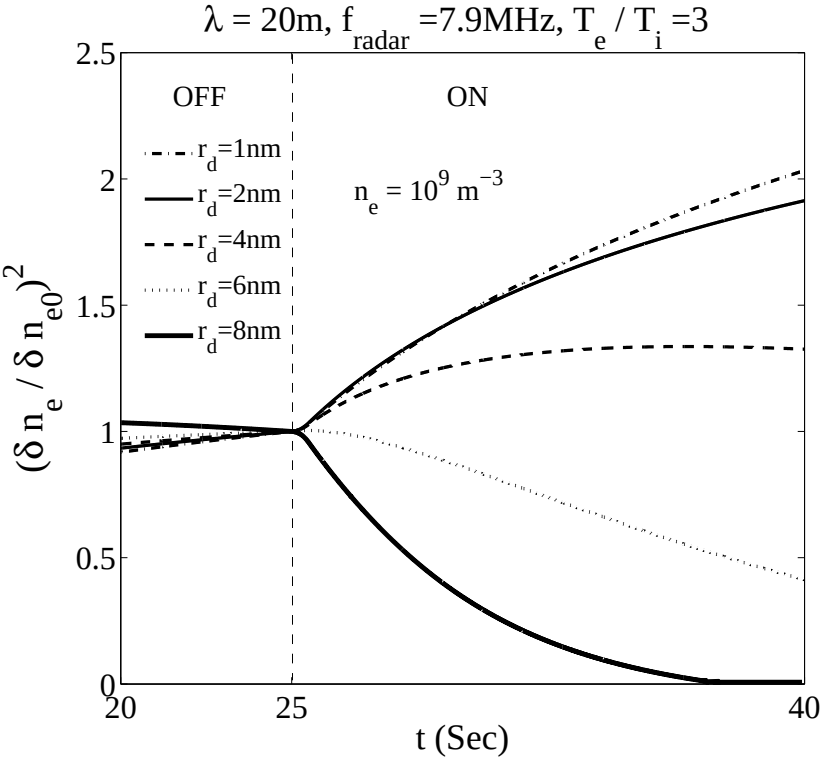

Figure 4.3: The time evolution of electron irregularities during radio wave heating with varying dust radius. The radio wave pump is turned on at 25 seconds.

is about 20m and this frequency band has been the subject of recent interest (Ramos et al., 2009). For a dust radius less than 5nm, the turn-on overshoot can be observed. However, by increasing the dust radius to 6nm, the enhancement of the irregularity amplitude is substituted by a suppression.

4.2 Temporal behavior after pump turn-off

The physics after turn-off of the radio wave pump is different than the physical process after turn-on. After the radio wave is turned-off, the electron temperature returns back to its initial value before the turn-on and the ion irregularities start to diffuse out. The ion current onto the dust will be dominant and ions drag along the electrons while diffusing back. Therefore the total current onto the dust can be approximated by $\tau_{chg} \approx \frac{e}{I_i} = \frac{1}{\sqrt{8\pi} n_i v_{ti} r_d^2 (1 - q_{\mathrm{i}} \phi_{\mathrm{d}} / K T_{\mathrm{i}})}$. The ion density gradient is steeper and has larger amplitude at smaller irregularity scale sizes. Therefore, ions drag along more electrons during the diffusion process and the turn-off overshoot is larger for higher radar frequencies. The computational model predicts an enhancement in electron irregularity amplitude for $\tau_{diff}/\tau_{chg} < 1$ which means the electron-

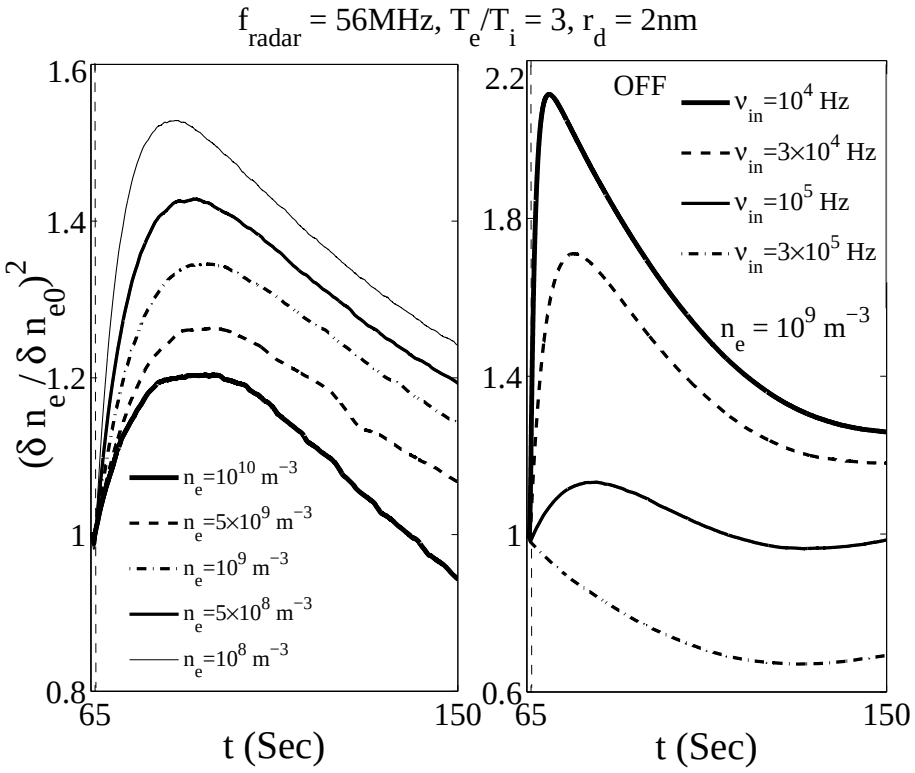

Figure 4.4: The time evolution of electron irregularities after turn-off of the radio wave heating with varying (a) electron density and (b) ion-neutral collision frequency utilizing the computational model for a radar frequency of 56MHz. The heating is turned off at 65 seconds.

ion ambipolar diffusion time is less than dust particle charging time.

Figure 4.4 shows the temporal evolution of electron irregularities for varying electron density and ion-neutral collision frequency after the heater turn-off for PMSE at 56MHz. As can be seen in Figure 4.4a, decreasing the electron density in 50% steps from $10^{10}m^{-3}$ to $10^{8}m^{-3}$ increases the turn-off overshoot in $\sim$ 8% steps. According to Figure 4.4b, increasing the ion-neutral collision frequency suppresses the turn-off overshoot and for $\nu_{in} = 3 \times 10^{5}$Hz no turn-off overshoot is observed. These results are consistent with experimental observations reported by La Hoz (2008) in which a modest turn-off overshoot at 56MHz was observed. The turn-off overshoot amplitude predicted by the computational model for 56MHz is near 20% which illustrates a weak enhancement in comparison with the turn-off overshoot observed at 224MHz and 930MHz. These were reported by Naesheim et al. (2008) to be of the order of 200%.

Figure 4.5 shows the temporal evolution of the electron irregularities after radio wave heating turn-off. As previously discussed, the turn-off overshoot can be seen for smaller irregularity scale sizes with the ratio of diffusion to charging time being approximately 1. The turn-off

overshoot was observed for UHF (930MHz) and VHF (224MHz) by Naesheim et al. (2008) in an active experiment using the EISCAT facilities. The overshoot amplitude is approximately the same for both frequencies according to Fig.12 of Naesheim et al. (2008), which is consistent with the computational model shown in Figure 4.5 for 224 and 930MHz. The predicted turn-off overshoot amplitude is comparable with the value measured in the experiment for 224 and 930MHz (Naesheim et al., 2008). Figure 4.5b shows that for smaller wavelengths, the diffusion to charging timescale ratio is much less than unity and has approximately the same amplitude at 224 and 930MHz. Therefore the turn-off overshoot is approximately the same for these two cases. When the charging timescale becomes much smaller than the diffusion timescale, the turn-off overshoot disappears. According to Figure 4.5b, for a radar frequency of 56MHz, the charging timescale is comparable to the diffusion timescale and the turn-off overshoot amplitude reduces dramatically in comparison to the UHF and VHF PMSE turn-off overshoot for the same background parameters. In fact, 56MHz is near the threshold of turn-off overshoot and suppression after pump turn-off since the charging process becomes dominant over the diffusion process and decreases the irregularity amplitude by increasing ion current onto the dust. There is no turn-off overshoot at 7.9MHz which is another difference in the transient signature of PMSE after the turn-on and turn-off of radio wave heating for VHF and HF wavelengths for these parameters. It should be noted that the behavior of the turn-off overshoot with frequency is approximately described by Eq.(17) in Scales and Chen (2008).

The modeling results discussed up to this point are for the investigation of the temporal behavior of a single irregularity scale size. This is a useful comparison since in an actual experiment, radars operate at a single frequency and are able to look at only one irregularity scale size. However, to get more insight and a holistic picture about the temporal evolution of plasma irregularities during turn-on and turn-off of radio wave pumping in the simulation, a case consisting of 10 irregularities scale sizes is considered. The simulation box is $\lambda/\lambda_D = 8192$ which is about 160m. An electron temperature enhancement during heating of the order of 10 and electron density of 10^9 m^{-3} are considered. Dust density and radius are 2×10^9 m^{-3} and 10nm, respectively. The neutral dust density is extended to include a superposition of irregularities written in the form:

$$n_d(x) = n_{d0}(1 + \sum A_i \sin(\frac{2\pi m_i x}{l} + 2\pi\alpha_i)) \tag{4.3}$$

where m_i represents the mode number of the irregularities. A_i is a random number in the interval [0-1] and α_i is a random number between -0.5 to 0.5 for each mode number produced by a random number generator. The 10 modes included correspond to irregularity scale sizes of $\lambda = 0.15$, 0.31, 0.62, 1.25, 2.5, 5, 10, 20, 40 and 80m which cover all radar frequencies from 2MHz to 1GHz according to the Bragg scattering condition. The radio wave heating is turned on at $t = 25$ seconds and turned-off at $t = 125$ seconds. Figure 4.6a and b show the variation of the wavenumber spectrum amplitude during radio wave heating turn 'on' and 'off'. Figure 4.6a shows the difference of the wavenumber spectrum between $t = 24$sec. and

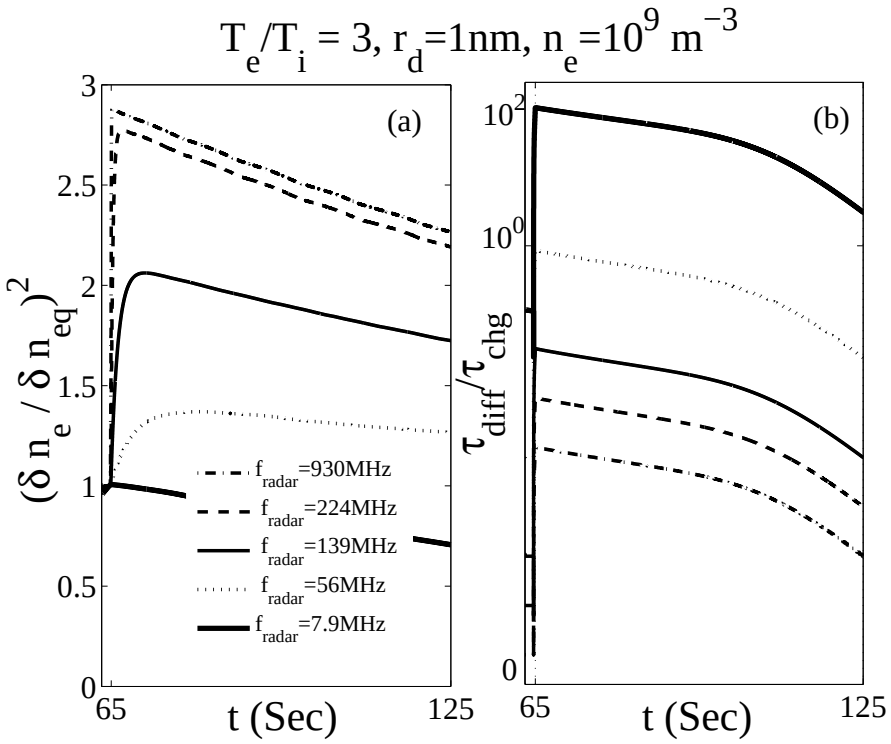

Figure 4.5: (a) The time evolution of electron irregularities after turn-off of the radio wave heating with varying irregularity scale size utilizing the computational model. The heating is turned off at 65 seconds. (b) Ratio of diffusion timescale to charging timescale.

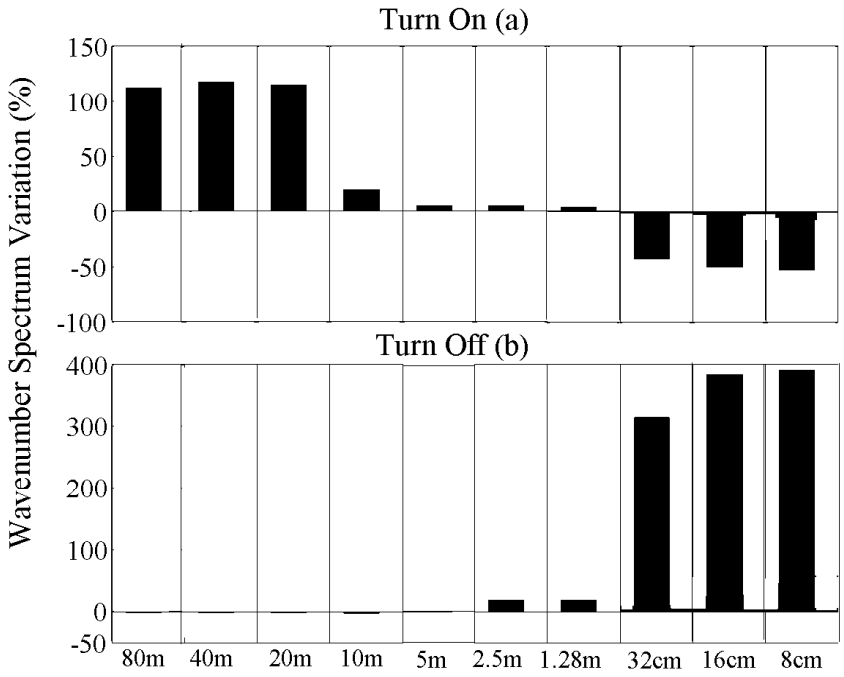

Figure 4.6: The wave number spectrum for electron density fluctuation evolution, during and after radio wave heating.

26sec., which corresponds to right before and after radio wave heating turn-on, respectively. Longer irregularity wavelengths of 80, 40 and 20m (lower frequencies) have about 100 percent increase in amplitude while the amplitude of shorter irregularity wavelengths are reduced by about 50 percent. This is consistent with the theory discussed before; i.e. that a turn-on overshoot is expected to happen at lower frequencies. In Figure 4.6b the change in the amplitude of the wavenumber spectrum from $t = 124$sec. to 126sec. is shown. Irregularity wavelengths of 32, 16 and 8cm have a 400 percent increase in amplitude in comparison with their amplitude before the turn-off of radio wave heating. The amplitude of longer irregularity wavelengths is suppressed by a few percent.

Figure 4.7 shows the possibility of observing the turn-on overshoot for radar frequencies of 56 and 7.9 MHz for varying dust radius and density assuming the electron temperature is elevated during the heating process to $T_e/T_i = 3$. Dust particles are assumed to be negatively charged in this calculation. The criterion for turn-on overshoot is defined as an enhancement in amplitude of at least 10 percent in irregularity amplitude for approximately 10 seconds after turn-on of the radio wave heating which should be observable during a typical radar experiment. The curves are determined by calculating several test cases with the computational model of Chapter. 3. and then using curve fits through these data points. Note that this procedure may introduce a slight error of approximately 10% or so in the boundary curves shown. Region I in the figure, which is to the left of each curve,

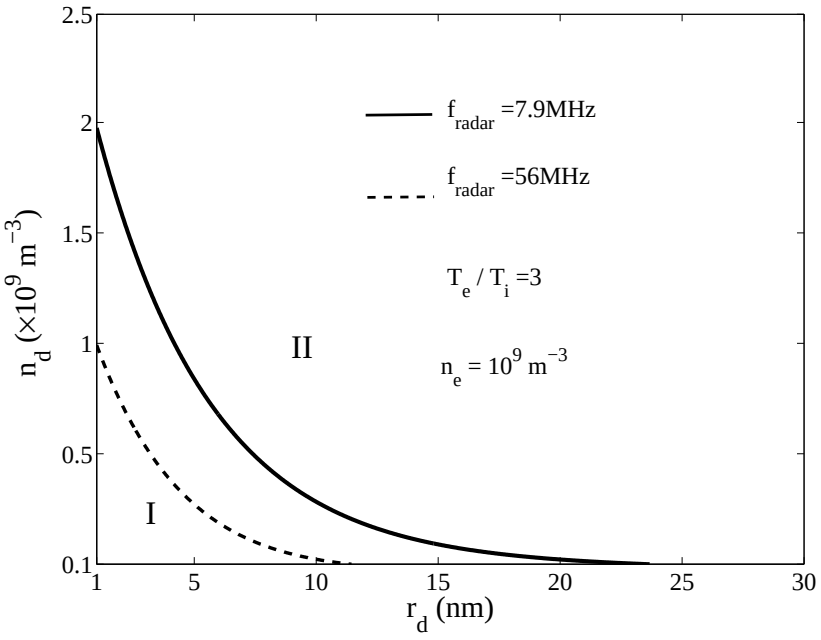

Figure 4.7: The possibility of observing the turn-on overshoot. Region I shows the possible dust cloud parameter range for which turn-on overshoot is predicted to be observed. In Region II, the classic suppression of the PMSE strength after turn-on of the radio wave heating should be observed

is the predicted parameter region for the pump turn-on overshoot to exist. In Region II, the classic suppression of the PMSE strength after turn-on of the radio wave heating should be observed. For instance, when the dust radius is 5nm and radar frequency is 7.9 MHz, there is a possibility of turn-on overshoot to exist for dust densities less than 1×10^9 m^{-3}. According to this figure, the possibility of a turn-on overshoot exists for a wider range of dust radius and density at 7.9MHz in comparison to 56 MHz. Note that the overshoot effect should still be observable by increasing the T_e/T_i ratio beyond the value of 3 as shown.

4.3 Experimental data and diagnostics

PMSE modification experiments took place at the EISCAT facility over six days from 22nd to 25th and 30th to 31st July 2009. The EISCAT facility in Tromso, northern Norway (69.58 N, 19.22 E), includes a 224 MHz VHF radar. The HF transmitter at EISCAT was used for artificially heating the ionosphere.

The HF transmitter was directed vertically and operated using O-mode polarization with a frequency of 5.423MHz and an effective radiated power of 235 MW. A 3-minute pump cycle was used for the HF radio wave heating with 40 seconds of pump on and 140 seconds of

pump off. During the heating, PMSE was observed at 224MHz to compare the behavior of the PMSE with the computational results and get useful diagnostic information about the charged dust layer. The integrated time resolution of the VHF radar data is 4 s with a range resolution of 300m. The time step used in the model is one tenth of second.

Figure 4.8a shows a superposed epoch analysis of the mean averaged VHF backscatter power for July 24th from 9UT to 12UT which is the average of 60 heating cycles with an altitude of 85km. This processing is necessary to reduce the measurement errors. At t=20s the pump is switched on and subsequently the PMSE intensity instantly decreases by about 23 percent below that of the unheated level. The heating cycle is 40s and at t=60s the radio wave pump is switched off. As can be seen, the PMSE intensity increases by about 30 percent above the background level which is known as turn-off overshoot (Havnes et al., 2003). The square of electron irregularity amplitude, which is related to the radar reflected power in the experiment during active modification, is shown in Figure 4.8b using the computational model. The simulation is run for typical PMSE parameters. Dust density and the ratio of electron to ion temperature during radio wave heating has been adjusted to get the closest model result to the experimental data as possible. According to Robertson et al., (2009) the dust radius is assumed to be 1-3 nm and number density $1 - 4.5 \times 10^9$ m^{-3}.

As was discussed in the first two sections, for the higher radar frequencies or smaller wavelengths like VHF and UHF, the scattering of the radar signal is expected to suppress after turn-on of the radio wave heating. Due to the short diffusion timescale, the irregularities diffuse out before the amplitude of electron irregularities can increase by electron charging of the dust under increasing electron temperature. From the discussion in the section 4.1 about the temporal behavior of the irregularity amplitude after pump turn-on, the amount of reduction in the scattered power for the VHF radar signal is a useful means to predict the dust density.

The irregularity amplitude associated with the parameters $T_e/T_i = 2, r_d = 1\text{nm}, n_d = 3.5 \times 10^9\text{m}^{-3}, \nu_{in} = 10^5$ Hz is consistent with the observed data during the pump on time interval. It should be noted that this dust density and radius are similar to that observed by in-situ experiment (Robertson et al., 2009). The computational model predicts the minimum normalized amplitude of backscattered power near 0.77 about 6.7s after heater turn-on and is consistent with the experimental data that shows the minimum amplitude of normalized backscatter power about 0.78 at 6s after pump turn-on. The amplitude of the scattered power after heater turn-off also reflects the effect of the dust density and electron temperature enhancement during heating. The small turn-off overshoot of about 30 percent shown in Figure 4.8a can be argued as a low electron temperature enhancement. In the results presented in this section T_e/T_i is assumed to be 2 which gives the best agreement with the data. The computational results for the parameters given above show 50% enhancement of electron irregularities after turn-off with the maximum at t=64s which is nearly the same time at which the maximum of radar echoes was observed after heater turn-off in the experiment. The irregularity amplitude associated with the parameters $T_e/T_i = 2, r_d = 3\text{nm}, n_d = 10^9$ m^{-3}, and $\nu_{in} = 10^5$Hz shows a reduction in the amplitude of the turn-off overshoot and pro-

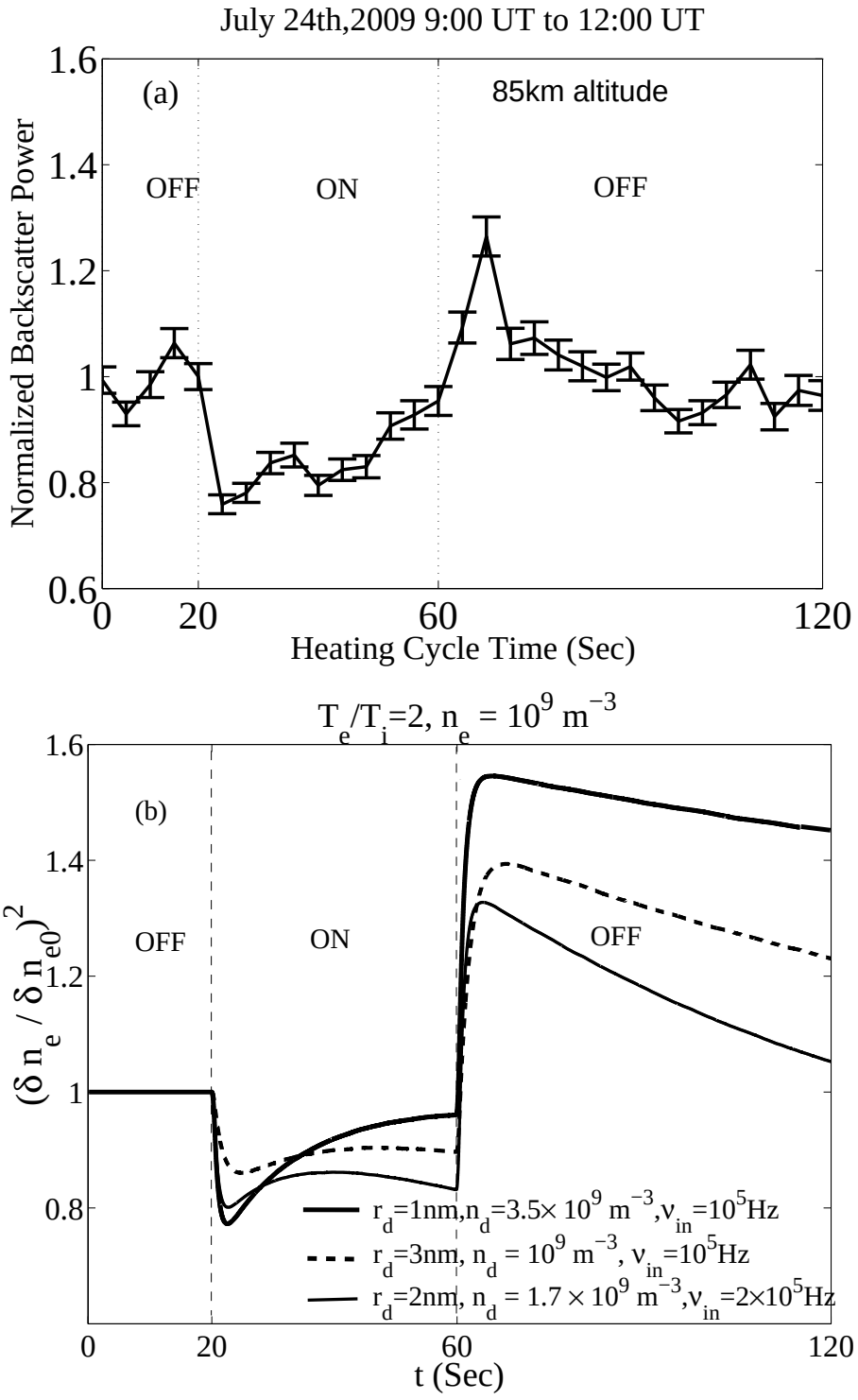

Figure 4.8: A comparison of VHF radar superposed epoch data during radiowave heating and result from the computational model. Panel (a) shows the superposed epoch of PMSE VHF backscatter power, and panel (b) the computational model result.

duces a faster decay which is closer to the data. In this case the dust radius has increased to 3nm and density reduced which is still consistent with in-situ experimental data (Robertson et al., 2009). Finally, the curve shown by the thin solid line and with parameter regime $T_e/T_i = 2, r_d = 2\text{nm}, n_d = 1.7 \times 10^9\text{m}^{-3}$, and $\nu_{in} = 2 \times 10^5$ Hz shows the best agreement with the observed data during the turn-off time interval. In this case dust radius and density are assumed in between the previous two cases and the ion-neutral collision frequency is increased. According to Fig 4.4 the suppression of turn-off overshoot is expected for increased collision frequency and gives better agreement with the EISCAT data. In summary, the thin solid line shows a better agreement with the observed data during the turn-off time interval. The reason that a model parameter change is needed for turn-on and turn-off to get better agreement with observed data may be because of the epoch analysis over 60 heating cycles corresponding to 3 hours and the PMSE changing over time.

Positive dust particles have been measured at PMSE altitudes during a recent rocket experiment by Robertson et al. (2009) and such contributions of positive dust particles will most likely have an important impact on the temporal evolution of electron irregularities during turn-on and turn-off of radio wave heating. Therefore, including positively charged particles in the model may have potential to solve this inconsistency. At this time there appears to be significant uncertainty as to the charging process producing the positive dust particles and these are not consistent with the standard charging theory as described in Chapter 3. One possibility is that the positive particles grow from small molecular or cluster ions and become neutral as they grow and capture an electron, and then become negative as they capture an additional electron later (Robertson et al. 2009). A simple model is then to consider a mixture of positive, neutral, and negative dust particles in the model of Chapter 3 in which the rough approximation is used that the positive particles do not undergo dynamical charging during radio wave heating. Figure 4.9 shows predictions using the model of Chapter 3 for a small percentage of positive dust particles under the charging approximations just described. Figure 4.9 shows reduced irregularity suppression during turn-on and reduced overshoot during turn-off at VHF frequencies (e.g. 224 MHZ). There is a tendency for enhancement of the turn-on overshoot effect at HF (not shown). This behavior across the frequency range has some consistency with simply a reduction in electron density due to the addition of positive dust. These predictions are directly dependent on the charging approximation made on the positive dust which is currently unknown. As a result, incorporation of the positive dust particles may bring closer agreement between the computational and observational results of Figure 4.8 particularly during turn-off, but a detailed study is beyond the scope of the current manuscript and the subject of ongoing work.

4.4 Conclusion

Modification of PMSEs by radio wave heating has significant potential for remote sensing of dust parameters in the mesosphere once suitable computational models have been developed.

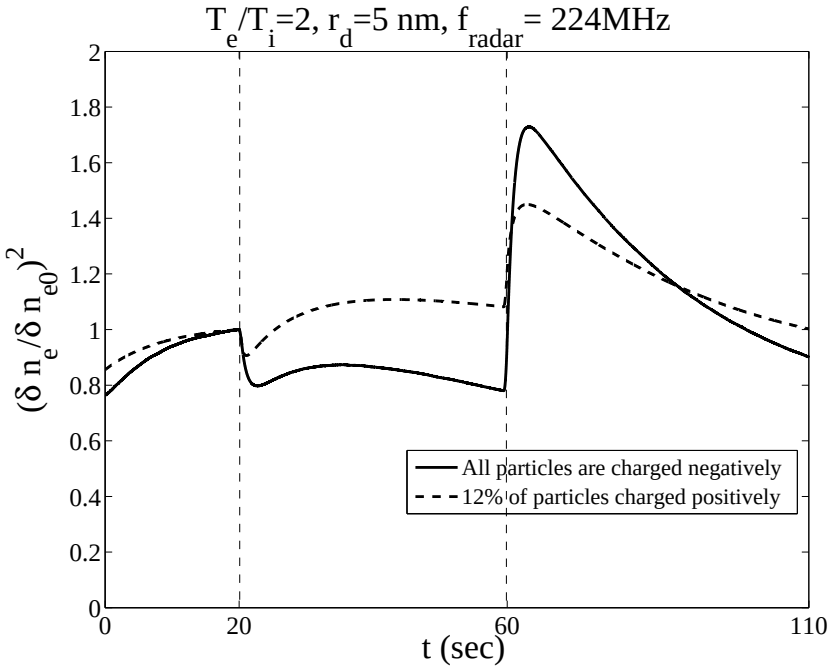

Figure 4.9: The predicted effect of positively charged dust particles on the electron irregularity amplitude during PMSE heating experiments at VHF (224MHz).

The work here has investigated the temporal behavior of irregularities after radio wave heating turn-on and turn-off to diagnose dusty space plasmas at mesopause altitudes. The physical process after turn-on and turn-off of radio wave heating is explained by competing diffusion and dust charging processes. Characteristics of the dusty space plasma, such as dust density and radius, charge state and plasma heating ratio, can be obtained from the temporal behavior of the irregularities observed by radars. The VHF PMSE data from a 2009 EISCAT campaign is presented. A comparison of the experimental data and computational model has demonstrated how the absolute amplitude of the pump-induced radar backscatter overshoot features vary with important dust and plasma parameters allowing these parameters to be extracted. The possibility of observing the turn-on overshoot in the HF radar band is discussed based on typical mesospheric parameters. Most past active experiments have concentrated on VHF PMSE. It is clear from the present study that lower frequency PMSE, including HF PMSE, has substantial potential as a diagnostic tool during active modification experiments. Since the dust charging dominates during pump turn-on in the HF band it causes an enhancement of radar echoes. Further experiments should be pursued since fundamental charging physics may be revealed which is critical to understanding dusty space plasmas.

Chapter 5

Diagnostic Techniques for Mesospheric Dust Layers

The object of this section is to develop and validate an analytical model to describe evolution after the turn-on of radiowave heating. This simplified model may then be used to provide more direct diagnostic information about the dust layer. The first attempt to develop an analytical model for temporal evolution of radar echoes associated with heater turn-on was done by Scales and Chen (2007). This work was very limited and will be greatly extended here in order to directly relate electron irregularity amplitude during turn-on of radio wave heating to dust layer and plasma parameters. The second objective is to bring to fruition a methodology for diagnosing the dust layer using a multifrequency measurement using information from all phases during the heating cycle (i.e. both turn-on and turn-off). The organization of the section is as follows. First, a full computational model is provided as a reference. The next part of the work is dedicated to the development of an analytical model which is applied to predict the irregularity amplitude after the pump turn-on of radio wave heating as well as providing possibilities for diagnostic information available during the turn-on period of the radiowave. This model is validated with the computational model of the previous section. Application of the simplified analytical models for HF and VHF bands is discussed. Afterward, from the temporal behavior of the electron irregularities during the turn-on of the radiowave, possibilities for using the analytical model to obtain diagnostic information for various charged dust and background plasma quantities from simultaneous PMSE modification experiments in the HF and VHF band is discussed. Finally a summary and conclusions are provided.

As was discussed in the previous section, the ambipolar diffusion process tends to suppress the radar echoes and the electron charging process acts to enhance the backscattered signal during the radiowave heating process. The diffusion timescale can be approximated by (Chen and Scales, 2005):

$$\tau_{\mathrm{d}} \approx \nu_{in}(\frac{\lambda}{2\pi v_{\mathrm{thi}}})^2 \frac{1}{(1+\frac{T_e}{T_{e0}}(1+\frac{z_{d0}n_{d0}}{n_{e0}}))} \tag{5.1}$$

where ν_{in}, λ, and v_{thi} are the ion-neutral collision frequency, irregularity wavelength and ion thermal velocity, respectively. Eq.(5.1) shows that the diffusion timescale depends on T_e/T_{e0}; therefore, after the radio wave heating turn-on, the time decreases. The diffusion timescale is of order of $1s$ for irregularities observed in the 50 MHz range. The timescale for electron attachment onto the dust immediately after heater turn-on is approximated (Chen and Scales, 2005):

$$\tau_c \approx \frac{1}{kn_{e0}} \tag{5.2}$$

where k can be approximated as $k \approx I_e/en_e = \sqrt{8\pi}r_d^2 v_{te0}\sqrt{r_h}e^{\frac{-x}{r_h}}$, $r_h = T_e/T_{e0}$ is the ratio of electron temperature enhancement, and $x = e\phi_d/kT_e$ denotes the equilibrium normalized floating potential of the dust prior to the radio wave heating. Therefore, while at lower radar frequencies (e.g. 7.9 MHz) the electron charging onto the dust dominates the ambipolar diffusion process and enhances the irregularity amplitude after the pump turn-on, at higher radar frequencies (e.g. 224 MHz) the diffusion timescale is less than the electron charging timescale, therefore, suppression of irregularities is predicted. It should be mentioned that during the heating cycle, the dust reaches a new charge state which can be obtained using the equilibrium condition. The reduction rate of electron density due to the electron charging is denoted by $\tau_r = 1/(kn_{d0})$. It is noted that this rate is related to the initial dust charging time by $\tau_r = \tau_c n_e/n_d$.

5.1 Layer characteristics modified by radiowave heating

Radio wave heating of the PMSE modifies at least four important parameters associated with the dusty plasma heated region. These parameters are electron temperature T_e, electron density n_e, electron density irregularity amplitude δn_e and dust charge number Z_d. Important parameters that are assumed unmodified by the radiowave heating are the dust density n_d, dust radius r_d and dust irregularity amplitude $\widetilde{\delta n}_{d0} = \delta n_d/n_{d0}$. This subsection provides relationships between the modified and unmodified parameters that are used along with the analytical model for the electron irregularity amplitude (the primary measurable parameter) of the following section to diagnose the heated region. In other words, to develop the analytical model, unmodified parameters (such as n_d, r_d and n_i) are assumed to be known in order to calculate modified parameters. In this section, the analytical model along with the measurable parameters (electron density irregularity amplitude δn_e variation) will

be implemented to predict unmodified parameters such as n_d, r_d, and $\widetilde{\delta n_{d0}}$ as well as the modified parameter Δn_{e0} to diagnose the layer.

There are models that can estimate the ratio of electron temperature increase T_e/T_{e0} with good precision (Senior et al., 2010). Therefore, to get an estimation of electron density irregularity amplitude during the pump heating, we start off finding the value of n_e, ϕ_d (dust floating potential) and Z_d before heater turn-off. After the turn-on of the radiowave heating, the electron temperature will be enhanced and electron current on to the dust increases rapidly and dominates the ion current during the pump turn-on period. Then, the ion current increases and another equilibrium is reached again with $|I_i| \approx |I_e|$ as result of decreased floating potential during continued heating. The electron I_e and ion currents I_i can be estimated with the following expression for the negatively charged dust particles (e.g. Havnes, 2004):

$$I_{\mathrm{e}} = \sqrt{8\pi} r_{\mathrm{d}}^2 q_{\mathrm{e}} n_{\mathrm{e}} r_h v_{\mathrm{te}} \exp(-q_{\mathrm{e}}\phi_{\mathrm{d}}/r_h K T_{\mathrm{e}}), \tag{5.3}$$

$$I_{\mathrm{i}} = \sqrt{8\pi} r_{\mathrm{d}}^2 q_{\mathrm{i}} n_{\mathrm{i}} v_{\mathrm{ti}} (1 - q_{\mathrm{i}}\phi_{\mathrm{d}}/K T_{\mathrm{i}}), \tag{5.4}$$

Here, r_d is the dust radius, $v_{te(i)}$ electron (ion) thermal velocity and ϕ_{d} dust floating potential. m_e and m_i are electron and ion mass, respectively. Therefore, the following expression can be written for the steady state after the heater turn-on using Eqs.(5.3) and (5.4) and $|I_i| = |I_e|$ (Chen and Scales, 2005):

$$n_e \sqrt{\frac{r_h}{m_e}} e^{\frac{x}{r_h}} = \frac{n_i}{\sqrt{m_i}} (1 - x) \tag{5.5}$$

where $x = \frac{e\phi_d}{kT}$ and $T = T_e \approx T_i$ represents the electron or ion temperature before heating that they are assumed to be equal. r_h is the ratio of electron temperature increase after the heater turn-on and ϕ_d is the new level of dust floating potential. It should be noted that after the pump turn-on, the reduction in the ion density is of the order of a few percent and negligible. Considering the steady state after the heater turn-on and negligible variation of ion density during heater turn-on cycle, the floating potential and electron density are the two unknown (modified) parameters in Eq.(5.5). According to the quasi-neutrality condition, the plasma densities and dust density can be written in the following form:

$$Z_d n_d + n_e = n_i \tag{5.6}$$

Considering that dust is assumed to be unmodified during the heating period and variation of ion density is very small in comparison with the electron density variation, the dust charge and electron density are the only two unknown parameters in this equation. The relation of the dust floating potential and the dust radius to the number of charges on the dust particle can be written in the form (Scales, 2004):

$$Z_d = \frac{4\pi\epsilon_0 r_d \phi_d}{q_e} \tag{5.7}$$

This expression can be used to relate the floating potential and the charge number on the dust at the steady state before the heater turn-off. Therefore, using equations (5.5), (5.6) and (5.7) and solving them, the three unknown modified parameters, dust charge number Z_d, electron density n_{e0} and dust floating potential ϕ_d can be estimated in the plasma steady state after the pump turn-on. The electron density n_{e0} is used in the analytical model to be described shortly.

For the shorter irregularity wavelengths, the diffusion time is sufficiently small and electrons and ions can be modeled with the Boltzmann approximation. This implies that the normalized electron and ion irregularity amplitude before the pump turn-off can be written in terms of the electrostatic potential irregularity amplitude $\delta\phi$ as (Scales and Chen, 2008)

$$\widetilde{\delta n_e} \approx -\frac{T_i}{T_e}\widetilde{\delta n_i} \approx \frac{e\delta\phi}{K_B T_e r_h} \tag{5.8}$$

where $\widetilde{\delta n_e} = \delta n_e/n_e$ and $\widetilde{\delta n_i} = \delta n_i/n_i$ are the normalized electron and ion irregularity amplitudes. Considering the Poisson equation for the irregularities in the Fourier spectral domain, the dust charge variation during the radio wave heating can be written in this form $\Delta Z_d \approx -(1+\lambda_{De}^2 k^2)\Delta\delta n_e/\delta n_d$ for irregularities in the VHF band where $\Delta\delta n_e$ and δn_d are electron irregularity amplitude variation during heating and dust irregularity amplitude, respectively. It will be discussed in the next section that $\Delta\delta n_e$ is observable and δn_d may be calculated from the analytical model.

5.2 Analytical model for electron irregularities during heating

The purpose of the present investigation is the use of temporal evolution of the electron density irregularity amplitude after the turn-on of radiowave heating to diagnose the charged dust layer. As was discussed before, the amplitude of electron irregularities after heating depends on diffusion and charging processes. Considering that the charging process tends to increase and diffusion process tends to suppress the amplitude of irregularities, depending upon which process has the shorter timescale after heater turn-on, the amplitude of irregularities may be suppressed or enhanced. Figure 5.1 shows the schematic of these characteristics after the pump turn-on. Therefore, as can be seen in this figure, there is diagnostic information that can be inferred regarding the charged dust layer. Depending on what the radar frequency or electron irregularity wavelength is, the irregularity may be enhanced or

suppressed following the heater turn-on and the maximum or minimum of irregularity amplitude, which is shown by δn_e^{max} and δn_e^{min}, respectively, is the unique characteristic that can be used as a diagnostic tool. The time at which the maximum or minimum amplitude has been reached τ_{max}, τ_{min}, are parameters that can place a diagnostic bound on the dust parameters and shows the transition from the domination of electron charging process to the domination of ambipolar diffusion process. The timescale for the decay of the electron irregularity amplitude after heater turn-on, when the maximum is reached, is another characteristic associated with the active modification of PMSEs.

A detailed study of radiowave modulation with local plasma at mesopause altitudes was done by Havnes et al., (2007) and Kassa et al., (2005) where it is shown that the ion density is not much affected during the heating but the electron density is reduced by a large factor within the bite-out. This is because the heated electrons attach themselves rapidly to the dust and become depleted as the dust is charged more negatively while the heavy and colder ions collide at a much slower rate.

Assuming the electron density n_e^{eq} before the heater turn-on, due to increasing and rapidly dominating electron current during the pump turn-on, the electron density reduces. The electron density is assumed to reach n_{e0} which is the electron density after steady state during heating. The electron density variation during radiowave heating is shown in Figure 5.1b. This happens when the floating potential decreases during continued heating and another equilibrium is reached again with $I_e \approx I_i$. As was mentioned before, the electron density before heater turn-off n_{e0} can be obtained using the equilibrium condition Eq.(5.5), the quasi-neutrality condition Eq.(5.6) and the expression of dust charge number Eq.(5.7).

The electron density variation with time can be approximately modeled with the diffusion and the dust charging, that corresponds to reduction of the electron density, during the initial turn-on of the radio wave. The temporal behavior of electron density at a fixed spatial point can be written as follows:

$$n_e(t) = n_e^{eq} e^{-t/\tau_r} e^{-t/\tau_d} + n_{e0}(1 - e^{-t/\tau_r} e^{-t/\tau_d} e^{-t/\tau_{rcb}}) \tag{5.9}$$

where turn-on of the radiowave is referenced to time t=0. At t=0, the electron density has its equilibrium value n_e^{eq} and for a longer time period after the heater turn-on, the second term in Eq.(5.9) shows the electron density at the steady state dominates the first term. n_{e0} is described by the solution of Eq. (5.5), (5.6) and (5.9) as discussed in the previous section. Another physical process that may have a secondary effect on electron irregularity amplitude before radiowave heating turn-off is the recombination of the electrons and ions. The recombination of electrons and ion is shown in the form of $e^{-t/\tau_{rcb}}$ since it causes the reduction of electron density. The recombination time $\tau_{rcb} \approx \frac{1}{\alpha n_{i0}} \frac{1}{\sqrt{r_h}}$ where α is the recombination rate and r_h is the ratio of electron temperature increase after the turn-on of radiowave heating. The recombination process is assumed to be important at the later time after heater turn-on. Considering that the effect of the recombination process on the

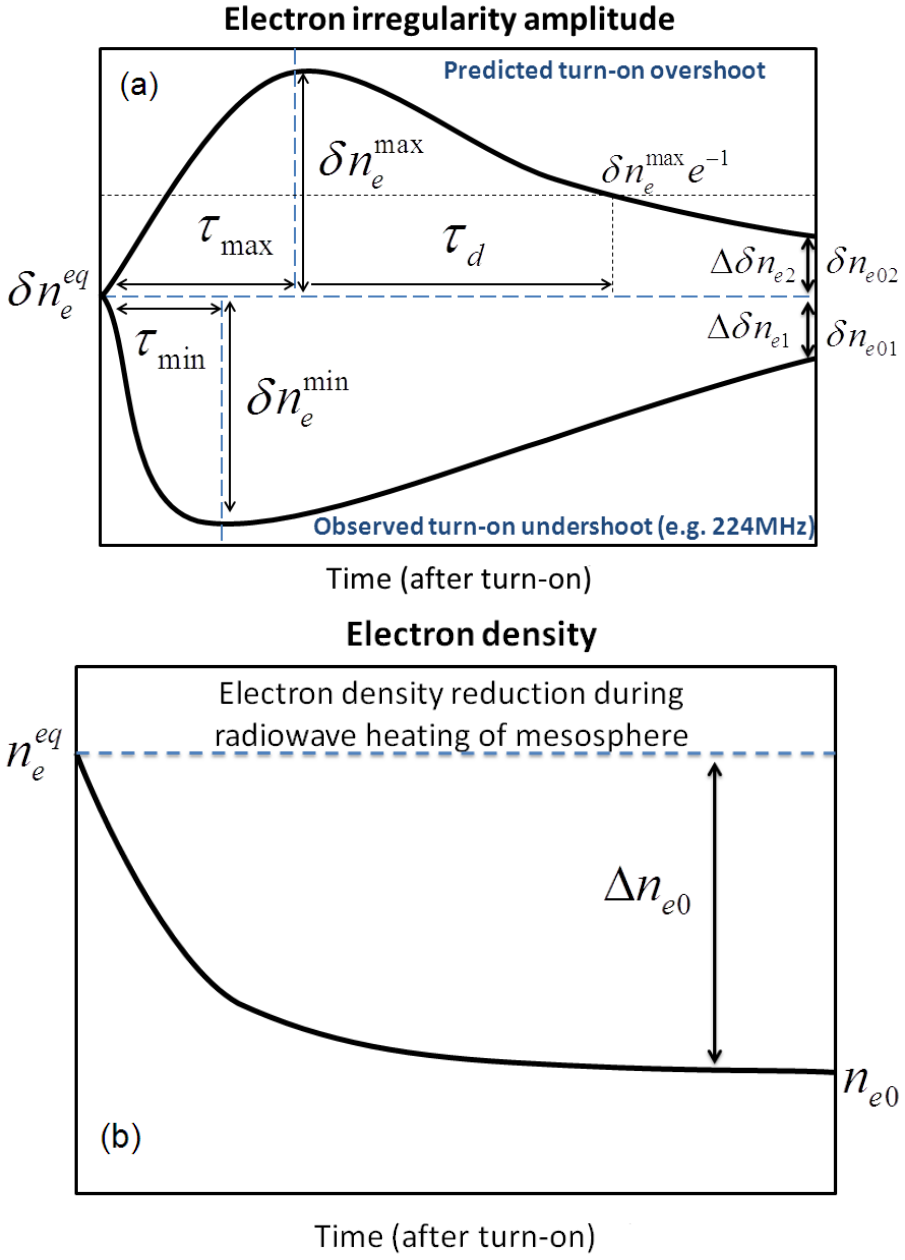

Figure 5.1: Schematic of (a) electron irregularity (b) electron density behavior subsequent to the turn-on of radio wave heating. Observables in panel (a) lead to diagnosis of the dust layer.

initial evolution of irregularities is negligible and the subject of this work is to study the temporal evolution of the irregularities at early time after heater turn-on, the effect of the recombination process is neglected. Therefore the temporal evolution of the electron density can be written as:

$$n_e(t) = (n_e^{eq} - n_{e0})e^{-kn_{d0}t}e^{-t/\tau_d} + n_{e0} \tag{5.10}$$

The background and perturbation components of electron and dust densities can be written in the form $n_0 + \delta n_0$, respectively. The fluctuation amplitude of electron density right before heater turn-on is assumed to be normalized to its value before heater turn-on and is one. δn_{e0} is the electron irregularity amplitude before heater turn-off. It should be noted that the irregularities on the electrons and dust are 180^0 out of phase while ions and dust have in phase irregularities (Lie-Svenson et al., 2003; Scales and Chen, 2008). As a result Eq.(5.10) can be simplified to

$$\begin{aligned} \delta n_e(t) \quad = \quad & (n_e^{eq} + \delta n_e^{eq})e^{-kn_{d0}t}e^{k\delta n_{d0}t}e^{-t/\tau_d} + (n_{e0} + \delta n_{e0}) \\ & (1 - e^{-kn_{d0}t}e^{k\delta n_{d0}t}e^{-t/\tau_d}) - n_e^{eq}e^{-kn_{d0}t}e^{-t/\tau_d} - n_{e0} \\ & (1 - e^{-kn_{d0}t}e^{-t/\tau_d}) \end{aligned} \tag{5.11}$$

By simplifying Eq.(5.11) we can write the following expression:

$$\delta n_e(t) = (A + B)e^{-kn_{d0}t}e^{k\delta n_{d0}t}e^{-t/\tau_d} - Be^{-kn_{d0}t}e^{-t/\tau_d} + \delta n_{e0} \tag{5.12}$$

where $B = (n_e^{eq} - n_{e0}) \equiv \Delta n_{e0}$ is the variation of the electron density after heater turn-on and $A = (\delta n_e^{eq} - \delta n_{e0})$ which represents the variation of electron density irregularity amplitude during the pump turn-on period. $\widetilde{\delta n_{d0}} = \delta n_d / n_{d0}$ is the dust irregularity amplitude normalized to the background dust density. The analytical model can be used as a diagnostic tool to estimate some parameters associated with the charged dust layer such as dust density, dust radius and ratio of electron temperature enhancement during heating using the temporal behavior of electron irregularity amplitude or the amplitude of the backscattered signal during the PMSE heating experiment. The analytical expression mentioned in Eq.(5.12) is incorporated for all figures which will be presented after this section. This model also will be simplified for HF and VHF bands in the following sections.

The mesopause temperature for both ions and electrons is taken to be $T_e = T_i = 130K$. Proton hydrates with mass between 59 and 109 proton masses are the dominant ion compositions at this height range. O_2^+ ions are more numerous than NO^+. NO^+ and O_2^+ together can be slightly more dense than the proton hydrates at 88km and above (Kopp et al., 1985). It should be noted that the variation of ion mass from 50 to 100 proton masses does not have a significant impact on the irregularity amplitude evolution during heating. The ion-neutral

collision frequency is of order $10^5 s^{-1}$ (Lie-Svenson et al., 2003). The variation of ion-neutral collision frequency is predicted to be between $3 \times 10^4 s^{-1}$ and $3 \times 10^5 s^{-1}$ in the altitude range 80-90km (Turunen et al., 1988). The electron-neutral collision frequency temperature dependence is assumed to be $\nu_{en} \sim T_e$ and recombination rate dependence on temperature is taken to be $\alpha \sim T_e^{-1/2}$. The size and density of dust particles are assumed to vary from 1-3 nm and 1-3 $\times 10^9 m^{-3}$, respectively. It should be noted that these parameter ranges are based on recent experimental observations (Robertson et al., 2009). The dust irregularity amplitude normalized to the background dust density is taken to be 0.2.

The accuracy of the analytical model is examined for the variation of radar frequency, the degree of temperature enhancement during heating and dust density. Figure 5.2 represents the irregularity amplitude after heater turn-on associated with the computational and analytical model for varying radar frequency which corresponds to the variation of electron irregularity wavelength according to the Bragg scattering condition. Figure 5.2 shows the electron irregularity amplitude 5s before the pump turn-on when the equilibrium of irregularities has been achieved. The radiowave heating is turned on at t=25s for heating cycle 30s. As can be seen, the simple analytical model has very reasonable agreement for 30s after the turn-on in comparison with the full computational model. It is much superior to previous analytical models for irregularity behavior during turn-on (e.g. Scales and Chen, 2007). The computational and analytical models predict an enhancement of electron irregularities for larger irregularity scale sizes 20 and 10m which correspond to radar frequencies 7.9 and 56 MHz. The τ_{max} estimated by the analytical model are 12 and 2.9s for radar frequencies 8 and 56 MHz, respectively. The τ_{max} according to the computational results are 13.3 and 3.1s which shows good agreement with the analytical model. While the computational model predicts a small enhancement of irregularity amplitude after the turn-on at 134 MHz, the analytical model shows a suppression. According to the analytical model results, the decay of irregularity amplitude after the peak at 7.9 and 56 MHz or after heater turn-on at 224 and 930 MHz is faster in comparison with the computational result and shows that the analytical model accentuates the diffusion process slightly. In summary, it turns out that the diffusion timescale in the analytical model is somewhat shorter for 134, 224 and 930 MHz in comparison with the computational model. The significance will be discussed in more detail shortly.

5.3 Application to temporal evolution of electron density irregularity amplitude in the VHF band

According to the equations of electron charging and ambipolar diffusion timescales, only the diffusion time depends on the dust density and it reduces as the dust density increases. It turns out that at higher radar frequencies (e.g. 224 MHz), the electron density irregularity amplitude which suppresses rapidly after the pump turn-on due to the short diffusion timescale, may increase in amplitude after continued heating as the result of the electron

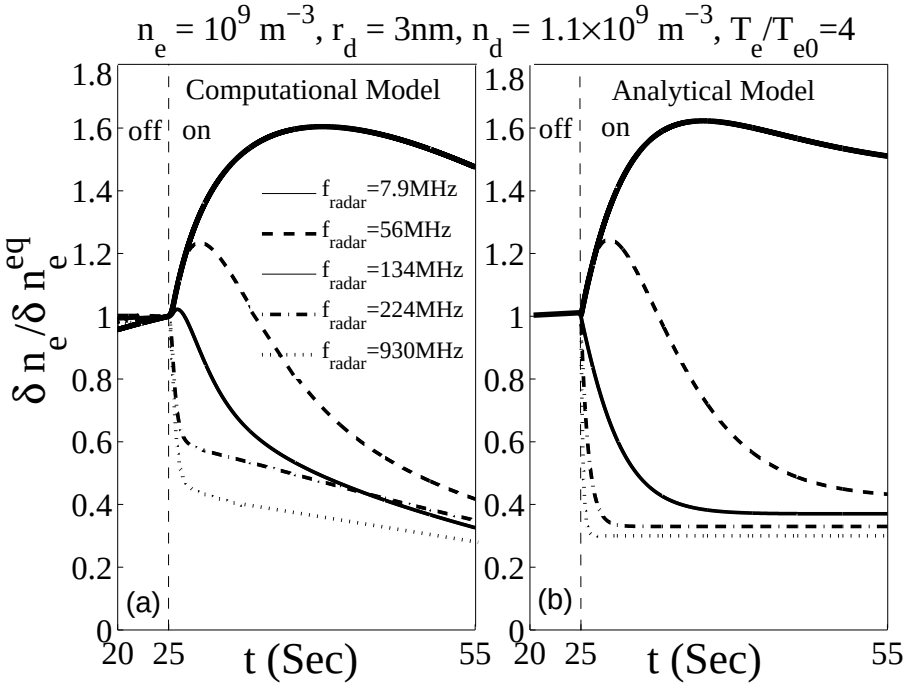

Figure 5.2: Comparison of the full computational model (a) with the analytical model (b) after the pump turn-on for varying radar frequencies. Note results represented in the form of $\delta n_e/\delta n_e^{eq}$ which is the normalized electron irregularity amplitude difference from the equilibrium before heating.

charging process for certain dust density and radii ranges. This has been observed both in experimental data and computational models (Naesheim et al., 2008). This enhancement of electron irregularity amplitude requires relatively small dust densities and radii. In the case of continued heating and at the time the ambipolar diffusion has ceased, the charging of electrons on to the dust takes the control of the electron irregularity amplitude, therefore temporal evolution can then be approximately described by:

$$\frac{\partial n_e}{\partial t} + k n_d n_e = 0 \tag{5.13}$$

The solution for the temporal evolution of electron density irregularity amplitude can be expressed as:

$$\delta n_e(t) = (n_{e0} + \delta n_e^{min}) e^{\widetilde{\delta n}_{d01} t/\tau_r} e^{-t/\tau_r} - n_{e0} e^{-t/\tau_r} \tag{5.14}$$

where $\widetilde{\delta n}_{d01}$ corresponds to the dust irregularity amplitude associated with the VHF radar. Considering the assumption $\tau_d \ll \tau_r$ for the smaller irregularity wavelengths (corresponding to the higher radar frequencies), the time at which the minimum amplitude has been reached after the turn-on of the radiowave can be obtained from the condition $\partial \delta n_e(t)/\partial t = 0$ and Eq. (5.12):

$$\tau_{min} = \frac{\tau_r}{\widetilde{\delta n}_{d01}} \log\left(\frac{\Delta n_{e0}}{\Delta n_{e0} + \Delta \delta n_{e1}}\right) \tag{5.15}$$

where Δn_{e0} and $\Delta \delta n_{e1}$ are the electron density variation and electron density irregularity amplitude variation during the pump heating (Figure 5.1a, b) and $\Delta \delta n_{e1} = \delta n_{e0} - \delta n_e^{eq}$. It should be noted that $\Delta \delta n_{e1}$ can be measured during the active experiment just by comparing the strength of the radar echo before the heater turn-off to its value at the steady state before the heater turn-on. This expression can be used to approximate the minimum amplitude of the electron irregularities after the turn-on of the radiowave heating as a result of the diffusion process. Substituting Eq.(5.15) into (5.12) implies the following expression for the minimum amplitude of electron irregularities in the VHF band during heating:

$$\delta n_e^{min} \approx \Delta \delta n_{e1} \left(1 + \frac{\Delta \delta n_{e1}}{\Delta n_{e0}}\right)^{\frac{\tau_r}{\tau_d} \frac{1}{\widetilde{\delta n}_{d01}}} + \delta n_{e01} \tag{5.16}$$

where $\Delta \delta n_{e1} = \delta n_{e01} - \delta n_e^{eq}$. Since at higher radar frequencies or shorter electron irregularity wavelengths, the ambipolar diffusion timescale is much less than the electron charging timescale, the approximate analytical expression can be used to investigate the behavior of the evolution of the dust associated electron irregularities at the initial turn-on of the radio waves. The condition for no enhancement of the electron irregularities at the initial turn-on

of the radiowave, typically observed in VHF experimental observations, $\partial \delta n_e / \partial t < 0$ for all t yields the condition:

$$\frac{\tau_r}{\tau_d} > \left(1 + \frac{\triangle n_e}{\Delta \delta n_{e1}}\right) \widetilde{\delta n}_{d01} - 1 \tag{5.17}$$

By assuming $\frac{\triangle n_e}{\Delta \delta n_{e1}} \widetilde{\delta n}_{d01} \gg 1$, this expression can be simplified to:

$$\frac{\tau_r}{\tau_d} > \frac{\triangle n_e}{\Delta \delta n_{e1}} \widetilde{\delta n}_{d01} \tag{5.18}$$

This condition imposes a lower diagnostic bound on the ratio of the electron density reduction rate to ambipolar diffusion rate which can be used as a quantitative condition to estimate the electron density reduction during heating by measuring the electron density irregularity amplitude variation according to the radar echo strength.

The effect of the varying dust density on the temporal evolution of the electron density irregularity amplitude is shown in Figure 5.3 for dust densities 0.8×10^9, 1.6×10^9, and 2.4×10^9 m^{-3} with dust radius 3 nm. Electron density and the ratio of electron temperature increase during heating are assumed to be 10^9 m^{-3} and 3, respectively. The left figure shows the computational results and right figure represents the analytical results. It is evident that the analytical model performs well in predicting the general behavior of irregularity amplitude after heater turn-on. The primary difference is that the rate of the irregularity's decay in analytical results is faster than computational results. This shows that the diffusion timescale is longer in the computational model. This can be explained based on Eq.(5.1) which shows the electron density dependency of diffusion timescale. Therefore, the electron density changes gradually with time in the simulation after the pump turn-on till it reaches its steady state value before pump turn-off, while the diffusion timescale used in the analytical model is calculated by making the assumption that electron density drops to its steady state value instantly. As a result, there is a tendency for the analytical model to slightly overestimate τ_{min} in this regard.

Figure 5.4 compares the variation of the electron irregularity amplitude with the ratio of electron temperature increase during the pump heating which is obtained using the both computational and analytical models. According to this figure, the electron irregularity has been suppressed at 224 MHz by increasing the ratio of electron temperature enhancement after the heater turn-on which is also predicted by Eq.(5.8) where $\widetilde{\delta n}_e$ depends on $1/T_e$. The irregularity amplitude decreases in the first 2s after the pump turn-on as a result of the diffusion process and then starts to increase which is due to the electron charging process as is described by Eq.(5.14). As can be seen from both computational and analytical models, irregularity amplitude increases more for continued heating at smaller electron temperature enhancement ratios. This is also consistent with the approximate expressions for ambipolar diffusion and electron charging timescales, Eqs. (4) and (5), where diffusion depends on

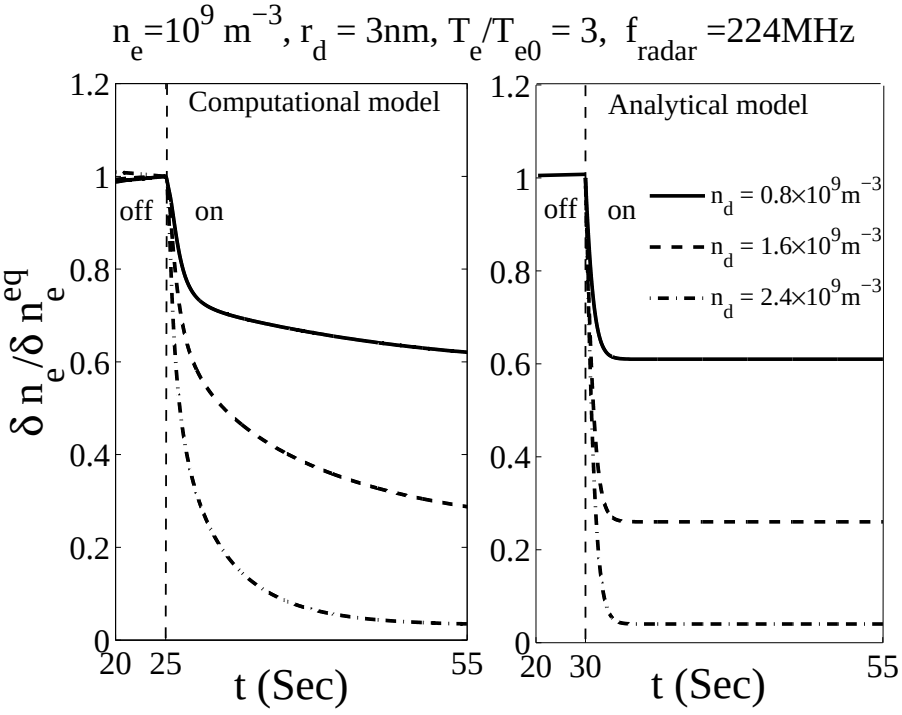

Figure 5.3: Comparison of (a) computational and (b) analytical model results for varying dust density at $f_{radar} = 224$ MHz.

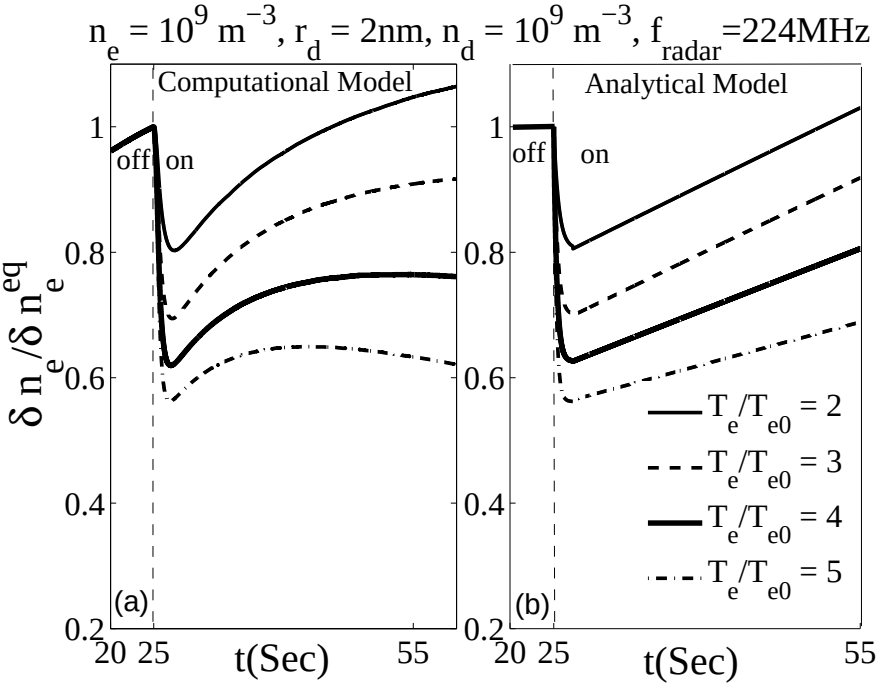

Figure 5.4: Time evolution of electron irregularities in the computational model (a) and corresponding analytical model (b) calculations for varying the ratio of electron temperature increase after the turn-on of the radio wave at t=25 s and f_{radar} = 224 MHz. Note low electron temperature increase cases exhibit enhancement in irregularity amplitude upon continued heating.

$1/r_h$ and electron charging $\approx 1/\sqrt{r_h}$. This shows that for smaller values of r_h, the charging timescale reduces more in comparison with diffusion timescale and leads to a larger electron irregularity amplitude with the continued heating.

5.4 Application to temporal evolution of electron density irregularity amplitude in the HF band

At higher frequency regimes (above 224 MHz), which would imply smaller irregularity wavelengths, the diffusion timescale is much less than the charging timescale and electron irregularities are suppressed quickly after the heater turn-on before they have chance to be enhanced by the charging process. But at lower frequencies such as 7.9 MHz where the charging timescale is less than the diffusion timescale initially, electron irregularity amplitudes starts to grow until the point at which the diffusion timescale becomes comparable to the charging timescale. After this point, the electron irregularity amplitude approaches to

the steady state value before turn-off of the radiowave where the dust charge reaches a new charge state by satisfying the equilibrium condition $I_e + I_i = 0$. The approximate temporal behavior after the electron irregularity amplitude has reached its maximum is given by:

$$\widetilde{\delta n_e}(t) \approx \delta n_e{}^{max} e^{-t/\tau_d} \tag{5.19}$$

Therefore the timescale for the decay of the irregularities after the maximum value is reached is the ambipolar diffusion time τ_d. In this case the time at which the maximum amplitude is reached after the turn-on of the radiowave can be estimated by making the assumption $\tau_r \ll \tau_d$. Hence τ_{max} obtained from $\partial \delta n_e(t)/\partial t = 0$ is:

$$\tau_{max} = \frac{\tau_r}{\widetilde{\delta n_{d02}}} \log\left[\frac{\Delta n_{e0}}{\Delta n_{e0} + \Delta\delta n_{e2}}\left(\frac{1}{1 - \widetilde{\delta n_{d02}}}\right)\right] \tag{5.20}$$

where $\widetilde{\delta n_{d02}}$ corresponds to the dust irregularity amplitude associated with the HF radar and $\Delta\delta n_{e2} = |\delta n_{e02} - \delta n_e^{eq}|$. This expression can be used to approximate the maximum amplitude of the electron irregularities after the turn-off of the radiowave heating. Substituting Eq. (5.20) into (5.12) implies the following expression for the maximum amplitude of electron irregularities in the HF band:

$$\delta n_e^{max} \approx \Delta\delta n_{e2}\left((1 - \widetilde{\delta n_{d02}})(1 + \frac{\Delta\delta n_{e2}}{\Delta n_{e0}})\right)^{\frac{1}{\widetilde{\delta n_{d02}}}} + \delta n_{e02} \tag{5.21}$$

These three characteristics of the irregularity temporal evolution after the turn-on may be used for diagnostic information. They are the time at which the maximum amplitude is reached Eq.(5.20), the maximum amplitude achieved Eq.(5.21) and the timescale of decay after the maximum amplitude has been reached. The $\partial\widetilde{\delta n_{e0}}/\partial t > 0$ condition determines the condition for enhancement of the electron irregularity after the turn-on of the radiowave. For the time period of about a few tenths of second after the turn-on of radiowave heating, this leads to the following condition:

$$\frac{\tau_r}{\tau_d} < \left(1 + \frac{\Delta n_{e0}}{\Delta\delta n_{e2}}\right)\frac{\widetilde{\delta n_{d02}}}{\tau_r} - 1 \tag{5.22}$$

Using the parameters presented in Figure 5.2, radar frequencies 7.9 MHz and 56 MHz with $\widetilde{\delta n_{d02}} = 0.2$ imply the right hand side of this equation to be approximately 8 and 80, respectively. The calculated ratio $\tau_r/\tau_d \approx 2$ and 34 compared to the right hand side of Eq.(5.21) which validates the condition.

Figure 5.5 compares the effects of dust densities on the evolution of irregularity amplitude during heating at 7.9 MHz in more detail. This figure indicates how the dust density can alter

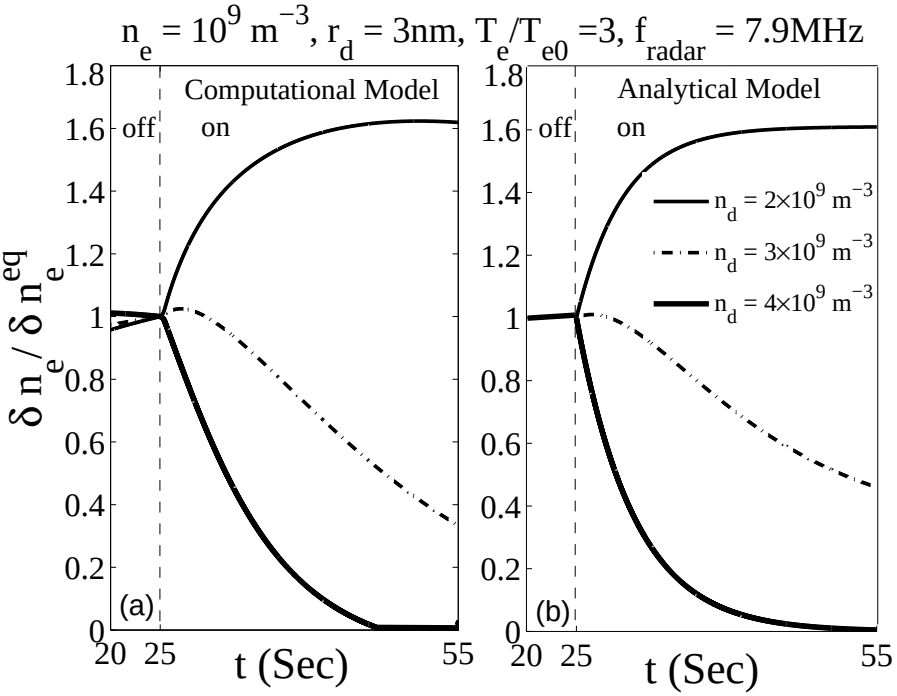

Figure 5.5: Comparison of (a) computational and (b) analytical model results for varying dust density at $f_{radar} = 7.9$ MHz. Note high dust density case exhibits suppression in irregularity amplitude after the pump turn-on.

the ambipolar diffusion and electron charging timescales such that the electron irregularity amplitude may be suppressed after the pump turn-on at 7.9 MHz. While the models represent the enhancement of radar echoes for $n_d = 10^9$ and 2×10^9 m^{-3}, a suppression of irregularity amplitude has been observed after the pump turn-on for 3×10^9 m^{-3} which shows a similar behavior to temporal evolution of radar echoes at 224 MHz.

The comparison of the computational and analytical models for various electron to ion temperatures are shown in Figure 5.6. The plasma parameters are $n_e = 10^9$ m$^{-3}, r_d = 2$ nm, $n_d = 2 \times 10^9$m^{-3} and r_h has been changed from 2 to 8. The results show good agreement between the two models and only the analytical model predicts a slower decay of irregularity amplitudes for $r_h = 4$, 6 and 8 with respect to the computational results. According to the result of the computational model, the τ_{max} is 30, 13.2, 6.8 and 4.5s for the temperature enhancement ratio 2, 4, 6 and 8, respectively, at the radar frequency 7.9 MHz. The time at which maximum amplitude has been achieved calculated using the Eq.(5.16) is 30, 15, 5.5 and 4.9s which shows that the analytical model provides very reasonable accuracy regarding the estimation of τ_{max}.

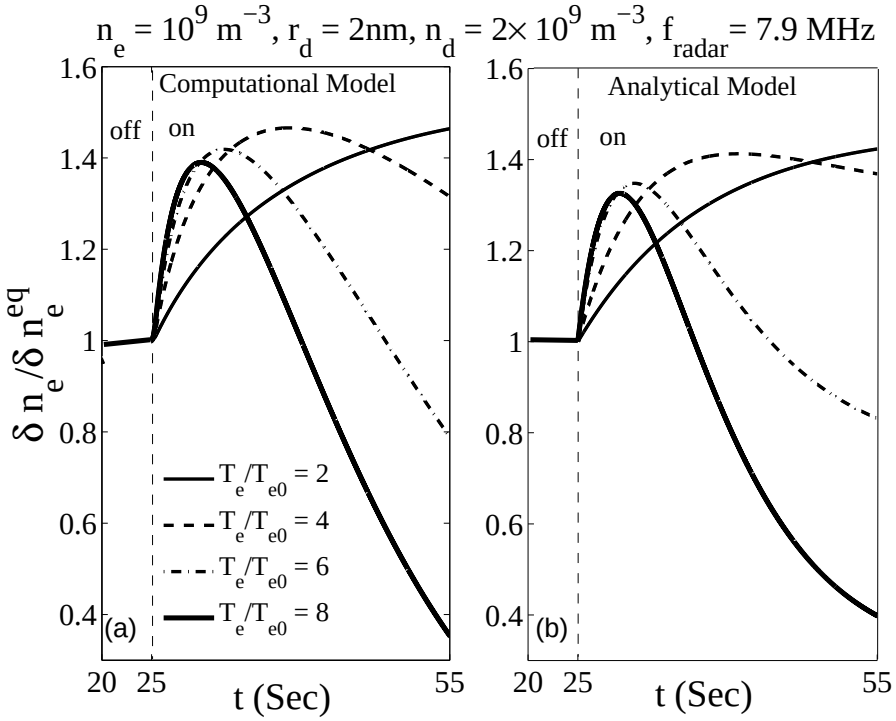

Figure 5.6: Comparison of (a) the computational model with (b) the analytical model after the turn-on of the radio wave heating for varying the ratio of electron temperature increase during heating at $f_{radar} = 7.9$ MHz. Note that τ_{max} decreases by increasing the electron temperature ratio during the pump heating.

5.5 Incorporation of information at turn-off

Utilizing the measurable parameters after heater turn-off with the parameters associated with the pump turn-on during a multi-frequency experiment may increase degrees of freedom to get more diagnostic information. Considering $\delta n_e^{\mathrm{OFF}}(t) \approx \delta n_e^{max,\mathrm{OFF}} e^{-t/\tau_{ri}}$ (Scales and Chen, 2008), which represents the timescale for the decay of the irregularities after the turn-off overshoot maximum is reached, the reduction rate of the ion density due to the dust charging from ion flux τ_{ri} can be estimated using the data collected during an active VHF PMSE experiment. Therefore, the electron density reduction time after the pump turn-on is given by:

$$\tau_r \approx 2\tau_{ri} r_h \sqrt{\frac{m_e}{m_i}} \tag{5.23}$$

Using the time at which the maximum value is reached after the pump turn-on τ_{max} during HF PMSE experiment to estimate the electron reduction time is another way of estimating of this parameter (i.e. $\tau_r \approx \tau_{max}$). As shown in Figure 12 in (Chen and Scales, 2005) the electron charging time is very short and at the time the maximum amplitude is reached, the plasma is expected to have reached the steady state. Another parameter that can be measured in the active PMSE experiment is the time at which the maximum electron irregularity amplitude is reached after the turn-off of the radiowave heating and can be written as (Scales and Chen, 2008):

$$\tau^{max,\mathrm{OFF}} \approx \tau_{di} \log\left[\left(1+\frac{\tau_{\mathrm{ri}}}{\tau_{\mathrm{di}}}\right)\left(1-\frac{\Delta\delta \mathrm{n_{e0}}}{\Delta \mathrm{Z_{d0}}\delta \mathrm{n_{d0}}}\right)\right] \tag{5.24}$$

ΔZ_{d0} denotes the net gain in electron charges during radiowave heating and τ_{di} is the diffusion time given by Eq.(5.1) for $T_e \approx T_{e0}$. The maximum amplitude of the electron irregularities is estimated to be (Scales and Chen, 2008):

$$\delta n_e^{max,\mathrm{OFF}} \approx \left[\frac{r_h + 1 - 2\widetilde{\delta} n_{e0}^{eq}}{(1-\widetilde{\delta} n_{e0}^{eq})(1+\frac{\tau_{di}}{\tau_{ri}})}\right]\left[\frac{(1+\frac{\tau_{ri}}{\tau_{di}})(r_h - \widetilde{\delta} n_{e0}^{eq})}{r_h + 1 - 2\widetilde{\delta} n_{e0}^{eq}}\right]^{\tau_{di}/\tau_{ri}} \tag{5.25}$$

where $\widetilde{\delta} n_{e0}^{eq} = \delta n_e^{eq}/\delta n_{e0}$. Since all parameters of Eq.(5.25) are measurable, this equation can be used to approximate the degree of the electron temperature enhancement $r_h = T_e/T_{e0}$. An alternative simple analytical expression to estimate the upper and lower limit of heated electron temperature by measuring the reflection coefficient, which is proportional to the electron gradient squared, was derived by Kassa et al.(2005). It has been shown that the condition for turn-on overshoot $\tau_d/\tau_c \gg 1$ and turn-off overshoot $\tau_d/\tau_c \ll 1$ may provide a possible range of dust radius. Therefore, conducting PMSE heating experiments in the HF and VHF band simultaneously, where turn-on overshoot in the HF band

and turn-off overshoot in the VHF band are observed, and using $C_l\sqrt{v_{thi}/n_e\nu_{in}}f_{radar} \ll r_d \ll C_u\sqrt{v_{thi}/n_e\nu_{in}}f_{radar}$ (Chen and Scales, 2005), where $C_u = 4\pi/\sqrt[4]{8\pi}c\sqrt{2/1-x}$,$C_l = 4\pi\exp(2/\mathrm{r_h})/\sqrt[4]{8\pi}c\sqrt[4]{m_e/m_i}\sqrt[4]{(1+r_h)^2/r_h}$, may possibly give fairly accurate bounds for r_d in comparison with recent rocket data (Robertson et al., 2009).

5.6 Calculation of dust layer diagnostic information

Considering the two types of distinct temporal behavior of radar echoes at HF (e.g. 7.9 MHz) and VHF (e.g. 56, 134 and 224 MHz) during active modification of PMSE, conducting these types of experiments in HF and VHF frequency band may provide enough observables to estimate dust layer parameters as well as background plasma quantities. The observable parameters during the experiment after the pump turn-on are τ_{max}, τ_{min}, δn_e^{max}, δn_e^{min}, τ_d, and $\Delta\delta n_{e1,2}$ as described in Figure 5.1a. Observables after turn-off includes the ion density reduction period τ_{ri}, maximum amplitude of the electron irregularities after the turn-off of the radiowave heating $\delta n_e^{max,\mathrm{OFF}}$, and the time at which the maximum amplitude is reached after the turn-off τ^{max}. These observables may be used in the method described here to provide information on the dust density, charge state, electron density variation during the radiowave heating and the degree of the electron temperature enhancement.

As discussed in section 5.2, τ_{ri} can be used to estimate the electron reduction time τ_r and the maximum irregularity amplitude after the heater turn-off $\delta n_e^{max,\mathrm{OFF}}$ may be used to predict the temperature enhancement ratio during heating r_h. Then, observing τ_{max}, τ_{min}, δn_e^{max}, δn_e^{min}, $\Delta\delta n_{e1,2}$, and τ_d during a two frequency experiment and using equations (5.15), (5.16), (5.20) and (5.21) gives a system of 4 equations that can be solved for the electron density variation during heating Δn_{e0}, and the dust irregularity amplitude associated with VHF radar δn_{d01} and associated with HF radar δn_{d02}. It can be noted that this solution is facilitated by the fact that the mean electron density is the same in both frequency bands. After some mathematical manipulation of Eqs.(5.6) and (5.8), it turns out that the dust density n_{d0} also can be estimated using:

$$n_{d0} \approx \frac{\Delta n_{e0}}{\left(1+\frac{\epsilon_0 k_B k_1^2 T_e r_h}{n_e e^2}\right)}\frac{\delta n_{d01}}{\Delta\delta n_{e1}} \tag{5.26}$$

where n_e and T_e are the electron density and temperature before active perturbation and e denotes the electron charge. $\Delta\delta n_{e1}$ corresponds to the electron irregularity amplitude variation and $k_1 = 2\pi/\lambda_1$ is the irregularity wavelength at the Bragg scatter of VHF radar. δn_{d01} and Δn_{e0} are calculated from the model. To access the capability of the analytical model in predicting the dust and plasma parameters, the computational results for 7.9 and 224 MHz shown in Figure 5.2 are used as the possible case that may be observed in the experiment. Then, the predicted parameters by the the technique just described is compared

Table 5.1: Computational model parameters comparison with those obtained by the analytical model.

Parameters	Computational parameters	Predicted by analytical model
Δn_{e0}	66%	$\approx 74\%$
T_e/T_{e0}	4	≈ 3
n_{d0}	$1.1 \times 10^9 \mathrm{m}^{-3}$	$\approx 0.5 \times 10^9 \mathrm{m}^{-3}$
δn_{d0}	$0.2 \times n_d$	$\approx 0.27 \times n_d$

with the computational model parameters and shown in Table 5.1 which show very reasonable agreement.

The irregularities in electron density are believed to be formed by fluctuation in the dust density. Looking at PMSE radar data represents a band of scattered signal over altitude range about 1 km which requires electron number density fluctuations at the Bragg scale (Kassa et al., 2005; Naesheim et al., 2008; Ramos et al., 2009). As shown in Figure 5.7, the overlapped region of HF and VHF PMSEs can be divided out to N subregions (Ramos et al., 2009). Therefore, the proposed active PMSE experiment in the HF and VHF bands simultaneously may be implemented to estimate the altitude profile of dust density by comparing the average of HF and VHF PMSE signal on the subdivided regions and using Eqs(18), (19), (23) and (24).

Although the focus of this section is on the multi-frequency PMSE heating experiment in the VHF and HF band, it may be possible to perform this type of experiment for 2 radar frequencies in the VHF band, where a significant difference in the amount of suppression of radar reflectivity after heater turn-on and turn-off overshoot amplitude is expected. Dust layer parameters may be estimated. In this case Eq. (5.15) and (5.16) can be written for both frequencies where τ_{min1}, τ_{min2}, δn_{e1}^{min}, δn_{e2}^{min}, and τ_{ri} are measurable in the experiment.

5.7 Conclusions

Using ground based ionospheric heating facilities to produce an artificial enhancement in electron temperature is shown as a rich source of diagnostic information for charged dust layers in the earth's upper atmosphere. The dependency of the backscatter signal strength after the turn-on and turn-off of the radio wave heating to the radar frequency is an unique phenomenon that can shed light on the unresolved issues associated with the basic physics of the natural dust layer. This work has attempted to provide further physical insight into the physical processes associated with temporal evolution of the electron irregularities during the turn-on of the radiowave heating and can be seen to be complementary to past work that has considered the physical processes after the turn-off of radio wave heating. The new

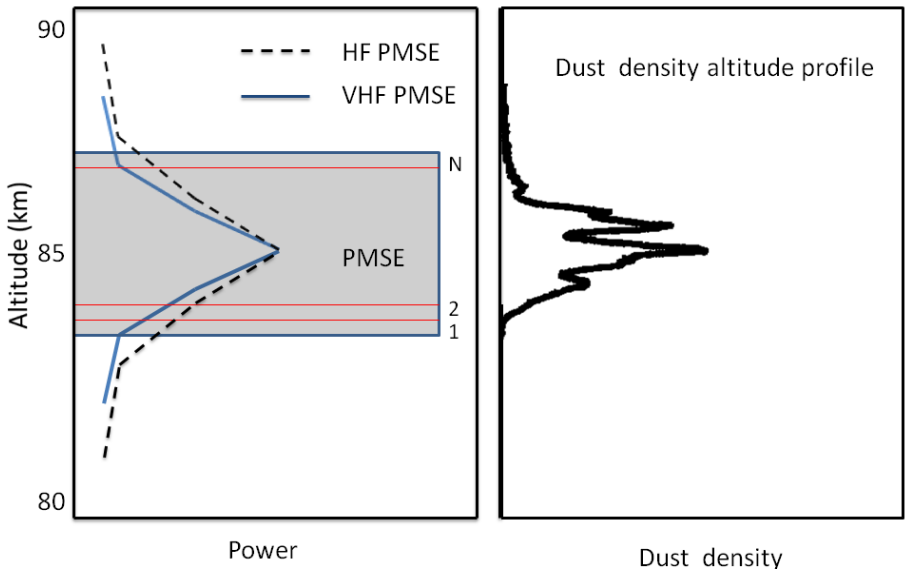

Figure 5.7: Schematic altitude profiles of HF and VHF PMSE. The shaded area indicates the altitude region where both HF and VHF PMSE may simultaneously occur and possibly allow dust density measurement via a two frequency heating experiment.

analytical model is able to describe the temporal evolution of electron irregularities during the early phase of the heating cycle. The simplified analytical models here provide quite reasonable agreement with full computational results. It turns out that active PMSE heating experiments involving multiple observing frequencies at 7.9 (HF), 56, and 224 MHz (VHF) may contribute further diagnostic capabilities since the temporal evolution of radar echoes is substantially different for these frequency ranges. Measuring radar echoes at multiple frequencies imposes enough information to estimate important plasma and dust parameters. Analytical expressions for observable parameters associated with the radiowave turn-on, τ_{max}, τ_{min}, δn_e^{max}, δn_e^{min}, $\Delta\delta n_e$, and τ_d as well as τ_{ri}, $\delta n_e^{max,\mathrm{OFF}}$ and τ^{max} after the pump turn-off, during active perturbation of PMSEs are derived here that may provide information on the dust layer such as dust density altitude profile, dust density irregularity amplitude, dust charge state variation, and degree of electron temperature enhancement during radio wave heating. It has been shown that predicted enhancement of irregularity amplitude after heater turn-on in the HF band is the direct manifestation of the dust charging process in the space. Therefore further active experiments of PMSEs should be pursued in the HF band to illuminate the fundamental charging physics in the space environment and get more insight on this unique medium.

It should be noted that proposed remote sensing technique enable us to study the time variation of ice cloud that could be used to be compared with time evolution of carbon dioxide and methane in order to study the link between the formation of Polar Mesospheric Clouds PMCs and global climate change.

Chapter 6

Modeling of Irregularities in Artificially Created Dusty Space Plasmas

Dust clouds artificially created by exhaust plume from rocket engines (Bernhardt et al., 1995; Bharuthram and Rosenberg 1998) or chemical release experiments (Bernhardt et al., 2011; Holmgren et al., 1980) have been known for many years to produce effects observable on spacecraft instruments and scattering of radar signals. In recent years, several ionospheric sounding rocket experiments such as the Charged Aerosol Release Experiment (CARE)(Bernhardt et al., 2011; Rosenberg et al., 2011), have involved the release of aerosols that result in a dust cloud in the background ambient plasma which captures electrons, and produces an electron depletion and a heavy negative ion cloud that expands into the background plasma (Ganguli et al., 1993). Often, the production of small-scale plasma irregularities are associated with these experiments. For example radar echoes have been observed from the space shuttle exhaust for many years (Scales et al., 1998; Bernhardt et al., 1998; Bernhar dt et al., 2005; Bernhardt and Sulzer, 2004; Scales et al., 1994). It has been proposed that the shuttle exhaust produces a dust cloud of ice particles that charges and expands into the background plasma (Bernhardt et al., 1995). The reason is that water vapor exhaust from the rocket engine condenses into ice nanoparticles that become charged in the plasma (Wu, 1975). The electron depletion (bite-outs) after burning of the space shuttle maneuver engine was reported in many observations by Incoherent Scatter Radar (ISR) (Bernhardt et al., 1975). Associated with the expansion of the dust into the background plasma is the production of plasma irregularities that scatter the radar signal. There is a different hypothesis proposed to justify the enhancement of radar backscatter such as excitation of ion acoustic wave or dust acoustic wave, charging of ice particles in exhaust, etc. (Bernhardt et al., 1995). In general, irregularities produced by expanding ionospheric dust clouds have relevance to remote sensing of ionospheric processes as well as creation and evolution of natural and artificial dusty plasmas in space.

Natural occurring dust clouds in the lower ionosphere where Noctilucent clouds exist, are believed to produce the Polar Mesospheric Summer Echoes (PMSEs) which are the strong radar echoes that have been observed typically in the 50 MHz to 1.3 GHz frequency range in the summer polar mesosphere (Cho et al., 1992; Rapp and Lubken 2004). In general, they are certainly produced by the structures in the electron number density at the radar half wavelength. But, what is uncertain, is what causes those structures to be present and persistent over relatively long time intervals (10s-100 of milliseconds). The deep electron density depletion associated with the formation of charged ice particles in the altitude range 80-90Km, known as 'bite-outs', may be of an order of magnitude as observed in the in-situ experiments and be associated with electric field irregularities (Pfaff et al., 2001; Croskey et al., 2001; Ulwick et al., 1988; Havnes et al., 1996). Boundary layers of the order of a hundred meters or less have been observed at edge of the electron bite-outs (Ulwick et al., 1988).

The self excited dust density waves in a suspended dust cloud has been reported in a variety of laboratory plasmas experiments (Fortov et al., 2003; Arp et al., 2007). An associated electric field is also measured in the boundary of the dust cloud (Fortov et al., 2003). Several theoretical predictions has been made to validate the observed dust density waves inside the dust cloud in the laboratory experiments.

The dust boundary layer between the background plasma region of primarily ions and electrons and a dusty plasma region with electrons, ions and dust has been shown to provide the free energy for generation of plasma irregularities in the case of expansion of a dust cloud across a magnetic field due to shear driven instability in the cross-field flows (e.g. Scales et al., 2010 and references therein).

6.1 Results and analysis

Considering that an important application of this model is related to the ionosphere and ionospheric active experiments, parameter regimes associated with altitude range 250km are considered. Other parameter regimes will be discussed shortly. Temperature for both ion and electron is taken to be $T_e = T_i = 1150K$. The dust is taken to be cold here $T_d = 0$, however, thermal dust will be considered for the expanding dust cloud boundary layer described shortly $T_d > 0$. Dust particles are assumed to have radius in the range of 10-100nm and have an equilibrium charge of $Z_{eq} = -10$ to -100 (Bernhardt et al., 2011 and Rosenberg et al, 2011). Dust particles may have sizes up to 1000 nm in radius. However, the reduced range in dust radius used, which is effectively a reduction in the dust mass, was used for computational efficiency. It can be shown that it does not produce qualitative difference in the physics (Winske et al., 1995). The electron-neutral collision frequency is $\nu_{en} \approx 5 \times 10^5$ Hz. The ion-neutral collision frequency is $\nu_{in} \approx 2 \times 10^4$ Hz, also the dust-neutral collision frequency is assumed to be of order of 1 Hz. Using these parameters for the Debye length, the boundary layer scale sizes from few meters up to 100 meters are considered in this work. In this part fundamental physics associated with dust cloud boundary layer is studied and

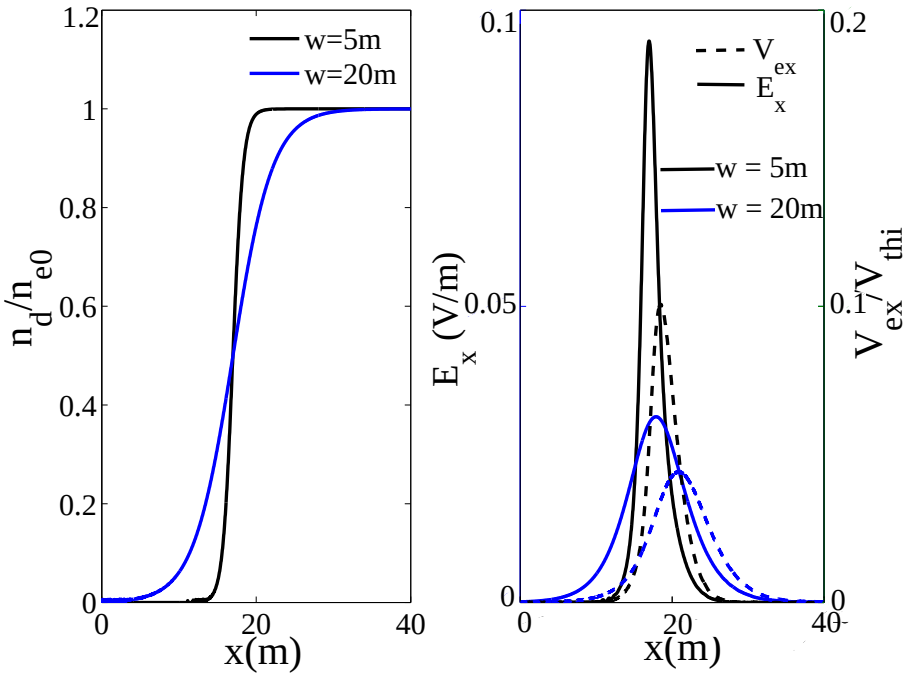

Figure 6.1: Variation of the electric field and electron flow velocity associated with the dust cloud for two different scale lengths.

detailed applications will be discussed subsequently.

Associated with the dust charging is the production of an electric field in the boundary layer. This electric field is due to the depletion of plasma in the presence of the heavy aerosol particles and causes the diffusion of electrons and ions. Therefore it can be considered as ambipolar in nature. The steady state of the electric field amplitude occurs on the timescale of the dust charging (Scales and Ganguli, 2004 a,b). This electric field is directed into the dust cloud. Therefore the dust charging produces electric fields at the boundary layer which may be considered as the free energy source for localized irregularities.

Different parameters may affect the strength of this electric field and the excitation time of irregularities. The parameters which are studied in this section are the scale length of boundary, dust density, dust radius and collision frequency. In the case of the current model parameters, this electric field is of the order of 10mV/m. The vertical electric fields have been postulated to exist in the region around NLCs and where PMSEs are generated. The observations have shown the electric field with the magnitude of 10 mV/m in this region (Pfaff et al., 2001). This is discussed in more detail in the section 6.3.2.

Figure 6.1 shows the variation of electric field and electron flow velocity for two dust cloud boundary layers using the cloud model of equation (8). This figure shows the cloud at

t=0.04s. As can be seen from this figure, the maximum of electron flow velocity is located at the middle of dust cloud where the dust density is half of its maximum. The ambipolar electric field also has a narrow structure inside the dust cloud boundary layer. The electric field energy for boundary scale lengths 2.5, 5, 10 and 20m is shown in Figure 6.2a. The electric field energy shows the growth of the waves at 0.2s, 0.4s, 0.8s and 1.4s for boundary layer scale lengths 2.5m, 5m, 10m, and 20m, respectively. The electric field energy increases in two steps. The first step which corresponds to the formation of the ambipolar electric field occurs after a short time for all boundary scale lengths. The second phase is the growth of electric field energy representing the formation of irregularities at the boundary layer that depends on the width of boundary layer. The saturation of electric field occurs at the time when the boundary starts to broaden and the source of free energy diminishes. It turns out that the scale length at the boundary layer of dust cloud is the most effective parameter on the excitation time of irregularities at the boundary layer of dust cloud. As will be shown later, other parameters also affect the excitation time of the wave, but the scale length of the dust boundary layer is the parameter which has the largest effect on this time.

It will be shown that the characteristics of the excited irregularity at the boundary layer of dust cloud matches well with the characteristics of the dust acoustic wave, as was predicted in the previous work by Scales and Ganguli (2004 a,b). The dust acoustic wave frequency is given by the expression (Shukla and Mamun, 2002):

$$\omega = \frac{kC_{ds}}{\sqrt{1+k^2\lambda_D^2}} = \frac{(2\pi/\lambda)\omega_{pd}\lambda_D}{\sqrt{1+k^2\lambda_D^2}} \tag{6.1}$$

where λ is the wavelength of the irregularity and ω_{pd} is the dust plasma frequency. For $k\lambda_D << 1$, this can be simplified to $\omega = kC_{ds}$. The case in which the dust density is equal to the background plasma density and the boundary scale length of the order of 5m is considered. To calculate the frequency spectrum of the electric field, the variation of the electric field at a point in the boundary of dust cloud is considered. The point which is used to calculate the frequency spectrum is located at a point in the boundary layer where the dust cloud has the maximum density. The variation of the dust density at this point after 6 dust plasma periods is found to be about 20 percent. Considering the small variation of dust density at this point, we expect that the frequency of the excited dust acoustic wave to be around the dust acoustic frequency calculated using Eq.(6.1) and maximum dust density. As can be seen in Figure 6.2b, the wave frequency is at the dust acoustic frequency.

One of the characteristics of the dust acoustic wave is that the fluctuation in the electron density is out of phase with the fluctuation in the dust density (D'Angelo, 1995). As can be seen in Figure 6.3, when the dust density reaches the local maximum amplitude, the electron density reaches the local minimum amplitude. This figure clearly shows the anticorrelation of the electron fluctuation relative to the dust fluctuation. It should be noted that the dust acoustic wave only stays in the dust cloud boundary region and the electric field out of this region damps out quickly.

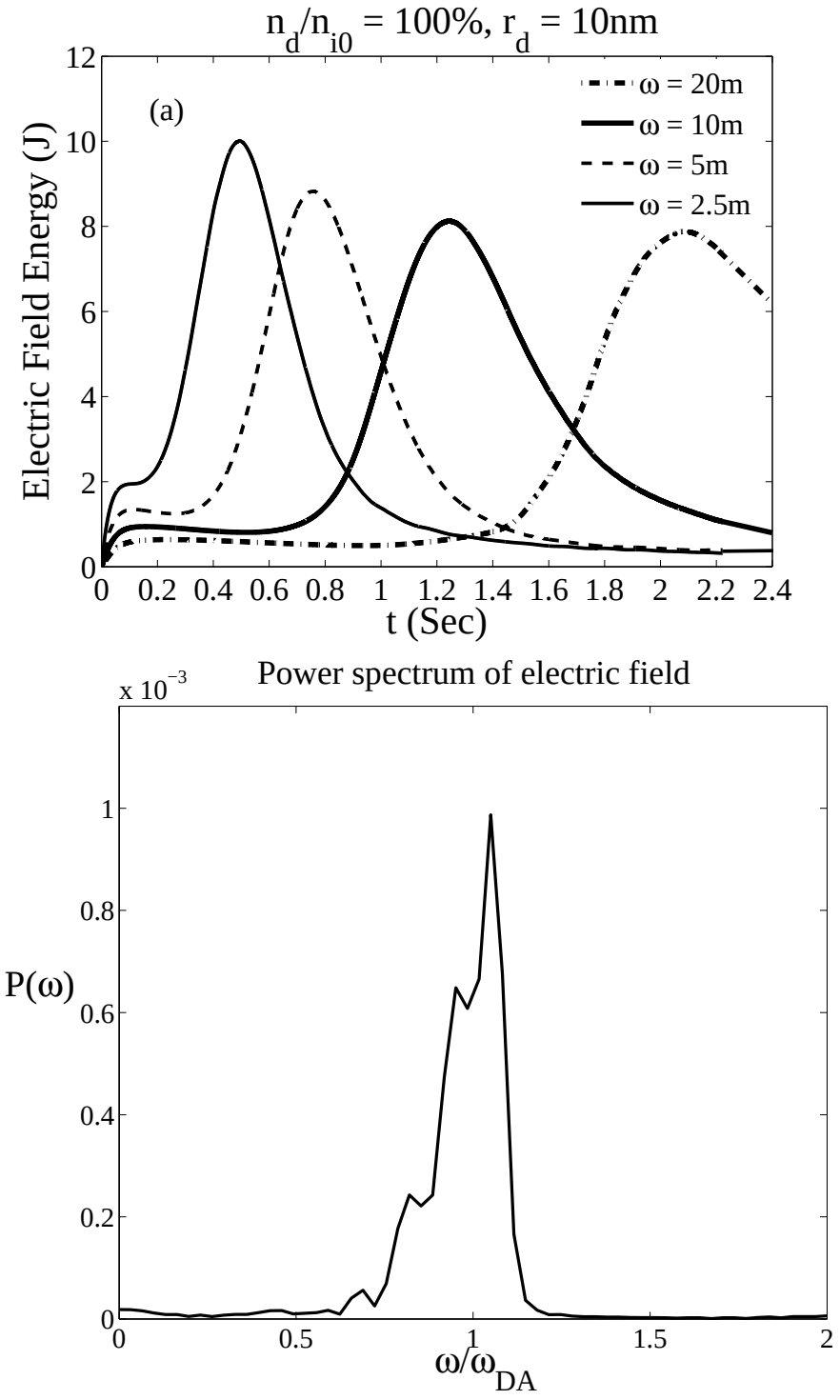

Figure 6.2: a) Electric field energy for varying boundary layer width. b) Frequency power spectrum of electric field for the case w= 5m, $n_d/n_{i0} = 100\%$. Note waves at dust acoustic frequency.

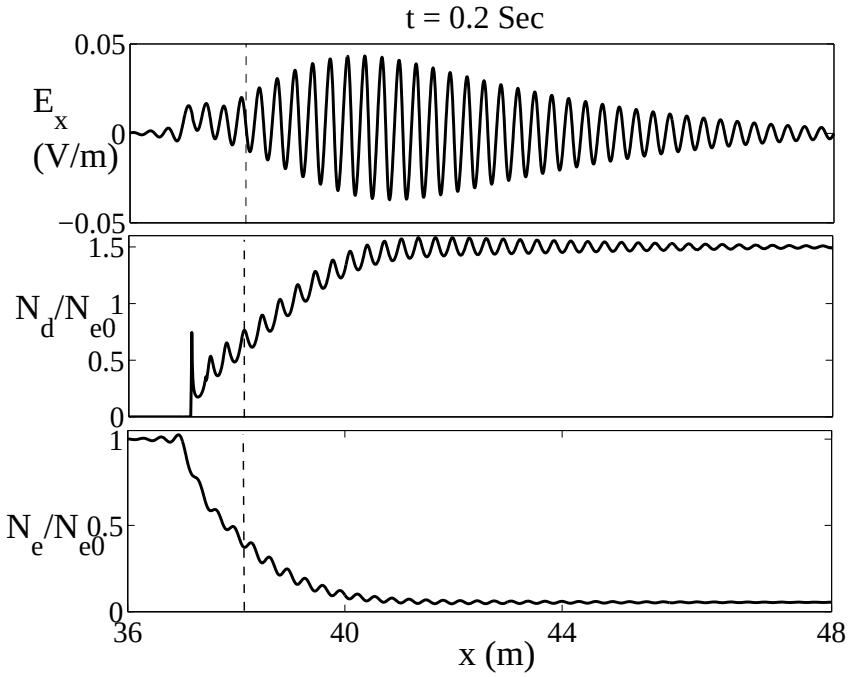

Figure 6.3: Electric field, dust density, and electron density variation in the dust cloud boundary layer showing dust acoustic wave structures.

The dust density relative to the background plasma density is another parameter expected to influence the excitation of irregularity. The dust radii is of the order of 10 nm in all cases presented in this section. As can be seen for the lower dust density case where $n_d/n_i = 80\%$, reduction in both electron and ion density can be observed with the electron density depletions commonly referred to as electron 'bite-outs'. According to Figure 6.4, the electron flow created in response to the electric field exists at the boundary layer of the dust cloud and its amplitude depends on the dust density. Increasing dust density from 80 percent of background plasma density to 100% and 150% enhances the depth of the electron "bite-outs" as well as electron flow velocity in the dust cloud boundary. In fact for the larger dust density, the depletion in the electron density is deeper and electric field at the boundary is stronger. Therefore the electron flow speed reaches the larger amplitude for the higher density case. A small ion flow also exists and is only several percent of V_{thi}. The localized flow may be significantly reduced by the nonlinear evolution of irregularities produced by free energy available in the flows. An important quantity that should be compared with these flow velocities is the dust acoustic speed which is given by (Shukla and Mamun, 2002):

$$C_{da} = \omega_{pd}\lambda_{Di} = Z_d v_{ti}\sqrt{\frac{n_d(x)m_i}{n_i(x)m_d}} \tag{6.2}$$

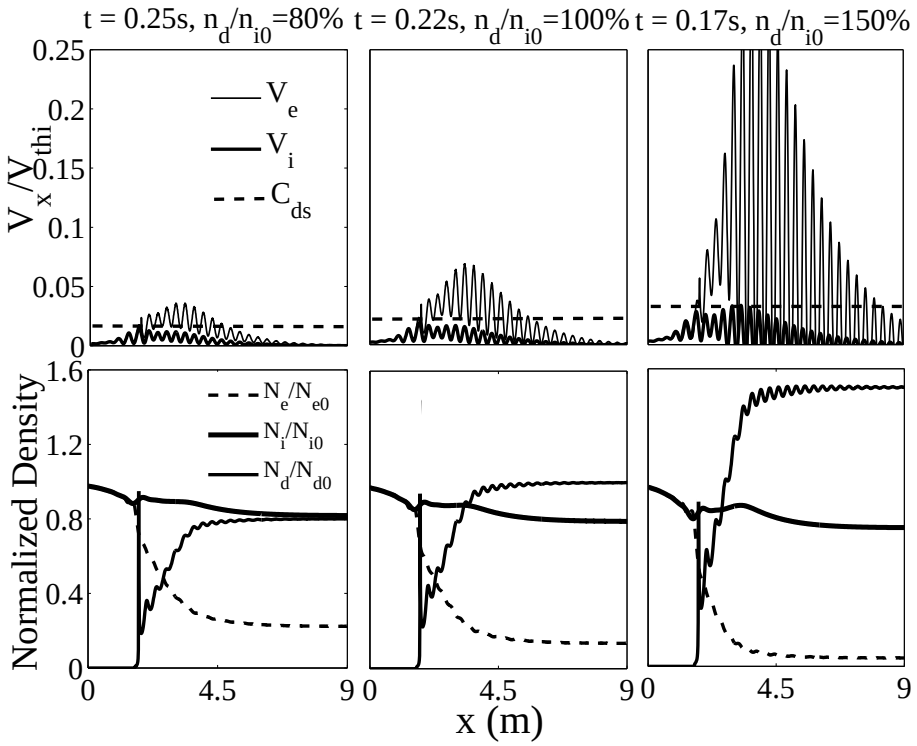

Figure 6.4: Behavior of normalized plasma flows and densities at the time the irregularities start to develop in the charged dust cloud boundary layer with varying dust density. Note in each case when V_e exceeds C_{da} dust acoustic waves begin to grow leading to irregularities in the dust cloud boundary layer.

where λ_{Di} is the Debye length of dusty plasma, ω_{pd} is the dust plasma frequency, Z_d the dust charge and m_d the dust mass. The dust acoustic speed is of the order of 1m/s for the typical mesospheric parameters. Due to variation of dust density over the cloud region, dust plasma frequency and dust sound speed have spatial dependence. The dashed line in the figure shows the dust acoustic speed. In all three cases the localized flow exceeds the dust sound speed before the wave starts to grow. This figure shows the wave at approximately about 0.25s, 0.22s and 0.17s for the dust densities 80%,100% and 150% of background plasma density, respectively. Therefore increasing dust density increases the equilibrium electron flow and reduces the time of dust acoustic wave to develop in the charged dust boundary. The formation of the dust acoustic wave structure can be seen in the dust and electron density as well as electron velocity. The irregularity wavelength varies from 20 to 45cm which corresponds to the radar frequency range 350MHz to GHz at the Bragg scale for the parameters considered. Considering the variation of dust acoustic speed with the dust density, the electron flow velocity reaches the corresponding dust acoustic speed in all three cases and then dust acoustic waves are excited. By increasing dust density, the acoustic speed also increases and it can be seen from the figure, the electron velocity achieves larger amplitude which corresponds to higher dust acoustic speed and then dust acoustic wave structures start to develop.

The effect of dust density variation on the electric field is shown in Figure 6.5. All four figures are at the same simulation time and show a stronger electric field for the higher density case. This figure also shows that for the higher dust density, the dust acoustic irregularities in the electric field form faster because the electron flow exceeds the threshold value (the dust acoustic speed) in a shorter time. It turns out that for the parameters used in the Figure 6.5, the dust density should be more than 60 percent of the background plasma in order to produce a strong enough electric field for the electron electron flow velocity to exceed the dust sound speed and excite the dust acoustic waves in the boundary layer.

The variation of equilibrium boundary layer with increasing dust radius is investigated in Figure 6.6. Three values are shown $r_d = 15$, 20, and 30 nm. Increasing the dust radius increases the depth of electron and ion depletion as well as electron flow velocity variations. As can be seen for all three cases electron flow reaches to threshold value which is larger than the dust acoustic speed. For the larger dust particles, irregularities start to develop faster. The reason is that increasing the dust radius enhances the depletion in the electron density and enhances the ambipolar electric field in the boundary region which is the generating source for the waves.

6.2 Instability analysis

A simplified analysis is provided here to provide a somewhat more quantitative validation of irregularity generation in the previous section. The simple local linear analysis consists of plasma drifting with respect to the dust particles. This is a reasonable assumption according

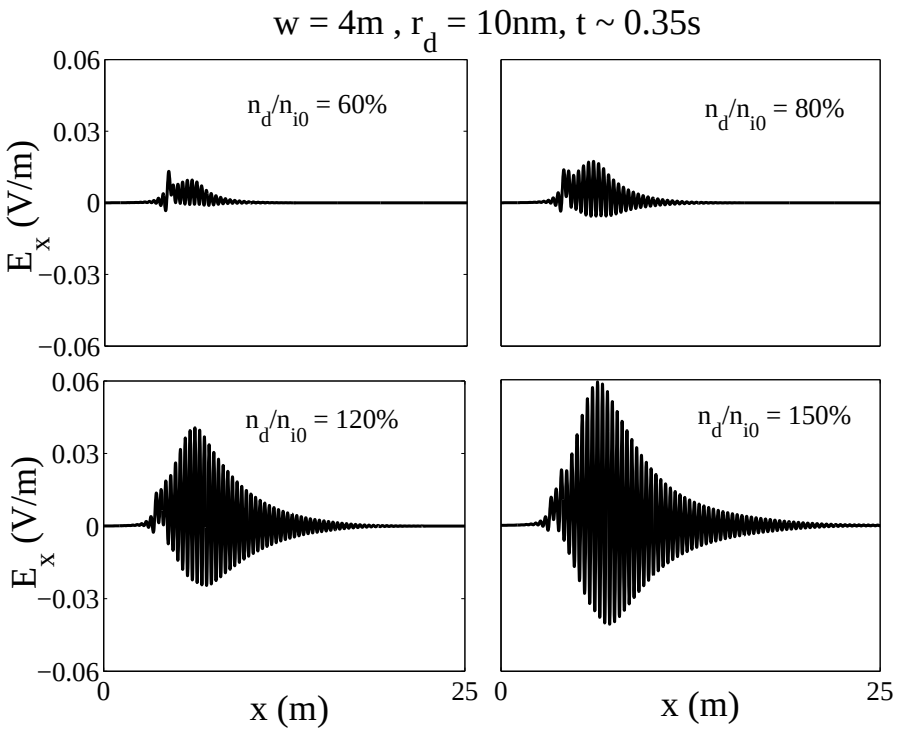

Figure 6.5: Variation of electric field strength with dust density.

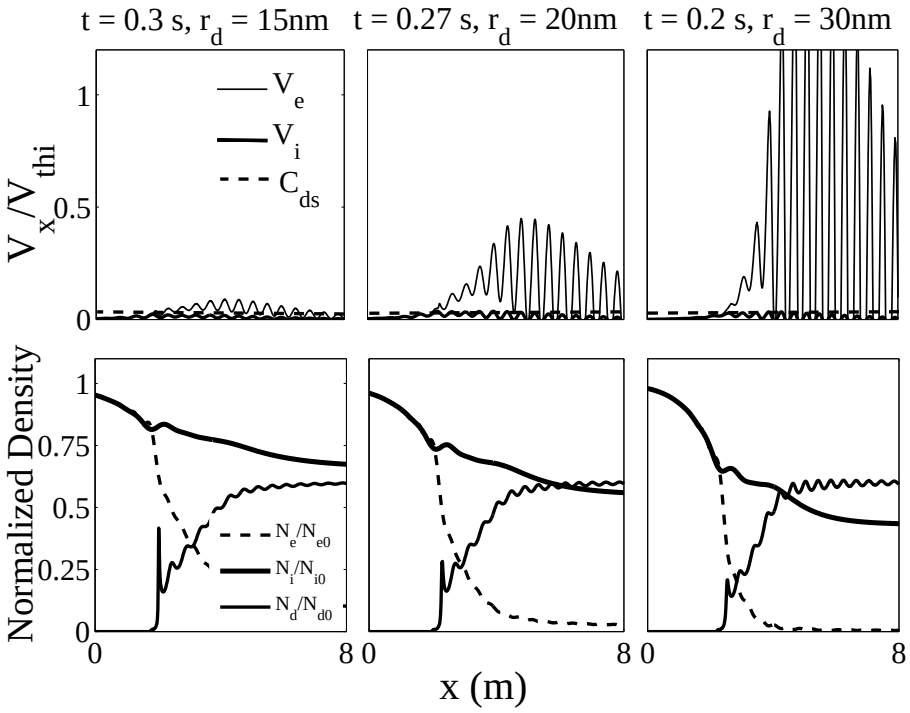

Figure 6.6: Variation of plasma and dust densities and plasma velocities with dust radius. When V_e exceeds C_{da} dust acoustic waves develop in the boundary layer.

to the result presented in the previous section where electron flow velocity exceeds the dust acoustic speed and then the waves start to develop. Using standard plasma instability theory, the linear dispersion relation for the irregularities in plasma consisting of electrons, ions and charged dust can be written as:

$$1 + \chi_e + \chi_i + \chi_d = 0 \tag{6.3}$$

where $\chi_{e,i,d}$ denotes the electron, ion and dust susceptibilities. According to the simulation set up, electrons and ions are assumed to have Maxwellian velocity distribution and drift relative to the dust. The electron and ion susceptibilities can be written in this form:

$$\chi_e = \frac{1}{k_x^2 \lambda_{De}^2}\{1 + \xi_e Z(\xi_e)\}\{1 + \frac{i\nu_{en}}{\sqrt{2}kv_{te}} Z(\xi_e)\}^{-1} \tag{6.4}$$

and

$$\chi_i = \frac{1}{k_x^2 \lambda_{Di}^2}\{1 + \xi_i Z(\xi_i)\}\{1 + \frac{i\nu_{in}}{\sqrt{2}kv_{ti}} Z(\xi_i)\}^{-1} \tag{6.5}$$

where $\lambda_{De,i}$ is the electron (ion) Debye length, Z is the Fried-Conte plasma dispersion function and $\xi_{e,i} = (\omega - k_x v_{de,i} + i\nu_{e,in})/\sqrt{2}k_x v_{te,i}$. According to Figure 6.4 and 6.6, the electron flow velocity exceeds the dust acoustic speed that may be considered as a source for dust acoustic wave generation which is consistent with earlier work on the generation of the dust acoustic instability in such a configuration (Scales and Ganguli, 2004 a,b). Considering that this flow speed is much less than ion thermal velocity, the flow itself would not be expected to drive ion waves or waves of higher frequency in the dust boundary layer. The dust is assumed to be cold; therefore, the dust susceptibility is taken to be

$$\chi_d = -\frac{(\omega_{pd})^2}{\omega(\omega + i\nu_{dn})} \tag{6.6}$$

where ω_{pd} is the dust plasma frequency. Figure 6.7 shows the solution of dispersion relation (6.3) based on the parameters used in the simulation for the dust density 100% of background plasma density and it can be seen the maximum growth rate is of the order of $0.001\omega_{pd}$. Considering that the irregularity is about $k_x\lambda_{Di} = 0.5$, the calculated growth rate from the electric field energy from the computational model is roughly $3 \times 10^{-3}\omega_{pd}$, which shows reasonable agreement. The analytical model may well underestimate the local growth rate in the simulation boundary layer as it evolves. This can be justified by considering that in the instability analysis only the flow velocity created by the electric field in the boundary layer is included and the effect of density gradient is overlooked. Therefore including spacial inhomogeneities in the dispersion relation may give us a better estimation for the growth rate which will be considered in future work.

It can be noted that a relatively broad spectrum of wave numbers are unstable with the maximum growth rate $k_x\lambda_{Di} \sim 1$. The wavelengths of irregularities are quite broad with

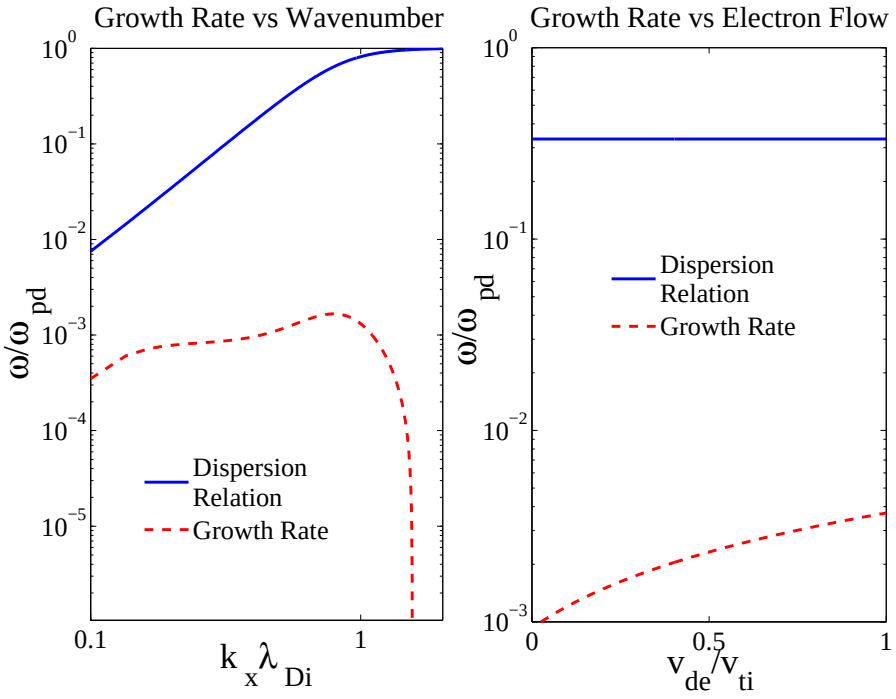

Figure 6.7: Linear growth rate for dust acoustic wave generation at the boundary of dust cloud associated with the simulation model results.

roughly $0.1 < k_x\lambda_{Di} < 2$ and for the ion Debye length of the order of centimeters, this implies the irregularity scale size roughly from meters to few centimeters which is consistent with the natural irregularity scale size observed in the mesospheric region as will be discussed later.

The threshold electron velocity to excite the dust acoustic wave for the 100 percent dust density to the background plasma density is about $0.05V_{thi}$ which is about two times of the dust acoustic speed. When the flow velocity reaches this value, the dust acoustic wave starts to propagate inside the dust cloud. Figure 6.7 which corresponds to the simulation parameters for the 100 percent dust density to the background plasma density, also shows that the electron flow can be an effective way of producing irregularities when $v_{de}/v_{thi} > 0.06$. This is on the order of $2C_{da}$. The electron flow in Figure 6.4 and 6.6 are in the range of $2-20C_{da}$ that can destabilize dust acoustic waves according to the solution of the dispersion relation. Therefore the solution of the dispersion relation shows that the electron flow can destabilize dust acoustic waves which were shown in the computational results in the last section and validate the results of computational model.

6.3 Applications

The most important consideration to the applicability of the present irregularity generation is the lifetime of the dust boundary. The parameter that determines this is the dust diffusion time. The dust diffusion time can be approximated by

$$\tau_{diff} \approx \frac{m_d \nu_{dn}}{KT} w^2 \tag{6.7}$$

where w is the scale length of boundary (Lie-Svendsen et al., 2003). For typical quantities used in the simulation, this time is predicted to be of the order of 10^4 s for ionospheric parameters. This time is much longer than the time irregularities needs to develop as described earlier. Therefore, dust irregularity can grow within the lifetime of the boundary layer.

6.3.1 Aerosol release space experiments

A rocket experiment has been conducted to test the theories of radar scatter from artificial charged dust clouds and also study the basic physics associated with natural dust clouds such as Noctilucent clouds. The Charged Aerosol Release Experiment (CARE) was conducted at the altitude region of 280 km and radar echoes and electron depletion were observed associated with this experiment (Bernhardt et al., 2011). This behavior was also observed in the past experiments regarding the space shuttle exhaust (Scales et al., 1994) and scattering of radar signals is believed to be produced because of the irregularities associated with the electron depletion shortly after release. The backscatter radar enhancement from the space

shuttle exhaust has been proposed to be due to two processes for the interaction of shuttle exhaust with background atmosphere (Bernhardt et al., 1995). The proposed expansion-cooling-condensation process that transforms the exhausted water vapors from the space shuttle engine to the ice is consistent with the assumption of the present work. These ice particles have been shown to have approximately 6 nm size and are negatively charged by pick up of ionospheric electrons (Bernhardt et al., 1995). Due to the expansion speed much higher than ion thermal velocity during this experiment, the excitation of dust acoustic wave as the cause of coherently scatter radar signals was overlooked according to the streaming instability analysis. It has been propounded by Bernhardt et al., (1995) that for the right parameter regime, the dust acoustic wave can be excited at the boundary region of the expanding dust cloud.

The dust acoustic wave was proposed as the generation source of radar echoes in a number of experiments. Therefore the dust acoustic wave excitation at the boundary layer of the expanding dust cloud that has direct application to such active space experiments will be considered here.

In this section, the excitation of dust acoustic waves at the boundary layer of an expanding dust cloud is studied which has the application to aerosol release experiments (Bernhardt et al., 2011; Rosenberg et al., 2011). The Gaussian dust cloud is considered in this section which diffusively expands by making $T_d >> T_e = T_i$. The dust density is assumed to be about 40 times of background plasma density which is reasonable for the early time after the aerosol release. Temperature for both ion and electron is taken to be $T_e = T_i = 1150K$. Dust radius is assumed to be 20nm. The electron-neutral collision frequency is $\nu_{en} \approx 5 \times 10^5$ Hz. The ion-neutral collision frequency is $\nu_{in} \approx 2 \times 10^4$ Hz, also the dust-neutral collision frequency is assumed to be of order of 1 Hz. Figure 8 shows the excited dust acoustic waves at the boundary layer of dust cloud. The location of peak of the ambipolar electric field formed at the boundary represents the leading edge of the dust cloud and moves as the dust cloud expands out. Therefore the maximum of electric field can be used as a marker to determine the distance that dust dust has expanded with respect to its initial location. The dust cloud expands out about 150m in 0.1s. The expansion speed of the dust cloud is of the order of few times the ion thermal velocity speed which is comparable to the expansion speed in the CARE experiment (Rosenberg et al., 2011). Figure 8.a and b show the electron flow inside the dust cloud boundary layer during the expansion. As can be seen in Figure 8.c, when the electron flow reaches the dust sound speed, the dust acoustic wave structures start to form in the electric field and electron flow velocity. The bottom panel also shows the excited and spread wave in the dust cloud region.

6.3.2 Polar Mesospheric Summer Echoes (PMSEs)

Polar Mesospheric Summer Echoes (PMSEs) are the strong echoes in the height range 80-90 km. In-situ experiments have shown the existence of aerosol and reduction of electron

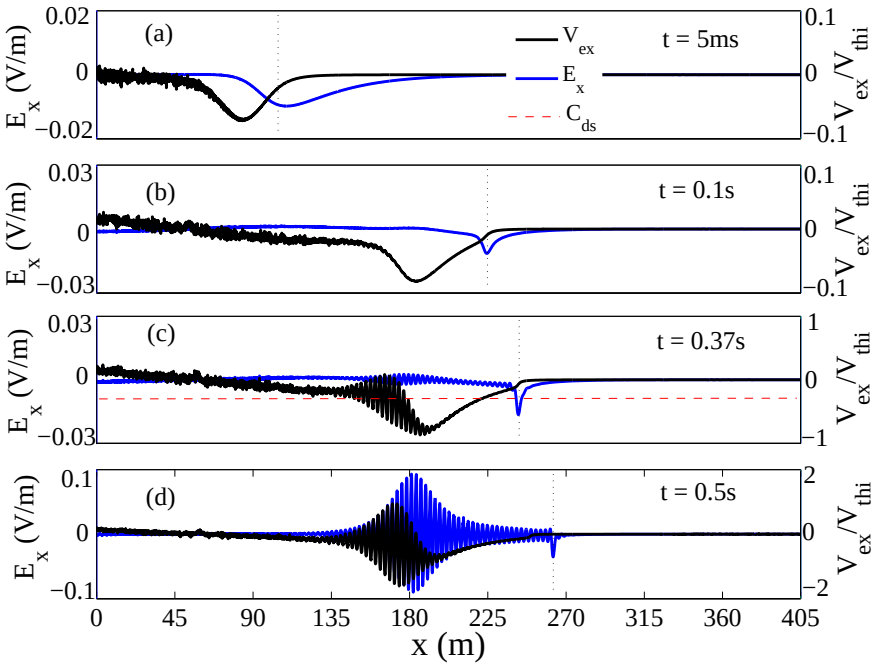

Figure 6.8: Moving dust clouds through the background plasma with the drift velocities 0.1, 0.5, 1 and 2Vthi

density or electron "bite-outs", up to 90% or more in the PMSE source region (Reid 1990; Pfaff et al., 2001; Croskey et al., 2001; Ulwick et al., 1988; Havnes et al., 1996). These density structures may extend several kilometers in altitude with the gradient scale lengths may be the order of 10s of meters or less. The boundary layer of the charged aerosol cloud is the boundary between ambient background plasma of electron and ion and the region which contains electron, ion and charged heavily aerosols. This inhomogeneous boundary layer may be considered as a region with free energy sources to produce plasma irregularities in the boundary that may lead to the PMSEs which is consistent with the assumption of this work (Scales and Ganguli, 2004a, b).

An in-situ measurement of electric field at PMSEs altitude was done by (Pfaff et al., 2001). The two electric field structures at the altitudes about 83-86 km were observed. The top structure which centered at 85.5km revealed a well defined electric field structure consisting of low frequency waves in the range of 7-15Hz. The region of these waves is consistent with the region of the electron depletion (bite-outs) and detected charged aerosol particles (size 1-10nm). The high frequency electric field structure also was observed near 1 KHz centered at 83.5km believed to correspond to the NLCs.

In recent years there has been an extensive effort to measure the size and density of ice particles in the mesosphere through the in-situ measurement by rockets (Robertson et al., 2009). Dust density 3×10^3 cm^{-3} and radius 3nm have been observed in the recent in-

situ experiments. Considering the application of this model to the mesosphere, mesospheric parameters are considered (Scales and Ganguli, 2004 a,b). The PMSE irregularity generation region is in the altitude near 85Km and plasma density $n_e = n_i \equiv n_0 \sim 10^9 \mathrm{m}^{-3}$. Temperature for both ion and electron is taken to be $T_e = T_i = 150K$. The ion-neutral collision frequency is of the order of 10^5 Hz. Proton hydrates with mass between 59 and 109 are the dominant ion compositions at this height range. O_2^+ ions are more numerous than NO^+. NO^+ and O_2^+ together can be slightly more than the proton hydrates at 88km and above (Kopp et al., 1985). Dust particles are assumed to have radius of the order of a few nanometers and have an equilibrium charge of one electron, i.e. $Z_{eq} = 1$ (Lie-Svendsen et al., 2003). The electron-neutral collision frequency to electron plasma frequency is $\nu_{en}/\omega_{pe} \approx 1$, also the aerosol-neutral collision frequency is assumed to be of order of one tenth dust plasma frequency.

According to linear theory, the presence of collisions between the dust and a neutral gas background reduces the growth rate of the instability. The approximate dust-neutral collision frequency can be calculated by the following expression when a hard sphere model is used (Cho et al., 1992)

$$\nu_{dn} \approx r_d^2 n_n \frac{m_n}{m_d} v_{tn} \tag{6.8}$$

where n_n, m_n and v_{tn} are the neutral density, mass and thermal velocity, respectively. Using typical mesospheric values, $n_n \sim 10^{20} m^{-3}$, $m_d/m_n \sim 10^5$ and $T = 150$K, yields $\nu_{dn} \sim 100$Hz which compares with $\omega_{pd} \sim 10$Hz. Therefore the dust-neutral collision frequency to dust plasma frequency ratio is of the order of 10 using mesospheric parameters. Figure 6.8 shows the dust-neutral collision effect on the electric field and the development of the dust acoustic waves for different dust-neutral collision frequencies. For the small value of dust-neutral collision frequency $\nu_{dn} = 2$Hz, dust acoustic wave starts to grow at the boundary layer and then propagates toward the middle of cloud. As can be seen in Figure 6.8, by increasing ν_{dn} to 20Hz, the wave starts to grow but the electric field amplitude is smaller in comparison with the previous case and the wave damps out faster. Using $\nu_{dn} = 100$Hz which is of the order of the collision frequency calculated at mesospheric altitudes, the excited dust acoustic wave fluctuations in the electric field are quite weak and are confined close to the boundary region. For the higher values of ν_{dn} such as 1000Hz, the wave does not grow and even exist inside the boundary layer due to high collisionality between dust and neutral particles.

Figure 6.9 shows the computational results of the electric field, dust cloud and electron and ion densities after $t = 5.2\tau_{pd}$ which corresponds to $t \sim 0.5s$. Dust density and radius are assumed to be 4×10^9 m^{-3} and 3nm, respectively. Dust collision frequency is about 10Hz. The propagation of dust acoustic waves away from the boundaries ultimately result in spiky electric field irregularities throughout the dust cloud. This is of a similar structure as observed in past experiment (Pfaff et al., 2001). Although the electric field calculated using the computational model is comparable to the measured electric field in the in-situ

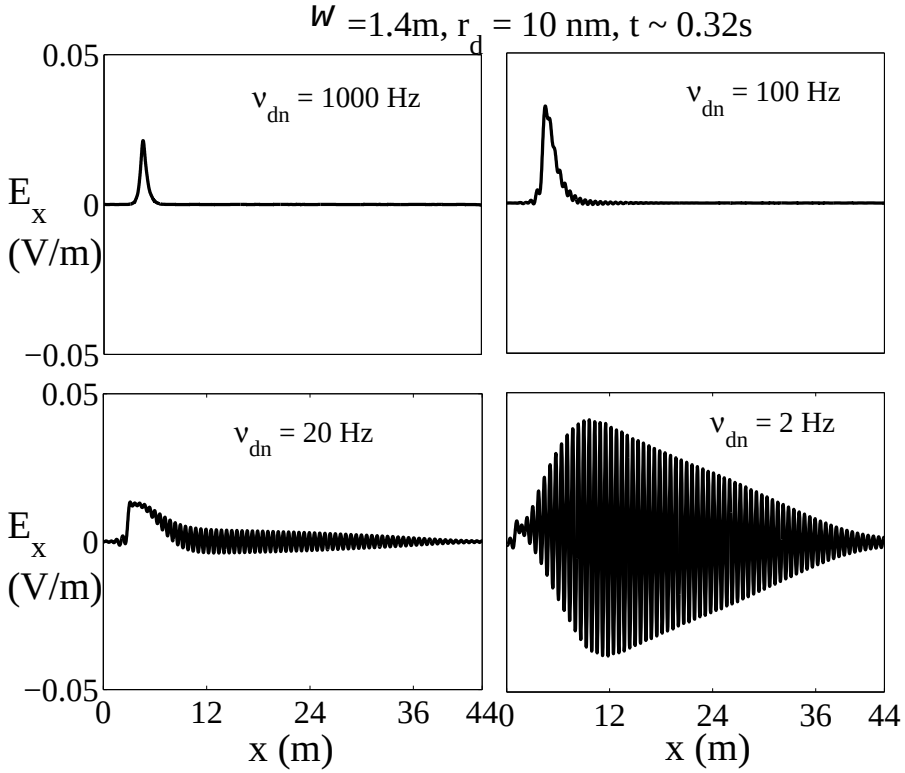

Figure 6.9: Dust-neutral collision frequency effect on the development of irregularity in the dust cloud boundary layer.

experiment, it should be noted that by increasing the dust-neutral collision frequency to the value at mesospheric altitudes, $\nu_{dn} \approx 100$Hz, these waves damp out fast as shown in Figure 6.8. The electron irregularity amplitude is of the order of 7 percent of the maximum electron density. Both radar echoes and in-situ turbulence during STATE 3 maximized at the the edge of steep electron bite-outs with density gradient scale length of the order of hundred meters (Ulwick et al., 1988). The sharp boundary could be as a result of steep temperature gradient that causes the drop of temperature to a value below what is needed for the formation of ice particles (Reid 1990). As it was discussed in the last section, the frequency of this wave is the dust acoustic wave frequency which is about 10Hz for the mesospheric parameters and is close to the measured frequency in the in-situ experiment. Considering the dust sound speed in the order of 1m/s using mesospheric parameters, the Doppler data measured in the experiment estimates 2m/s upward PMSE motion at 500MHz which is consistent with gravity wave energy propagation through DAW (Hall and Rottger, 2001). As mentioned in the last section, fluctuations in the dust density and electron density are out of phase which is consistent with experiments that found that electron density and dust density are anti-correlated in this region (Rapp and Lubken, 2004; Havnes et al., 1996).

6.3.3 Laboratory plasma

Self-excited dust density waves in the boundary region of dust cloud has been observed in laboratory plasma experiments (Fortov et al., 2003; Arp et al., 2007). Directed plasma flow that propagates into the dust cloud is argued as the generation source of the self-excited dust density waves (Arp et al., 2007). The experiments are also done under microgravity conditions which consistent with the simulation configuration. It has been shown in (Fortov et al., 2003) that existence of a permanent electric field is the necessary condition to excite the dust acoustic wave at the diffusive edge of the suspended dust cloud. This is in agreement with the computational results shown in this paper. The excitation of dust acoustic wave in the laboratory plasma has been shown in many experiments but there has been no self-consistent model of the excitation process of this wave inside the dust cloud in vacuum chamber. The model and results shown in this paper can be generalized to these types of experiments as well. It has also observed during experiments that the wave originated in the upper part of the dust cloud and then propagates downward which is in agreement with our model results.

In the laboratory plasma, the neutral density is larger and the dust grains are about 1000 times larger which gives a mass 10^6 larger in comparison with the plasmas in the mesosphere and ionosphere considered here. Therefore, this results in the smaller wavelengths for the generated DAW in laboratory plasma. Considering that pressure used in lab experiments is comparable to the pressure in ionosphere, the frequency would remain about the same.

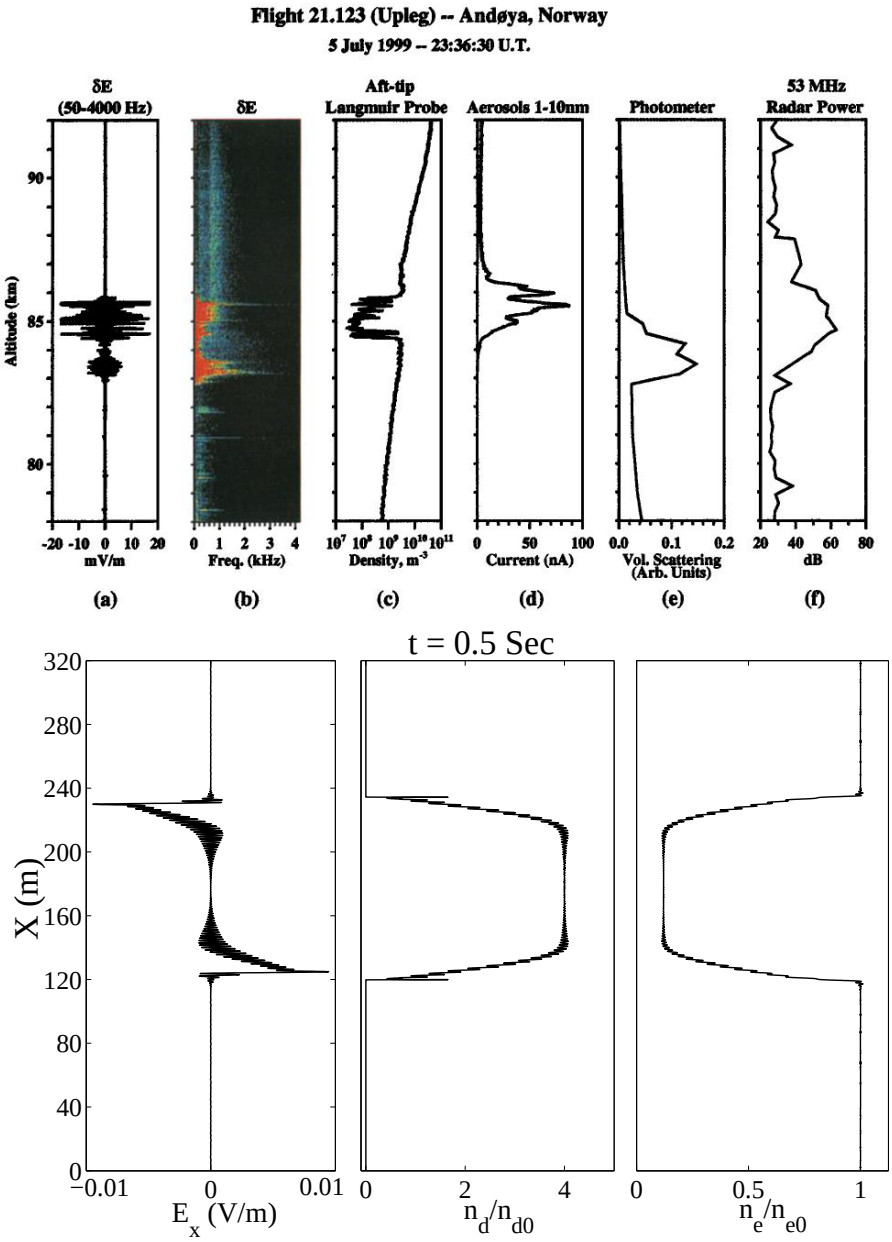

Figure 6.10: Electric field, dust, electron, and ion density associated with irregularity generation at the dust cloud boundary. Note spiky electric field structure created inside the dust cloud due to the dust acoustic waves and is of the order of 10mV/m and frequency range about 10Hz. a) experimental data b) computational results.

6.4 Conclusions

The inhomogeneity at the boundary of a dust cloud and background plasma was proposed as the possibility for providing free energy to generate dust acoustic waves that may cause plasma irregularities with applications to space and laboratory experiments. Computational and analytical models were provided to study the development of these irregularities. It turns out that electric fields generated at the boundary in response to the electron bite-outs during the dust-charging process, produce electron flows inside the dust cloud. When the amplitude of the excited electron flow exceeds the dust sound speed, dust acoustic waves will be formed and propagate throughout the dust cloud. Various parameters such as electron flow speed at the boundary layer, frequency spectrum of electric field and instability threshold were used to characterize and validate the wave characteristics. Anti-correlation of fluctuations in the dust and electron densities was observed. The growth rate from the linear theory and computational model were compared to validate that the excited plasma flow in the boundary can generate the observed dust acoustic waves. The application of these results to the naturally created dust cloud in the space to polar mesospheric summer echoes were discussed in some detail. The possibilities and a restriction of the present mechanism to be applied to mesospheric applications such as PMSE has been discussed. It was shown that for high collision frequencies, the waves may be very weakly excited (or even quenched) and confined to the boundary layer. This would possibly produce both significant electric field fluctuations and electron density fluctuations propagation throughout the cloud as described here. It would therefore be useful for future in-situ space experiments to try to investigate the generation of dust acoustic waves in measurements through the probing near the leading edge of the expanding cloud. More laboratory dusty plasma experiments under the micro gravity conditions may further expand upon the conclusions presented here.

Chapter 7

Signatures of Positive Dust in Mesospheric Dusty Plasmas

This section is based on the experimental data observed during the 2007 ECOMA/MASS campaign and the conclusion made by Robertson et al., (2009) that the positive dust particles observed were possibly formed by nucleation on the cluster ions. First, a computational model with continuous charging models based on the Orbital-Motion-Limited (OML) approach (Bernstein and Rabinowitz, 1959) and also the Natanson model (Natanson, 1960; Robertson and Sternovsky, 2008) is introduced. The correlation and anti-correlation of electron, ion and dust density fluctuations are investigated using the proposed hypothesis for the presence of positive dust particles observed during the 2007 ECOMA/MASS campaign (Robertson et al., 2009). The important similarities between the simulation results and experimental data is discussed. Afterwards, as an application, the effect of positive dust particles on the electron irregularity amplitude during PMSE radiowave heating is studied. Finally a summary and conclusion is provided.

The ECOMA project (Existence and Charge state Of Meteoric smoke particles in the middle Atmosphere) was conducted in 2007 and aimed to measure in-situ the number densities of both charged and uncharged aerosol particles in the mesosphere and lower thermosphere (Brattli et al., 2009). Total negative charge density consisting of negatively charged dust particles and electron density measured by the ECOMA and Faraday instruments, respectively, was $4 - 5 \times 10^9$ m^{-3}. The negative charge density was more than the positive density measured by the positive ion probe which violates the charge quasi-neutrality condition. A computational model developed by Lie-Svendson et al. (2003) was incorporated to study under what conditions both the reduction in positive ion density and formation of positively charged smoke particles can be expected. It turns out that both processes need extreme circumstances to happen. This argument also has been made by Brattli et al (2009) that positively charged, small (< 2 nm) particles must have existed and been undetected by all the charged particle instruments. To solve the problem of the ECOMMA campaign and

measure smaller charged particles, a new instrument called MASS (Mesospheric Aerosol Sampling Spectrometer) which is a multichannel mass spectrometer for charged aerosol particles was incorporated and used in the 2007 ECOMA/MASS campaign. Positive dust particles in the mesosphere were detected in the recent in-situ measurements. Significant numbers of positively charged aerosol particles of any size measured in the recent experiment are unexpected from the standard theory of aerosol charging in plasma (i.e. Lie-Svendson et al., 2003). Considering that negative dust particles observed in the experiment had a radii less than 3 nm coexisting with small positive particles, this charge distribution is not consistent with the theory of plasma charging, since the ion capture by larger negative dust particles is more likely than the attachment of ions to the small neutral particles. The first possibility proposed by Robertson et al., (2009) to justify the presence of positive dust particles is an enhanced photoemission current. But, the photoemission process for the nanometer sized particles is very small due to small absorption cross section and large work function of ice. The second possibility of the positive dust particles formation is that the icy particles may be contaminated by Na or Fe that can significantly lower the work function. It has been shown that even enhanced photoelectron emission rate is much lower than the electron capture rate however. The third possibility for the positive particles is that the particle grow from small molecular ions or cluster ions and become neutral by capturing electron as they grow. The particle may later charge negatively by collecting an additional electron. The nucleation process of ice particles in the mesosphere was studied in more detail by Gumbel and Megner, (2009). Condensation on meteoritic smoke particles has also been proposed as an alternative scenario for nucleation which requires a minimum particle radius near 0.5 nm (Megner et al., 2008; Gumbel and Megner, 2009; Winkler et al., 2008). It turns out that nucleation on the smoke particles has two major restrictions. Smoke particles should be larger than the critical radius. Surface parameter is another factor which determines the capability of the smoke particle surface to absorb water vapor and form water ice particles. Low meteoritic smoke densities in the summer and high possibility of charging negatively for small particles formed on these condensation nuclei also impose a restriction on this hypothesis to account for the observation of positively charged particles. It has been shown that problems which arise for the ice particle formation on the smoke particles can be avoided by the nucleation on cluster ions. The only limitation attributed to this process is the competition step between particle growth (the addition of water vapor) and recombination with the surrounding electrons. This is because the neutral particle formed by the recombination of ion clusters with a surrounding electron implies the neutral critical radius condition and impacts the growing ice embryos. Therefore for the nucleation on the cluster ion, growth must lead to a particle size beyond the critical radius before the recombination with electrons occurs which takes a few minutes for typical D-region conditions (Gumbel and Megner, 2009).

7.1 Computational Model

A one dimensional hybrid computational model is incorporated to study time evolution of the fluctuations in the electron and ion density for growing ice embryos at mesopause altitudes. In this model electrons and ions are treated as fluid and dust particles are treated as Particle in Cell (PIC) which allows for a range of dust particle mass and charges (Scales, 2004; Chen and Scales, 2005; Mahmoudian et al., 2011). Two charging models are adopted in this work for comparison. Dust particles are considered to charge up by collecting electrons and ions embodied by the dynamical charging equation which is given by:

$$\frac{dQ_d}{dt} = I_e + I_i \tag{7.1}$$

where I_e and I_i are the currents onto each individual dust particle by electron and ion flux and Q_d denotes time-varying charge on the dust grain.

For the first model, continuous charging is considered and the electron and ion current on the negative and neutral dust particles ($Z \leq 0$) based on the Orbital-Motion-Limited (OML) model are given by (Bernstein and Rabinowitz, 1959; Shukla and Mamun, 2002; Cui and Goree, 1994):

$$I^{\mathrm{OML}}_{\mathrm{e,Z\leq 0}} = \sqrt{8\pi} r_{\mathrm{d}}^2 q_{\mathrm{e}} n_{\mathrm{e}} v_{\mathrm{te}} \exp(-q_{\mathrm{e}}\phi_{\mathrm{d}}/KT_{\mathrm{e}}), \tag{7.2}$$

$$I^{\mathrm{OML}}_{\mathrm{i,Z\leq 0}} = \sqrt{8\pi} r_{\mathrm{d}}^2 q_{\mathrm{i}} n_{\mathrm{i}} v_{\mathrm{ti}} (1 - q_{\mathrm{i}}\phi_{\mathrm{d}}/KT_{\mathrm{i}}), \tag{7.3}$$

For positive dust particles ($Z > 0$), the ion and electron currents are given by (Shukla and Mamun, 2002):

$$I^{\mathrm{OML}}_{\mathrm{e,Z>0}} = \sqrt{8\pi} r_{\mathrm{d}}^2 q_{\mathrm{e}} n_{\mathrm{e}} v_{\mathrm{te}} (1 - q_{\mathrm{e}}\phi_{\mathrm{d}}/KT_{\mathrm{i}}), \tag{7.4}$$

$$I^{\mathrm{OML}}_{\mathrm{i,Z>0}} = \sqrt{8\pi} r_{\mathrm{d}}^2 q_{\mathrm{i}} n_{\mathrm{i}} v_{\mathrm{ti}} \exp(-q_{\mathrm{i}}\phi_{\mathrm{d}}/KT_{\mathrm{e}}), \tag{7.5}$$

Here, r_d is the dust radius, $v_{te}(i)$ electron (ion) thermal velocity and ϕ_{d} dust floating potential. The currents for capture of electrons and ions by aerosol particles are derived by Orbital-Motion-Limited (OML) theory (Bernstein and Rabinowitz, 1959) and Natanson (1960).

The second model considered is the modified Natanson model. The Natanson model has recently been modifed by Robertson and Sternovsky, (2008) where they adopted the effect of the induced-dipole force for the case of attractive aerosol particles. It has been shown that the induced-dipole force increases ion collection rates by about a factor of 2 for the smallest aerosol particles (Brattli et al., 2009). Electron and ion currents for neutral aerosol particles

($Z = 0$) could be represented as follows (Natanson, 1960; Rapp, 2000; Lie-Svendsen et al., 2003; Brattli et al., 2009):

$$I^{\mathrm{NAT}}_{\mathrm{e,Z=0}} = \sqrt{8\pi} r^2_{\mathrm{d}} q_{\mathrm{e}} n_{\mathrm{e}} v_{\mathrm{te}} \left(1 + \sqrt{\frac{e\phi_d}{2kT_e r_h}}\right), \tag{7.6}$$

$$I^{\mathrm{NAT}}_{\mathrm{i,Z=0}} = \sqrt{8\pi} r^2_{\mathrm{d}} q_{\mathrm{i}} n_{\mathrm{i}} v_{\mathrm{ti}} \left(1 + \sqrt{\frac{e\phi_d}{2kT_i}}\right), \tag{7.7}$$

where ϕ_d denotes floating potential, q_α plasma charge, r_d is dust radius, k the Boltzmann constant, $v_{\mathrm{t}\alpha}$ is thermal velocity, n_α is plasma density, T_α is plasma temperature and $\alpha = e$ or i for electrons or ions, respectively. The electron and ion currents for negatively ($Z < 0$) and positively ($Z > 0$) charged dust particles, respectively, including the induced-dipole force derived by Robertson and Sternovsky (2008) are given by:

$$I^{\mathrm{NAT}}_{\alpha,\mathrm{Z<0}} = \sqrt{8\pi} r^2_{\mathrm{d}} q_\alpha n_\alpha v_{\mathrm{t}\alpha} \gamma^2 \exp\left[\frac{-|Z|e\phi_d}{kT_\alpha \gamma}\left(1 - \frac{1}{2\gamma(\gamma^2 - 1)|Z|}\right)\right], \tag{7.8}$$

$$I^{\mathrm{NAT}}_{\alpha,\mathrm{Z>0}} = \sqrt{8\pi} r^2_{\mathrm{d}} q_\alpha n_\alpha v_{\mathrm{t}\alpha} \left(1 + C_z \sqrt{\frac{e^2}{16\epsilon_0 kT_\alpha r_d}} + D_z \frac{|Z|e\phi_d}{kT_\alpha}\right), \tag{7.9}$$

where α denotes electrons or ions (e,i), γ is given by Natanson (1960)and ranges from γ =1.62 for $|Z| = 1$ to 1.22 for $|Z| = 7$; and D_z and C_z are given in Table 1 of Robertson and Sternovsky (2008).

Due to the fact that dust size ranges under consideration are less than 3 nm, and dust particles only obtain a few charges, it may be appropriate to consider a quantized stochastic charging version of the Natanson model described. Therefore the Natanson model has been implemented as such. The discrete charging model used here incorporates attachment of either ions or electrons that obey probabilities that depend on the dust grain potential ϕ_d. The modified Natanson charging currents are converted into attachment rates by (Chen and Scales, 2007; Cui and Goree, 1994):

$$p_\alpha = \frac{I_\alpha}{q_\alpha} \tag{7.10}$$

where $p_\alpha(\alpha = i \text{ or } e)$ denotes electron or ion attachments rates, $I_\alpha(\alpha = i \text{ or } e)$ is the electron or ion current shown in Eqs.(7.6-7.9). The probability of both ion and electron attachments using the attachment rates shown in Eq.(7.10) can be written for a given time interval dt (Chen and Scales, 2007):

$$P_\alpha = 1 - e^{-dtp_\alpha} \tag{7.11}$$

The probability P_α is compared to two uniform random numbers generated, R_i and R_e, where $0 < R_\alpha < 1$, ($\alpha = e$ or i). They are compared with the ion and electron attachment probabilities. If $R_\alpha > P_\alpha$, then the plasma species will be collected by the dust grain and the corresponding dust charge number will be changed by one charge unit.

A distribution of dust masses (or equivalently dust radii) is also allowed with the PIC model. Uniform as well as Gaussian dust radii distributions are considered for positive particles as will be discussed later. The uniform dust distribution has the form:

where r_{dmax} and r_{dmin} are maximum and minimum dust radius allowed in the simulation, respectively. A Gaussian dust radius distribution of the following form is considered:

$$f(r_d) = \frac{1}{\sigma_{r_d}\sqrt{2\pi}} e^{-(r_d - r_{d0})^2/2\sigma_{r_d}^2} \tag{7.12}$$

where r_{d0} is the mean dust radius and σ_{r_d} is the standard deviation in the dust radius (Chen and Scales, 2005). It is assumed that $\sigma_{r_d} = r_{d0}/2.5$ for reasonable consistency with the results of Berger and von Zahn (2002). As will be shown in section 7.3.3, the differences between the results produced by Gaussian and uniform dust radius distribution are relatively small. Therefore, a uniform dust distribution is used for most of the results in this paper. The growth of particles may take an hour or so to reach critical radius (1 nm) that allows capture of electrons (Megner and Gumbel, 2009). The dust particles are assumed to be stationary for this investigation although the model allows for study of collective effects such as dust acoustic waves (e.g. Mahmoudian and Scales, 2012a). The dust irregularity amplitude is given by (Chen and Scales, 2005):

$$n_{\mathrm{d}}(x) = n_{\mathrm{d0}} \left(1 + \frac{\delta n_{\mathrm{d0}}}{n_{\mathrm{d0}}} \sin(2\pi m x/\ell) \right) \tag{7.13}$$

where n_{d0} is the undisturbed dust density, δn_{d0} is the dust density irregularity amplitude, l is the length of the simulation box and m denotes the number of modes present in the system length. The computational model presented here (Scales, 2004; Chen and Scales, 2005) is now solved by using different numerical algorithms. The governing fluid equations are written in the formulation described by Bernhardt et al. (1991). The continuity equation is solved using an implicit method. The new algorithms not only reduce the computational time substantially but also provide greater accuracy.

The mesopause temperature for both ions and electrons is taken to be $\mathrm{T}_e = \mathrm{T}_i = 150$ K. Proton hydrates with mass between 59 and 109 proton masses are the dominant ion compositions at the PMSE height range. It should be noted that the variation of ion mass from 50 to 100 proton masses does not have a significant impact on the irregularity amplitude

evolution during heating. The ion-neutral collision frequency is of order 10^5 s^{-1} (Lie-Svenson et al., 2003). An electron density of 10^9 m^{-3} is used for the PMSE altitude near 85 km which is reasonable (Friedrich and Rapp, 2009). Considering that gravitational time-scale for a 10 nm particle is on the order of 120 s, the gravitation process for small particles (0.3-3 nm) used in this paper is neglected. The physical processes which are included in this study based on their timescale of occurrence, are charging, diffusion, photoionization and recombination (Mahmoudian et al., 2011).

While it is widely believed that neutral air turbulence (Fossil turbulence) is one of the driving sources of electron density fluctuations (Rapp and Lubken, 2004), most published explanations for PMSE agree that charged aerosol particles play a key role in PMSE source region (Lie-Svenson et al.,2003). This study is focused on the relationship between positively and negatively charged dust particles and plasma density fluctuations measured by rocket instruments.

7.2 Correlation and anti-correlation of plasma density fluctuations

Charging of electrons onto the subvisible irregularity structures in the dust density and ambipolar diffusion have the major effect on the correlation and anti-correlation of the irregularities in electron and ion densities (Lie-Svendsen et al., 2003). Both correlation and anti-correlation of electron and ion density fluctuations were measured in situ by rocket as shown in Fig 7.1. Fig 7.1a illustrates an anti-correlation measured in a sounding rocket experiment in 1993 (Lie-Svendsen et al., 2003). The solid line denotes the electron fluctuations and dashed line corresponds to the ion density fluctuations. Looking at the fluctuation in the electron and ion densities over different spatial regions in Fig 7.1b shows more variable behavior (Lie-Svendsen et al., 2003). This figure shows both strong and weak correlations between electron and ion density fluctuations and while spatial correlation is dominant and more pronounced, in some spatial regions anti-correlation is observed.

According to the Lie-Svendson et al. (2003) model, irregularities formed by dust particles larger than 30 nm may produce the correlation of electron and ion density fluctuations shown. Considering that particle diffusion is very sensitive to the size of the particles ($\propto r_p^2$ where r_p is particle radius)(Lie-Svendson et al., 2003), the diffusion time-scale increases for the irregularities generated by larger dust particles (Lie-Svendson et al., 2003; Chen and Scales, 2005), therefore anti-correlation between the electron and ion fluctuations which is mainly a result of ambipolar diffusion, is not the case anymore. Due to large particle size, the charging time-scale will be very short and almost all particles become multiply charged instantly. The gravitational time-scale (13 s) is less than the diffusion time-scale (25 s) such that particles fall so electrons and ions are not able to establish a diffusive electron equilibrium (Lie-Svendson et al., 2003). On the other hand ion attachment onto the dust

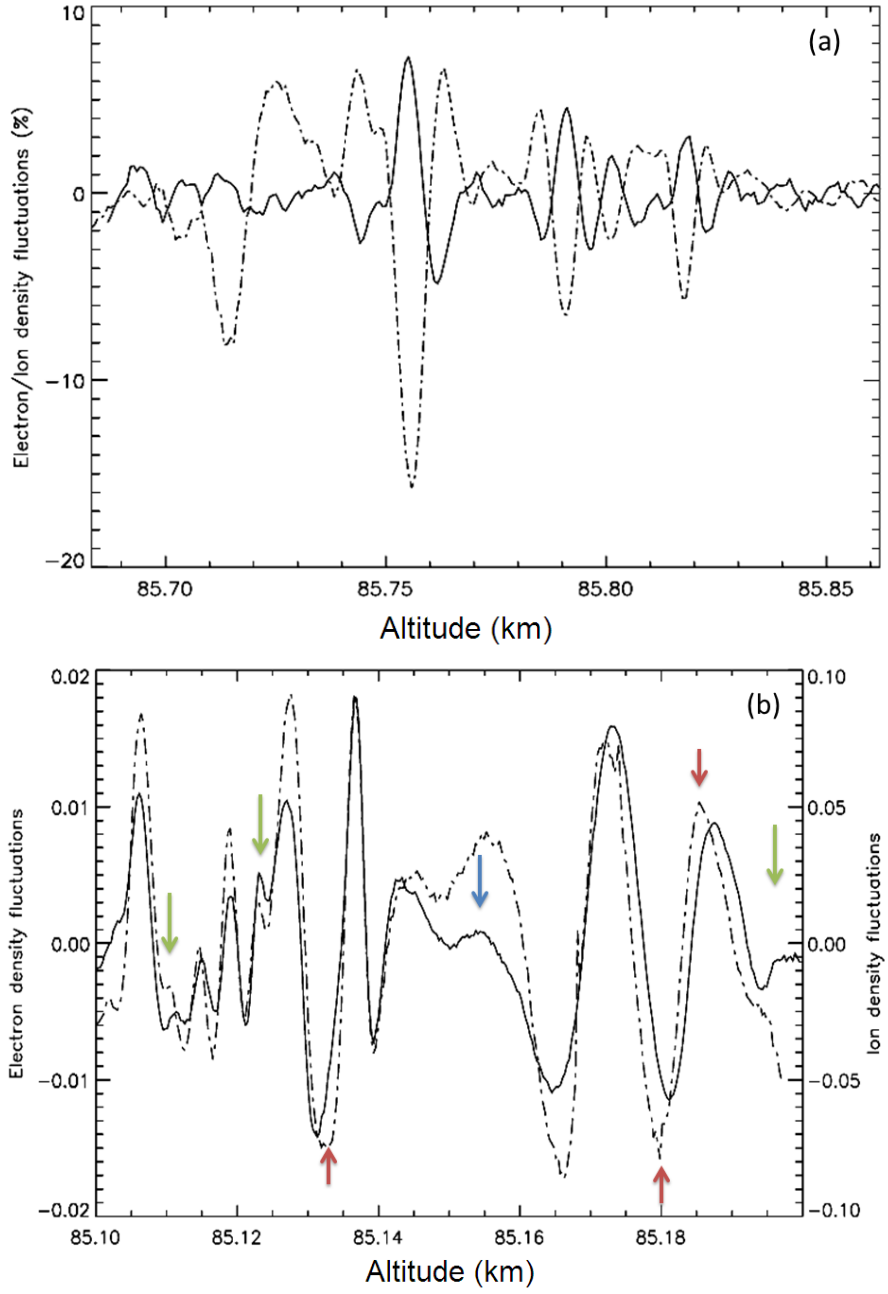

Figure 7.1: Relative ion (solid curves) and electron (dashdotted curves) density fluctuations as a function of altitude(in km), a) measured in situ by the SCT-06 rocket payload, launched from Andoya Rocket Range on 1 August 1993 at 0146 UT. b) measured by the SO-MI-05 rocket launched from Andya on 17 June 2001 at 0005 UT. Reproduced from Lie-Svendson et al. (2003).

particles is less than the gravitational time-scale and significant numbers of ions will have time to attach to dust particles before they fall which causes the correlation of electron and ion densities as a result of depletion. In other words, the heavy particles must be so large that ion attachment becomes more rapid than ion diffusion. But it should be noted that having such large dust particles at mesopause altitudes is rare (Robertson et al., 2009, and special issue devoted to the measurements of ice particles) and the result of recent in-situ experiments revealed that much smaller dust particles might be in charge of the electron density irregularities in this region (Robertson et al., 2009). Another hypothesis proposed by Lie-Svendsen to justify the observed correlation of the electron and ion irregularities is the evaporation of the negatively charged ice particles at the bottom of the ice layer. The free electron release into the plasma as a result of this evaporation may cause a correlation. This scenario requires large ice particles and it is confined to the timescale of evaporation that must be shorter than the ambipolar diffusion timescale for this process to produce a correlation. The release should be rapid enough to increase electron density to fill in the electron depletion and create an enhancement.

The model proposed here is based on the conclusion made on the measured data that positive dust particles grow from small molecular ions or cluster ions (Robertson et al., 2009). Then, they start to capture free electrons and become neutral as they grow. It addresses some of the difficulties of the need for large negatively charged particles. To have stable ice particles, the assumption that ice embryos reach 1 nm before capturing an electron and becoming neutral is taken into account. It should be noted that the anti-correlation of electron and ion density fluctuations was predicted for positively charged particles by Lie-Svendson et al. (2003). However the specific size distribution of particles and growth in size of the particles with time were ignored in the previous work by Lie-Svendson et al.(2003). Detailed simulations are provided here for the first time.

The relationship between the electron, ion and dust irregularities can be approximated from a perturbation analysis (Chen, 1984). For the case of shorter wavelength irregularities, the ambipolar diffusion time is sufficiently small so the electrons and ions may be modeled with the Boltzmann approximation. This implies the electron and ion irregularity amplitudes, δn_e and δn_i, can be written in terms of the electrostatic potential irregularity amplitude $\delta\phi$ as:

$$\frac{\delta n_e}{n_{e0}} \approx -\frac{T_i}{T_e}\frac{\delta n_i}{n_{i0}} \approx \frac{e\delta\phi}{k_B T_e} \tag{7.14}$$

The Poisson equation can be used to determine the relationship of the dust irregularity amplitude to the electron irregularity amplitude. In the Fourier spectral domain, the Poisson equation for the irregularities is

$$k^2\delta\phi \approx \frac{1}{\epsilon_0}(-e\delta n_e + e\delta n_i + eZ_d\delta n_d) \tag{7.15}$$

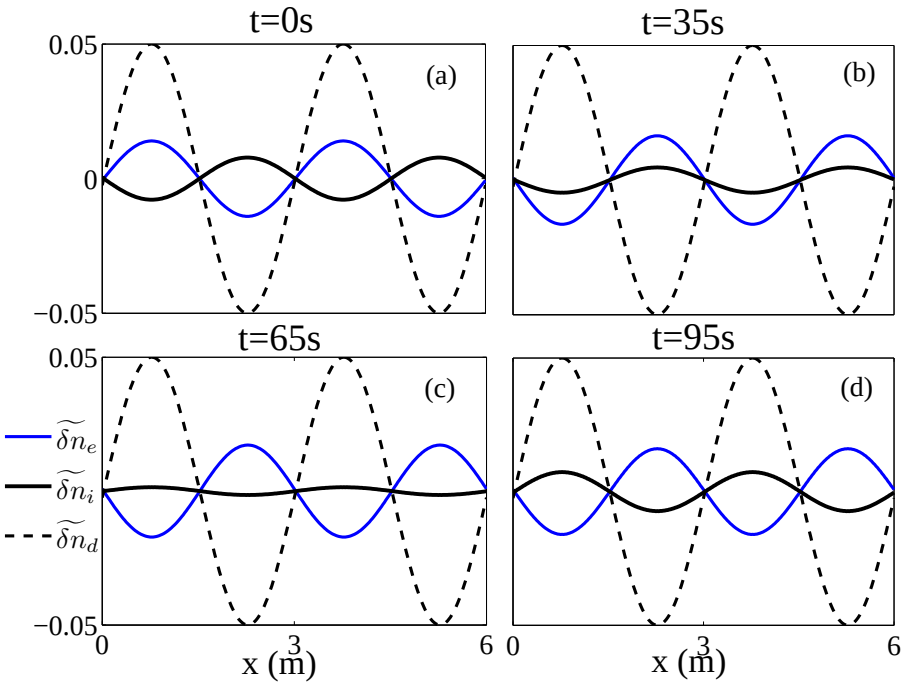

Figure 7.2: Ion and electron density spatial fluctuations. Dust particles are assumed to have positive charge initially and become negatively charged as they grow in size. $\widetilde{\delta}$ denote the normalized density fluctuations. All positive dust particles grow to become negative/neutral.

where the wavenumber is denoted by k. Note here that the dust is assumed to be positively charged with charge number Z_d. Using Eq. (7.14) and (7.15) implies the relationship

$$\delta n_e \approx \frac{Z_d n_d}{n_e} \frac{1}{1 + \lambda_{De}^2/\lambda_{Di}^2 + \lambda_{De}^2 k^2} \delta n_d \tag{7.16}$$

where $\lambda_{De,i}$ is the electron (ion) Debye length. Therefore the electron irregularities are in phase with dust irregularities (which are 180^0 out of phase with the ion irregularities).

Electron, ion and dust fluctuations for total dust density 2×10^9 m^{-3} and $n_e = 10^9$ m^{-3} are illustrated in Fig 7.2 as calculated from the model of Chapter 3. A uniform mass distribution for dust particles is used throughout here since it is found that there is very small differences between the uniform and Gaussian distributions. It is found for the parameters under consideration that the charging model, whether OML or modified Natanson, has a small impact on the correlation, anti-correlation properties of the electron and ion fluctuations. Therefore the OML model is used in this section. However, more significant differences between the charging models are noted for the case of fluctuation evolution during radiowave heating experiments and these differences are provided and discussed in detail in sections 4.2 and 4.3. The normalized fluctuation amplitudes in Fig 7.2 are defined as $\widetilde{\delta n_e} = \delta n_e/n_e, \widetilde{\delta n_i} = \delta n_i/n_i$

and $\widetilde{\delta n_d} = \delta n_d / 2n_{d0}$. It is assumed that positive dust particles with density of 50 percent of the plasma density are formed on ion clusters and $T_e \approx T_i = 150$k. The ion and electron fluctuations shown in Fig 7.2 support the theoretical predictions (Eq. 7.16). Fig 7.2a shows an anti-correlation of electron and ion irregularities while electron and dust fluctuations are correlated which is consistent with Eq.(7.17). In this case, all positive dust particles are considered to have grown to a size from 1 to 1.5 nm and at t=0 s they undergo charging and capture electrons. Both stepwise and linear growth of dust grains in size have been considered in this study and considering the small difference in the results produced by each case, linear growth is used for simulations presented in this paper. As can be seen from the panel b, electron charging onto the dust when the particles start to grow may produce a correlation as the result of electron depletion. This process and correlation may last for several minutes depending upon the rate of particle growth and before the ambipolar diffusion process can act to cause a new equilibrium and anti-correlation. A mixture of positive and negative dust particles could exist during the time period when the electron and ion fluctuations are correlated. As the diffusion process becomes prominent the correlation of fluctuation in electron and ion densities will be replaced by anti-correlation due to the ion diffusion (panel c). Although the model proposed by Lie-Svendson requires that a rocket would have to pass through the volume after evaporation is almost complete but before diffusion has removed the structure, this model shows that the correlation may last for a longer time period as a result of the particle growth period. Based on the model results the size and charge state of dust particles can be estimated based on the observed correlation or anti-correlation. This behavior is demonstrated with computational results here and in fact reflects the stage of particle formation and charge state evolution from positive to negative charge. This can be seen with the case of panel (b) in Fig 7.2. In fact when the growth rate of particles is very small, it may take several minutes for the electron density fluctuations to go from case (b) to (c) and get deep enough to cause the ion diffusion into the depleted electron region. When the electron density gets deep and a large fraction of dust particles obtain negative charge, the anti-correlation of ion and electron density fluctuations happen as the result of ambipolar diffusion which is shown in Fig 7.2d. For the negatively charged dust particles the relationship between electron and dust irregularity amplitude is given by (Scales and Chen, 2008):

$$\delta n_e \approx \frac{-Z_d n_d}{n_e} \frac{1}{1 + \lambda_{De}^2/\lambda_{Di}^2 + \lambda_{De}^2 k^2} \delta n_d \tag{7.17}$$

This not only is consistent with recent experimental data and hypotheses proposed by Robertson et al., (2009), but also covers all the possible combinations of correlation and anti-correlation in the electron and ion densities. Fig 7.3 shows the normalized irregularity amplitude for a case in which only a fraction of positive dust particles (50 percent) grow and become neutral or negatively charged while in the previous case (Figure 7.2) all positive dust parties were assumed to grow and capture electrons. This assumption is more realistic and results obtained with the new assumption show much better agreement with

the experimental data shown in Fig 7.1. The OML charging model and uniform dust radius distribution for dust particles from 0.5 nm to 1 nm are incorporated in this simulation. Arrows with the same color in Fig 7.3 and in Fig 7.1 show the similarity and agreement between the experimental and computational results (Arrows are explained in the caption). It is assumed that positive dust particles are formed on cluster ions and the quasi-neutrality condition is satisfied. Therefore, Fig 7.3a shows the equilibrium state before the positive dust particles start to grow and capture electrons. The time evolution of irregularities shown in Fig 7.3 are similar to Fig 7.2.1) initially electron and ion fluctuations are anti-correlated (t=0s) 2) as positive dust particles start to charge up a correlation forms 3) as a result of ion density diffusion, ion and electron irregularities become anti-correlated again. In this case, the correlation phase exists for a longer time period which may take a few minutes because only a fraction of positive dust particles capture electrons and others remain positive. The similarities between the simulation results in Fig 7.3 and and experimental data in Fig 7.1a are shown by arrows with the same color. The phase difference between peaks, while the irregularities are correlated, are observed in the simulation results and pointed out with red arrows. This behavior has also been observed in the experiment (Fig 7.1b). In the case correlation exists in most periods, anti-correlation of irregularities has been observed in a few spatial regions and shown with green arrows which is consistent with the experimental data. The gravity effect is overlooked in this study because of the small size of the dust particles (0.5-3 nm) considered in the simulation which is based on the recent experimental data (Robertson et al., 2009).

7.3 Application: Impact of positive dust during PMSE modulation experiments

The radar scattering phenomenon polar mesospheric summer echoes PMSE which was first observed in 1981 by radars operating at 50 MHz (Eklund and Balsley, 1981) has since been observed at frequencies up to more than a GHz (Cho and Kelley, 1993; Rapp and Lubken, 2004). Scattering is from electron irregularities on the irregular dust background due to charging of electrons and ions. Investigating the differences in reaction between PMSEs at various frequency bands to artificial electron heating by high powered radiowaves was introduced as a powerful and promising development to help investigate the PMSE and the physical conditions and dust parameters near the mesopause (Naesheim et al., 2008; La Hoz et al., 2010). The first PMSE heating experiment conducted by Chilson et al.,(2000) and followed by Havnes (2003; 2004) demonstrated the modulation of PMSE with radiowaves and PMSE pump wave turn-off PMSE overshoot effect. Since then, the physics associated with active perturbation of PMSE has been most intensely studied (e.g. Biebricher et al., 2006; Scales, 2004; Chen and Scales, 2005; Mahmoudian et al, 2011; Mahmoudian and Scales, 2012b). In recent years there has been an extensive effort in performing PMSE heating experiments at higher radar frequencies such as 224 MHz and 930 MHz (Naesheim et al.,

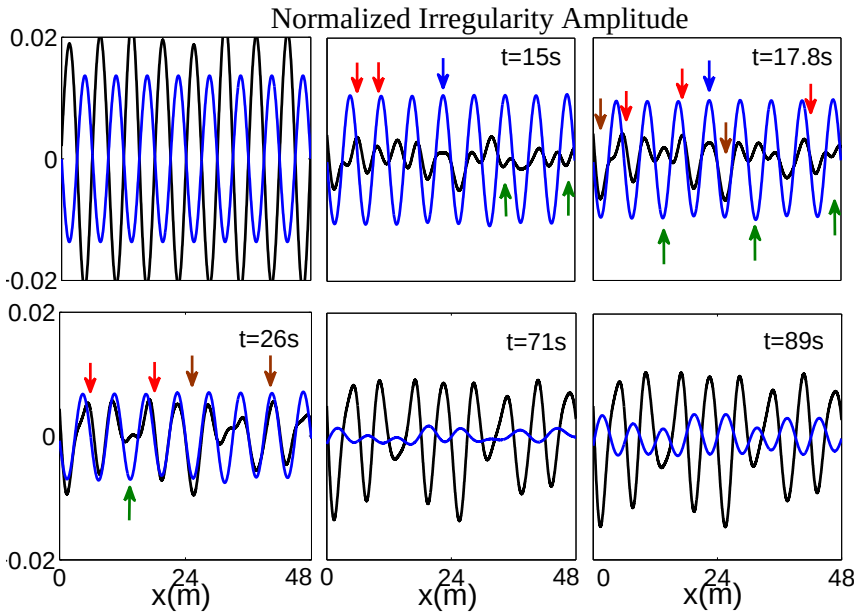

Figure 7.3: Six snapshots of time evolution of ion and electron spatial fluctuations are shown. Dust particles are assumed to have positive charge initially and 50% become neutral/negatively charged as they grow in size. Electron fluctuations are shown with blue color and black lines represent the ion irregularities. Arrows represent the similarity between computational model results and the experimental data (Fig.1). red arrow: correlation with a phase difference, blue arrow: weak correlation with ion fluctuations on the margin of correlation and anti-correlation, green arrow: weak anti-correlation among dominant correlation and brown arrow: strong correlation.

2008) as well as lower radar frequencies such as 56 MHz (Morro radar) and 7.9 MHz at EISCAT, Norway (La Hoz et al., 2010). The radar echoes are believed to be produced by Bragg scatter from electron density irregularities at half the radar wavelength.

To consider the effect of positive dust particles on the temporal behavior of irregularity amplitude using the model described, two possibilities are considered. The first possibility is to consider a mixture of positive ice particles, neutral and negatively charged particles before heater turn-on while ignoring the charging process of positive particles due to their small size 0.5-1.5 nm. In fact positive particles with the smaller radii in comparison with negative particles represent particles grown on the positive condensation nuclei. This has been studied for 224 MHz in the previous work by Mahmoudian et al. (2011) and is elaborated on further in this work. The second assumption is that positive particles with radii larger than 1 nm undergo charging.

7.3.1 Spatial structure of density fluctuations

The aim of Fig 7.4.1 is to show the effect of radiowave heating on the correlation and anti-correlation of the irregularities in the electron, ion and dust densities without positive particles for reference. A uniform mass distribution and OML charging model are used in this section. Top panels in Fig 7.4.1 show the irregularity amplitude before turn-on and bottom panels represent the irregularities after the pump turn-on. Panel (a) shows a clear anti-correlation between n_e and n_i which is the result of short diffusion time at higher radar frequencies (e.g. 224MHz) or smaller irregularity wavelengths. As seen in panel (b) for the radar frequency of 56MHz, the diffusion and charging timescales are of the same order and although a small enhancement of ion irregularities exists inside the electron depletion, the irregularities in ion and electron densities are weakly anti-correlated. At 7.9MHz, due to the large ambipolar diffusion timescale even a small enhancement of ion density is not seen inside the electron depletion region and the n_e and n_i tends to be correlated. Therefore, it is observed there is a transition from anti-correlation of electron and ion fluctuations slightly below the 56 MHz radar spatial scales for these parameters. The electron to ion temperature is assumed to be $T_e/T_{e0} = 3$ during the pump heating, where T_{e0} is electron temperature before radiowave heating. The effect of pump heating on the irregularities associated with radar frequency of 224MHz is shown in panel (d) which shows a more pronounced anti-correlation of irregularities in ion and electron densities. The heating reduces ambipolar diffusion times more than electron charging time at 56MHz (panel (e)) which results in the peak of ion density in the middle and more pronounced anti-correlation. Different from the 56MHz case at 7.9MHz, the pump heating strengthens the charging process more and leads to a correlation between the n_e and n_i according to the panel (f).

The variation of ion and electron fluctuations at 224 MHz in the absence and presence of positive dust particles is shown in Fig 7.4.2 left and right panels, respectively, prior to and after heater turn-off. The blue curves show the corresponding electron fluctuations. Total

dust density is 10^9 m^{-3} with 20 percent positive dust particles formed on background ions. Positive dust particles are uniformly distributed from 0.5 to 1 nm. Negative dust particles are assumed to have constant radius of 3 nm. The anti-correlation and correlation stays the same in the presence of positive dust particles, although the irregularity amplitude changes slightly. The ion irregularity amplitude is larger and anti-correlation is more pronounced when all particles are charged negatively in comparison with the case positive dust particles present. The ambipolar diffusion reduces the large ion irregularity gradients and correspondingly enhances the gradients in the electron irregularities after turn-off of the radiowave. The ambipolar diffusion is slower in the presence of positive dust particles as a result of a small ion irregularity gradient. Therefore a smaller pump turn-off overshoot is expected in the case of positive dust particles present as will be shown shortly.

7.3.2 Case I: Temporal evolution ignoring positive dust charging

The first and simplest hypothesis (Case I) is to overlook the charging process of positive dust particles due to their small size in comparison with the negative dust particles. This is a reasonable assumption, since during the in-situ measurement and in the equilibrium condition a large number of small positive particles were observed which is expected to show that the dust charging process may not affect these particles. Therefore during heating with radio waves, this charging process might be negligible. The case consisting of positive dust particles shows less reduction of radar power echoes for radar frequency of 224MHz (and larger turn-on overshoot amplitude at 7.9 MHz) in comparison with the case all particles are charged negatively. The case including positive dust particles can be considered as a case with less dust density, because less negative dust particles exist that can be charged during heating than the other case in which all particles are charged negatively (Mahmoudian et al., 2011).

After the pump turn-off, when the electron temperature returns back to its initial value before the turn-on, ion irregularities start to smooth out and the ion current onto the dust increases. Considering the case with positive dust particles to have less ion particles present in the plasma (Brattli et al., 2009; Robertson et al., 2009), a smaller ion current should exist in comparison with the case all particles are charged negatively. It has also been shown in Fig 7.4.2 that anti-correlation of electron and ion irregularities is weaker in the presence of positive dust particles which may lead to a slower ambipolar diffusion. Therefore a smaller pump turn-off overshoot is expected when positive dust particles exist in the PMSE source region which is also predicted by the computational model as will be shown in Fig 7.5. It should be noted that the amount of irregularity amplitude enhancement after the pump turn-off relative to its value right before turn-off is considered as the turn-off overshoot amplitude in this work.

Fig 7.5 shows electron irregularity amplitude for two radar frequencies of 7.9 and 224 MHz. The thin line shows the case in which all particles are charged negatively and the thick line

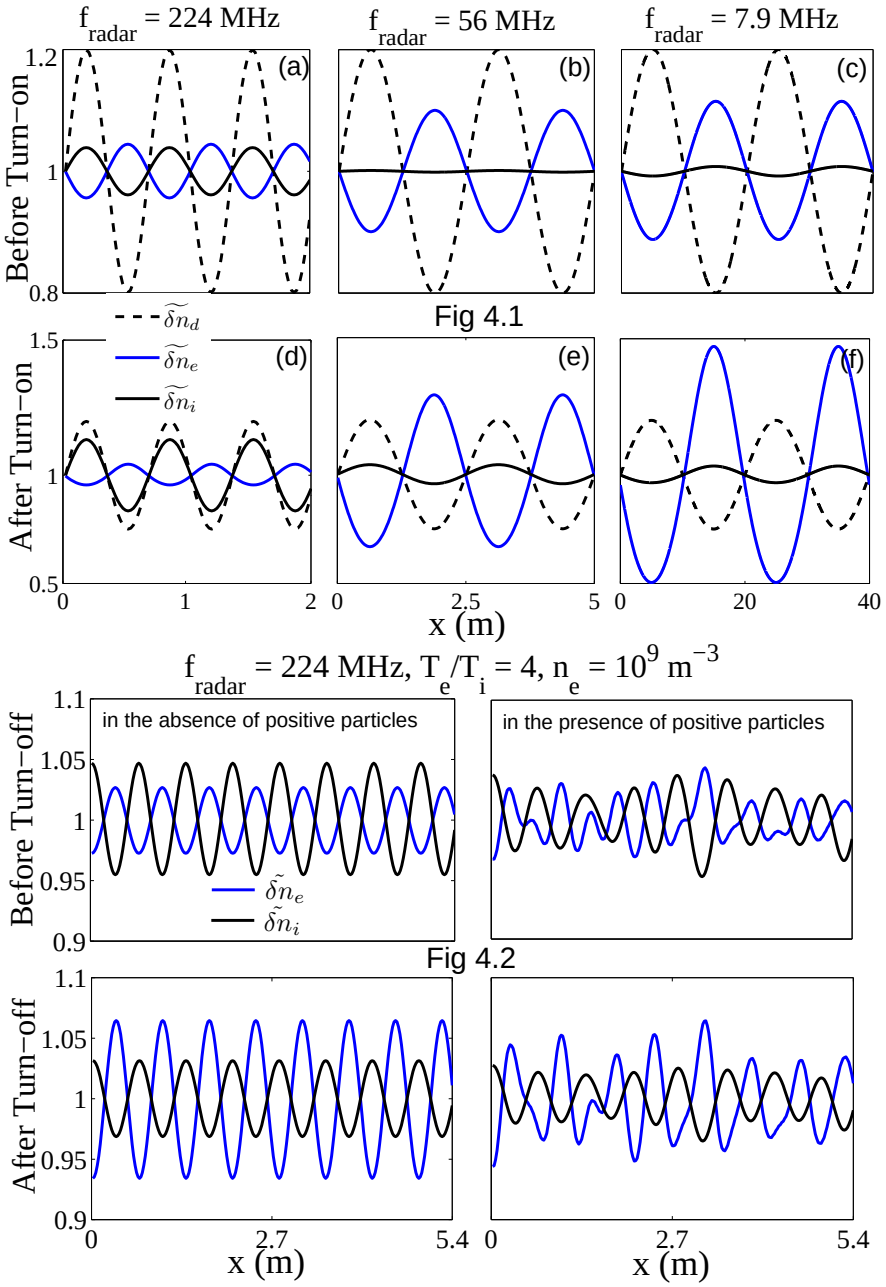

Figure 7.4: 1) Electron, ion and dust charge density irregularities associated with radar frequencies of 224 MHz, 56 MHz, and 7.9 MHz before and after radio wave pump heating. 2) Ion and electron density irregularities in the presence of positive dust particles when a fraction of them grow and capture electrons. $\widetilde{\delta}$ denotes the normalized density fluctuations. Note positive particles reduce ion spatial gradients upon turn-off.

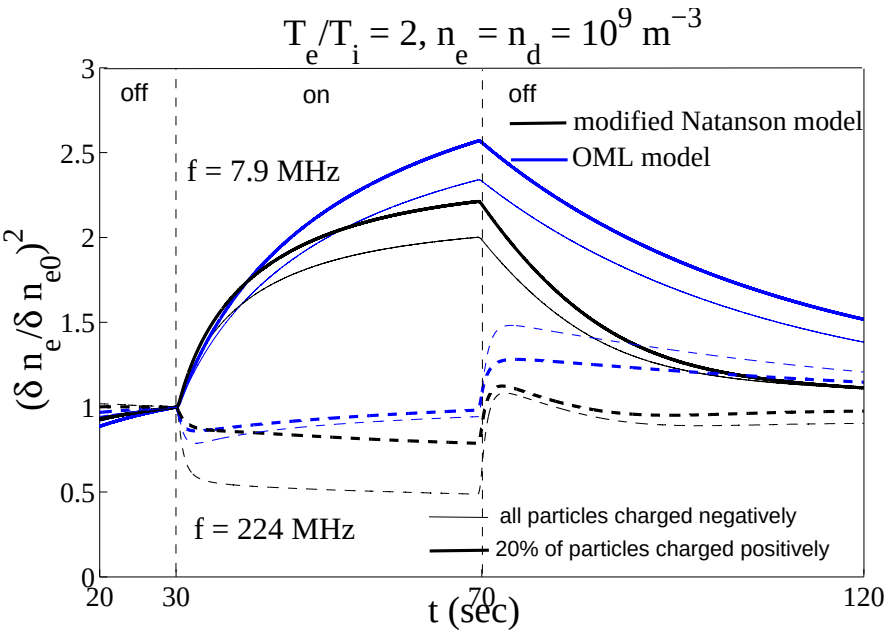

Figure 7.5: The time evolution of electron irregularities during radio wave heating with the effect of positively charged dust particles for OML and modified Natanson charging models. Dashed line represents a radar frequency 224 MHz and solid line 7.9 MHz. Blue line corresponds to the modified Natanson model and black line OML charging model.

represents the case with 20% positive dust particles. Total dust density is 10^9 m^{-3} and dust radius for negatively and positively charged particles are 3 nm and 0.5-1 nm, respectively. Electron temperature enhancement during the heating is taken to be $T_e/T_{e0} = 2$. The blue line denotes the result of the OML charging model and the black line denotes the result of the modified Natanson charging model. The figure shows the same trend which is expected according to the theory; and the case with positive dust particles represents less suppression after pump turn-on at 224MHz (or large turn-on overshoot at 7.9 MHz) and smaller turn-off overshoot. It should be noted that the Natanson model is more accurate at smaller dust radius in comparison with the OML model.

7.3.3 Case II: Temporal evolution including positive dust charging

The second assumption (Case II) is to consider the dust charging process for positive dust particles larger than 1 nm as described in section 7.2. The system is assumed to be at the equilibrium conditions observed during the in-situ measurement. In this case, negative dust particles have the electron and ion charging currents according to the Eq. (7.8), and positive dust particles will be charged based on Eq. (7.9). Both Gaussian and uniform dust radius distributions in the range from 0.5 to 1.5 nm for positive dust particles and 2 to 4 nm for negative particles are considered in this section for comparison. The electron temperature

enhancement during heating is $T_e/T_{e0} = 4$. The electron density is 10^9 m^{-3}. Total dust density (including both positive and negative dust) is 50 percent of the background plasma density. The positive dust density is 20% of the total dust density.

The time evolution of the average spatial dust charge distribution during radio wave heating at 224 MHz for two cases is shown in Fig 7.6a and b using the Natanson charging model. Fig 7.6a shows the average dust charge distribution for the case no positive dust particles exist. Before heater turn-on as shown in the top panel, most particles are neutral and after heater turn-on, as a result of electron charging onto dust particles as the electron temperature increases, particles will charge negatively as shown in the panel in the bottom of Fig 7.6a. Fig 7.6b shows the time evolution of the average dust charge distribution for the case with positive dust particles that undergo charging. In this case, as the dust particles larger than 1nm undergo charging, they acquire less charge after pump turn-on which implies less reduction in electron density and therefore less irregularity suppression after turn-on is expected.

The effect of the two positive dust particle charging processes, considered in Fig 7.6, on the 224 MHz PMSE radar power during a heating experiment is shown in Fig 7.7. In this case, also due to enhancement of the electron current and reduction of the dust charging timescale, less suppression of irregularity amplitude after the pump turn-on for the 224MHz radar frequency is seen in Fig 7.7. The dashed line shows the results using a Gaussian radius distribution and solid lines represent the uniform distribution. The case with a mixture of positive dust particles that undergo charging and those that remain positive show behavior between the other two cases where either no positive dust particles exist or all positive dust particles remain positive. This behavior is consistent with the theory explained in section 7.2, because when a fraction of positive dust particles charge up instantly this case will be similar to Case I where a portion of particles are charged negatively and the remaining particles do not undergo charging. Therefore more suppression of irregularity amplitude is expected in this case with what may be considered more realistic modeling of the positive dust charging. It turns out that dust radius distribution has a small impact on the predicted electron irregularity amplitude during PMSE modification and an impact less than 20 percent after the turn-off which were also predicted in the previous study by Chen and Scales, (2007).

7.4 Conclusions

The proposed possibility for the presence of positive dust particles observed during ECOMA/MASS campaign in the PMSE source region growing from cluster ion condensation nuclei is adopted in this paper. Positive particles are assumed to reach the critical radius ($\approx$1 nm) before becoming neutral by electron capture in order to have a stable ice particle and complete the nucleation process on cluster ions. Then as particles grow, they are neutralized by electron capture and later charge negatively by collecting an additional electron. The correlation and anti-correlation of fluctuations in electron and ion density is studied using the proposed

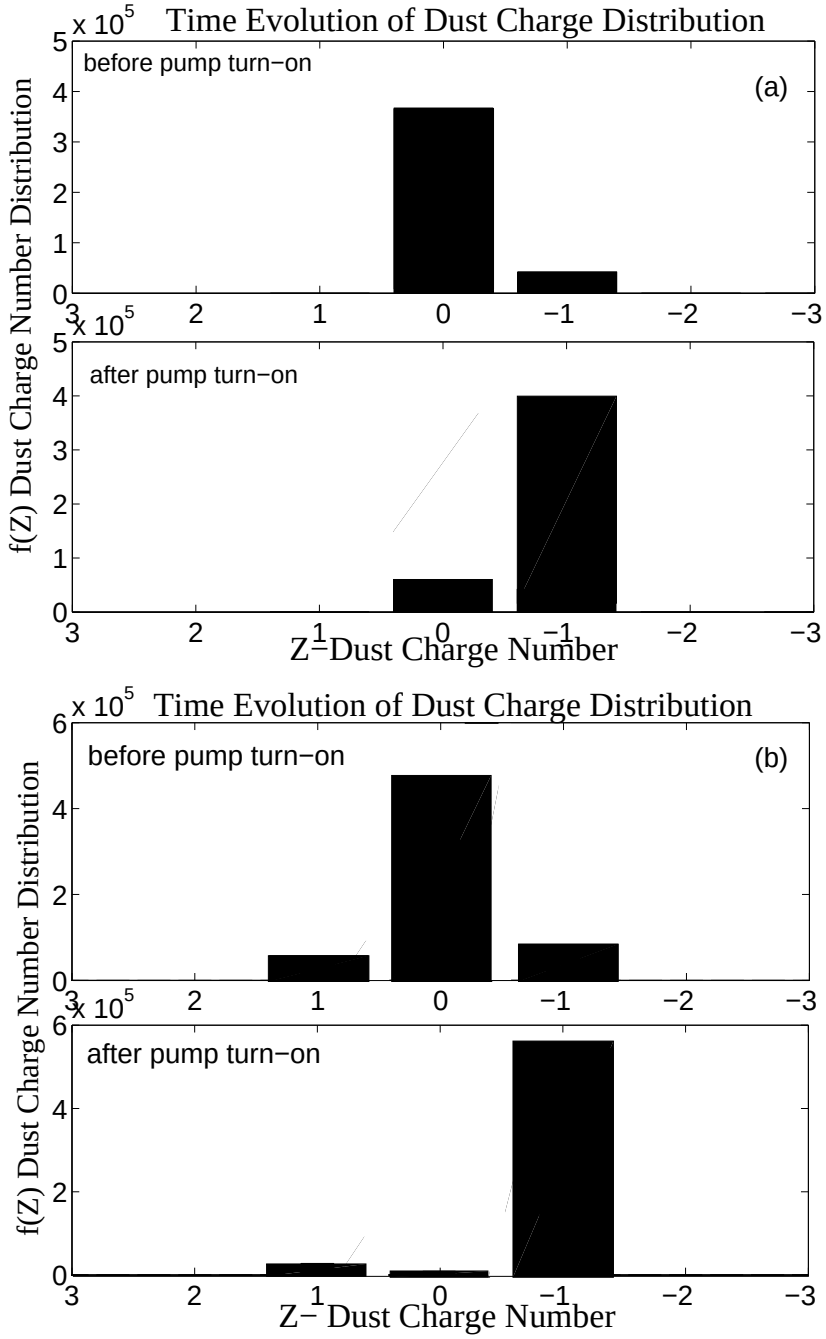

Figure 7.6: Time evolution of dust-charge-number distributions during radio wave heating for a) no positive dust present b) 20% positive dust exists and undergo charging

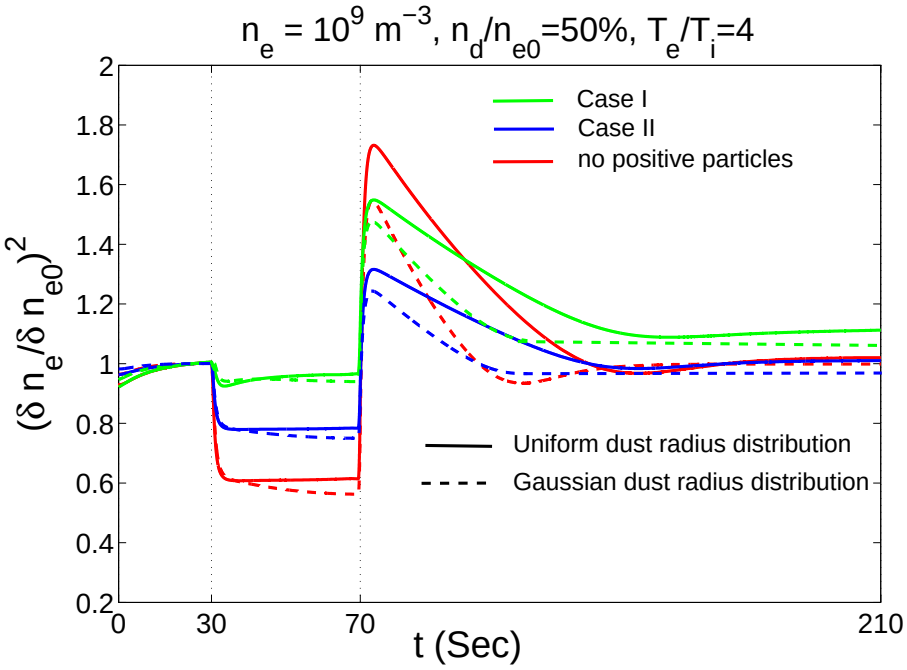

Figure 7.7: The predicted effect of positively charged dust particles on the electron irregularity amplitude during PMSE heating experiments at VHF (224 MHz).

theory of positive ice particle formation which matches recent observational data (Robertson et al., 2009). It turns out that during this process all the possible cases for correlation and anti-correlation between electron, ion and, dust fluctuations occur. This hypothesis seems to be more reasonable in comparison with other theories proposed to justify observations of fluctuations (e.g. Lie-Svendsen et al., 2003). Therefore, observing these correlation and anti-correlations may provide insight into the state of ice particle formation in the PMSE source region and possibly indicate the range of ice radii and charge states. Temporal evolution of radar echoes during PMSE modulation experiments in the presence of positive dust particles is studied for two cases. In the first assumption, the charging of positive dust particles by electrons is ignored. In the second case, the positive particles undergo dynamical charging during radio wave heating. It turns out that in the presence of positive dust particles, anti-correlation of ion and electron fluctuations is weaker before the turn-off of radiowave and as a result of a slower ambipolar diffusion and smaller ion irregularity amplitude, a weakened turn-off overshoot is predicted in the presence of positive particles. Due to the presence and importance of positive dust on mesospheric plasma irregularities, further work must be performed to refine the charging models within the guidance of both ground-based and space-based observations.

Chapter 8

Diagnostic Techniques using Magnetized Stimulated Brillioun Scatter MSBS in the SEE Spectrum

8.1 Introduction

Interaction of a high power electromagnetic wave transmitted from the ground with local plasma in the ionosphere has been used as a powerful remote sensing tool for the modified ionospheric environment. Stimulated Electromagnetic Emissions SEE induced by the pump wave can be detected by ground receivers. SEE is believed to be produced locally by parametric instability processes in the plasma involving the pump field which may decay into electrostatic ES and electromagnetic waves (Leyser, 2001). The generated EM wave propagates back to the earth and can be detected by an SEE receiver. Parametric instability processes was first provided by Stubbe et al. (1984). A wide variety of electrostatic and electromagnetic waves may be produced during the SEE generation process (Leyser, 2001). The SEE spectral sidebands were found to depend on a number of ionospheric parameters in addition to the heater wave characteristics. It was later postulated that the sidebands in the SEE spectrum should develop in the altitude region where the heater interacts with the local plasma.

There has been an extensive study on the physical processes and irregularities associated with SEE features at higher frequency band (1-100 kHz) in the last two decades (Leyser, 2001). Downshifted maximum DM, a distinct peak at a frequency approximately 10 kHz downshifted from the pump frequency (Bernhardt et al., 1994) as result of nonlinear interaction of upper hybrid UH and lower hybrid waves (Leyser et al., 1989, 1990), and Broad Upshifted Maximum BUM, a broadband peak upshifted from the pump about 14 kHz-200 kHz generated by interaction of UH waves and striations (Mityakov et al., 1975; Wong et

al., 1981), and usually seen with the pump frequency slightly below to 100 kHz above the harmonics of electron gyro-frequency nf_{ce}, are two of the prominent spectral features that have been observed in many experiments (Leyser et al., 1992; Thide et al., 2005; Leyser, 2001).

The heating facilities at the High Frequency Active Auroral Research Program HAARP facility, in Gakone, Alaska HAARP has opened the door to investigate parametric decay instabilities that have higher pump threshold such as magnetized stimulated Brillouin scatter MSBS that appears with emission lines at much narrower bandwidths relative to the pump frequency. Stimulated Brillouin scatter is a strong SEE mode involving a direct parametric decay of the pump wave into an ES and a secondary EM wave that sometimes could be stronger than the HF pump. The SBS has been studied in laboratory plasma experiments by the interaction of high power lasers with plasmas. This parametric decay instability has been studied in theory and excited ion acoustic and an electron plasma wave has been observed in laboratory experiments [Kruer, 1988; Eliezer 2002]. But the stimulated Brillouin scatter process excited by high power HF wave-ionospheric experiments was only observed recently by Norin et al. (2010). All the previous theory and experiments were based on the unmagnetized SBS instability. The SBS instability in a magnetized ionospheric plasma was studied for the first time by Bernhardt [2009; 2010]. It has been shown that an ordinary mode electromagnetic wave can decay into an electrostatic wave and a scattered electromagnetic wave by a process called magnetized stimulated Brillouin scatter (MSBS). Depending upon the angle between the wave normal direction and the background magnetic field vector, the excited electrostatic wave could be either Ion Acoustic IA or Electrostatic Ion Cyclotron. In fact, enhanced electron temperature in the modified ionosphere by pump wave excites the naturally existing IA waves but heavily damped by Landau damping as a result of $T_e \approx T_i$. Therefore, IA emission lines are expected to be seen in spectra as a result of enhanced electron temperature and for small propagation angle relative to the magnetic zenith. EIC lines can be excited with oblique propagation angles (Bernhardt et al., 2010).

The excited plasma waves in the MSBS process in the interaction region, that could be the reflection altitude where refractive index goes to zero or the altitude where pump frequency equals the local Upper Hybrid UH frequency, appear in the SEE spectrum as spectral lines with offset from the pump frequency. Stimulated Brillouin scatter produces extremely strong SEE emissions up to 10 dB below the HF pump amplitude and are excited at the reflection region and the UH resonance region. The received SEE spectral lines originating from the UH and reflection regions are distinguished by their frequencies. The SBS emission originating near the reflection altitude has a downshifted peak (SBS-1 or NP) frequency of about 15 Hz. The SBS emission from the upper-hybrid region has a downshifted peak (SBS-2 or 2NP) frequency of about 30 Hz. Both SBS lines can have weaker upshifted peaks with the same magnitude frequency offsets.

The mode-converted UH wave has a first downshifted maximum DM1 frequency of about 8 kHz with no corresponding upshifted component. The SBS and mode-conversion/parametric-decay process compete for the electromagnetic pump source to drive each instability mode.

Before field-aligned irregularities FAI form, the SBS instability dominates. After FAI form, the pump wave may be depleted in the UH region and there may not be sufficient electromagnetic pump amplitude near the reflection altitude. The experimental observations presented in this paper illustrate the transition between a strong SBS-1 line and a weaker DM1 emission. This transition is abrupt for the SBS instability indicating that there is a threshold for excitation and maintenance of the SBS instability.

The theory shows that the growth for the EIC waves is much lower than the growth rate for the IA waves in the plasma near the reflection or upper-hybrid altitudes (Bernhardt et al., 2009; 2010). The spectrum was found to be highly dependent on the proximity of the pump frequency to the harmonics of the electron cyclotron frequency. To study this effect on the MSBS generated in the ionosphere, a pump frequency near third harmonic of the electron cyclotron frequency $3f_{ce}$ was employed in the experiment.

The primary purpose of this chapter is to extend the work of Norin et al., (2009) and Bernhardt et al., (2009; 2011) by providing more experimental observations and theory of magnetized stimulated Brillouin scatter MSBS. The results of matching condition and ray tracing are discussed in the first section. Then, solution of wave equation and an estimation of electric field amplitude near the interaction region is provided. New measurements of the MSBS for pump frequency variation near the $3f_{ce}$, beam angle and amplitude of pump power are presented that were not explored in the previous works. Finally a conclusion is provided.

8.2 MSBS Dispersion Relation and Instability Growth Rate

Using the electromagnetic wave equations derived from the Maxwell equations, the electric field for the initial pump wave gives the Forsterling's (1949) equation for the ordinary mode and extraordinary mode as:

$$\frac{\partial^2 F_p^{(o,x)}(z)}{\partial^2 z} + (\frac{\omega_p}{c})^2 [n_p^{(o,x)}]^2 F_p^{(o,x)}(z) = 0 \tag{8.1}$$

where P denotes the pump wave along the propagation path, c is the sound speed, and $n_p^{(o,x)}$ is the ordinary and extraordinary refractive index, respectively, based on the Appleton-Hartree formula. The scattered EM wave at ω_S is driven by the pump wave electric fields E_p and the EIC/IA fluctuations in the ion density at $\omega_{L\pm}$. The wave equation for the scattered EM component becomes:

$$\frac{\partial^2 F_S^{(o,x)}(z)}{\partial^2 z} + (\frac{\omega_S}{c})^2 [n_S^{(o,x)}]^2 F_S^{(o,x)}(z) = -\frac{(\omega_S/c)^2(1-[n_S^{(o,x)}]^2)}{\omega_L} F_S^{(o,x)}(z) \frac{\partial \tilde{v}_{iz}}{\partial z} \tag{8.2}$$

The mixing between the pump wave and the low frequency ion wave in the left side of Eq. (8.2) can provide both the down-shifted Stokes mode at frequency $\omega_S = \omega_p - \omega_L$ and the up-shifted anti-Stokes mode at frequency $\omega_{AS} = \omega_p + \omega_L$. The mixing of two electromagnetic waves provides the source for low frequency electrostatic wave equations that describe the ion acoustic and electrostatic ion cyclotron waves. This mixing is the result of the effects of the gradient of the radiation pressure or ponderomotive force as derived later in this section for a magnetized electron plasma.

Consider a single electron acting under the nonlinear influence of the electromagnetic fields just described. The ponderomotive force of a single particle in an electromagnetic field has been derived for unmagnetized plasma by Schmidt (1966), Chen (1984), and Eliezer (2002) and for magnetized plasma that is warm, spatially dispersive, non-stationary, and inhomogeneous by Lee and Parks (1983). A comparison of single particle and fluid approaches to this derivation is discussed by Vaclivik et al., (1986). In this paper, where the phase velocities of the high frequency pump EM waves are much larger than thermal velocities of the electrons and ions in the plasma, the single particle method will be used.

The nonlinear ponderomotive force couples the pump wave into the scattered electromagnetic waves. The ponderomotive force in an electromagnetic field using the single particle approach for a magnetized plasma and assuming small density and velocity fluctuation can be written as (Bernhardt et al., 2010):

$$\nabla(\nabla.\tilde{v_i}) + \frac{\omega_{L\pm}^2}{c_{IA}^2}\left(U_i\tilde{v_i} + i\frac{\Omega_i \times \tilde{v_i}}{\omega_{L\pm}^2}\right) = \frac{i\omega_{L\pm}q_e^2}{4m_e m_i \omega_p^2 c_{IA}^2}\left[\frac{\nabla(\Omega_e.E_T)^2 - \omega_p^2\nabla(E_T.E_T)}{\Omega_e^2 - \omega_p^2}\right] \tag{8.3}$$

where E_T is the total electric field including pump and scattered electric field, $c_{IA} = \sqrt{\gamma_e T_e + \gamma_i T_i/m_i}$, and $\Omega = eB/m$. The low frequency electrostatic and scattered electromagnetic waves grow together with the energy supplied by the pump wave amplitude $F_P^{(0)}$. Damping of the SBS mode is specified by ion-neutral collisions in $U_i = 1 - i\nu_i/\omega_{L\pm}$ and the electron-neutral and electron-ion collisions in $n_S^{(0)}$. Additional damping of the ion acoustic wave occurs with ion Landau damping but this can be neglected if $T_e \gg T_i$ (Ichimaru, 1973).

The coupled set of low- and high-frequency waves equations (1)-(3) provides a complete description of the SBS instability in a magnetized plasma that leads to the growth rate for the MSBS (Bernhardt et al., 2010). The ratio of EIC growth rate γ_{LO+} to IA acoustic growth rate γ_{LO-} is given by:

$$\frac{\gamma_{LO+}}{\gamma_{LO-}} = \sqrt{\frac{\omega_{L+}}{\omega_{L-}}}\sqrt{\frac{(\Omega_{iz}^2 - \omega_{L+}^2)(\Omega_{iz}^2 k_L^2 c_{IA}^2 - \omega_{L-}^4)}{(\Omega_{iz}^2 - \omega_{L-}^2)(\Omega_{iz}^2 k_L^2 c_{IA}^2 - \omega_{L+}^4)}} \tag{8.4}$$

where Ω_{iy} is the electron gyro vector transverse to the electromagnetic wave vector. The instability occurs at the characteristic electrostatic frequency that is a normal mode. $\omega_{L\pm}$ is

the undamped mode frequency and with the ± signs representing the two roots for the EIC and IA modes respectively above and below the ion gyro frequency.

For small wavenumbers such that $k_L \ll \Omega_i/c_{ia}$ or for propagation at small angle to the magnetic field so $\Omega_{iy} \ll \Omega_i$, Eq.(8.4) is much less than unity, the IA wave (L-) grows much faster than the EIC wave (L+).

Threshold fields for each mode are dependent on the propagation angle in the plasma. The SBS will generate IA waves rather than EIC waves because the ion-acoustic waves grow much more rapidly than the EIC waves. The conditions for this growth are favorable in the modified ionosphere over HAARP. The EM pump wave elevates the electron temperature so $T_e \gg T_i$ and the IA waves are not subject to strong Landau damping. The electrostatic wave number is equal to twice the EM wave number which becomes small near the EM wave reflection altitude. Finally, at HAARP the beam of the EM wave is tilted up the magnetic field line so the transverse component of the EIC vector is small. In summary, the MSBS preferentially yields IA waves over EIC waves. The MSBS instability threshold is controlled by the strength of the pump wave and the rate of the ion collisional damping.

A simplified expression for the ratio of the EIC and IA growth rates using the assumption $|k_L C_{IA}| \ll \Omega_i$ can be written as (Bernhardt et al., 2010):

$$\frac{\gamma_{EIC}}{\gamma_{IA}} = \sqrt{\frac{\omega_{IA}}{\Omega_i}} \tan^3\theta \tag{8.5}$$

where θ is the angle between the wave normal direction and background magnetic field where the maximum amplitude of the standing wave of the EM pump occurs.

Another theoretical model of MSBS was developed by Shukla and Stenflo, (2010) assuming that the square of the pump wave frequency is much larger than the square of the electron gyro-frequency Ω_{ce}. Considering the IA wave excited by SBS instability with assumptions of $\omega \ll \Omega_{IC}$ and $k_z \ll k_\perp$ maximum growth rate of IA wave is given by (Shukla and Stenflo, 2010):

$$\gamma_{IA} \approx \frac{k_z u_0 \omega_{pi}}{2(1+b)\sqrt{\omega_0 \Omega_{IA}}} \tag{8.6}$$

where $b = k^2 C_s^2/\Omega_i^2$, C_s is ion sound speed, $u_0 = eE_0 m_e \omega_0$ is the oscillation velocity, ω_o is pump frequency, E_0 is pump electric field, and ω_{pi} denotes ion plasma frequency. It has been shown for $\omega > \Omega_{IC}$ that maximum growth rate for EIC wave also can be written as (Shukla and Stenflo, 2010):

$$\gamma_{IC} \approx \frac{k_\perp u_0 \omega_{pi} \left[1 + \frac{b k_z^2}{k_\perp^2 (1+b)}\right]^{1/2}}{2\sqrt{\omega_0 \Omega_{IC}}} \tag{8.7}$$

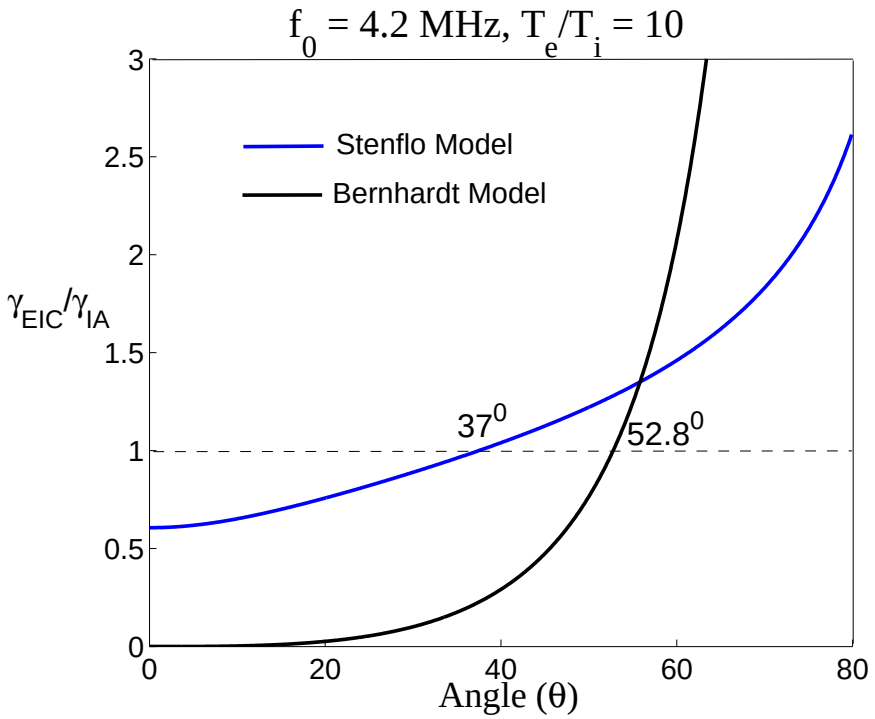

Figure 8.1: Dispersive characteristics and growth rate of electrostatic ion cyclotron waves for varying the electric field amplitude

where $k \perp$ is the perpendicular wavenumber and k_z is the parallel wavenumber to the magnetic field. The IA growth rate in this case also is greater than the EIC growth at smaller angle relative to magnetic field which validates the analytical expressions of IA and EIC growth rate given by Bernhardt et al. (2010). According to the Fig 8.1, Bernhardt's model predicts that EIC growth rate should exceed IA growth rate for $\theta_0 > 45°$ while Shukla's model predicts the same trend for $\theta_0 > 37°$. This figure shows the transition between IA and EIC wave excitation as a function of propagation angle relative to B. Ion acoustic waves grow much faster than EIC waves for propagation angle close to magnetic zenith. For propagation at larger angles and nearly perpendicular to B, the EIC mode is dominant.

8.3 Ray racing and wave matching conditions for MSBS

The Hamiltons equations for ray paths using the refractive index in a magnetized plasma are given by Hazelgrove (1955), Yeh and Liu (1972) and Budden (1985). These equations were solved numerically for propagation in the measured ionosphere over the HAARP transmitter. When the HF beam is tilted off magnetic zenith, the wave normal angle relative to the magnetic field direction will vary with altitude. Ray tracing in the anisotropic plasma can

provide both the wave number magnitude k_0 and the wave normal angle θ. The magnetic zenith (MZ) path starts out along the magnetic field direction with a propagation angle of zero. This angle stays near zero except within a few kilometers below the plasma resonance altitude where the angle becomes 90 degrees at reflection. The wave propagation angle θ at the upper hybrid resonance altitude is 12 degrees for the upgoing MZ ray. The ray propagates horizontally for about 10 km with a wave normal nearly perpendicular to B. The ray returns to earth with a 28 degree angle relative to B. The observations of upshifted MSBS lines indicate the presence of EM waves with simultaneous upward and downward propagation along the same field-aligned path.

Downshifted emission lines are a result of interaction of pump wave with plasma below the reflection altitude. As the EM pump loses energy to generate parametric decay instability, downshifted MSBS- line is weaker than the pump line. The weakened upward pump due to the interaction below the plasma resonance altitude will reflect near where refractive index goes to zero. This wave interacts with low frequency IA waves excited through previous interaction and generate a secondary upward scattered electromagnetic wave with wave vector $k_{S+} = k_0 + k_L$ at frequency $\omega_{S+} = \omega_0 + \omega_L$. This scattered wave also reflects back and produces an upshifted spectral line in the spectra. Since this mode is generated by a weaker pump wave, upshifted emission lines are expected to be weaker than downshifted spectral lines.

According to the matching condition, the IA wave mode is limited to frequencies less than the ion cyclotron frequency f_{ci} while the EIC mode is found for frequencies just above f_{ci}. The energy and momentum conservation requires that the wave frequency and propagation direction satisfy these expressions:

$$\omega_0 = \omega_S + \omega_L \tag{8.8}$$

$$k_0 = k_S + k_L \tag{8.9}$$

where k_0, k_S , and k_L denote the wave numbers for the upward electromagnetic pump, scattered electromagnetic wave and IA/EIC waves, respectively (Kruer, 1988; Eliezer, 2002). The frequency of low frequency products ω_L is given by (Bernhardt et al., 2010):

$$\omega_L^2 = \frac{1}{2}\left(4c_I A^2 k_0^2 + \Omega_i^2 \pm \sqrt{16c_I A^4 k_0^4 + \Omega_i^4 - 8c_I A^2 k_0^2 \Omega_i^2 \cos(2\theta)}\right) \tag{8.10}$$

where + sign represents the EIC wave and - sign denotes the IA wave. The computed matching conditions for the HAARP experimental parameters and two propagation angles with respect to magnetic field are shown in Fig 8.2b based on the numerical solution of Eqs. (3) and (4). The ion acoustic wave is limited to frequencies less than the longitudinal component ($f_{ci}Cos(\theta)$) of the ion cyclotron frequency. Fig 8.2b illustrates that O-Mode

can excite the IA wave and EIC at both Upper Hybrid (UH) and reflection altitudes. The generated IA wave at the reflection altitude is expected to be near 10 Hz and the IA emission originated at the upper hybrid altitude has frequency of about 20-30 Hz. EIC wave excited at the reflection and upper hybrid altitude also has a frequency just above the f_{ci}. As can be seen, increasing the electric field angle at the reflection altitude from 14° to 42° reduces the frequency of excited IA waves and also increase the EIC frequency however to a lesser degree. It turns out that increasing C_s also has the similar effect as the electric field angle on the frequency of the excited modes

8.4 The electromagnetic pump in the ionosphere and dispersion relation

For vertical propagation in a horizontally stratified plasma layer, the second order differential equation for O- and X-mode can be written as follows:

$$\frac{\partial^2 F_P^{(O,X)}(z)}{\partial z^2} + k^{(O,X)}(z)^2 F_P^{(O,X)}(z) = 0 \tag{8.11}$$

The refractive index for these modes is given by (Budden, 1985):

$$n^{(O,X)} = \sqrt{1 - \frac{X}{U + iY R_{O,X} \cos\theta}} \tag{8.12}$$

where wave polarization is given by (Yeh and Liu, 1972):

$$R_{O,X} = \frac{i}{\cos\theta}\left[\frac{Y\sin^2\theta}{2(U-X)} \pm \sqrt{\frac{Y^2\sin^4\theta}{4(U-X)^2} + \cos^2\theta}\right] \tag{8.13}$$

$U = 1 - i\frac{\nu_{en}}{\omega}$ denotes collisional loss between electrons and ions and ν_{en} is electron-neutral collision frequency. Finite difference approximations are used for solving Eq.(8.11) numerically. The boundary conditions above and below the resonance altitude are specified by the WKB approximation.

The relationships between the electric field components of the wave and the function $F^{(O,X)}(z)$ for O- and X-mode are given by (Yeh and Liu, 1972):

$$\left\{E_x^{(O)}(z), E_y^{(O)}(z), E_z^{(O)}(z)\right\} = \left\{1, R^{(X)}(z), Q_P^{(O)}\right\} \frac{F^{(O)}(z)}{\sqrt{R^{(X)}(z)^2 - 1}} \tag{8.14}$$

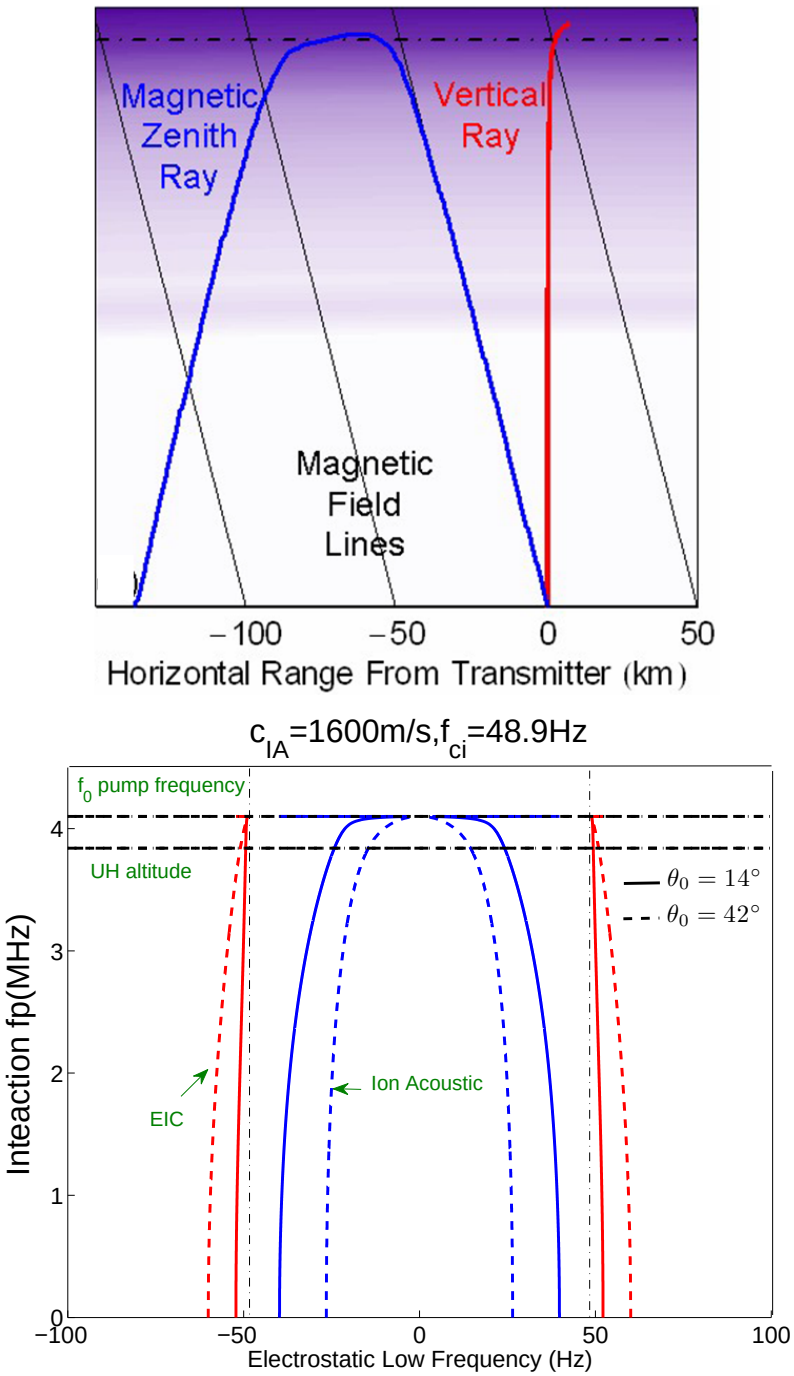

Figure 8.2: a) Ray paths for wave propagation to the magnetic zenith and the vertical b) Generalized SBS matching conditions for O-Mode electromagnetic waves at 4.1MHz for an ionosphere with an ion sound speed of 1600 m/s and an ion gyro frequency f_{ci}=49.6 Hz propagating at an angle of 14.5° with respect to magnetic field direction.

$$\left\{E_x^{(X)}(z), E_y^{(X)}(z), E_z^{(X)}(z)\right\} = \left\{R^{(X)}(z), 1, R^{(X)}(z)Q_P^{(X)}\right\} \frac{F^{(O)}(z)}{\sqrt{R^{(X)}(z)^2 - 1}} \tag{8.15}$$

with the magnetic field B in the y-z plane, $R_P(X)$ is the extraordinary mode polarization, and $Q_P^{(O,X)}$ is the ordinary and extraordinary mode longitudinal polarization for the pump wave. Details on the derivation are given by Yeh and Liu (1972) equations 5.17.11 and 5.17.12 and Budden (1985). In terms of refractive index, the polarizations for both the O- and X- mode waves are (Yeh and Liu, 1972):

$$R^{(O,X)} = \frac{X_e - 1 + (n^{(O,X)})^2}{iY_e \cos\theta[1 - (n^{(O,X)})^2]} \tag{8.16}$$

$$Q^{(O,X)} = \frac{iY_e \sin\theta[1 - (n^{(O,X)})^2]}{1 - X_e} \tag{8.17}$$

For stimulated Brillouin scatter, the largest interactions occur near the O-Mode reflection altitude where $X_e \longrightarrow 1$ and the Quasi-longitudinal QL conditions do not apply. For this reason, the QL approximation is not employed for simplifications in this work. Near the X-Mode reflection altitude where $X_e = 1 - Y_e$, the transverse ($E_x(X)$, $E_y(X)$) electric field amplitudes become large but the longitudinal $E_z(X)$ may remain small.

A solution of the wave equation is shown in Fig 8.3 for the three components of electric field for altitude range 172-177 km. The numerical solution starts at altitude 172.4 km with an upward propagating wave with a transverse electric field of 1.2 V/m corresponding to 1GW ERP at 4.5MHz in the ionosphere neglecting any D-region absorption. As the pump wave approaches the plasma resonance altitude where the pump frequency 4.5 MHz equals the plasma frequency, the amplitude of the transverse component E_y increases to 3 V/m while the amplitude of the other transverse component drops to 0.5 v/m. The vertical/longitudinal electric field has the largest amplitude of $\sim$ 200 v/m only a few tenths of kilometers below the plasma resonance altitude. Such a strong electric field can strongly modify the plasma and the linear dispersion relation used to derive the matching condition is no longer valid in this region. For the simulation illustrated in Fig 8.3, the peak electric fields near the UH resonance altitude are (E_x , E_y , E_z)=(1.6, 1.9, 2.3) V/m.

8.5 Experimental Observations of MSBS

We present data from 5 different experiments performed on July 18-23, 2010, July 19-27, 2010, and August 5-9, 2012 at the HAARP facility (geographical coordinates 62.39^0 N, 145.15^0 W). The effective radiated power was 1 GW, which exceeds the capability of all

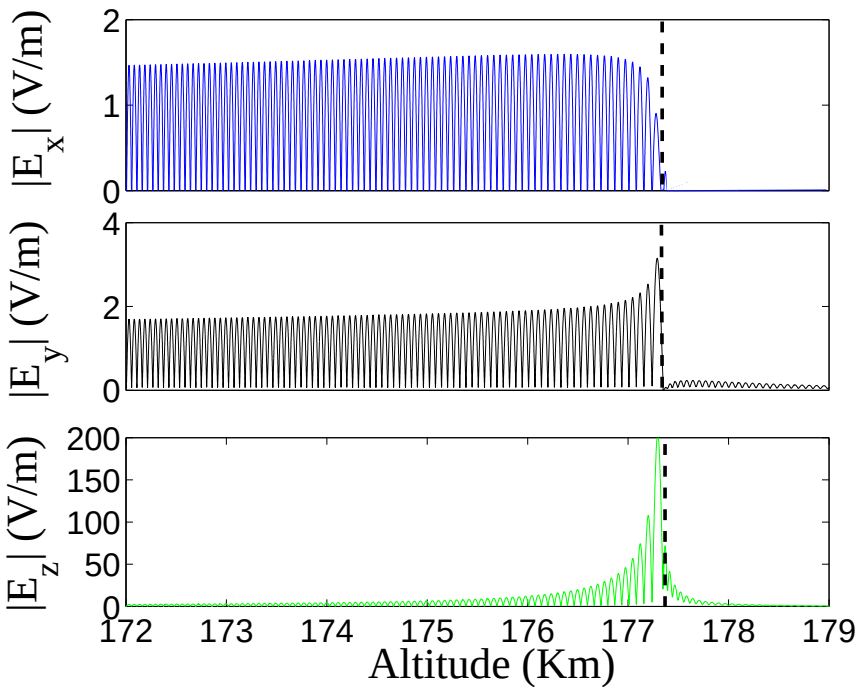

Figure 8.3: Computed transverse and longitudinal electric fields produced by the 4.5MHz HAARP transmitter. The maximum electric field is found in the longitudinal component E_z=200 V/m just below the plasma resonance at 177.74 km altitude where the local plasma frequency is 4.48 MHz.

other similar HF facilities. A large dynamic range HF receiver was set up at HAARP to record stimulated electromagnetic emissions SEE. The reflected EM signal was measured using a digital receiving system sampled the HF signals from a 30 m folded-dipole antenna at a rate of 250 kHz.

The HF radio waves had O-mode polarization and the pump beam direction was alternated between the geomagnetic zenith (MZ), (202^0 azimuth, 14^0 zenith) up to 202^0 azimuth, 28^0 zenith. The beam was transmitted in a continuous or quasi continuous wave mode (for example 30 s on, 30 s off) for up to two hours per experiment. The recorded time series were analyzed by applying a fast Fourier transform with a Blackmann window, corresponding to 0.8 s, revealing sideband emissions in the frequency domain with a resolution of 1.25 Hz.

Observations of the Magnetized Stimulated Brillouin Scatter MSBS were obtained with HAARP by tuning the transmitter near the third harmonic of the electron cyclotron frequency $3f_{ce}$. In the previous study by Bernhardt (2010), it has been shown that excited electrostatic waves through the MSBS process in the ionosphere, that could be IA and EIC waves, depend on the value of θ_0 (angle between the wave vector and magnetic field) at the interaction altitude that could be either upper hybrid or refection altitude. Although the theoretical calculation suggests the excitation of MSBS process with X-mode pump wave, it should be noted no IA or EIC emission line was observed during X-mode heating.

Fig 8.4 illustrates an SEE spectrum immediately after the turn on of the HAARP transmitter at 4.1 MHz for o-mode polarization. This figure represents the effect of angular variation on the excitation of EIC emission line associated with MSBS. The data was taken during the 2011 campaign. The HF signal data were acquired with the Australian developed GBox-5 receiver that digitizes a 250 kHz band around the pump frequency for digital signal processing to produce the SEE spectra. The spectrum for a full power beam pointed at 3 different zenith angle ZA= 0°, 7° and 14° with azimuth angle 202° is shown. The spectrum shows the upshifted and downshifted IA emission lines excited at reflection altitude at frequency around 10 Hz. In this case for the beam offset from the MZ by 0° and 7°, only IA emission lines appear in the spectrum and when the beam tilted more to 14° a strong EIC line is produced at 51 Hz corresponding to the ion gyro frequency for the Oxygen ion. It has been shown that f_{ci} at 225 km altitude over HAARP is estimated to be 49 Hz. This is consistent with the previous observation of MSBS (Bernhardt et al., 2010) that a stronger excitation of EIC spectral line was observed and predicted at larger angles with respect to the MZ. The 120 Hz lines are produced by power ripple in the transmitter power system. As mentioned before, the upshifted IA lines are the result of scatter by the reflected pump wave from the IA waves to produce an upgoing, up-shifted EM wave that reflects in the ionosphere and is received on the ground.

A more extensive study on MSBS excited at the third harmonic of electron cyclotron frequency was conducted during 2012 campaign at HAARP. Fig 8.5 shows SEE spectra for the experiment carried out on Aug 12, 2012 from 4:30 UT- 5:30 UT. The transmitter was pointed at ZA=18°, AZ=202° and operated with O-mode polarization at full power alter-

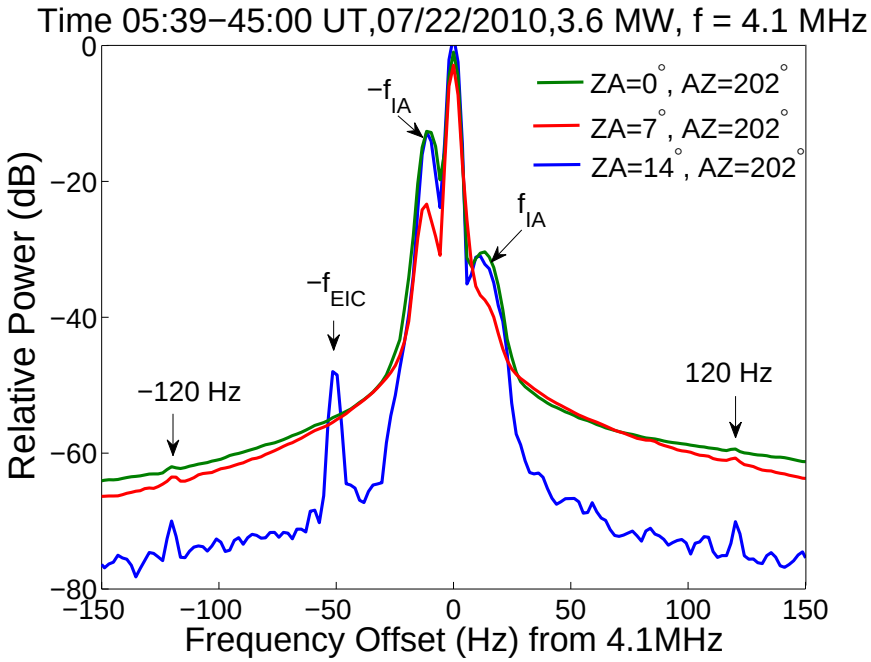

Figure 8.4: Low-frequency SEE spectra showing ion-acoustic spectral lines when the beam is offset from the magnetic zenith is 0° and 7°, and when the beam tilted more to 14° a strong EIC line is produced.

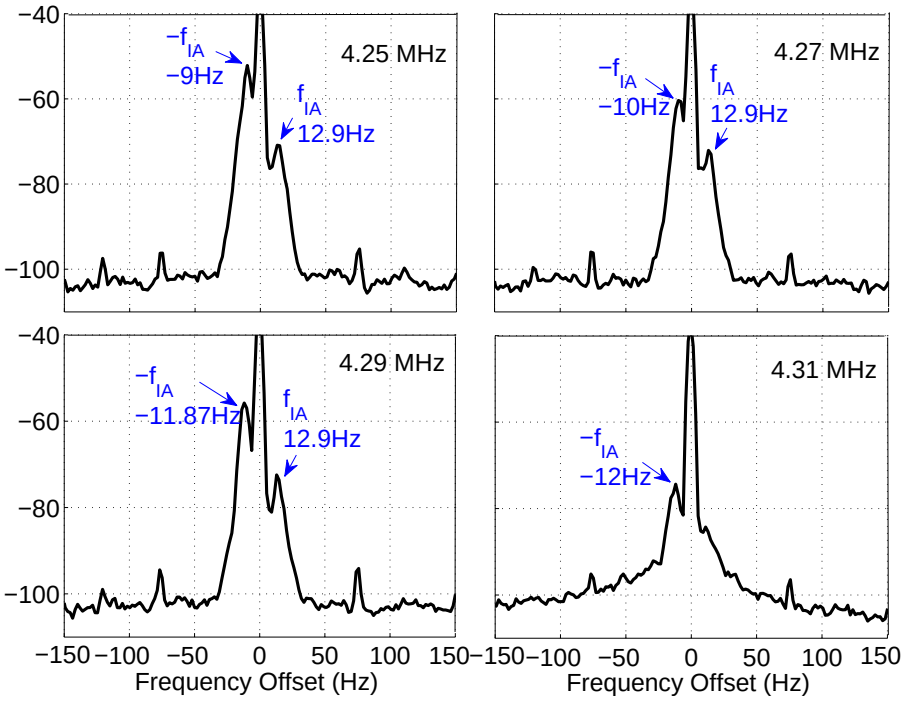

Figure 8.5: Experimental observations of IA emission lines associated with MSBS during which the heater frequency was tuned to 4.25 MHz, 4.27 MHz, 4.29 MHz, and 4.31 MHz and heating cycle was 30 s.

nating between 30 sec at full power and 30 sec off to allow recovery from artificially induced effects. The transmitter frequency stepped through $3f_{ce}$ from 4.25 MHz to 4.31 MHz in 20 kHz steps every other "on" period to compare effects away and near $3f_{ce}$. Stronger IA emission lines are observed when the pump frequency is further away from the $3f_{ce}$ and as the pump frequency gets closer to the gyro-harmonic MSBS process becomes very weak. As can be seen, upshifted IA emission line almost disappears at 4.31 MHz and the strength of the downshifted IA emission lines drop about 20 dB. Increasing the pump frequency towards the gyro-harmonic also shifts the SBS-1 line from -9 Hz to -12 Hz while the SBS+1 stays almost at the same frequency.

The 2010 campaign at HAARP aimed at measuring the threshold of EIC and IA emission lines. Variation of the spectrum with transmitter power for three values of power is illustrated in Fig 8.6. The previous study by Bernhardt (2010) has shown that EIC lines have much smaller growth than IA lines. Therefore, in order to estimate the threshold for the EIC emission lines the experiment was conducted for 3 transmitter powers 3.6 MW, 2.9 MW and 1.9 MW. The pump wave frequency was at 4.18 MHz and 4.1 MHz and transmitter beam was pointed 14 degrees off the MZ. The EIC emission line can be clearly seen in the spectra of Fig 8.6a for pump power 3.6 MW around 52 Hz downshifted from the pump. This frequency is consistent with the frequency range predicted by the matching condition in the

first section and shows that both IA and EIC lines are produced by the interaction at the reflection altitude. This figure shows that reduction of the pump amplitude may bring the pump altitude at the reflection altitude below the EIC mode threshold which is necessary for MSBS process and turn-off the EIC instability. This happens when the pump amplitude reduces to 2.9 MW where strength of EIC line drops significantly relative to the full power case. No EIC line is observed for pump power 1.9 MW. As can be seen, the strength of the IA emission line does not change by reducing the power amplitude from 3.6 MW to 1.9 MW which indicates that the IA waves have much larger growth rate than EIC waves. To measure the threshold of IA lines another experiment with fine power step at lower amplitude was carried out that will be presented shortly. Fig 8.6b shows the same behavior for the pump frequency 4.1 MHz. This case also shows a similar behavior with Fig 8.6a and the EIC line almost disappears by reducing the pump amplitude to 2.9 MW. Reducing the power amplitude to 1.9MW in this case makes the upshifted IA line very weak.

Pump amplitude reduced in 3-dB steps in order to measuring the threshold for the excitation of IA lines. The MSBS experiment on July 19, 2010 used power beam at magnetic zenith, vertical and anti-magnetic zenith with pump amplitude varying from 3.6 MW to 0.11 MW. Fig 8.7a shows the temporal evolution of IA emission lines with pump amplitude for the beam pointed at magnetic zenith and the spectra illustrates a pair of weak upshifted MSBS lines (anti-stokes lines) and two stronger downshifted SBS lines. The past theoretical works on the stimulated Brillouin spectra in an unmagnetized plasma by Kruer (1988) and Eliezer (2002) have also predicted that a stronger downshifted IA lined should be produced. All the IA SBS lines presented in this investigation show stronger downshifted lines than upshifted lines. Fig 8.7a and b shows that when the pump beam was directed vertically and towards MZ SBS$\pm$1 and SBS$\pm$2 emission lines appear symmetrically around f_0 with frequency shifts $\sim$10Hz and $\sim$26Hz, respectively. The downshifted SBS$-$1 is well developed in most spectra but the upshifted SBS+1 cannot always be identified. It turns out that the downshifted lines have the lowest threshold among the IA emission lines. When the HF beam was pointed toward the magnetic zenith spectra shows two set of lines. One set is near 27 Hz which represents excited IA waves due to the interaction at the UH altitude and there is a second set of lines near 10 Hz that corresponds to the interaction at reflection altitude. This is in agreement with the wave matching condition and theory presented in the section 3. The SBS$-$1 line has a frequency offset 11.4 Hz from the pump and SBS$\pm$1 are located at 26.7 Hz and 29 Hz from the pump wave. Upshifted lines are weaker than the stokes lines which is consistent with the theory and represents the weak interaction of the reflected wave with the local plasma at the UH and reflection altitudes. It turns out that SBS+1 has the lowest threshold of about 1.8 MW and SBS$\pm$2 lines disappear from the spectra by reducing the pump amplitude to a value less than 0.45 MW. Spectra for the beam pointed at vertical are illustrated in Fig 8.7b which shows the same trend as panel (a). The SBS+1 line has the lowest threshold and only appears for 3.6 MW pump power. SBS$\pm$2 lines are weaker in comparison with MZ, but they have almost the same threshold of about 0.4 MW. As expected from theory, increasing the angle between wave normal and magnetic field line reduces the growth rate of IA lines and increases the threshold. As the result, no IA emission line

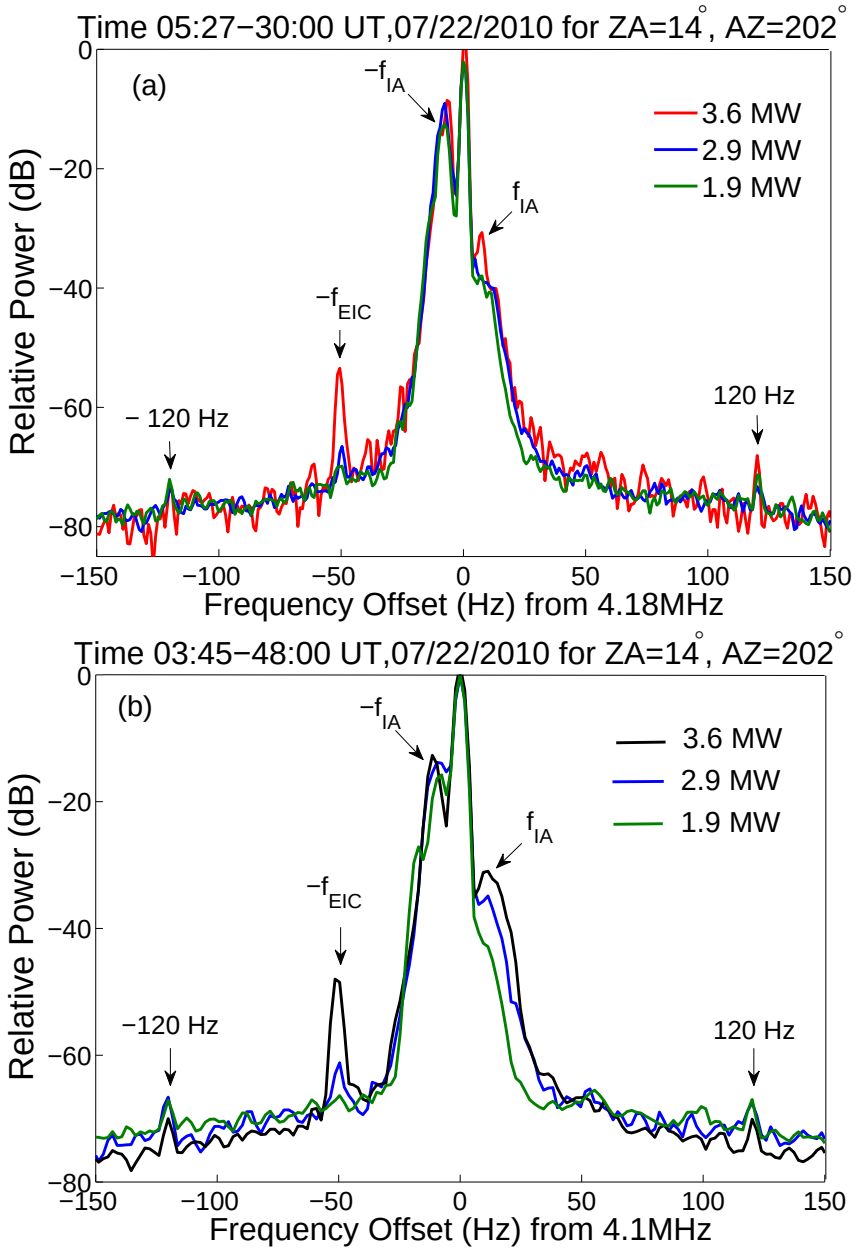

Figure 8.6: Variation of EIC line with the pump amplitude (a) f = 4.18 MHz (b) 4.1 MHz

originating from the UH altitude is seen and the SBS−1 line has a threshold about 1.9 MW. It should be noted that naturally existing IA waves damp out in the ambient ionosphere as the result of ion Landau damping but this can be neglected if $T_e \gg T_i$ (Ichimaru, 1973). In the ionospheric modification experiment using HAARP HF transmitter, it is assumed that the electron temperature is much larger than the ion temperature so ion Landau damping can be neglected.

To get a better estimation of the threshold of MSBS processes including both IA and EIC lines, a new experiment was designed and carried out on July 24, 2011. The transmitter was operated with 4 minute on and 1 minute off cycles. The power increased from 0.1 MW to 3.6 MW in 210 s and 35 steps; and set at full power with 3.6 MW for 30 s. The beam was tilted from magnetic zenith to 15 degree off with 3 degrees increment to excite both IA and EIC emission lines. The measured threshold of MSBS emission lines is similar to the previous experiments in which the pump power was increases in 3-dB steps every "on" and "off" period. The upshifted IA emission lines has a power threshold near 1 MW and EIC emission line appears in the spectra when the amplitude of the pump power exceeds 3 MW. The dynamic spectra recorded for a pump beam at (ZA=18° and AZ=202°) (1GW ERP) at 4.2MHz is illustrated in Fig 8.8c and pump power is increased from 0.1 MW to 3.6 MW. After a transient produced by the HAARP transmitter at turn on, the SEE spectra shows the central pump line, two MSBS around the pump at 10 Hz which correspond to the excited IA lines near the reflection altitude. IA lines appear in the spectra when pump amplitude exceeds 1.15 MW around t=60 s after pump turn-on. When the power exceeds 2.9 MW at t = 170 s, a strong emission line appears in the spectra at 50 Hz as a result of excited EIC wave.

A competing process for excitation of SEE involves mode conversion of the O-Mode EM pump wave into an upper hybrid wave. This upper-hybrid wave undergoes parametric decay into a lower frequency upper-hybrid wave and a lower hybrid wave. The daughter UH wave mode converts on field aligned irregularities into an O-Mode electromagnetic wave which is received on the ground as a down shifted maximum (DM) peak. The side-by-side spectrograms in Fig 8.9 show the disappearance of the MSBS line relative to the subsequent appearance of the field-aligned irregularity and upper hybrid line (DM). Weaker lines at 120 and 180 Hz are produced by power-line harmonics in the pump transmissions as illustrated by the vertical lines in the spectra on the left side of Fig 8.9. The fast narrow continuum (FNC) is a smooth, down-shifted feature seen immediately after pump start (Leyser, 2001). The 8 kHz offset of DM from the pump frequency is consistent with an estimated lower-hybrid frequency of 8.18 kHz. This feature narrows to less than 5 kHz when the DM starts to appear. The spectral features below the dashed line in Fig 8.9 are formed without field-aligned irregularities (FAI). Above the dashed line, the effects of FAI, especially in the UH resonance region, are important.

The temporal variations in the peak amplitude of the MSBS lines are shown in Fig 8.10 where the dB power scale has been chosen to make average received pump power about 0 dB. The MSBS line (NP) appears immediately after the pump turn on at 21:35:30 UT.

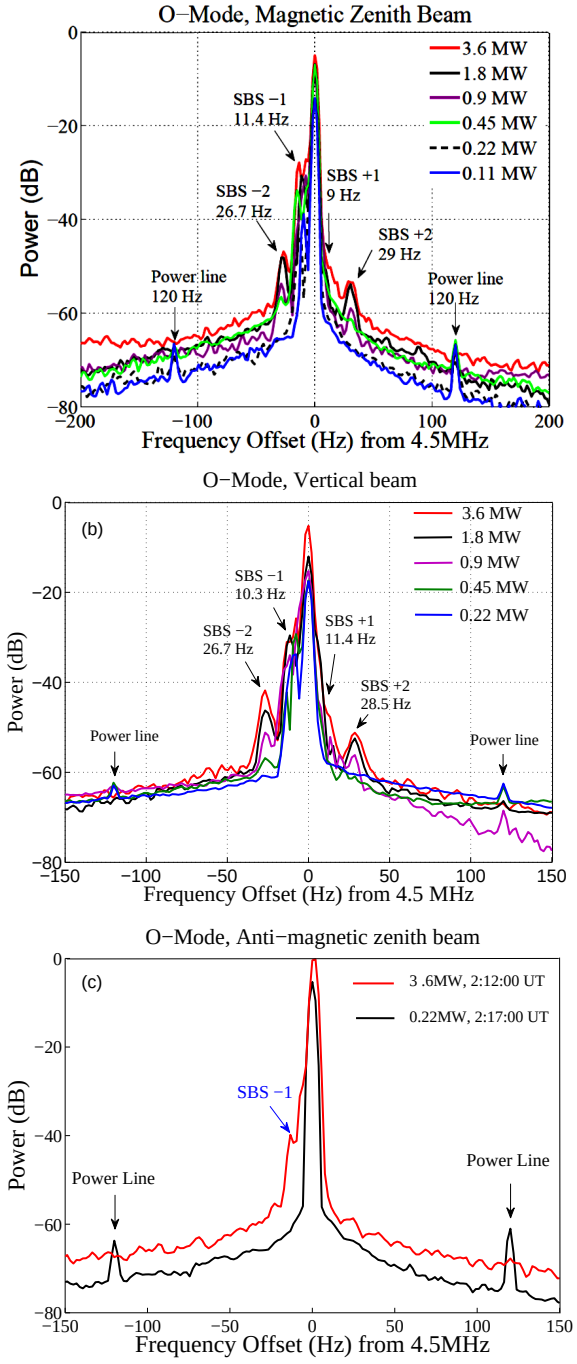

Figure 8.7: Spectra of scattered electromagnetic waves from the HAARP transmitter operating at 4.5MHz with 1GW effective radiated power. All the data were taken within a 1 hour period on July 20, 2011. The downshifted lines are also called the Stokes lines, downshifted SBS- lines or the downshifted narrow peaks (np-). The upshifted lines are similarly called the anti-Stokes lines, upshifted SBS+ lines or the upshifted narrow peaks (np+). The 120 Hz lines are produced by power ripple in the transmitter power system.

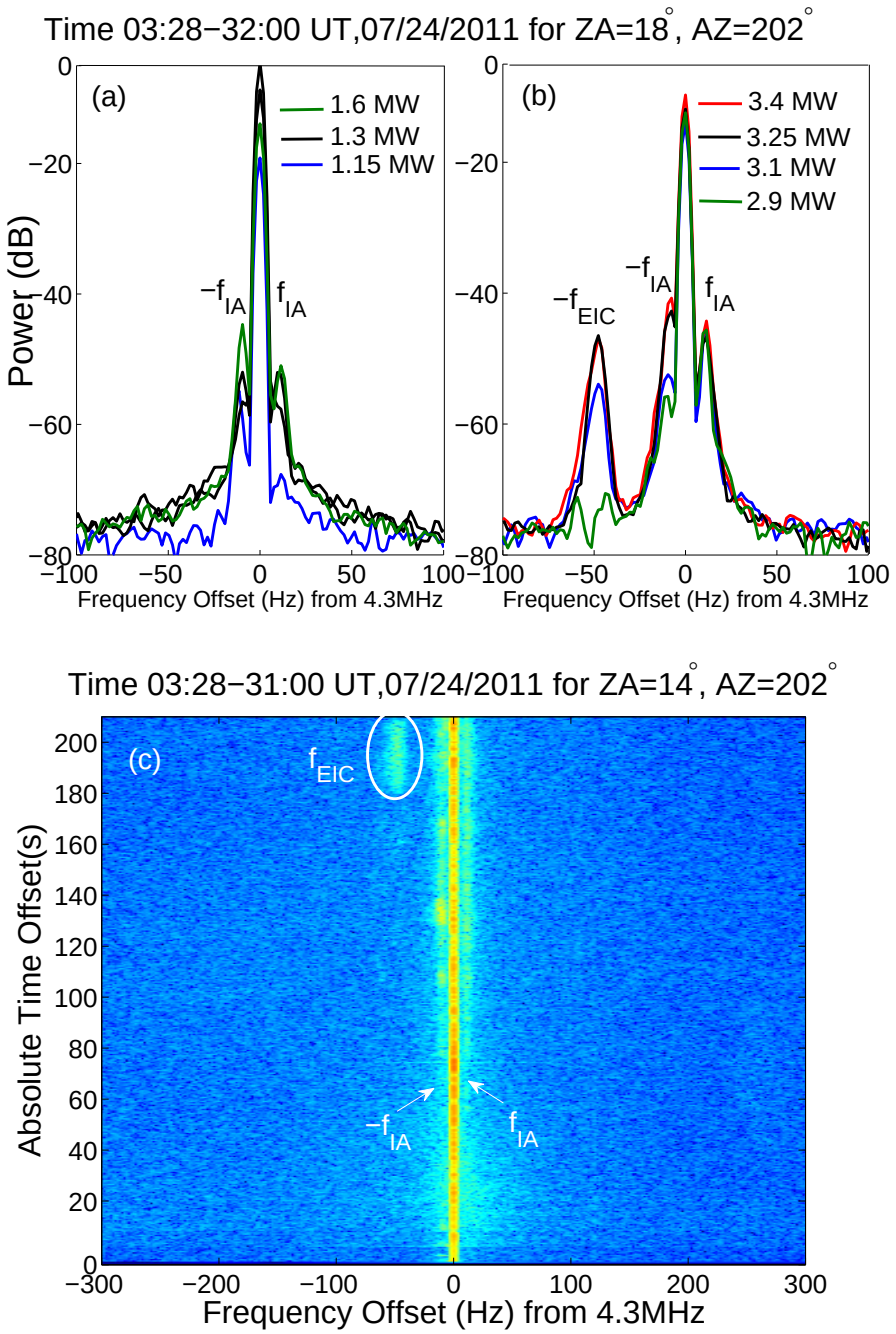

Figure 8.8: Spectrogram of the stimulated Brillouin scatter lines for a pump wave beam offset 14 degrees from the magnetic field direction.

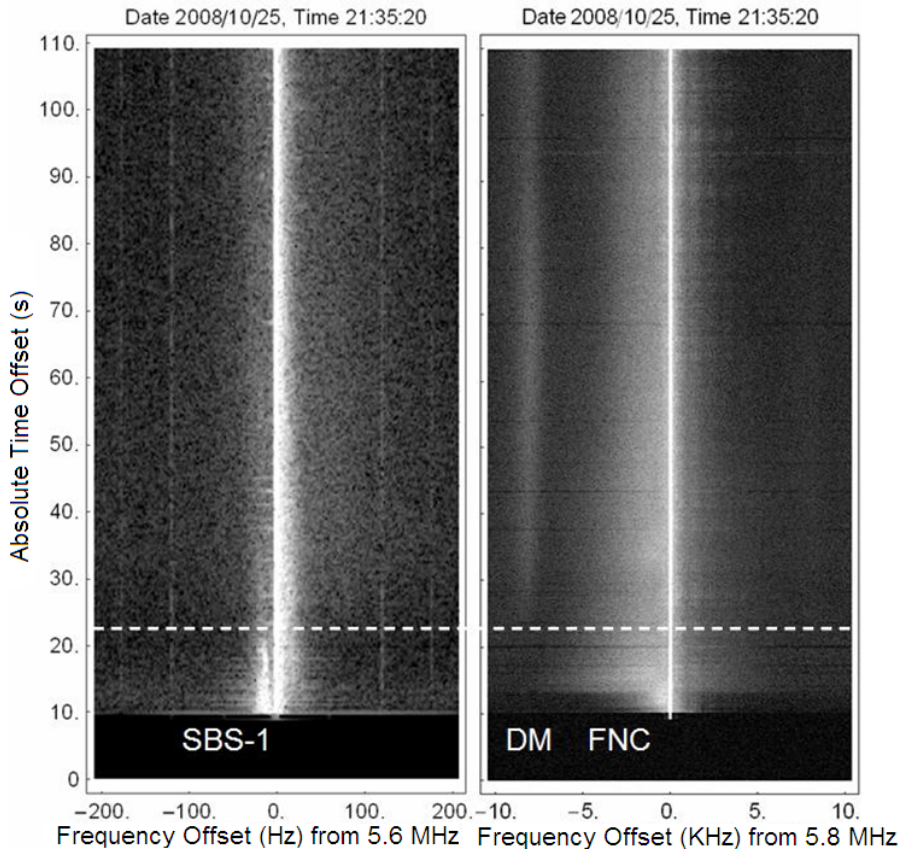

Figure 8.9: Low and medium frequency spectrograms of the SEE emissions around the 5.8 MHz carrier. The downshifted maximum (DM) starts a pump turn-on and disappears after 12 seconds. The Fast Narrow Continuum (FNC) broadens a few seconds after turn-on and then decays in width after 12 seconds. The downshifted maximum (DM) starts to appear soon after the DP has vanished.

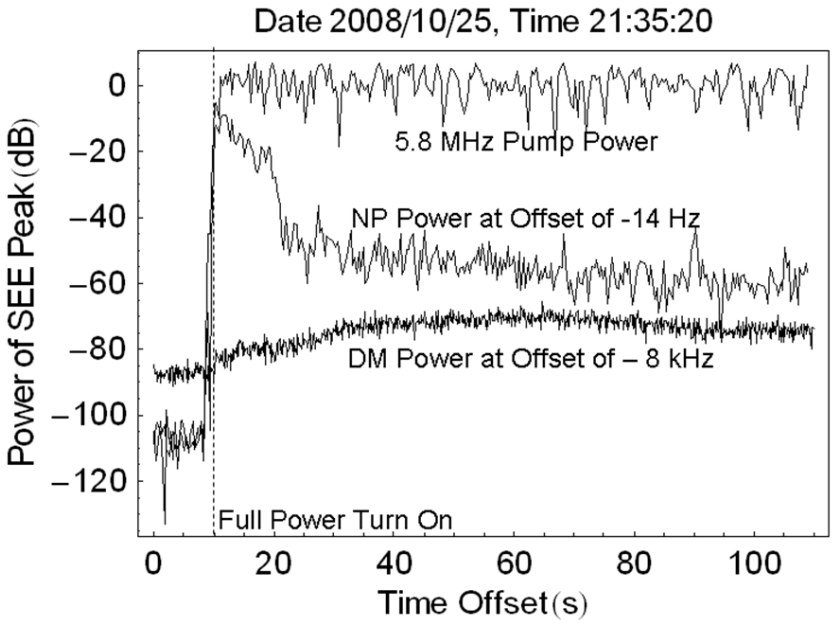

Figure 8.10: Time history of the reflected pump amplitude, the downshifted SBS line, and downshifted maximum DM after turn on of the 5.8 MHz pump. The average pump power shows no systematic drop but the narrow peak (NP) associated with the SBS instability decays and then precipitously drops. The drop occurs just before the DM power begins to increase.

The MSBS line decays for 11 seconds at a rate of 1.14 dB/second. At 21:35:41, the NP or SBS-1 line power drops by 30 dB vanishing from the spectra. Past this time, the spectrum is composed of the upshifted continuum and power-line harmonics in the pump wave. The DM power starts to increase at 21:35:42, 12 seconds after turn on. During this whole process, the average received pump power stays at about 0 dB.

The explanation for the sudden drop in the SBS amplitude is that the pump wave becomes depleted by absorption at the UH resonance level in the ionosphere. The electromagnetic wave power near the reflection height can be reduced by the formation of field aligned irregularities at the upper hybrid altitude were the pump wave is then converted into UH waves.

8.6 Conclusions

The generalized magnetized stimulated Brillouin scatter MSBS was studied with both theory and ionospheric heating experiment. A dispersion relation of MSBS, wave matching condition

and ray tracing were employed to investigate the required conditions for excitation of MSBS instability in the modified ionospheric plasma. The theory predicts a beam angle dependence for the excitation of the IA and EIC lines of MSBS. For propagation at small angles to the magnetic field, the IA lines grow much faster than the EIC lines and EIC lines are excited when the transmitter beam is titled off MZ. It turns out that IA waves have lower thresholds than EIC waves and expected to appear in the spectra at much lower pump power. Tuning the pump frequency to frequencies close the gyro-harmonic also weakens the MSBS process. Variation of IA and EIC emission lines with pump wave frequency sweeping near the $3f_{ce}$ and beam angle were examined during 2010, 2011 and 2012 campaigns at HAARP. The threshold of each emission line was measured by stepping and sweeping the amplitude of the pump wave that gives an estimation of the electric field at the interaction altitude needed to derive each mode. Experimental observations show good agreement with theoretical calculation. Competition of the downshifted maximum DM produced by artificial field aligned irregularities and MSBS for the electromagnetic pump field was observed and growth rate of the formation of the FAIs was measured.

Chapter 9

Diagnostic Techniques using Stimulated Ion Bernstein Scatter SIBS in the SEE Spectrum

This section is organized as follows. In the next section, the experimental procedure is described. Then experimental observations are provided for two experimental campaigns. Next, an analytical model is used to study the parametric decay instability in the interaction region. Parametric decay instability is then considered for a variety of parameters. The impact of 1) the pump field strength, 2) its frequency relative to the electron gyro-harmonic frequency, and 3) angle of the pump field relative to the geomagnetic field on the SEE spectrum are considered. A corresponding mode associated with the broadband feature is investigated. Finally, summary and conclusions are provided.

9.1 Experimental Procedure

The data from four different experiments performed 21-26 July 2011 and 5-9 August 2012 at the HAARP facility (geographical coordinates 62.39^0 N, 145.15^0 W) are presented. The effective radiated power was 1 GW, which exceeds the capability of all other similar HF facilities. The reflected EM signal was measured using a 30 m folded dipole antenna and a receiver with around 90 dB dynamic range at a rate of 250 kHz. A large dynamic range HF receiver was set up during the 2011 campaign at HAARP to record Stimulated Electromagnetic Emissions SEE. Four measurement sites were used during the 2012 campaign at different locations with respect to the HF transmitter.The experiments were carried out in O-mode. Different sets of experiments were designed to investigate the effect of the pump field strength, antenna beam angle of transmission and frequency sweeping near $2f_{ce}$ and $3f_{ce}$.

One set of experiments on July 24, 2011 between 03:58 UT-04:58 UT was designed to measure the excitation threshold of the SIBS decay instability near $3f_{ce}$. The heater beam was pointed at 5 different zenith angles to study the variation and the strength of the SIBS emission lines. The zenith angles were 14, 18, 21, 24 and 27 degrees. The azimuth angle was 200 degrees for all cases. The power was increased from 0.1MW to 3.6MW in 0.1MW steps every 6 sec. The power spectrum of the experiments shows discrete structures both upshifted and downshifted from the pump frequency (4.3 MHz) as soon as the pump amplitude exceeds 0.7MW. This was the first observation of SIBS excited near $3f_{ce}$ and will be presented in the next section. Variation of previously observed discrete and broadband features at $2f_{ce}$ with pump frequency sweeping was examined on July 25, 2011 between 5:55 UT-6:55UT. The heater beam was pointed at magnetic zenith and vertical, and the pump frequency was increased from 2.9 MHz to 2.96 MHz in 20kHz steps. The corresponding spectra show the ion gyro-structures embedded in the broadband feature, broadband feature, discrete structures as well as low frequency ion acoustic IA emission lines associated with the MSBS process.

Experiments during the 2012 campaign were designed to produce SIBS near the $3f_{ce}$. A more detailed study on the effect of the proximity of pump field to $3f_{ce}$ and angle of antenna beam were considered. The zenith angle was varied from 14° to 27° in 4 steps. The heater duty cycle was 45 sec on, 45 sec off for the beam pointed at MZ and was 30 sec on, 30 sec off for all other transmission angles. During all 2012 experiments, the HAARP heater was operated transmitting O-mode continuous wave at full power of 3.6 MW. In the first set of experiments, the pump frequency was increased 4.17 to 4.35 MHz in 0.2 MHz steps. This experiment was carried out on August 7, 2012 between 4:30 UT -5:30 UT.

The last set of experiments was dedicated to a joint observation of optical emissions and SEE to study the physics associated with artificial airglow excited by high power radio waves. Coordinated optical and SEE observations were carried out during the 2012 campaign in order to provide a better understanding of electron acceleration and precipitation processes. Optical emissions were observed with multiple wide- and narrow-field imagers at HAARP during the experiment. Results for correlation between SEE SIBS features and airglow is provided for pump heating near $2f_{ce}$ during the campaign. The observations affirm strong correlation between the SIBS and the airglow. On 9 August 2012, the HAARP facility was operated at 2.7 MHz between 11:56 and 11:57 UT after sunset, and then the transmitter frequency was increased in 20 kHz steps every 30 sec up to 2.9 MHz. The beam was pointed at the MZ (202° azimuth, 14° elevation).

The International Geomagnetic Reference Field (IGRF) model provided the magnetic field strength and direction in the upper atmosphere over HAARP. The magnetic field near the HF reflection altitude is estimated to be $|B| = 5.01210^{-5}$ Tesla for a typical interaction altitude 220 km which was the case during most experiments. This magnetic field corresponds to an ion gyro-frequency f_{ci} near 48 Hz and electron cyclotron frequency 1.4 MHz.

The ionospheric plasma at F region heights above the heater was probed with HF transmissions from the SuperDARN HF radar located at Kodiak, Alaska. This radar detects

backscatter when decameter-scale irregularities are present in the ionization.

9.2 Experimental Results

9.2.1 Discrete Ion Gyro-Features For $f_0 \approx 3f_{ce}$

Discrete narrowband spectral features within 1 kHz of the pump frequency separated by multiples of the ion gyro-frequency f_{ci} observed in the SEE spectrum have been attributed to the simultaneous parametric decay of upper hybrid/electron Bernstein waves into multiple upper hybrid/electron Bernstein and ion Bernstein waves (Bernhardt et al 2011, Scales et al. 2011, Samimi et al 2012a, b). As stated in section 1., this process will be referred to here as Stimulated Ion Bernstein SIB Scatter SIBS (Bernhardt et al., 2011). Observations of SIBS for the pump frequency f_0 near $3f_{ce}$ are described here for the first time.

The effect of the amplitude of the pump field on SIBS was examined on July 24, 2011 from 4:43 UT-4:48 UT. The transmitter was operated with 4 minute on and 1 minute off cycles. The power increased from 0.1 MW to 3.6 MW in 210 s and 35 steps; and set at full power with 3.6 MW for 30 s. SIBS was observed by tuning the transmitter to 4.3 MHz ($\sim 3f_{ce}$). The O-Mode HF beam was pointed to the azimuth angle of 202° and a zenith angle of larger than 21°. When the transmitter was turned on at 04:43 UT on 24 July 2011 with power 0.1 MW, the spectra do not show any emission lines. When the amplitude exceeds 0.7 MW emissions are observed. The spectra then immediately showed downshifted and upshifted emissions at harmonics of f_{ci} as well as ion acoustic IA emission lines near 10 Hz. The discrete structures are attributed to SIBS instability and the IA emission lines are a result of Magnetized Stimulate Brillioun Scatter MSBS process (Norin et al., 2009; Bernhardt et al., 2009; 2010). Fig 9.1 shows four snapshots of high resolution power spectrum for P_{heater} =0.1 MW, P_{heater} =0.7 MW, P_{heater} =2 MW, and P_{heater} =3.6 MW. This figure illustrates that increase of the pump power above 0.7 MW brings it above the threshold and turns on both the MSBS and SIBS process. As can be seen in Fig 9.1, when the power of the pump wave is near 0.7 MW the first few harmonics of the SIBS emission lines and much stronger IA emission line appear in the spectra. This shows that the IA emissions have lower threshold and larger growth rate in comparison with ion gyro-structures. Increasing power to 2 MW makes the IA lines much stronger and 10 harmonics of the SIBS appear clearly in upshifted and downshifted spectral emissions close to half multiples of the ion gyro frequency near 48.5 Hz. The structures upshifted from the heater frequency correspond to the 2^{nd}-11^{th} harmonics of the ion gyro frequency respectively. A distinct emission line appears in the spectra near 62 Hz for full power which is most likely the electrostatic ion cyclotron EIC mode generated through MSBS (Bernhardt et al., 2009 and 2010). Therefore, the IA line (MSBS process), ion gyro-harmonic lines (SIBS), and EIC line (MSBS process) have the lowest thresholds, respectively. It should be noted that in most of our observations upshifted SIBS lines are stronger which is possibly because of weaker interaction of the up-going pump wave than the

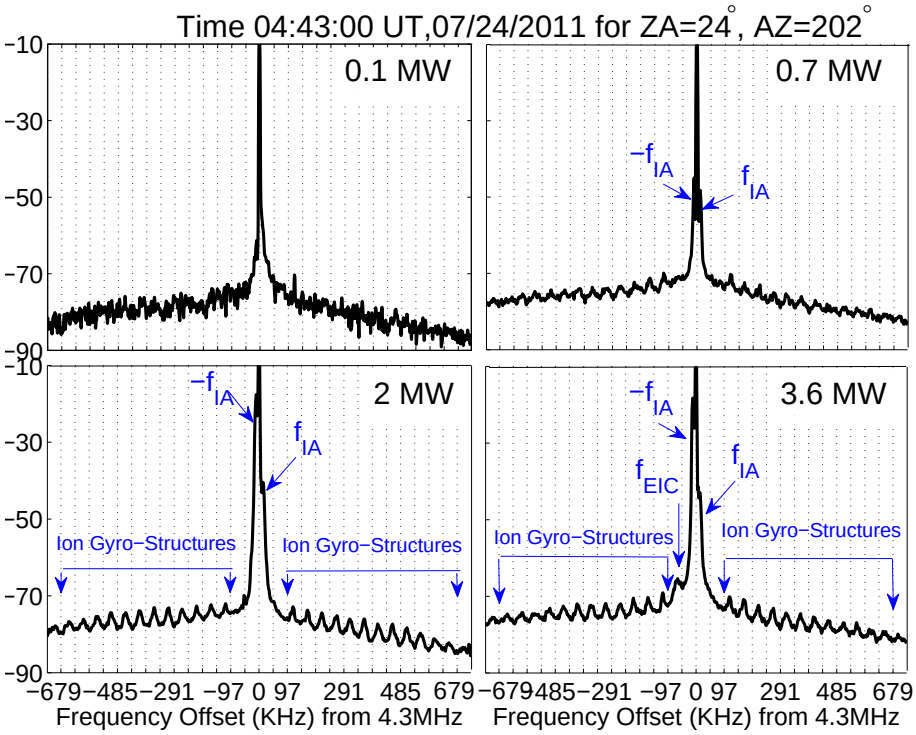

Figure 9.1: Stimulated Ion Bernstein Scatter SIBS with the transmitter tuned to $3f_{ce}$. Two other SEE emissions are observed within 10 Hz of the pump frequency as well as one emission line near 62 Hz generated by the MSBS process. Dotted lines at f_{ci} ≈48 Hz. The threshold is near 0.7 MW for SIBS.

down-going pump wave with the plasma, because of the ray paths. Detailed investigation is beyond the scope of this work and is the subject of future investigations.

Fig 9.2 shows the spectrogram of SIBS for the power range 0.1 MW to 2 MW. The first 20 sec of the spectrogram corresponds to powers less than 0.6 MW and no emission lines exist. Almost all the SIBS emission lines appear above the noise level of the spectrum approximately 20 s after the heater was turned on. Thus, it could be inferred that the pump field decays into different IB modes simultaneously rather than through a cascading process (e.g. Zhou et al. 1994).

A more extensive study of SIBS excited at $3f_{ce}$ was conducted during the 2012 campaign at HAARP. Fig 9.3 shows SEE spectra for the experiment carried out on Aug 12, 2012 from 4:30 UT- 5:30 UT. The transmitter was pointed at the magnetic zenith (ZA=14°, AZ=202°) and operated with O-mode polarization at full power alternating between 45 sec at full power and 45 sec off to allow recovery from artificially induced effects. The transmitter frequency stepped through $3f_{ce}$ from 4.21 MHz to 4.31 MHz in 20 kHz steps every other "on" period to compare effects away and near $3f_{ce}$. No SIBS was observed for the pump frequency at 4.21 MHz and 4.31 MHz which are far away from $3f_{ce}$. As the pump frequency gets closer to $3f_{ce}$,

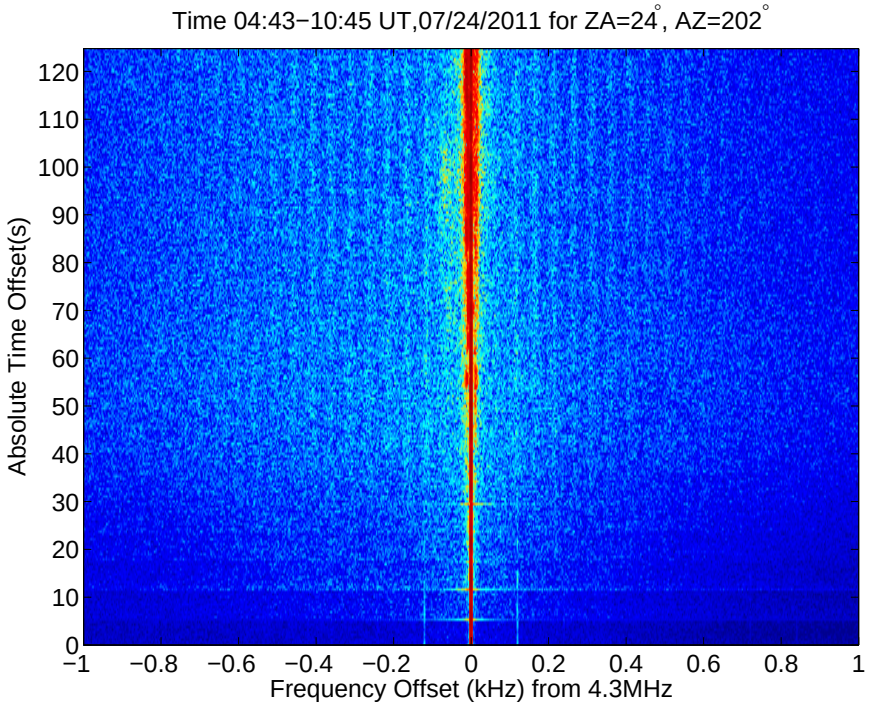

Figure 9.2: Time history of the SEE spectra of Stimulated Ion Bernstein Scatter SIBS associated with Figure 1. The pump power increased from 0.1 MW at t=0 sec in 0.1 MW steps every 6sec. The maximum value of power at end of cycle at 120 seconds is 2MW.

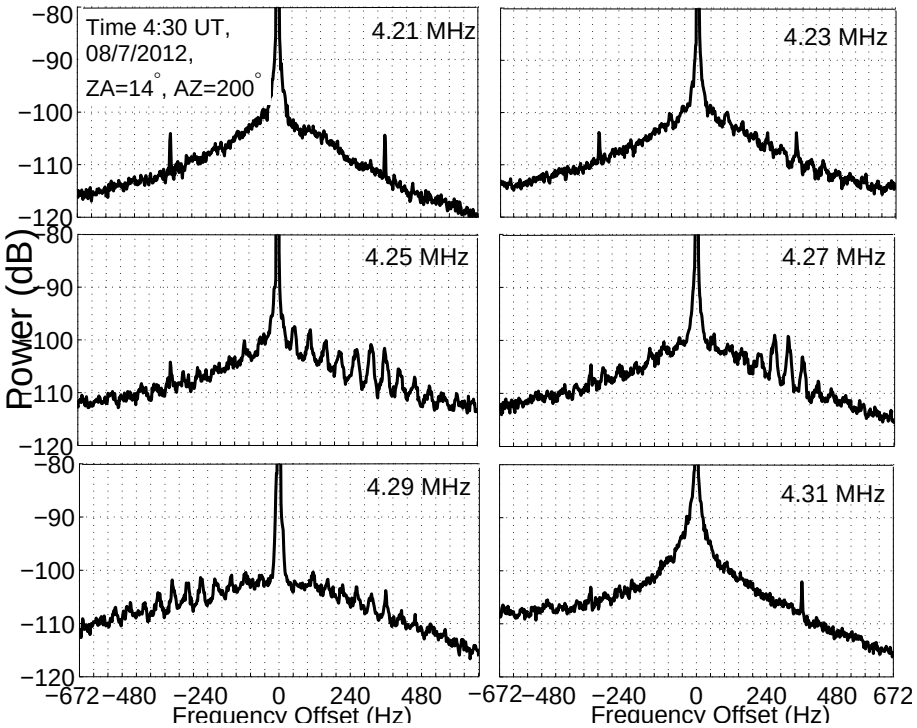

Figure 9.3: Stimulated Ion Bernstein Scatter SIBS with the transmitter tuned to $3f_{ce}$. Spectra showing SIBS for ZA=14°, AZ=202°, P_{heater} = 3.6 MW, and pump frequencies 4.21 MHz, 4.23 MHz, 4.25 MHz, 4.27 MHz, 4.29 MHz, 4.31 MHz. Pump frequencies 4.25 MHz and 4.27 MHz show strong upshifted SIBS and weak downshifted, and 4.29 MHz shows more strong downshifted SIBS.

weak upshifted ion gyro-structures are observed at 4.23 MHz. SEE spectra shows strong upshifted structures at 4.25 MHz and 4.27 MHz which are shifted by approximately half harmonics of the ion gyro-frequency f_{ci}. The strongest lines are the 7^{th} and 5^{th} harmonics for 4.25 MHz and 4.27 MHz, respectively. The structures extend up to 500 Hz above $3f_{ce}$. Symmetric upshifted and downshifted ion cyclotron harmonics appear in the spectra for the case of pump frequency tuned at 4.29 MHz. The behavior of SIBS with changing the pump frequency was investigated at larger angles relative to the MZ. A similar trend was observed at ZA= 18°, 24°, and 27°, except that IA and EIC emission lines also appear due to the excitation of the MSBS process. It should be noted that for the transmitter beam pointed at 21° only the MSBS process was excited.

The effect of heater beam angle with respect to the magnetic zenith on the excited SIBS emission lines were examined during the campaign on August 7, 2012 from 4:30 UT to 5:30 UT and on August 9, 2012 from 4 UT to 5 UT. Figure 9.4 shows the SEE spectra for ZA=14°, ZA=18°, ZA=24°, and ZA=27°. The azimuth angle was fixed at 202° for all cases. The most clear excited SIBS was observed when the HF transmitter at HAARP was pointed at MZ. As can be seen, beam angle does not affect the most strongly excited SIBS emission

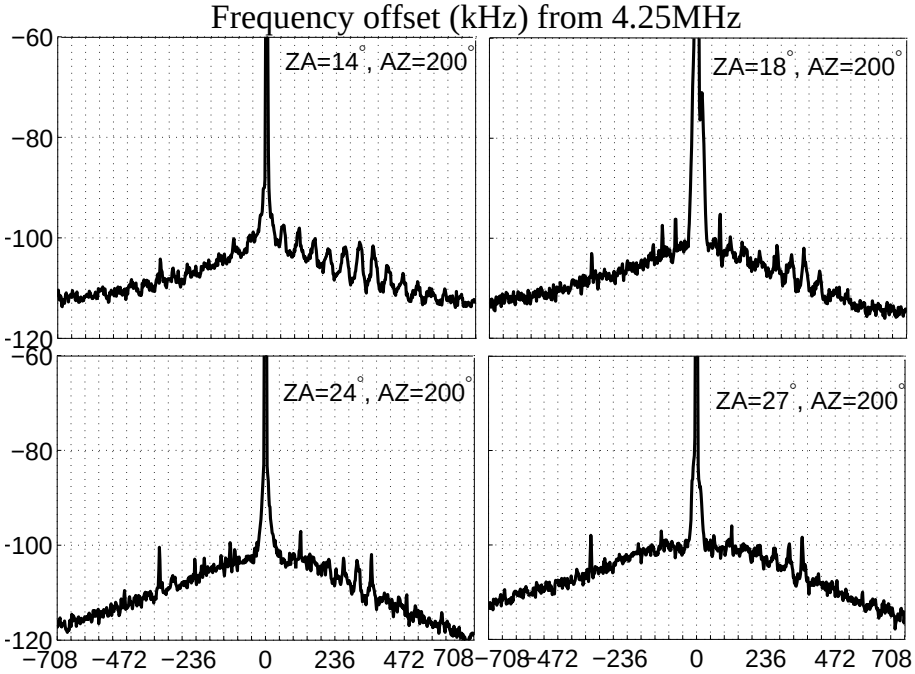

Figure 9.4: SIBS lines for ZA=14°, ZA=18°, ZA=24°, and ZA=27°. Heater beam pointed at MZ generates the strongest lines. The power spectrum corresponds to $P_{heater} = 3.6$ MW and pump frequency 4.25 MHz. IA emission lines at 10 Hz from the pump frequency appear for ZA=18° generated through MSBS processes (off scale).

line significantly since the most strongly excited line shifts only from 5^{th} to 7^{th} as the zenith angle changes from 14° to 18°. It turns out that for the zenith angles smaller than 18° SIBS is the only parametric decay process and when the beam is tilted to an angle larger than 18 degrees the MSBS process occurs simultaneously producing intense IA emission lines.

Considering the geometry of HAARP and location of the Kodiak SuperDARN radar, the signal transmitted by the Kodiak radar could be scattered only by electron density fluctuations in the direction normal to the magnetic field B. It has been shown that Langmuir waves propagate along B while UH waves propagate normal to B. Therefore, the enhancement of the Kodiak SuperDARN radar signal is expected to be due to the interaction with UH waves. The first detection and observation of UH waves during O-mode heating of the ionosphere was reported by Hughes et al., (2003). The HF scattering mode detected by the Kodiak SuperDARN radar during the O-mode heating on August 7, 2012 from 4:30 UT to 5:25 UT is shown in Fig 9.5. The horizontal axis shows the time and vertical axis represents the slant range. This figure shows a strong correlation between the heating cycle of the HF transmitter and enhancement of the detected SuperDARN echoes. This figure corresponds to f_p variation from 4.17 MHz to 4.33 MHz in 0.2 MHz steps and 5 beam angles. The strength of radar echoes increases significantly as the pump frequency gets closer to $3f_{ce}$. This is consistent with the strength of SIBS lines in the spectra shown in Fig 9.3. It should

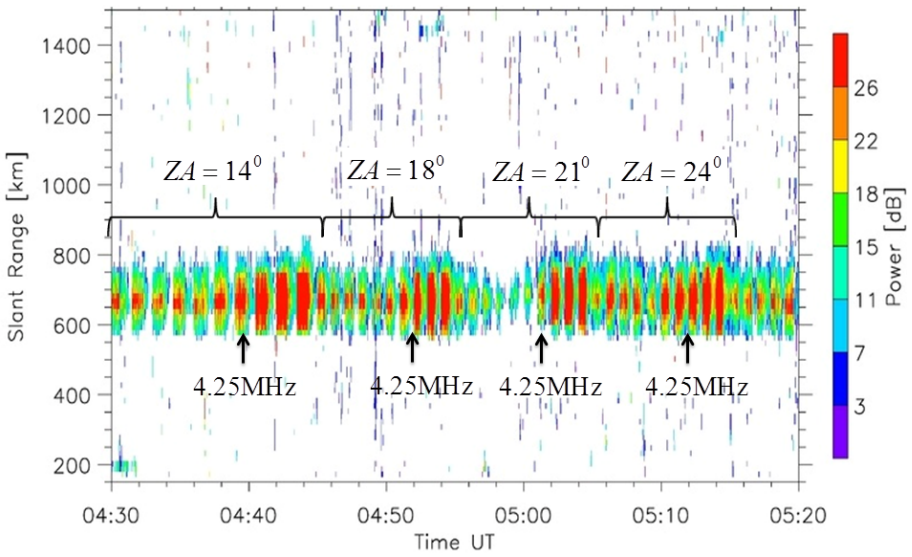

Figure 9.5: Artificial backscatter generated in the Kodiak SuperDARN radar during the ionospheric heating experiment on August 7, 2012. Beam angle was pointed at zenith angles 14°, 18°, 21°, and 24° and pump frequency was swept from 4.17 MHz to 4.33 MHz. During the heating at MZ heater was on for 45 s and off for 45 s. During other experiments heater was on for 30s. Note radar scatter maximizes when $f_p \approx 3f_{pe}$.

also be noted that no SIBS lines were observed for the beam angle 21°. As can be seen in this figure the radar echoes also reduce between 4:55 UT and 5:02 UT which denote the absence of UH waves responsible for the SIBS parametric decay process proposed in section 4.

9.2.2 Associated Broadband SEE Features for $f_0 \approx 3f_{ce}$

In this section spectral features in a wider frequency band relative to the pump frequency are discussed and the relationship between these wideband features and the narrowband emission lines SIBS, IA and EIC (MSBS) is investigated. It is observed that the previously observed SEE downshifted peak DP feature (Leyser, 2001) and the newly discovered SIBS appear simultaneously in the SEE spectra which may show that these two features are produced by the same physical process but at different altitudes as a result of different propagation angle of the electrostatic waves relative to the magnetic field. The correlation of appearance of the so-called downshifted peak DP feature (Leyser, 2001) and SIBS has been observed for ZA= 14°, 18°, and 24°. The observed DP has frequency band between 700 Hz to 1.5 kHz. The temporal evolution of the spectrum for ZA= 14° is shown in Fig 9.6 and the power spectrum is taken over 5 s intervals during the heating process in which the heater power was 3.6 MW. The SEE spectra of emissions from 3kHz below the pump frequency to 1 kHz above are shown in right panel in Fig 9.6, and left panel show the spectra in frequency range -600

Hz-600 Hz. According to this figure, DP appears in the spectra almost immediately after the heater turn-on while the spectra shows a slower growth for SIBS lines with time. 7^{th}, 8^{th} and 9^{th} lines appear above the noise level of the spectrum approximately 5 s after the heater was turned on. SIBS lines below 5 appear in the spectra after 10 s. Further relationships between these features and the well known DP feature in SEE will be discussed in light of these recent observations. A power spectral maximum near 2kHz from the pump is observed.

Since the SIBS and DP are correlated, DP, DM, and BUM can be used to estimate the proximity of the pump frequency to nf_{ce} just as the classical SEE features. Fig 9.7 shows variation of wideband spectral features with pump frequency. Considering that the DM vanishes as f_0 get closer to $3f_{ce}$, the DP can be used as an indicator of proximity of pump frequency to the gyro-frequency (Tereshchenko et al., 2006). According to this figure, the DP gets very weak at 2.9 MHz. The UM and DM peaks become more pronounced for pump frequencies closer to $3f_{ce}$. Spectra shows the BUM peak as the pump frequency goes above 2.9 MHz which is expected from the theory that BUM should becomes stronger for $3f_{ce} \leq f_0 < 3f_{ce} + 100$kHz. The offset frequency of the DP decreases from 1636 Hz 1350 Hz as f_0 is increased from 4.25 MHz to 4.27 MHz which is consistent with the previous studies that f_{DP} decreases as pump frequency increases toward $3f_{ce}$ (Huang and Kuo, 1995).

9.2.3 Ion Gyro-Features and Airglow for $f_0 \approx 2f_{ce}$

SIBS for heating at $2f_{ce}$ was first investigated for a broad range of pump parameters by Samimi et al., (2012b). During the 2012 campaign a set of experiments was dedicated to a more detailed study of SIBS with pump frequency sweeping through $2f_{ce}$ and $3f_{ce}$. This experiment aimed at considering the connection with airglow and comparison of the cases with $f_0 = 2f_{ce}$ and $3f_{ce}$. Coordinated optical and SEE observations were carried out in order to provide a better understanding of electron acceleration and precipitation processes. Results for correlation between SEE SIBS emission lines and airglow is provided for pump heating near $2f_{ce}$ during the campaign. The observations affirm strong correlation between the SIBS and the airglow.

The transmitter frequency was tuned near the local $2f_{ce}$ at f_0 =2.7 MHz for the first 60 sec of the heating cycle and increased in 0.1 MHz every 30 sec. The experiment was conducted at night time on August 9, 2012 from 10:56 UT to 11:08 UT and 10:30 UT-10:42 UT. The HF beam was pointed to the magnetic zenith with an azimuth of 202 degrees and a zenith angle of 14 degrees at full power (3.6 MW) during a 12 minute heating cycle. The spectra shown in Fig 9.8 illustrates the variation of discrete SIBS lines with the pump frequencies 2.7 MHz, 2.71 MHz, 2.72 MHz, 2.73 MHz, 2.74 MHz, and 2.75 MHz. The spectra shows weakly excited lines between the 7^{th} and 10^{th} harmonics for the pump frequency tuned at 2.7 MHz. 6^{th}-9^{th} lines appear in the spectra much stronger than the previous case at 2.71 MHz and 2.72 MHz, and a strong emission line near 61 Hz also shows up in the spectra. This newly observed emission line is shown to be related to observed optical emissions. Collision

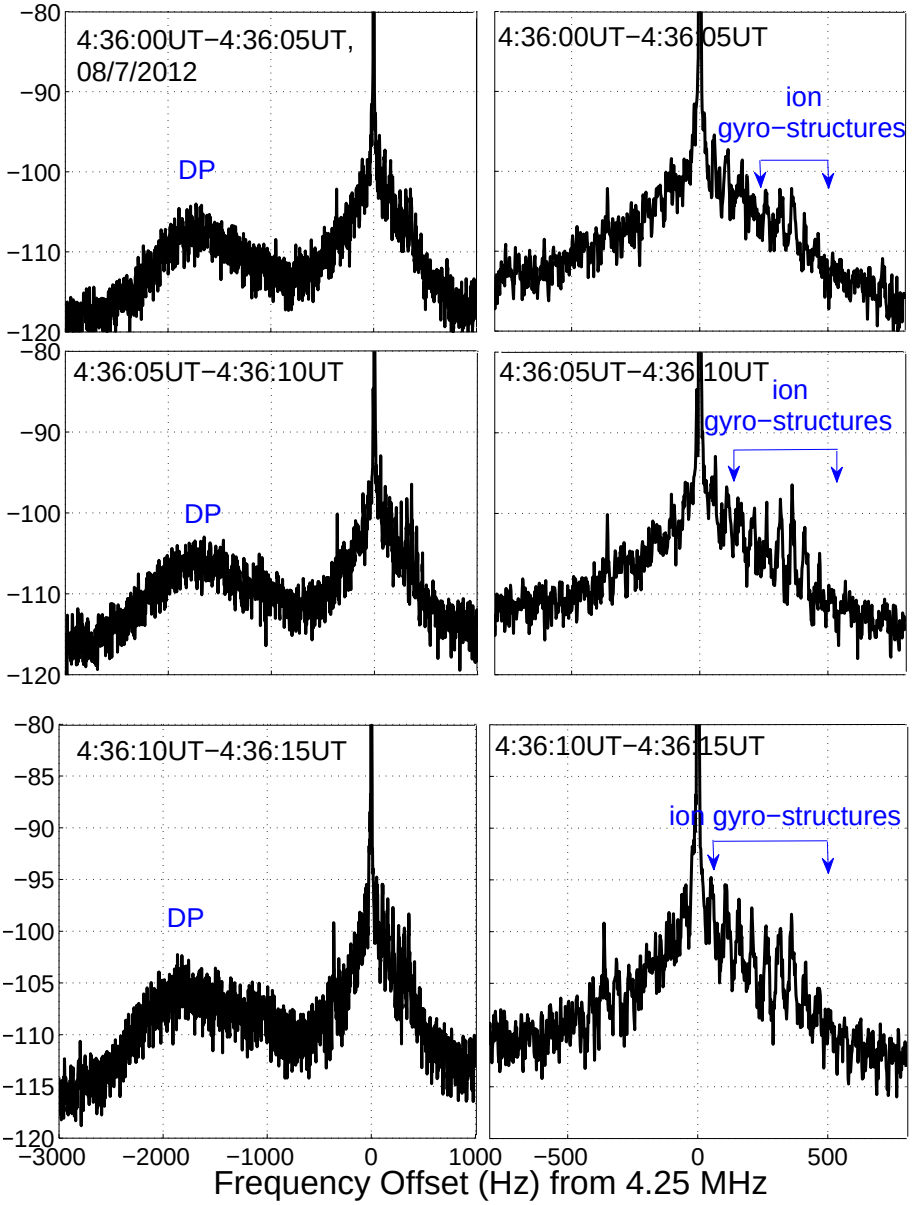

Figure 9.6: SEE spectra taken over 5 s intervals during 45 s heating demonstrate temporal evolution of DP (left panels) and SIBS emission lines (right panel). Note structures start to appear above the noise level approximately 6 s after the heater turn-on. Note that the 6^{th}, 7^{th} and 8^{th} have the fastest growth initially. The DP appears in the spectra almost immediately after turn-on.

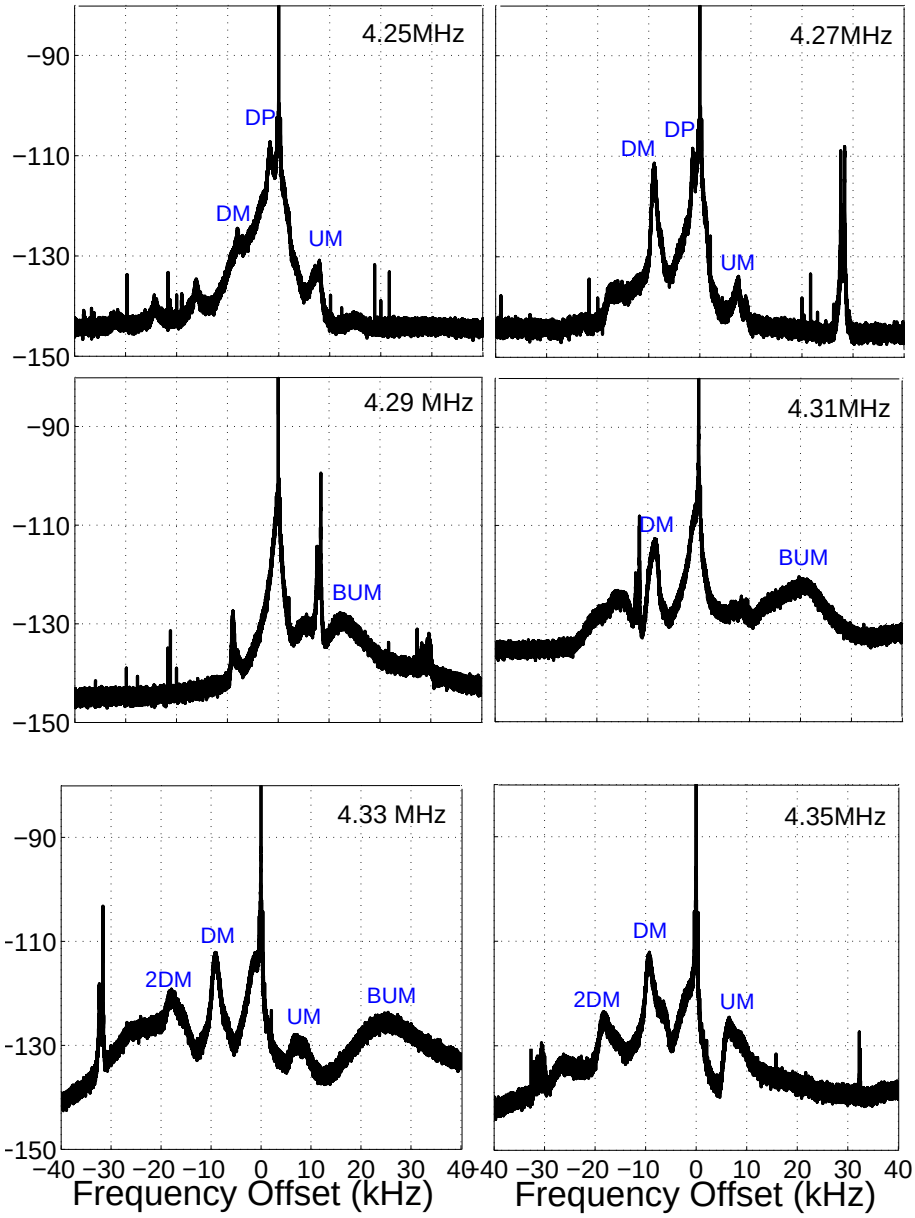

Figure 9.7: Variation of wideband SEE spectrum with the sweeping of the pump wave frequency near $3f_{ce}$. The spectra shows different classic SEE spectral features including the downshifted maximum DM (at -9kHz), the upshifted maximum UM (at +9kHz), and the broad upshifted maximum BUM (at +20kHz). These are all observed simultaneously with the narrowband features of Figure 9.3.

of accelerated electrons with neutral species may excite neutral particles and as a result produce airglow. This is the subject of future investigation. It turns out that increasing the pump frequency toward $2f_{ce}$ moves the most strongly excited SIBS lines to lower harmonic numbers. The 7^{th}, 6^{th}, 5^{th}, and 3^{rd} lines are the strongest for 2.72 MHz, 2.73 MHz, 2.74 MHz, and 2.75 MHz, respectively.

Artificially enhanced airglow due to excitation of oxygen atoms by accelerated electrons was first reported at Arecibo, Puerto Rico by Gordon and Carlson (1974) and later in Tromso by Stubbe et al., (1982). The electron acceleration is due to modified electron distributions by plasma waves such as Langmuir waves (Weinstock, 1975). Optical observations were carried out with multiple wide- and narrow-field systems at the HAARP site observing 557.7 nm emissions from the 1S state of atomic oxygen corresponding to >4 eV electron energy and 427.8 nm N_2^+ emissions indicating ionization production at >18 eV. Fig 9.9 shows a series of optical images from looking up the magnetic field from HAARP (557.7 nm) during an artificial layer creation event and corresponding to Fig 9.8. The figure shows a clear correlation of airglow strength and SIBS lines (shown in Fig 9.8). During another heating experiment near $2f_{ce}$, it has been observed that when airglow enhances substantially the SIBS instability quenches. It has also been predicted that the amount of pump wave transmitted to the reflection layer decreases as a result of absorbtion of pump power by accelerated electrons (anomalous absorption) (Weinstock, 1975).

In addition to the discrete SIBS emission lines, a possible variation of the previously observed broadband spectral feature was observed within 1 kHz of the pump frequency during the 2011 heating experiments near $2f_{ce}$. This broadband spectral feature may be observed alone or with embedded discrete ion gyro-harmonic structures and due to parametric decay into oblique ion acoustic waves (Samimi et al., 2012b). Fig 9.10 demonstrates the broadband feature as well as discrete spectral feature for the experiment in which the heater was on for 60 s and off for 90 s at $f_0 = 2.9$ MHz, 2.92 MHz, 2.94 MHz, and 2.96 MHz. The transmitter beam was pointed at MZ and vertical. The data were obtained on 24 July 2011 when the HF wave was turned on at 11:48UT. As can be seen in Fig 9.10a, the first broadband feature peaks at -235 Hz downshifted and +239 Hz upshifted from the pump frequency of 2.92 MHz for vertical beam. A second broadband spectral feature at -475 Hz and +460 Hz as well as a third broadband spectral feature at -760 Hz of the heater frequency were also observed. Increasing the pump frequency to 2.94 MHz suppresses the excited broadband spectral features such that only a downshifted broadband feature is observed at -170 Hz. At frequencies far away from $2f_{ce}$ 2.96 MHz spectra only shows emission lines at $\pm$19 Hz which is as a result of domination of the MSBS process. It has also been shown in the previous study by Samimi et al., (2012) that the SIBS instability is stronger for the pump frequency near $2f_{ce}$.

Fig 9.10b provides the spectra for a MZ beam that shows broadband spectral features at $\pm$270 Hz with embedded discrete ion gyro-structures for 2.9 MHz. As the pump frequency increases to 2.92 MHz only the 3^{rd} and 4^{th} harmonics of discrete ion gyro-structures appear in the spectra and the broadband feature is suppressed. Similar to the previous case as the

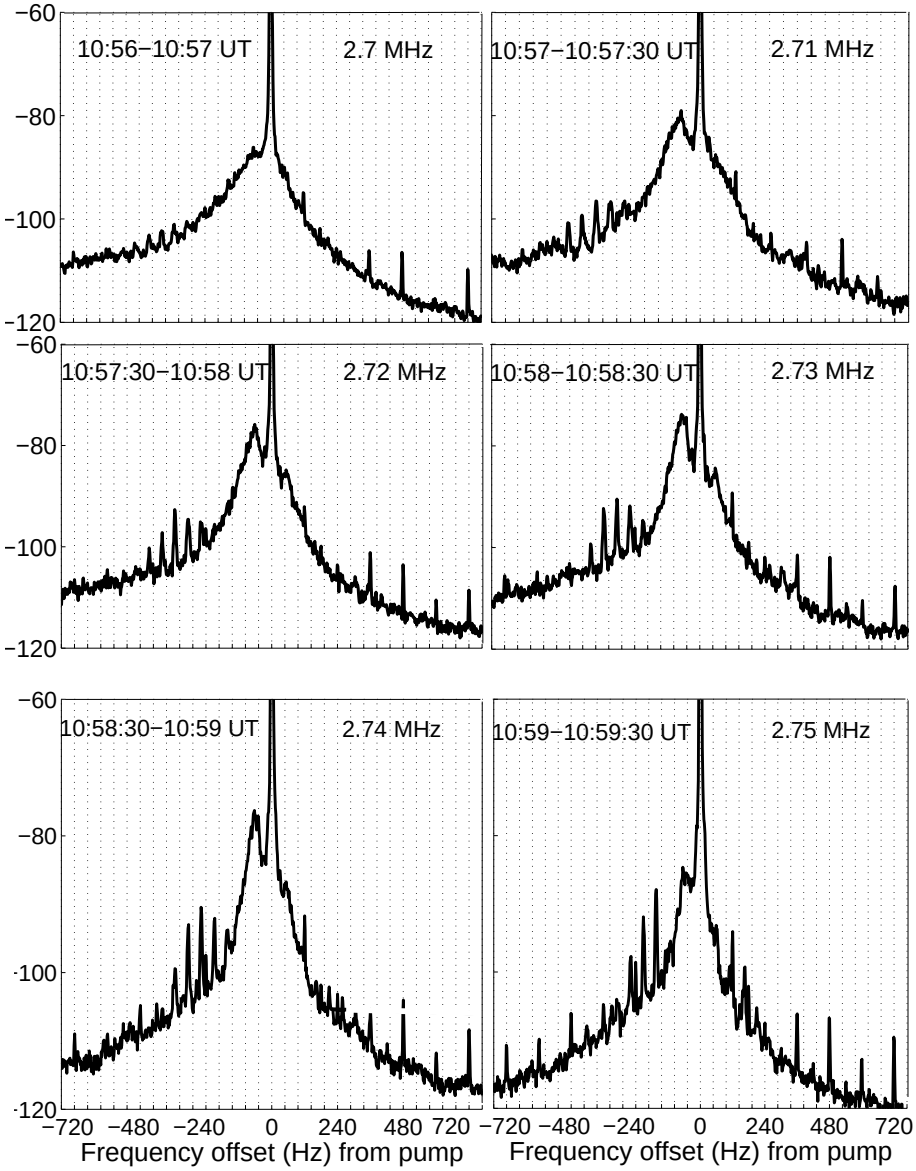

Figure 9.8: SEE Spectra showing SIBS for $P_{heater} = 3.6$ MW and f_0 being tuned near $2f_{ce}$. Heater duty cycle is 30 s on, 30s off and transmitter beam was pointed at MZ. As the pump frequency gets closer to $2f_{ce}$, SIBS become stronger and the most excited harmonic shifts toward the lower harmonics.

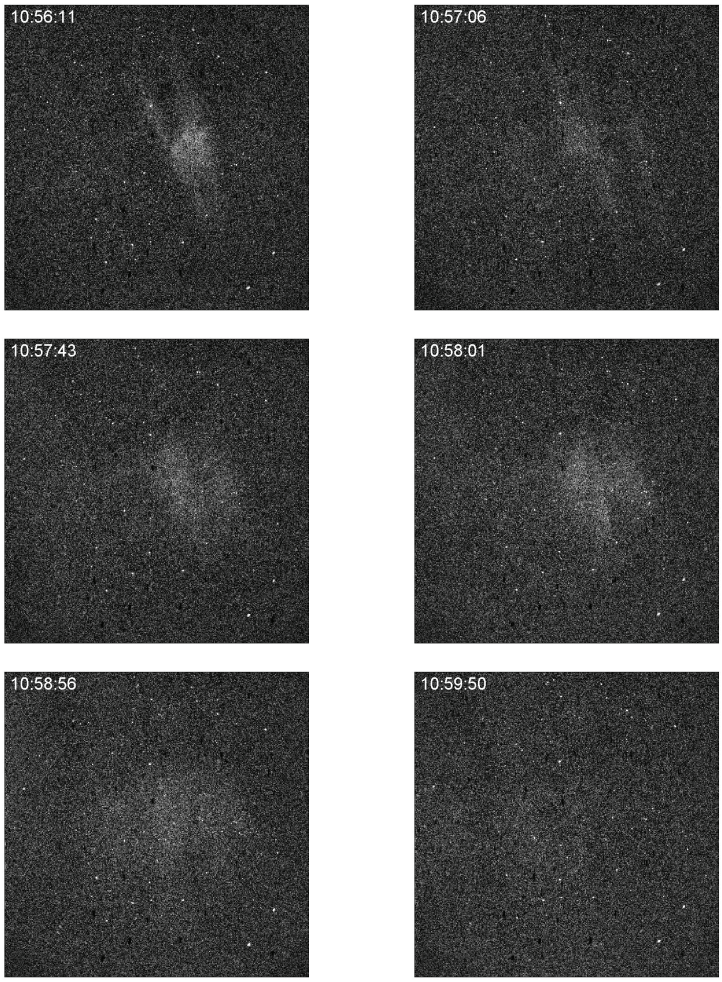

Figure 9.9: Images of artificial optical emissions as viewed from the HAARP site looking up the field line with high resolution at 557.7 nm. This figure corresponds to the observed SIBS lines shown in Figure 9.8.

pump frequency gets further above $2f_{ce}$, the SIBS process vanishes and the MSBS process dominates at 2.94 MHz. No emission line associated with parametric decay instability is observed at 2.96 MHz.

9.3 Theory and Results

In the SIBS process first the long wavelength EM wave is assumed to be converted to an electrostatic UH/EB pump wave and field aligned irregularities from the oscillating two stream instability OTSI (Huang and Kuo 1995; Dysthe et al., 1983). The parametric decay instability then occurs which will be investigated here. The theory is based on the decay of the UH/EB pump wave into another UH/EB wave and neutralized/pure IB waves. While the pure ion Bernstein wave propagates virtually perpendicular to the magnetic field, neutralized ion Bernstein waves propagates slightly off perpendicular ($k_\parallel/k_\perp > \sqrt{m_e/m_i}$) and have different dispersive characteristics due to Boltzmann electron behavior (Chen, 1984). Here $k_\parallel$ and $k_\perp$ are the wavevector k parallel and perpendicular to the magnetic field and m_e and m_i are the electron and ion mass. The wave frequency and wave propagation direction are given by the energy and momentum conservation equations $\omega_0 = \omega_1 + \omega_S$, $k_0 = k_1 + k_S$ where (ω_0, k_0), (ω_1, k_1) and (ω_s, k_s) are the (radian) frequency and wavenumber for the pump, high frequency decay mode (UH/EB) and low frequency decay mode (IB/IA), respectively (Kruer, 1988; Eliezer, 2002). The low frequency and high frequency waves are related with the following dispersion relation (Porkolab, 1974):

$$\varepsilon(\omega_s) + \frac{\beta_e^2}{4}\chi_i(\omega_s)\left\{\frac{\varepsilon_e(\omega_s)}{\varepsilon_e(-\omega_L^*)} - 2\right\} = 0 \tag{9.1}$$

where β_e is the coupling coefficient, $\varepsilon(\omega) = 1 + \chi_e(\omega) + \chi_i(\omega)$, and $\varepsilon_e(\omega) = 1 + \chi_e(\omega)$. The susceptibility of the j^{th} species is given by:

$$\chi_j(\omega) = \frac{1}{k^2\lambda_{Dj}^2}\left\{\frac{1 + \zeta_{j0}\sum\limits_{n=-\infty}^{+\infty}\Gamma_n(b_j)Z(\zeta_{jn})}{1 + \frac{i\nu_j}{k_\parallel v_{tj}}\sum\limits_{n=-\infty}^{+\infty}\Gamma_n(b_j)Z(\zeta_{jn})}\right\} \tag{9.2}$$

where $b_j = k_\perp^2\rho_j^2$, k is the wavenumber, and ρ_j is the gyro-radius. ζ_{jn} is given by:

$$\zeta_{jn} = \frac{\omega + i\nu_j - n\Omega_n}{k_\parallel v_{tj}} \tag{9.3}$$

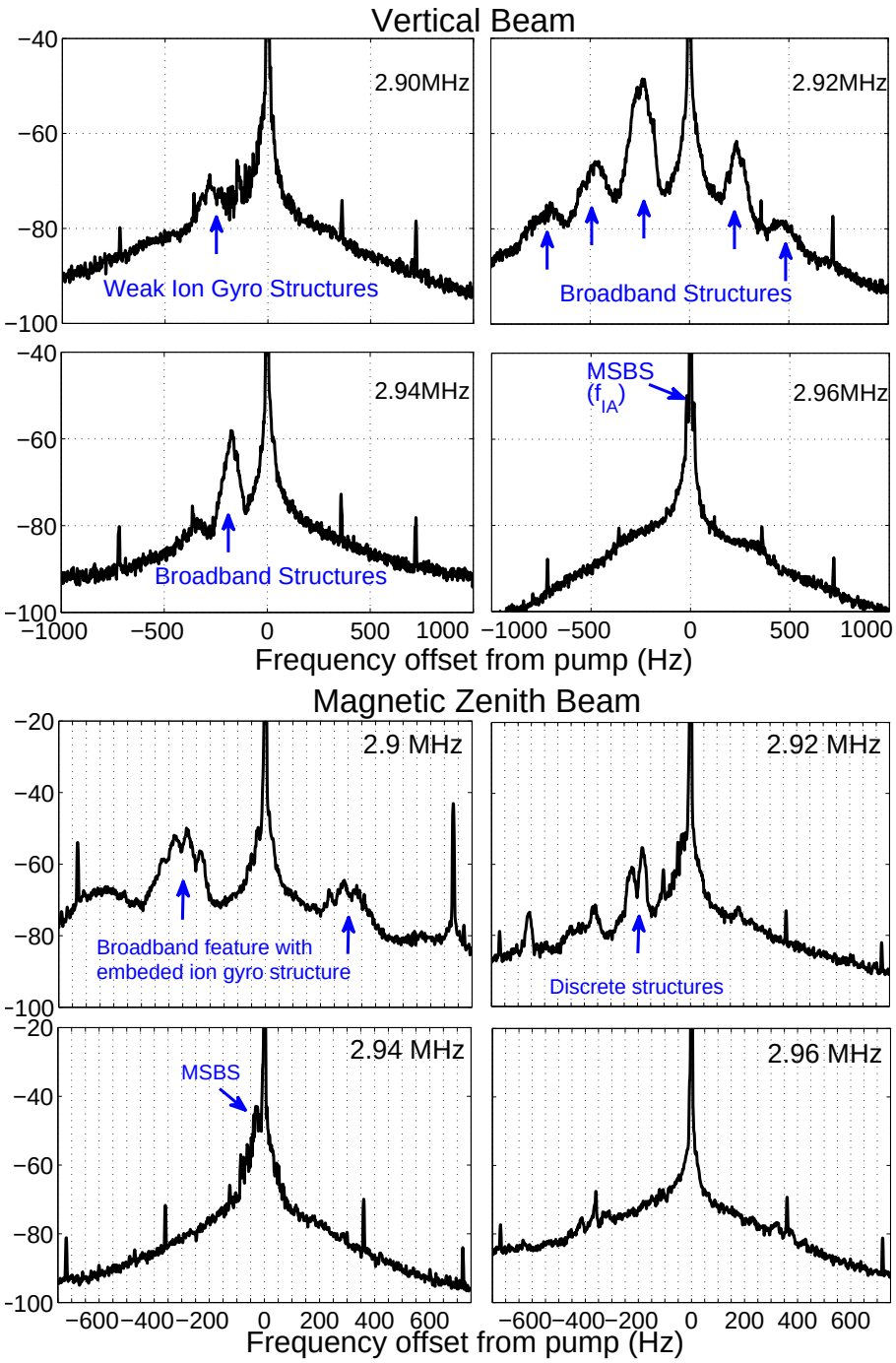

Figure 9.10: Experimental observations of broadband spectral features during which the heater frequency was tuned to 2.9 MHz, 2.92 MHz, 2.94 MHz, and 2.96 MHz and heating cycle was 30 s. Spectra also shows broadband spectral feature with embedded ion gyroharmonic structures at 2.9 MHz and for MZ beam. Note disappearance of broadband feature and appearance of MSBS feature as the pump frequency moves further from $2f_{ce}$. Dotted lines are at f_{ci}.

v_{tj} is the thermal velocity, Ω_n is the gyro-frequency, ν_j is the collision frequency, $\Gamma_n(bj) = I_n(bj)\exp(-bj)$, Z is the Fried Conte function, and I_n is the first order modified Bessel function. The coupling coefficient β_e is given by:

$$\beta_e = \frac{e}{m_e}\left[\left(\frac{E_{0\parallel}k_{\parallel}}{\omega_0^2} + \frac{E_{0x}k_x + E_{0y}k_y}{\omega_0^2 - \Omega_{ci}^2}\right)^2 + \frac{(E_{0x}k_y + E_{0y}k_x)^2\Omega_{ce}^2}{\omega_0^2(\omega_0^2 - \Omega_{ci}^2)^2}\right]^{1/2} \tag{9.4}$$

Considering the almost perpendicular propagation of Bernstein waves relative to the magnetic field, it is assumed that the interaction occurs at the upper hybrid altitude. The dipole approximation ($k_0 \approx 0$) is used in this work where k_0 is the pump wavenumber. It should be noted that this is a simplified approach and the wavenumber of the pump field is more appropriately calculated by assuming a value determined from the scale size of irregularities generated from the oscillating two stream instability (Huang and Kuo 1995). However, the simplified approach is adequate for initial characterization of the experimental data and more refined calculations will be pursued in future investigations. The pump field strength is described by the electron oscillating velocity $v_{osc} = eE_0/m_e\omega_0$ where e is the electron charge. The angle between electric field and the background magnetic field is denoted by θ_E.

Fig 9.11 demonstrates the influence of pump field strength (electron oscillating velocity) on the parametric decay instability for $\theta_E = 0.66°$ and $\omega_0 = 3\Omega_{ce} + 40\Omega_{ci}$. The left vertical axis is normalized frequency (blue lines); at the right is normalized growth rate (green lines) and the horizontal axis is the perpendicular normalized wavenumber. As can be seen, increasing the normalized oscillating velocity $\tilde{v}_{osc} = v_{osc}/v_{the}$ increases the number of destabilized modes from 5 up to 20, and changes the most excited modes from fourth to fifteenth. The fourth and fifth harmonics have the lowest threshold while according the previous study by Samimi et al., (2012b), the second and third harmonics have the lowest threshold near the second electron gyro-harmonic ($2\Omega_{ce}$). As in Scales et al., (2011) and Samimi et al. (2012ab) the wavelength is in the range $k_\perp\rho_{ci} \sim n$ where n is the harmonic number. The increase in $\tilde{v}_{osc}$ from 0.15 to 0.40 corresponds to electric field amplitude 3 V/m to ∼8 V/m.

Variation of the parametric decay instability growth rate with pump frequency offset relative to $3\Omega_{ce}$ for $\theta_E = 0.66°$, $T_e/T_i = 4$ and $\tilde{v}_{osc} = 0.15$ is shown in Fig 9.12. The $\nu_{en} = 400$ Hz and $\nu_{in} = 1$ Hz are assumed. As the pump offset frequency increases further above and below the gyro-harmonic $3\Omega_{ce}$, the number of destabilized harmonics decreases. Increasing the offset frequency further above $3\Omega_{ce}$ also shifts the most excited mode toward the lower harmonics. The maximum growth rate of all destabilized harmonics from 1 to 19 is approximately the same for the pump frequency $\omega_0 = 3\Omega_{ce} - 30\Omega_{ci}$ and the maximum growth rate is obtained for offset frequency $20 - 30\Omega_{ci}$ above $3\Omega_{ce}$. Unstable harmonics excited by $\omega_0 < 3\Omega_{ce}$ are weaker. Therefore, whereas all harmonics are stable for frequency offset $50\Omega_{ci}$ below the gyro-harmonic, positive growth rate is obtained for lower harmonics with frequency offset up to $80\Omega_{ci}$ above $3\Omega_{ce}$. Therefore the theory is consistent with observations of enhancement of SIBS instability for the pump frequency being tuned to $2f_{ce}$ or $3f_{ce}$ from either below or

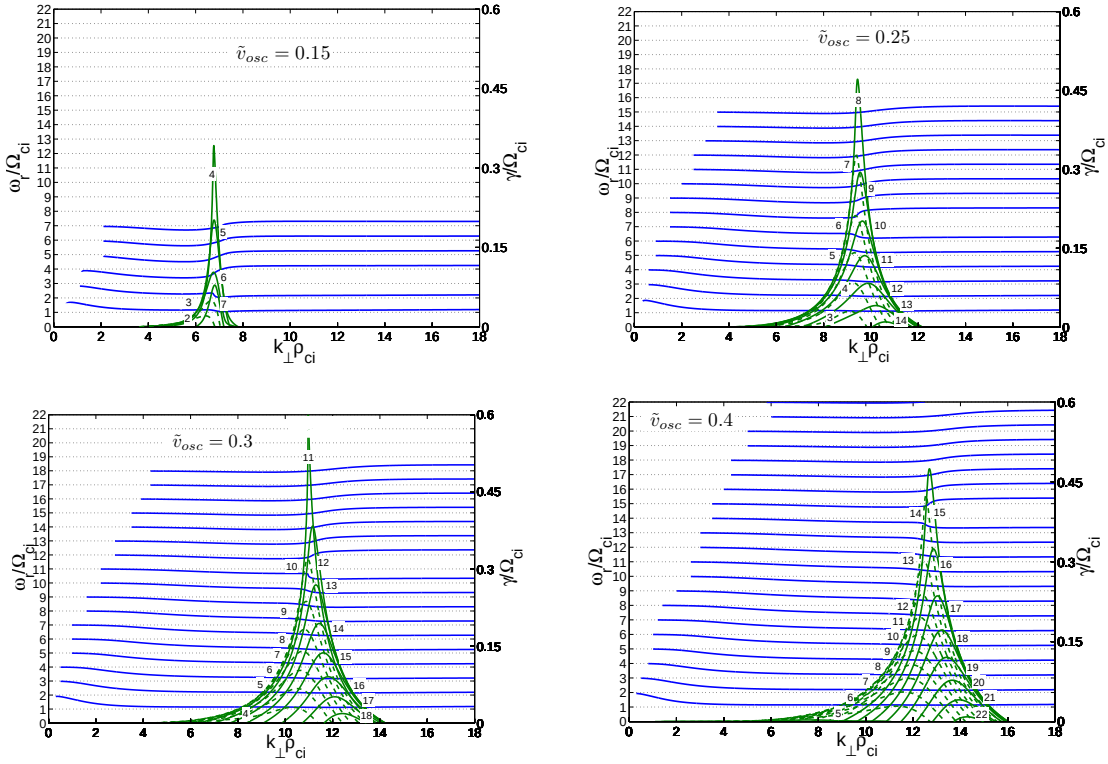

Figure 9.11: Dispersion relation of the low frequency decay mode (blue lines) and corresponding parametric decay instability growth rate (green lines) for $\theta_0 = 0.65$, $\omega_0 = 3\Omega_{ce} + 5\Omega_{ci}$, ν_{in}=3Hz, $\nu_{en} = 400$ Hz a) $\tilde{v}_{osc} = 0.15$ b) $\tilde{v}_{osc} = 0.25$ c) $\tilde{v}_{osc} = 0.3$ d) $\tilde{v}_{osc}$= 0.4 obtained from equation (9.1). Note that as the pump strength increases more harmonics are destabilized.

above. Stepping the frequency through the gyro-harmonic from below to above shifts the most excited mode to the lower harmonics. This is also consistent with the observational data shown in Fig 9.3 that increasing f_0 from 4.25 MHz to 4.27 MHz moves the strongest harmonic from 7^{th} to 5^{th} and no discrete emission lines were observed at 4.21 MHz and 4.31 MHz since these frequencies are further away from $3f_{ce}$.

Dispersive characteristics and growth rate as well as growth rate versus frequency of excited low frequency decay modes near $3\Omega_{ce}$ are shown in Fig 9.13 for three angles of pump field a) θ_E =0.5°, b) θ_E =1°, and c) 2°. $\tilde{v}_{osc} = 0.13$, $T_e/T_i = 3$, and pump frequency is shifted by $5\Omega_{ci}$ above $3\Omega_{ce}$. The influence of θ_E on the most excited harmonic is negligible in comparison with offset of pump frequency relative to $3\Omega_{ce}$. It turns out that increasing the angle of pump field relative to the magnetic field reduces the growth rate significantly. This is also in agreement with experimental observations shown in Fig 9.4 that spectra shows the strongest SIBS lines for magnetic zenith beam and variation of the most excited line with beam angle is negligible. It should be noted that angle of pump field in the ionosphere depends on the density of the ionosphere but it is expected to be roughly related to the transmitter beam angle.

The correlation between the Downshifted Peak DP and SIBS in Fig 9.6 suggests the DP is most likely due to parametric decay into an IA wave that is excited at larger θ_E (Huang and Kuo, 1995; Samimi 2012a,b). In fact, there is a possibility that the SIBS are produced at a different altitude than the DP as a result of smaller θ_E and parametric decay of UH/EB waves into low frequency pure/neutralized ion Bernstein modes. Fig 9.14 investigates the possibility of simultaneous parametric decay of the pump field into broadband oblique IA waves and discrete ion Bernstein waves at different altitudes which requires similar parameters except a different θ_E. Generation of an oblique IA mode in such plasma conditions was first proposed by Huang and Kuo (1995) and studied in Particle-In-Cell PIC simulations by Hussein and Scales (1997). To reiterate, a similar process is proposed for $2f_{ce}$ heating (Samimi et al. 2012a,b) to explain the broadband spectral features as seen in Fig 9.10. Figure 9.14 shows the growth rate versus frequency for $\theta_E = 1.33°$ and 17.3° which correspond to the excited ion Bernstein modes and oblique IA mode, respectively. T_e/T_i =5 and $\tilde{v}_{osc}$ =0.1 are assumed in the calculations. At higher θ_E, highly oblique IA waves with dispersion relation $\omega \approx kc_s$ are destabilized instead of discrete neutralized IB modes. Comparison with experimental observations and results of the growth rate calculations suggests that the broadband spectral feature (DP) most likely involves this decay mode. The simultaneous occurrence of the broadband spectral feature (DP) and the discrete SIBS lines in Fig 9.6 most likely corresponds to the neutralized IB modes and oblique IA mode being generated at different altitudes. As will be shown in the next section, theory predicts simultaneous excitation of IB and oblique IA waves for the same ionospheric parameters but different θ_E. This suggests the generation at different altitudes. Discrete spectral lines are observed at smaller angle of electric field while there is no signature of the broadband mode. As can be seen, the first 6 harmonics correspond to SIBS lines and have frequency shift slightly below the harmonic of Ω_{ci} and involve the IB modes. The seventh harmonic has the highest growth rate. As shown

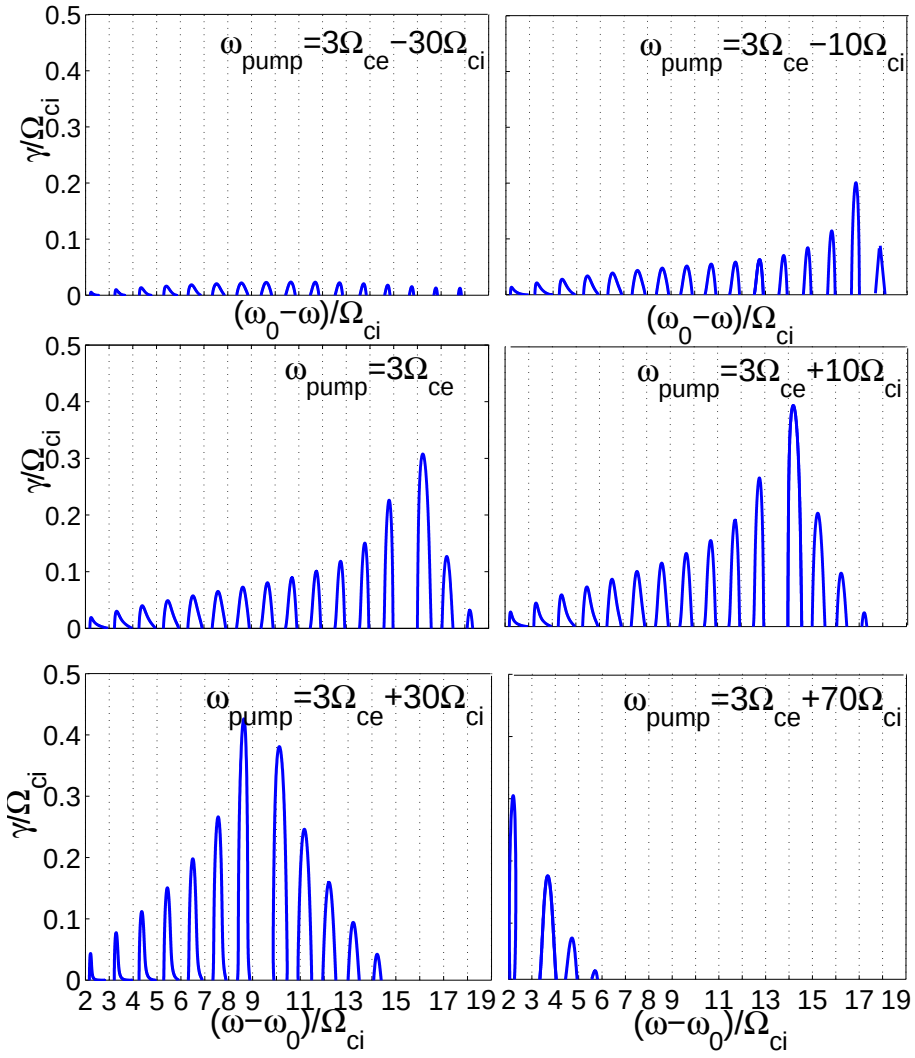

Figure 9.12: Growth rate versus frequency for $\theta_E = 0.66°$, $T_e/T_i = 4$ and $\tilde{v}_{osc} = 0.15$ obtained from equation (9.1). Pump frequency is varied near $3f_{ce}$ to show variation in growth rate of harmonics.

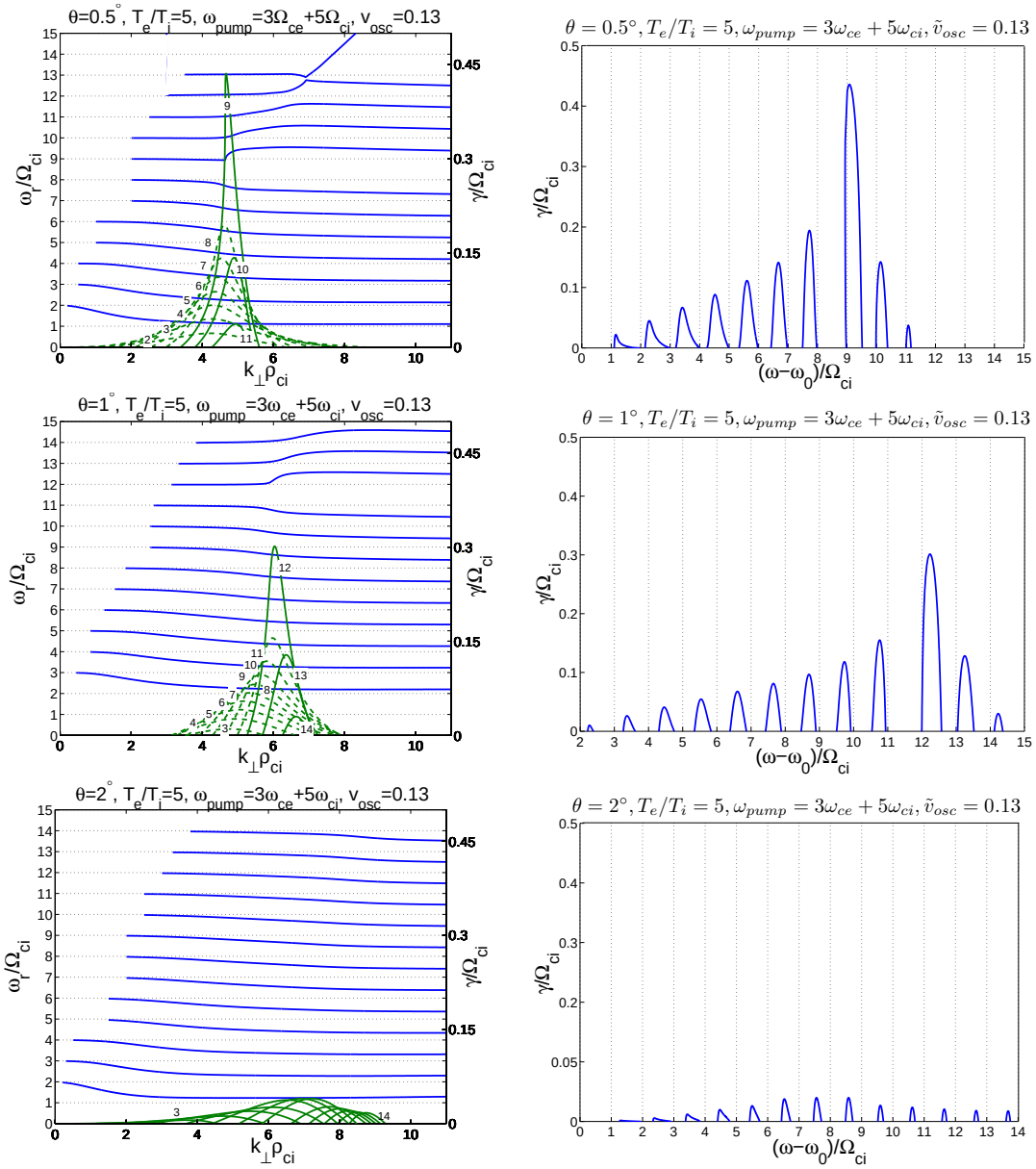

Figure 9.13: Left figures: Dispersion relation for the low frequency decay mode (blue lines) and corresponding parametric decay instability growth rate (green lines), right figure: Growth rate versus frequency for $T_e/T_i = 5$, $\omega_{pump} = 3\Omega_{ce} + 5\Omega_{ci}$, $\tilde{v}_{osc} = 0.13$, $\nu_i = 3$ Hz, and $\nu_e = 400$Hz, a)$\theta_E = 0.5°$, b)$\theta_E = 1°$, c)$\theta_E = 2°$.

in the right panel of Fig 9.14, the dispersion relation shows a broadband feature extending from $23\Omega_{ci}$ to $33\Omega_{ci}$ that corresponds to the frequency band 1.1-1.6 kHz as θ_E increases. This matches well with the experimental observations shown in Fig 9.6 that SIBS and DP (in frequency range 1.2-1.8 kHz) were observed at the same time. The predicted oblique IA wave from the theory appears in the frequency range 1.1-1.6 kHz. According to the Fig 9.6, the observed DP may have bandwidth up to 1kHz in the frequency range 1 to 2 kHz. Some of this broadening may be due to higher order nonlinear processes that are not included in the theory presented in this work. It turns out that the ratio of electron temperature enhancement is the most effective parameter on the bandwidth of the excited oblique IA mode and increasing θ_E reduces the center frequency. The previous work by Samimi et al., (2012) also predicted oblique IA wave through parametric decay instability for $2f_{ce}$ heating and showed that IA waves can be excited at larger θ_E. However these broadband emission lines exist at a smaller frequency shift from the pump frequency as observed in Fig 9.10 and discussed in section 3.2. The IA growth rate is larger than the IB growth rate by a factor of 10 in Fig 9.14 which is consistent with the experimental observations shown in Fig 9.6 that DP appears in the spectra instantaneously after the pump turn-on while it takes about 10s for SIBS lines to evolve and grow above the noise level.

9.4 Conclusions

First observations of the discrete ion gyro-structures known as Stimulated Ion Bernstein Scatter SIBS in the SEE spectrum when the pump frequency is near $3f_{ce}$ have been presented. Coordinated observations of these SEE features and optical emissions have also been presented. It is shown that increasing the heater power above 0.7 MW can excite SIBS at the HAARP facility. This threshold power is to be compared to an approximately 0.8 MW threshold power quoted for generation of SIBS for $2f_{ce}$ (Samimi et al. 2012ab). Parametric decay of the UH/EB pump field into another UH/EB and IB waves in the upper hybrid altitude has been shown as a viable process for generation of these discrete ion gyro-harmonic structures in the SEE spectrum. Evidence of enhanced electrostatic waves (i.e. UH) for $f_p \approx f_{ce}$ were observed in simultaneous SuperDARN radar observations. Variation of discrete spectral lines with the pump frequency stepping near the 2^{nd} and 3^{rd} gyro-harmonics and heater beam angle was studied during the experiment and observations show agreement with theoretical calculations. The excitation threshold of ion acoustic IA and electrostatic ion cyclotron EIC emission lines associated with magnetized stimulated Brillouin scatter MSBS also were measured. It turns out that SIBS lines have threshold of about 0.7 MW, and IA and EIC lines appear in the spectra when pump power exceeds 0.4 MW and 3 MW, respectively. A correlation of appearance and disappearance of the Downshifted Peak DP and SIB scatter lines for $3f_{ce}$ heating was observed. The theory suggests the decay of the UH/EB pump field into another UH/EB mode and a broadband oblique IA mode as a generation mechanism for the downshifted peak between 1.2 kHz and 1.6 kHz that could occur at a different altitude relative to the SIBS generation region. It was shown that the

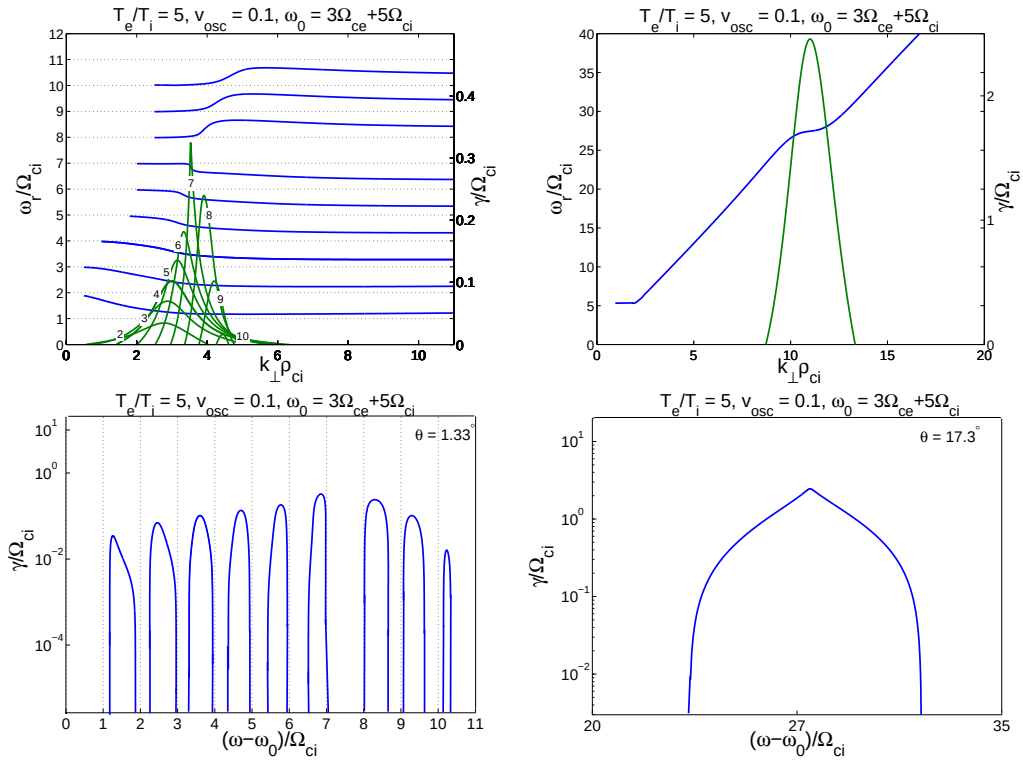

Figure 9.14: Growth rate versus frequency for $\theta_E = 1.33°$ and 17.3°. Top panel shows the dispersive characteristics and corresponding growth rate, and figures in the bottom represent the growth rate versus frequency. Note simultaneous parametric decay involving ion Bernstein and oblique ion acoustic modes at different angles of propagation to B that may allow both narrowband and wideband SEE as seen in Figure 9.6.

IA mode (DP) grow faster than SIBS lines in both theory and experimental observations. Simultaneous observation of SIBS and airglow during heating near $2f_{ce}$ is presented which shows a correlation with the strength of optical emissions. This could shed light on the physical processes associated with artificial field alighted irregularities FAIs and electron precipitation.

Chapter 10

Conclusions and Future Work

10.1 Summary and contributions

Chapter 1 and 2 provide a detailed study of the extant literature on the mesospheric conditions required for the formation of PMC, as well as PMSE and active modification experiments. The proposed cooling mechanism and source of water vapors in the mesosphere were reviewed.

The new computational model is described in chapter 3. The continuity equation is now solved by using an implicit method based on the formulation described by Bernhardt et al. (1991). The new algorithms not only reduce the computational time substantially but also provide greater accuracy. The capability of model in including more ion species and gravity effect was explained.

In chapter 4, temporal evolution of radar echoes during PMSE heating experiment with typical mesospheric parameters measured in recent in-situ rocket experiments and actual radar frequencies availed at heating facilities in Tromso, Norway (EISCAT) and Alaska, USA (HAARP) was studied. Transition radar frequency from the turn-on overshoot to turn-on undershoot was studied in detail. VHF PMSE data from recent campaign at EISCAT was presented and compared against the computational model. The possible dust and plasma parameter regime associated with observed data as well as probability of the presence of positive dust particles were discussed.

The first comprehensive analytical model for the temporal evolution of radar echoes after the heater turn-on was presented in chapter 5. It has been shown that Measuring radar echoes at multiple frequencies (especially at HF and VHF band) during PMSE heating experiment imposes enough information to estimate important plasma and dust parameters. Conducting these types of experiments in HF and VHF frequency band provide observables such as the maximum and minimum values of radar echoes (electron irregularity amplitude) and the

time at which these amplitudes are reached after the heater turn-on.

The irregularities generated at the boundary layer of dust cloud thought to be responsible to the PMSEs are discussed in chapter 6 and analyzed using theoretical and numerical simulation models. The similarities of the observed dust acoustic wave in the simulations with the measured electric field and electron density depletion associated with PMSE source region by sounding rocket were studied. The application of this study to other problems such as charged aerosol aerosols release experiment and laboratory dusty-plasma experiments was discussed.

Chapter 7 focuses on the positive dust particles which have been observed in recent in-situ experiments. The formation of positive dust particles on the cluster ions was considered to study the time evolution of the correlation and anti-correlation of plasma density fluctuations. The first explanation of the observed correlation and anti-correlation based on the measured dust parameters in the mesopause was introduced. The effect of positive dust particles on the temporal evolution of radar echoes during heating experiment was also studied.

The last two chapters are dedicated to Stimulated Electromagnetic Emissions SEE. Two parametric decay instabilities were studied extensively in theory and experiment. Variation of IA and EIC emission lines associated with MSBS process with heater pump parameters were studied. The first observations of SIBS instability during the heating near $3f_{ce}$ is shown and compared with the analytical model. Artificially created optical emission with pump heating near $2f_{ce}$ was also presented.

This research has made the following original contributions:

1. A comparison of the experimental data and computational model has demonstrated how the absolute amplitude of the pump-induced radar backscatter overshoot features vary with important dust and plasma parameters allowing these parameters to be extracted. The possibility of observing the turn-on overshoot in the HF radar band is discussed based on typical mesospheric parameters.

2. Considering that predicted enhancement of irregularity amplitude after heater turn-on in the HF band is the direct manifestation of the dust charging process in the space, it was shown that HF PMSE heating experiment has substantial potential as a diagnostic tool to shed light on the fundamental physics of charging that has been unresolved issue for decades. Based on our research at Virginia Tech a new HF radar is built by researchers at University of Lancaster and will be used in the future HF PMSE experiments.

3. The first comprehensive analytical model was developed based on the physical processes associated with temporal evolution of irregularities after the turn-on and turn-off of radio wave heating. It was found Measuring radar echoes at multiple frequencies imposes enough information to estimate important plasma and dust parameters. It is shown that active PMSE heating experiments involving multiple observing frequencies at 7.9 (HF), 56, and 224 MHz (VHF) may contribute to estimate dust density altitude profile, dust charge state variation during the heating cycle, and ratio of electron temperature enhancement in the

irregularity source region. It was noted that proposed remote sensing technique enable us to study the time variation of ice cloud that could be used to be compared with time evolution of carbon dioxide and methane in order to study the link between the formation of Polar Mesospheric Clouds PMCs and global climate change.

4. Basic physics of the evolution of relevant dusty plasma instabilities in the boundary layer of charged dust clouds was studied which is thought to play an important role in irregularity production in mesospheric dust layers and the artificially created dust clouds at higher altitudes in the ionosphere including space shuttle exhaust. It has been shown that the observed radar echoes associated with PMC and artificially created dust clouds could be related to the excited dust acoustic waves.

5. Variation of spatial structures of plasma and dust (ice) irregularities in the PMSE source region in the presence of positively charged dust particles is investigated. A new generation mechanism for the observed correlation and anti-correlation of fluctuations in the electron and ion densities in the background plasma is proposed considering the presence of positive dust particle formation.

6. Two parametric decay instabilities produced by interaction of high power electromagnetic waves in the ionosphere were studied extensively in experiment and theory. IA and EIC lines produced by MSBS process can be used to estimate electron temperature and ion compositions in the interaction region, respectively. The data from three research campaigns at HAARP were presented. The first observation of SIB scatter at $3f_{ce}$ was reported and corresponding theoretical model was introduced which validates the experimental observations. A correlation of appearance and disappearance of the Downshifted Peak DP and SIB scatter lines for $3f_{ce}$ heating was observed. The theory suggests the decay of the UH/EB pump field into another UH/EB mode and a broadband oblique IA mode as a generation mechanism for the downshifted peak between 1.2 kHz and 1.6 kHz that could occur at a different altitude relative to the SIBS generation region. Simultaneous observation of SIBS and airglow during heating near 2fce is presented which shows a correlation with the strength of optical emissions. This could shed light on the physical processes associated with artificial field alighted irregularities FAIs and electron precipitation. Evidence of enhanced electrostatic waves (i.e. UH) for $f_0 \approx f_{ce}$ were observed in simultaneous SuperDARN radar observations.

10.2 Future work

10.2.1 Electric Field and Dust Density Fluctuations via Neutral Turbulence Coupling

Neutral air turbulence can couple into mesospheric dust plasmas to generate electric fields and density fluctuations in the charged particle species including the electrons, ions and dust. A theoretical model has been provided for some of the important consequences by

Robertson, (2008). This also has some important consequences for measurement of electric field and potential measurements on rocket probes (Sternovsky et al., 2004). The model of section 2 may be utilized to demonstrate some of the important concepts. To model the neutral air turbulence a driving velocity field is considered to be of the sinusoidal form

$$\vec{v_n}(x,t) = \delta\vec{v_n} cos(kx - \omega t) \tag{10.1}$$

This monochromatic field will be used for demonstration purposes, however, a 'turbulent' spectrum could be constructed from a superposition of such fields. An acoustic wave is assumed with the dispersion relationship $\omega = kC_{ns}$ where $C_{ns} = \sqrt{\gamma_n KT_n/m_n}$ is the neutral sound speed. Assuming small amplitudes of the neutral fluctuations, a linearized continuity equation can be used to relate the fluctuating amplitude of the velocity field and the amplitude of the fluctuating neutral density

$$\delta v_n = C_{dn}\frac{\delta n_n}{n_{n0}} \tag{10.2}$$

The effectiveness of coupling into the dusty plasma is dependent upon at least two important paramenters as discussed by Robertson (2008). These include the wavenumber of the neutral turbulence k (or equivalently for the model in this case the frequency ω) and the relative density of the negative charged dust to charged density. An important result is that in a 'bite-out' region the electric field amplitude may be enhanced by neutral turbulence due to the reduction in electron density. Using linearized continuity and momentum equations for the charged particle species and neutral air and Poisson's equation, then simplified expressions relating the electron, ion, dust, and electric field to the neutral air fluctuations can be obtained as (Robertson, 2007)

$$\frac{\delta n_e}{n_{e0}} = \frac{i\omega\nu_{en}}{\omega^2 + \nu_{en}[i\omega - \gamma_e D_e k^2]}\left(\frac{\delta n_n}{n_{n0}}\right) \tag{10.3}$$

$$\frac{\delta n_i}{n_{i0}} = \frac{\delta n_n}{n_{n0}} \tag{10.4}$$

$$\frac{\delta n_d}{n_{d0}} = \left[\frac{1}{1 - i\omega/\nu_{dn}}\right]\frac{\delta n_n}{n_{n0}} \tag{10.5}$$

$$\delta\vec{E} = -ik\left(\frac{\gamma_e KT_e}{n_e q_e^2}\right)\left(\frac{n_i q_i + \frac{n_d Z_d q_d}{1 - i\omega/\nu_{dn}}}{1 + \gamma_e k^2\lambda_{De}^2}\right) \tag{10.6}$$

Equation (9.6) demonstrates that for $k\lambda_{De} \gg 1$ electron Debye shielding is ineffective and electric fields are effectively generated by the neutral turbulence by the bare ion and dust

charge. Due to reduced λ_{De} (and therefore reduced Debye shielding $k\lambda_{De} \ll 1$) in an electron bite-out region, electric fields may be expected to be enhanced by neutral turbulence. This also may have consequences for in-situ measurements. Due to the fact that typically the dust-neutral collision frequency ν_{dn} is much larger than the frequency associated with the frequency associated with the passage of the shock wave created around a measurement rocket payload with, from equation 9.5 then the dust fluctuation are much smaller than the neutral fluctuations $\delta n_d/n_{d0} \ll \delta n_n/n_{n0}$. In a bite-out region where there is a shock compression on the ions and not on the dust produces a positive charge in the wake of the shock which can be observed during measurements (Sternovsky et al., 2004). 'Fossil turbulence' refers to inhomogeneities in the dust density when neutral air turbulence is absent (Cho et al. 1996, Rapp and Lubken, 2003). The spatial scales of this turbulence of course do not match the dispersive nature of driving neutral air turbulence, i.e. $\omega = kC_{ns}$. It can typically be described within the Robertson (2007) model to be of spatial scales such that $\omega \ll kC_{ns}$. It was shown the electron and ion density fluctuations are out of phase in this case compared to active turbulence since the fluctuations are driven by the electric field force for fossil turbulence rather than the driving velocity field for active turbulence.

Figure 10.1 shows the simulation results of the coupling of the neutral wind with electron, ion, and dust density. The coupling of neutral wind with plasma densities is considered through the momentum equation, and dust-neutral collision equation is used to couple the neutral wind with the dust density. The figure shows the clear enhancement of electric fields by neutral turbulence in electron bite-out region as expected by the theory.

10.2.2 Numerical Model Improvement

The current physical model assumes that after the heater turn-on, electron temperature rises suddenly. This assumption may be valid for low values of the ratio between charge density of dust and electron charge density, throughout the PMSE layer, since the dust has little effect on the electron density. A new model for time evolution of electron temperature T_e during heating may consider the variation of electron temperature with time and as a function of electron density variation. Radio wave propagation in the ionospheric D region is described by the well known Appleton Hartree relation for refractive index:

$$n^2 = 1 - \frac{X}{1 - iZ - \frac{(Ysin(\theta))^2}{2(1-X-iZ)} \pm \sqrt{\frac{(Ysin(\theta))^4}{4(1-X-iZ)^2} + (Ycos(\theta))^2}} \tag{10.7}$$

where $X = \omega_{pe}^2/\omega^2$,$Y = \Omega_{ce}/\omega$ and $Z = \nu_{en}/\omega$ are the normalized frequencies, ω is the frequency of radio wave, θ is the angle between wave vector and the direction of the magnetic field, B is the earth's magnetic field, and ν_{en} is the electron-neutral frequency.

When electron neutral collision frequency $Z > 0$, imaginary part of refractive index n is negative and shows damping of the wave. The physical interpretation of damping is the

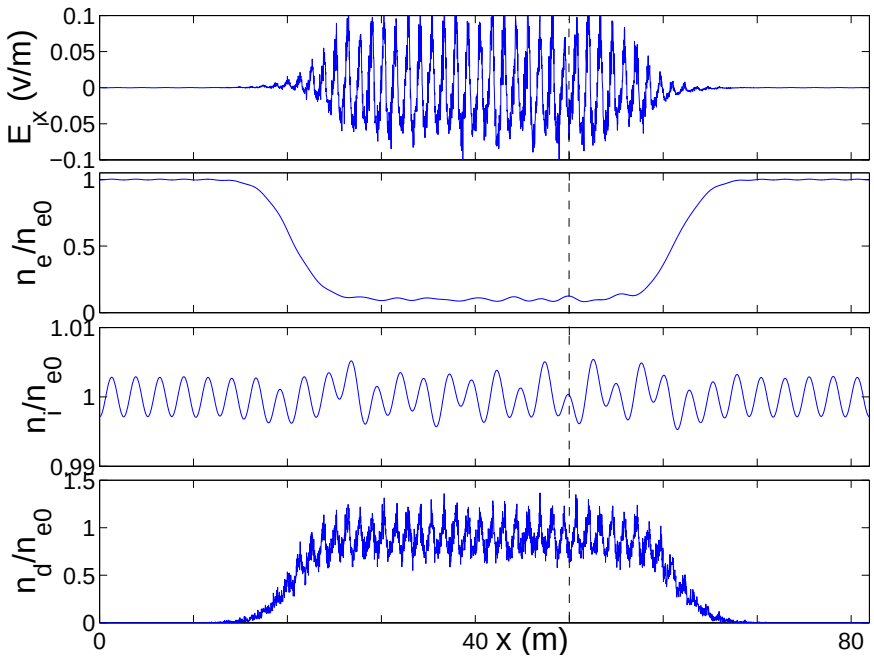

Figure 10.1: Figure shows the coupling of the neutral wind with electron, ion, and dust density. note electric fields is enhanced by neutral turbulence in electron bite-out region as expected by the theory.

wave energy transfer to plasma. Due to the huge mass difference between the electrons and ions, the electron approximately takes all of the transferred energy. Therefore, electron temperature enhancement during radio wave heating can be written as:

$$\frac{dT_e}{dt} = \frac{2}{3k_B N_e}\left(-Im(n\frac{2\omega I}{c}) - L\right) \tag{10.8}$$

where I is the intensity of the wave and should be calculated for each altitude

$$I = \frac{ERP}{4\pi h^2} e^{(\int_0^h \frac{2\omega}{c} Im(n) dh)} \tag{10.9}$$

The equilibrium state can be determined by solving this equation for $dT_e/dt = 0$. The model for electron density profile which is given by the Sodankyla Ion Chemistry SIS model (Turunen et al.,1996) should be used. L is the sum of all electron energy loss-functions (Prasad et al., 1973; Stubbe et al., 1972). The neutral atmosphere parameters are taken from MSISE90-model (Hedin, 1991). This method may show the effect of electron depletion on the ratio of electron temperature enhancement and how much heating is effective in the bite-out region.

Bibliography

Bibliography

Arp, O., K. Menzel, M. Klindworth, A. piel, A. Melzer, M. Wolter (2007), Self-excited dust density waves in the boundary region of a complex plasma under microgravity,*34th EPS conference on plasma phys. Warsaw*, 2-6 July 2007 ECA vol.31F, P-5.060.

Backhouse, T. W. (1885), The luminous cirrus cloud of June and July, Meteorol. Mag., 20, 133.

Bacmeister, J. T., M. R. Schoeberl, L. R. Lait, P. A. Newman, and B. L. Gary, ER-2 mountain wave encounter over Antarctica: Evidence for blocking, Geophys. Res. Lett., 17, 81 84, 1990.

Balsley, B. B., W. L. Ecklund, D. C. Fritts (1983), VHF echoes from high-latitude mesosphere and lower 390 thermosphere observations and interpretations. *J.Atmos.Sci.*, 40:2451.

Baumgarten, G., J. Fiedler, F.-J. Lubken, and G. von Cossart (2008), Particle properties and water content of noctilucent clouds and their interannual variation,*J. Geophys. Res.*, 113, D06203, doi:10.1029/2007JD008884.

Belova, E., P. B. Chilson, M. Rapp, and S. Kirkwood (2001), Electron temperature dependence of PMSE power,*Adv. Space Res.*, 28, 1077 1082.

Belova, E., Chilson, P. B., Rapp, M., and Rietveld, M. T.: The response time of PMSE to ionospheric heating, J. Geophys. Res., 108, 8446, doi:10.1029/2002JD002385, 2003.

Bernhardt, P. A., C. G. Park, and P. M. Banks (1975), Depletion of the F2 region ionosphere and the protonosphere by the release of molecular hydrogen,*Geophys. Res. Lett.*, 2(8), 341344, doi:10.1029/GL002i008p00341.

Bernhardt, P. A., L. M. Duncan, and C. A. Tepley (1988), Artificial airglow excited by highpower HF waves, Science, 242(4881), 1022.1027, doi:10.1126/science.242.4881.1022.

Bernhardt, P. A., L. S. Wagner, J. A. Goldstein, V. Y. Trakhtengerts, E. N. Ermakova, V. O. Rapoport, G. P. Komrakov, and A.M. Babichenko, Enhancement of stimulated electromagnetic emission during two frequency ionospheric heating, Phys. Rev. Lett., 72, 2879, 1994.

Bernhardt, P. A., G. Ganguli, M. C. Kelley, W. E. Swartz (1995), Enhanced radar backscatter from space shuttle exhaust in the ionosphere, *J. Geophys. Res.*, vol. 100, NO. A12, pages 23,811-23,818.

Bernhardt, P. A., J. D. Huba, W. E. Swartz, and M. C. Kelley (1998), Incoherent scatter from space shuttle and rocket engine plumes in the ionosphere,*J. Geophys. Res.*, 103, 2239-2251.

Bernhardt, P. A., and M. J. Sulzer (2004), Incoherent scatter measurements of ion beam disturbances produced by space shuttle exhaust injections into the ionosphere,*J. Geophys. Res.*, 109, A02303, doi:10.1029/2002JA009693.

Bernhardt, P. A., P. J. Erickson, F. D. Lind, J. C. Foster, and B. Reinisch(2005), Artificial disturbances of the ionosphere over the Millstone hill radar during dedicated burns of the space shuttle OMS engines,*J. Geophys.Res.*, 110, A05311, doi:10.1029/2004JA010795.

P. Bernhardt, C. Selcher, R. Lehmberg, S. Rodriguez, J. Thomason, M. McCarrick, and G. Frazer, Determination of the Electron Temperature in the Modified Ionosphere over HAARP using the HF Pumped Stimulated Brillouin Scatter (SBS) Emission Lines, Ann. Geophys., 27, pp. 44094427, 2009.

Bernhardt, P.A, J.B. Baumgardner, A. Bhatt, A. Coster, P.J. Erickson, C.R. Kaplan, R.A. Hasser, M.F. Larsen, F.D. Lind, T.R. Pedersen, R.F. Pfaff (2011), Ground and space-based measurment of rocket engine burns in the ionosphere,*IEEE Trans. Plamsa Sci.*, in press.

P. Bernhardt, C. Selcher, R. Lehmberg, S. Rodriguez, J. Thomason, M. McCarrick, and G. Frazer, Stimulated Brillouin Scatter in a Magnetized Ionospheric Plasma, Phy. Rev. Lett., 104, DOI: 10.1103/PhysRevLett.104.165004, 2010.

Bernhardt, P. A., C. A. Selcher, and S. Kowtha (2011), Electron and ion Bernstein waves excited in the ionosphere by high power EM waves at the second harmonic of the electron cyclotron frequency, Geophys. Res. Lett., 38, L19107, doi:10.1029/2011GL049390.

Bernstein, I. B. and I. N. Rabinowitz, 1959. Theory of electrostatic probes in a low density plasma,*Phys. Fluids*, vol. 2, pp. 112121.

Bharuthram, R., and M. Rosenberg, (1998), A note on the generation of fluctuations by Space Shuttle exhaust in the ionosphere. *Planet.Space Sci.* 46, 425.

Biebricher, A., O. Havnes, T. W. Hartquist, and C. La Hoz, 2006. On the influence of plasma absorption by dust on the PMSE overshoot effect, *Adv. Space Res.*, 38(11), 2541 2550, doi:10.1016/j.asr.2005.02.061.

Blix, T. A.: Small-scale plasma and charged aerosol variations and their importance for polar mesosphere summer echoes, Adv. Space Res., 24, 537546, 1999.

Blix, T. A., Bekkeng, J. K., Latteck, R., Lubken, F.-J., Rapp, M., Schoch, A., Singer, W., Smiley, B., and Strelnikov, B., 2003. Rocket probing of PMSE and NLC Results from the recent MIDAS/MACWAVE campaign, Adv. Space Res., 31(9), 2061 2067.

Brattli, A., Lie-Svendsen, ., Svenes, K., Hoppe, U.-P., Strelnikova, I., Rapp, M., Latteck, R., and Friedrich, M.: The ECOMA 2007 campaign: rocket observations and numerical modelling of aerosol particle charging and plasma depletion in a PMSE/NLC layer, Ann. Geophys., 27, 781-796, doi:10.5194/angeo-27-781-2009,2009.

Budden, K. G.: The Propagation of Radio Waves, Cambridge University Press, Cambridge, 1985.

Chandran, A., D. W. Rusch, A. W. Merkel, S. E. Palo, G. E. Thomas, M. J. Taylor, S. M. Bailey, and J. M. Russell III (2010), Polar mesospheric cloud structures observed from the cloud imaging and particle size experiment on the Aeronomy of Ice in the Mesosphere spacecraft: Atmospheric gravity waves as drivers for longitudinal variability in polar mesospheric cloud occurrence, *J. Geophys. Res.*, 115, D13102, doi:10.1029/2009JD013185.

Chen, C. and W.A. Scales, 2005. Electron temperature enhancement effects on plasma irregularities associated with charged dust in the Earth's mesosphere, *J. Geophys. Res., 110*, doi:10.1029/2005JA011341.

Chen, F. R.: Introduction to Plasma Physics and Controlled Fusion, New York, Plenum, 1984.

Chilson, P. B., E. Belova, M. T. Rietveld, S. Kirkwood, and U. Hoppe, 2000. First artificially induced modulation of PMSE using the EISCAT heating facility, Geophys. Res. Lett., 27, 3801 3804.

Cho, J., T. Hall, and M. Kelley (1992), On the Role of Charged Aerosols in Polar Mesosphere Summer Echoes,*J. Geophys. Res.*, 97(D1), 875-886.

Cho, J.Y.N., and Kelley, M.C., 1993. Polar mesospheric summer radar echoes: Observations and current theories, Rev. Geophys., 31, 243 265.

Cho, J. Y. N. (1993), Radar scattering from the summer polar mesosphere: Theory and observations, doctoral dissertation, Cornell Univ., Ithaca, New York.

Cho, J.Y.N., and J. Rottger (1997), An updated review of polar mesospheric summer echoes: Observation, theory, and their relationship to noctilucent clouds and subvisible aerosols, *J. Geophys. Res.*, 102, 2001 2020.

Croskey, C., J. Mitchell, M. Friedrich, K. Torkar, U. Hoppe, and R. Goldberg, 2001. Electrical structure of PMSE and NLC regions during the DROPPS program, Geophys. Res. Lett., 28, 1427 1430.

Dornbrack, A., Leutbecher, M., Kivi, R., Kyro, E. Mountain-wave induced record low stratospheric temperatures above northern Scandinavia. Tellus, Ser. A, 51:951963, 1999.

Durran, D. R., Klemp, J. B. Another look at downslope winds, part II, Nonlinear amplification beneath wave overturning layers. J.Atmos.Sci., 44:34023412, 1987.

Dysthe, K. B., E. Mjlhus, H. L. Pecseli, and K. Rypdal (1983), A thermal oscillating two-stream instability, Phys. Fluids, 26, 146, doi: http://dx.doi.org/10.1063/1.863993.

Eklund, W.L., and Balsley B.B., 1981. Long-term observations of the Artic mesophere with MST radar at Poker Flat, Alaska, J. Geophys. Res., 86, 7775.

Eliezer, S.: The Interaction of High-Power Lasers with Plasmas, Institute of Physics, Bristol, UK, 2002.

Farmer, D., Armi, L. Stratified flow over topography: The role of smale-scale entrainment and mixing in flow establishment. Proc.R.Soc.London, Ser. A, 455:32213258, 1999.

Fortov, V. E. , A. D. Usachev, A. V. Zobnin, et al (2003), Dust-acoustic wave instability at the diffuse edge of radio frequency inductive low-pressure gas discharge plasma, *Phys. Plasmas* 10, 1199 (2003); doi:10.1063/1.1563667.

Friedrich, M. and Rapp, M.: News from the Lower Ionosphere: A Review of Recent Developments, Surv. Geophys., 30, 525559, 2009.

Fritts, D. C., Tsuda, T., VanZandt, T. E., Smith, S. A., Sato, T., Fukao, S., Kato, S. Studies of velocity fluctuations in the lower atmosphere using the MU radar, II, Momentum fluxes and energy densities. J.Atmos.Sci, 47:5166, 1990.

Fritts, D. C. and M. J. Alexander (2003), Gravity wave dynamics and effects in the middle atmosphere, Rev. Geophys., 41(1), 1003, doi:10.1029/2001RG000106.

Gadsden, M., Schroder, W., 1989. Noctilucent Clouds. Springer, New York.

Ganguli, G., P. Bernhardt, W. Scales, P. Rodriguez, C. Siefring, and H. A. Romero [1993], Physics of Negative Ion Plasmas Created by Chemical Releases in Space, in T. Chang (ed.),*Physics of Space Plasmas* (1992), 12 (SPI Conference Proceedings and Reprint Series), Cambridge, Massachusetts, Scientific Publishers, Inc, p. 161.

Gelinas, L. J., Lynch, K. A., Kelley, M. C., Collins, S., Baker, S., Zhou, Q., and Friedman, J. S., 1998. First observation of meteoric charged dust in the tropical mesosphere, Geophys. Res. Lett., 25, 40474050.

Goldberg, R. A., et al. (2001), DROPPS: A study of the polar summer mesosphere with rocket, radar and lidar, *Geophys. Res. Lett.*, 28(8), 1407-1410.

Gumbel, J. and G. Witt (2001), Rocket-borne photometry of NLC particle populations, *Adv. Space Res.*, 28(7), 10531058.

Gustavsson, B., T. B. Leyser, M. Kosch, M. T. Rietveld, A. Steen, B. U. E. Brandstrom, and T. Aso (2006), Electron gyroharmonic effects in ionization and electron acceleration during highfrequency pumping in the ionosphere, Phys. Rev. Lett., 97, 195002, doi:10.1103/PhysRevLett.97.195002.

Hagfors, T. (1992), Note on the scattering of electromagnetic waves from charged dust particles in a plasma, J. Atmos. Terr. Phys., 54, 333338.

Hall, C. M., and J. Rttger (2001), Initial observations of polar mesospheric summer echoes using the EISCAT Svalbard Radar,*Geophys. Res. Lett.*, 28(1), 131 134, doi:10.1029/2000GL003821.

Havnes, O., J. Trim, T. Blix, W. Mortensen, L. I. Nsheim, E. Thrane, and T. Tnnesen (1996), First detection of charged dust particles in the Earth's mesosphere,*J. Geophys. Res.*, 101(A5), 10,83910,847, doi:10.1029/96JA00003.

Havnes, O., L. I. Nsheima, T. W. Hartquistb, G. E. Morfillb, F. Melandsa, B. Schleichera, J. Trimc, T. Blixc and E. Thranec (1996b), Meter-scale variations of the charge carried by mesospheric dust,*Planet.Space Sci.* Vol 44, 10.

Havnes, O., U. de Angelis, R. Bingham, C. K. Goertz, G. E. Morfil, and V. Tsytovich (1990), On the role of dust in the summer mesopause, J. Atmos. Terr. Phys., 52, 637 643.

Havnes, O., C. La Hoz, and L. L. Naesheim, First Observations of the PMSE overshoot effect and its use for investigating the conditions in the summer mesosphere, Geophys. Res. Lett., 30(23), 2229, doi:10.1029/ 2003GL018429,2003.

Havnes, O., Polar Mesospheric Summer Echoes (PMSE) overshoot effect due to cycling of artificial electron heating, J. Geophys. Res., 109, A02309, doi:10.1029/2003JA010159,2004.

Havnes, O., La Hoz, C., Biebricher, A., Kassa, M., Meseret, T., Naesheim, I., and Zivkovic, T.: Investigation of the Mesospheric PMSE Conditions by Use of the New Overshoot Effect, Physica Scripta Volume T, 107 , 70, 2004.

Hervig, M. E., L. L. Gordley, M. H. Stevens, S. M. Bailey, and G. Baumgarten (2008), Interpretation of SOFIE PMC measurements: Cloud identication and derivation of mass density, particle shape, and particle size,*J. Atmos. Sol. Terr. Phys.*, 71, 316 330, doi:10.1016/j.jastp.2008.07.009.

Hedin, A. E. (1991), Extension of the MSIS Thermosphere Model into the middle and lower atmosphere, J. Geophys. Res., 96(A2), 11591172, doi:10.1029/90JA02125.

Holmgren, G., R. Bostrm, M. C. Kelley, P. M. Kintner, R. Lundin, U. V. Fahleson, E. A. Bering, and W. R. Sheldon (1980), Trigger, An Active Release Experiment That Stimulated Auroral Particle Precipitation and Wave Emissions, *J. Geophys. Res.*, 85(A10), 50435053, doi:10.1029/JA085iA10p05043.

Hussein, A. A., and W. A. Scales (1997), Simulation studies of parametric decay processes associated with ionospheric stimulated radiation, Radio Sci., 32(5), 20992107, doi:10.1029/97RS01349.

Hussein, A. A., W. A. Scales, and J. Huang, Theoretical and simulational studies of broad upshifted sidebands generation in the ionospheric stimulated radiation, Geophys. Res. Lett., 25, 955-958, 1998.

Huang, J. and S. P. Kuo (1995), A generation mechanism for the downshifted peak in stimulated electromagnetic emission spectrum, J. Geophys. Res., 100(A11), 21,43321,438, doi:10.1029/95JA02302.

Hughes, J. M., W. A. Bristow, R. T. Parris, and E. Lundell (2003), SuperDARN observations of ionospheric heaterinduced upper hybrid waves, Geophys. Res. Lett., 30(24), 2276, doi:10.1029/2003GL018772.

Hysell, D. L. and Nossa, E.: Artificial E-region field-aligned plasma irregularities generated at pump frequencies near the second electron gyroharmonic, Ann. Geophys., 27, 2711-2720, doi:10.5194/angeo-27-2711-2009, 2009.

S. Ichimaru, Basic Principles Of Plasma Physics: A Statistical Approach, 1973.

Inhester, B., J. Klostermeyer, F. Lubken, and U. von Zahn (1994), Evidence for ice clouds causing polar mesospheric summer echoes, *J. Geophys. Res.*, 99(D10), 20937-20954.

Kassa, M., Havnes, O., and Belova, E.: The effect of electron bite-outs on artificial electron heating and the PMSE overshoot, Ann. Geophys., 23, 36333643, doi:10.5194/angeo-23-3633-2005, 2005.

Kennedy, P. J., Shapiro, M. A. Further encounters with clear air turbulence in research aircraft. J.Atmos.Sci., 37:986993, 1979.

Khalil,M . A. K., and R . A. Rasmussen, Global decrease in atmospheric carbon monoxide, Nature, 370, 639-641, 1994.

Kopp, E., P. Eberhardt, U. Herrmann, and L. G. Bjrn (1985), Positive Ion Composition of the High-Latitude Summer D Region With Noctilucent Clouds,*J. Geophys. Res.*, 90(D7), 13,04113,053, doi:10.1029/JD090iD07p13041.

Kosch, M. J., Pedersen, T., Mishin, E., Oyama, S., Hughes, J., Senior, A., Watkins, B., and Bristow, B.: Coordinated optical and radar observations of ionospheric pumping for a frequency pass through the second electron gyroharmonic at HAARP, J. Geophys. Res., 112, A06325, doi:10.1029/2006JA012,146, 2007.

Kruer, W. L.: The Physics of Laser Plasma Interactions, Addison- Wesley, New York, 1988.

La Hoz, C. (1992), Radar scattering from dusty plasmas, Phys. Scr., 45, 529534.

La Hoz, C., O. Havnes, L. I. Naesheim, and D. L. Hysell (2006), Observations and theories of Polar Mesospheric Summer Echoes at a Bragg wavelength of 16 cm, J. Geophys. Res., 111, D04203, doi:10.1029/2005JD006044.

La Hoz, C., and O. Havnes (2008), Artificial modification of polar mesospheric winter echoes with an RF heater: Do charged dust particles play an active role,*J. Geophys. Res.*, 113, D19205, doi:10.1029/2008JD010460.

La Hoz, C., O. Havnes, and M. Rietveld (2010), First joint measurements of the overshoot effect of Polar Mesospheric Summer Echoes (PMSE) at 54 and 224 MHz excited by artificial electron heating: AGU Fall Meeting Abstracts, pp. C7+.

Lee, N.C., and G.K Parks, Ponderomotive force in a warm two-frequency plasma, Phys. Fluids, 26, 724-729, 1983.

Leutbecher, M., Volkert, H. Propagation of mountain waves into the stratosphere: Quantitative evaluation of three-dimensional simulations. J.Atmos.Sci., 57:30903108, 2000.

Leyser, T. B., B. Thid6, H. Derblom, A. Hedberg, and B. Lundborg, Stimulated electromagnetic emission near electron cyclotron harmonics in the ionosphere, Phys. Rev. Lett., 63, 1145, 1989

Leyser, T. B., B. Thid, H. Derblom, . Hedberg, B. Lundborg, P. Stubbe, and H. Kopka (1990), Dependence of stimulated electromagnetic emission on the ionosphere and pump wave, J. Geophys. Res., 95(A10), 17,23317,244, doi:10.1029/JA095iA10p17233.

Leyser, T. B., B. Thide, S. Goodman, M. Waldenvik, E. Veszelei, S. M. Grach, A. N. Karashtin, G. P. Kom- rakov, and D. S. Kotik, Narrow cyclotron harmonic absorption resonances of stimulated electromagnetic emis- sion in the ionosphere, Phys. Rev. Left., 68, 3299, 1992.

Leyser, T. B.: Stimulated Electromagnetic Emissions By High-Frequency Electromagnetic Pumping Of The Ionospheric Plasma, Space Sci. Rev., 98, 223328, 2001.

Lie-Svenson, O., T. A. Blix, and U. P. Hoppe, Modeling the plasma response to small-scale aerosol particle perturbations in the mesopause region, J. Geophys. Res., 108(D8), 8442, doi:10.1029/2002JD002753,2003

Lilly, D. K., Kennedy, P. J. Observations of a stationary mountain wave and its associated momentum flux and energy dissipation. J.Atmos.Sci., 30:11351152, 1973.

Liu, C. S., and V. K. Tripathi (1986), Parametric instabilities in a magnetized plasma, Phys. Rep., 130, 143216, doi:10.1016/0370-1573(86)90108-0.

Li, Q., Rapp, M., Rottger, J., Latteck, R., Zecha, M., Strelnikova, I., Baumgarten, G., Hervig, M., Hall, C., and Tsutsumi, M.: Microphysical parameters of mesospheric ice clouds derived from calibrated observations of polar mesosphere summer echoes at Bragg wavelengths of 2.8m and 30 cm, J. Geophys. Res., 115, doi:10.1029/2009JD012271, 2010.

Lubken, F.-J., 1999. Thermal structure of the Arctic summer mesosphere. Journal of Geophysical Research 104, 91359149.

Mahmoudian, A., W. A. Scales, M. J. Kosch, A. Senior and M. Rietveld (2011), Dusty space plasma diagnosis using temporal behavior of polar mesospheric summer echoes during active modification, *Ann. Geophys.*, 29, 2169-2179, doi:10.5194/angeo-29-2169-2011.

Mahmoudian, A., and W. A. Scales (2012a), Irregularity excitation associated with charged dust cloud boundary layers, J. Geophys. Res., 117, A02304, doi:10.1029/2011JA017204.

Mahmoudian, A., and W. A. Scales (2012b), Temporal evolution of radar echoes associated with mesospheric dust clouds after turn-on of radiowave heating, J. Geophys. Res., doi:10.1029/2011JD017166, in press.

Megner, L., Gumbel, J., Rapp, M., and Siskind, D. E.: Reduced meteoric smoke particle density at the summer pole Implications for mesospheric ice particle nucleation, Adv. Space Res., 41, 4149, 2008.

Megner, L. and Gumbel, J.: Charged meteoric particles as ice nuclei in the mesosphere: Part 2 A feasibility study, J. Atmos. Sol. Terr. Phys., submitted, 2009.

Mityakov, N. A., V. O. Rapoport, and V. Y. Trakhtengerts (1975), Scattering of the extraordinary wave by small-scale irregularities near the reflection point, Radiophys. Quantum. Electron., 18(9), 1273 1278, doi:10.1007/ BF01038188.

Naesheim, L.I., O. Havnes, and C. La Hoz, A comparison of polar mesosphere summer echo at VHF (224 MHz) and UHF (930 MHz) and the effects of artificial electron heating, J. Geophys. Res., 113, D08205, doi:10.1029/2007JD009245, 2008.

Nance, L. B., Durran, D. D. A modeling study of nonstationary trapped mountain lee waves, part II, Nonlinearity. J.Atmos.Sci., 55:1429 1445, 1998.

Nastrom, G. D., Fritts, D. C. Source of mesoscale variability of gravity waves, part I, Topographic excitation. J.Atmos.Sci., 49:101110, 1992.

Natanson, G. L., On the theory of the charging of amicroscopic aerosol particles as a result of capture of gas ions, Sov. Phys. Tech. Phys., Engl. Transl., 5, 538 551, 1960.

Norin, L., S. M. Grach, T. B. Leyser, B. Thide, E. N. Sergeev, and M. Berlin (2008), Ionospheric plasma density irregularities measured by stimulated electromagnetic emission, J. Geophys. Res., 113, A09314, doi:10.1029/2008JA013338.

Norin, L., Leyser, T. B., Nordblad, E., Thide, B., and McCarrick, M.: Unprecedentedly strong and narrow electromagnetic emissions stimulated by high-frequency radio waves in the ionosphere, Phys. Rev. Lett., 102, 065003, doi:PhysRevLett 102.065003, 2009.

Nygren, T., (1996),Introduction to incoherent scatter measurments, Inversoy, Sodankyla, Finland.

Pedersen, T. R., and E. A. Gerken (2005), Creation of visible artificial optical emissions in the aurora by highpower radio waves, Nature, 433(7025), 498.500, doi:10.1038/nature03243.

Pedersen, T., B. Gustavsson, E. Mishin, E. Kendall, T. Mills, H. C. Carlson,a nd A. L. Snyder (2010), Creation of artificial ionospheric layers using high power HF waves, Geophys. Res. Lett., 37, L02106, doi:10.1029/2009GL041895, 2010

Pfaff, R., et al , Rocket probe observations of electric field irregularities in the polar summer mesosphere, 2001 Geophys. Res. Lett. 28 1431

M. Porkolab, Parametric Instabilities in a Magnetic Field and Possible Applications to Heating of Plasmas, J. Nuclear Fusion,12, pp. 329-, 1972.

Prasad, S. S. and D. R. Furman, Electron cooling by molecular oxygen, J. Geophys. Res., 78, 67016707, 1973.

Ramos, C., M. C. Kelley, F. T. Djuth, K. M. Groves, Y. Murayama, S. Kawamura, and D. Thorsen, Multifrequency observations of Polar Mesosphere Summer Echoes using Alaskan radar facilities: Comparisons and scattering calculations, Radio Sci., 44, RS5011,2009 doi:10.1029/2008RS004102.

Rapp, M.: Capture rates of electrons and positive ions by mesospheric aerosol particles, J. Aerosol Sci., 31, 13671369, 2000.

Rapp, M., Lubken, F.-J., Mullemann, A., Thomas, G.E., Jensen, E.J., 2002. Small scale temperature variations in the vicinity of NLC: experimental and model results. Journal of Geophysical Research 107 (D19).

Rapp, M. and Lubken, F.J.: Polar mesosphere summer echoes (PMSE): review of observations and current understanding. Atmos. Chem. Phys. 4, 26012633, 2004.

Rapp, M., and G. E. Thomas (2006), Modeling the microphysics of mesospheric ice particles: Assessment of current capabilities and basic sensitivities, J. Atmos. Sol. Terr. Phys., 68(7), 715744, doi:10.1016/j. jastp.2005.10.015.

Reid, G. C. (1990), Ice particles and electron "bite-outs" at the summer polar mesopause,*J. Geophys. Res.*, 95, 13,891- 13,896.

Robertson, S., Hornyi, M., Knappmiller, S., Sternovsky, Z., Holzworth, R., Shimogawa, M., Friedrich, M., Torkar, K., Gumbel, J., Megner, L., Baumgarten, G., Latteck, R., Rapp, M., Hoppe, U.-P., and Hervig, M. E.: Mass analysis of charged aerosol particles in NLC and PMSE during the ECOMA/MASS campaign, Ann. Geophys., 27, 1213-1232, doi:10.5194/angeo-27-1213-2009, 2009.(*http* : *//www.ann* − *geophys.net/special*$_i$*ssue*219.*html*)

Robertson, S. and Z., Sternovsky, (2008), Effect of the induced-dipole force on charging rates of aerosol particles, Physics of Plasmas, 15,040702.

Rosenberg, M., P.A.Bernhardt, S.E.Clark (2011), Excitation of ion waves by charged dust beams in ionospheric aerosol release experiments,*Planet.Space Sci.* Vol 59, 4.

Rottger, J., Polar mesosphere summer echoes: dynamics and aeronomy on the mesosphere, Adv. Space Res., 14, (9)123(9)137, 1994.

Routledge, G., Kosch, M. J., Senior, A., Kavanagh, A. J., McCrea, I. W., and Rietveld, M. T.: A statistical survey of electron temperature enhancements in heater modulated polar mesospheric summer echoes at EISCAT, J. Atmos. Sol.-Terr. Phys., 73, 472482, 2011.

Russell, J. M., et al. (2009), Aeronomy of Ice in the Mesosphere (AIM): Overview and early science results, J. Atmos. Sol. Terr. Phys., 71, 289299, doi:10.1016/j.jastp.2008.08.011.

A. Samimi, W. A. Scales, P. A. Bernhardt, S. J. Briczinski, C. A. Selcher, and M. J. McCarrick (2012a), On Ion Gyro-Harmonic Structuring in the Stimulated Electromagnetic Emission Spectrum During Second Electron Gyro-Harmonic Heating, submitted to Ann. Geophys.

A. Samimi, W. A. Scales, H. Fu, P. A. Bernhardt, S. J. Briczinski, and M. J. McCarrick (2012b), Ion Gyro-Harmonic Structures in Stimulated Radiation During Second Electron Gyro-Harmonic Heating: Part I: Theory, submitted to J. Geophys. Res.

Scales, W. A., G. Ganguli, P. A. Bernhardt, M. Lampe (1998), Wave Generation Associated with Dust Cloud Expansion into a Plasma, *Physica Scripta.,* Vol. T75, 238-240.

Scales, W. A., P. A. Bernhardt, G. Ganguli, C. L. Siefring, and P. Rodriguez (1994), Small-scale plasma irregularities produced during electron attachment chemical releases, *Geophys. Res. Lett.*, 21(7), 605-608.

Scales. W.A, M. Ranade Bordikar, A. Mahmoudian and H. Fu (2010), Irregularities Associated With Creation of Dusty Plasmas in the Near-Earth Space Environment,*IEEE Trans. Plamsa Sci.*, VOL. 38, NO. 4.

Scales, W.A, and G. Ganguli (2004a), Electrodynamic structure of charged dust clouds in the earth's middle atmosphere, *New J. Phys.* 6, 12.

Scales, W.A, and G. Ganguli (2004b), Investigation of plasma irregularity sources associated with charged dust in the earth's mesosphere, *Advances in Space Research*, Vol 34, Issue 11, pp.2402-2408.

Scales, W. A. (2004), Electron temperature effects on small-scale plasma irregularities associated with charged dust in the earth's mesosphere,*IEEE Trans. Plamsa Sci.*, 32, 724.

Scales, W. A. and C. Chen (2008), On initial enhancement of mesospheric dust associated plasma irregularities subsequent to radio wave heating,*Annales Geophysicae,* Vol 26, Issue 8, pp.2265-2271

Scales, W. A., M. R. Bordikar, A. Samimi, P. A. Bernhardt, S. Briczinski, C. A. Selcher, and M. McCarrick (2011), Observations and theory of ion gyro-harmonic structures in the stimulated radiation spectrum during second electron gyro-harmonic heating, General Assembly and Scientific Symposium, URSI, doi:10.1109/URSIGASS.2011.6051126.

G. Schmidt, Physics of High Temperature Plasmas, Academic Press, 1966.

Senior, A., M. T. Rietveld, M. J. Kosch, and W. Singer (2010), Diagnosing radio plasma heating in the polar summer mesosphere using cross modulation: Theory and observations, *J. Geophys. Res.*, 115, A09318, doi:10.1029/2010JA015379.

Shukla, P. K., and A. A. Mamun (2002), Introduction to Dusty Plasma Physics (IOP Publishing, Bristol).

P. K. Shukla and L. Stenflo, Stimulated Brillouin scattering of electromagnetic waves in magnetized plasmas, Journal of Plasma Physics (2010), 76 : pp 853-855

Shutts, G. J., Kitchen, M., Hoare, P. H. A large amplitude gravity wave detected by radiosonde. Meteorol.Mag., 117:306310, 1988.

Smiley, B., S. Robertson, M. Horanyi, T. Blix, M. Rapp, R. Latteck, and J. Gumbel, Measurement of positively and negatively charged particles inside PMSE during MIDAS SOLSTICE 2001, J. Geophys. Res., 108(D8), 8444, doi:10.1029/2002JD002425, 2003.

Smith, R. B. A measurement of mountain drag. J.Atmos.Sci., 35:16441654, 1978.

Stubbe, P., and W. S. Varnum, Electron energy transfer rates in the ionosphere, Planet. Space Sci., 20, 11211126, 1972.

Thide, B., H. Kopka, and P. Stubbe (1982), Observation of stimulated scattering of a strong high frequency radio wave in the ionosphere, Phys. Rev. Lett., 49, 1561-1564, doi:10.1103/PhysRevLett.49.1561.

Thide, B., H. Derblom, . Hedberg, H. Kopka, and P. Stubbe (1983), Observations of stimulated electromagnetic emissions in ionospheric heating experiments, Radio Sci., 18, 6, 851-859, doi:10.1029/RS018i006p00851.

Thide, B., Sergeev, E.N., Grach, S.M., Leyser, T.B., Carozzi, T.D. Competition between langmuir and upper-hybrid turbulence in a high-frequency-pumped ionosphere. Phys. Rev. Lett. 95 (25), 255002, 2005.

Thomas, G.E., 1991. Mesopheric clouds and the physics of the mesopause region. Reviews of Geophysics 29, 553575.

Thomas, G. E., and J. J. Olivero (2001), Noctilucent clouds as possible indicators of global change in the mesosphere, Adv. Space Res., 28(7), 937 946.

Turunen, E., Collis, P.N., and Turunen, T.: Incoherent scatter spectral measurements of the summertime high-latitude D-region with the EISCAT UHF radar, J. Atmos. Terr. Phys. 50 , p. 289, 1988.

Ulwick, J. C., K. D. Baker, M. C. Kelley, B. B. Balsley, and W. L. Ecklund (1988), Comparison of simultaneous MST radar and electron density probe measurements during STATE,*J. Geophys. Res.*, 93, 69897000.

Varney, R. H., M. C. Kelley, M. J. Nicolls, C. J. Heinselman, and R. L. Collins (2011), The electron density dependence of polar mesospheric summer echoes, J. Atmos. Solar-Terr. Phys., 73, 2153-2165, doi:10.1016/j.jastp.2010.07.020.

Vaclivik, J., M.L. Sawley, and F. Anderegg, The ponderomotive force in a magnetized plasma: the effect of radio-frequency-induced magnetization, Phys. Fluids, 29, 2034-2037, 1986.

Von Savigny, C., Petelina, S. V., Karlsson, B., Llewellyn, E. J., Degenstein, D. A., Lloyd, N. D., and Burrows, J. P.: Vertical variation of NLC particle sizes retrieved from Odin/OSIRIS limb scattering observations, Geophys. Res. Lett., 32, L07806, doi:10.1029/2004GL021982, 2005.

Winske D., and M. Rosenberg (1998), Nonlinear development of the dust acoustic instability in a collisional dusty plasma,*IEEE Trans. Plasma Sci.*, vol. 26, pp. 92-99.

Winkler, P. M., Steiner, G., Vrtala, A., Vehkamaki, H., Noppel, M., Lehtinen, K. E. J., Reischl, G. P., Wagner, P. E., and Kulmala, M.: Heterogeneous nucleation experiments bridging the scale from molecular ion clusters to nanoparticles, Science, 319, 13741377, 2008.

Wong, A. Y., G. J. Morales, D. Eggleston, J. Santoru, and R. Behnke (1981), Rapid conversion of electromagnetic waves to electrostatic waves in the ionosphere, Phys. Rev. Lett., 47(18), 1340 1343, doi:10.1103/ PhysRevLett.47.1340.

Winske, D., S. P. Gary, M. E. Jones, M. Rosenberg, V. W. Chow, and D. A. Mendis (1995), Ion heating in a dusty plasma due to the dust/ion acoustic instability, Geophys. *Res. Lett.*, 22(15), 2069-2072, doi:10.1029/95GL01983.

Witt, G., Martin Lof, J., Wilhelm, N., Smith, W.S., 1964. High latitude summer mesospheric temperatures and winds with particular regard to noctilucent clouds. Space Research V, 820821.

Wu, B. J. C. (1975), Possible water vapor condensation in rocket exhaust plumes, AIAA J., 13, 797-802.

Xi, H. and W. A. Sclaes, Numerical simulation studies on the broad upshifted maximum of ionospheric stimulated electromagnetic emission, J. Geophys. Res., 106, 12,787-12,801, 2001.

Yeh, K. C.: and CH Liu, IonosphericWaves, Academic Press, 1972.

Zargham, S., and C. E. Seyler (1987), Collisional Interchange Instability, 1. Numerical Simulations of Intermediate-Scale Irregularities, J. Geophys. Res., 92(A9), 10,07310,088, doi:10.1029/JA092iA09p10073.